

OBSERVATIONS AND MODELS OF INFRARED DEBRIS DISK SIGNATURES
AND THEIR EVOLUTION

by
András Gáspár

A Dissertation Submitted to the Faculty of the
DEPARTMENT OF ASTRONOMY
In Partial Fulfillment of the Requirements
For the Degree of
DOCTOR OF PHILOSOPHY
In the Graduate College
THE UNIVERSITY OF ARIZONA

2011

THE UNIVERSITY OF ARIZONA
GRADUATE COLLEGE

As members of the Dissertation Committee, we certify that we have read the dissertation prepared by András Gáspár entitled “Observations and models of infrared debris disk signatures and their evolution” and recommend that it be accepted as fulfilling the dissertation requirement for the Degree of Doctor of Philosophy.

Dr. George Rieke

Date: 3 November 2011

Dr. Dimitrios Psaltis

Date: 3 November 2011

Dr. Feryal Özel

Date: 3 November 2011

Dr. Kate Y. L. Su

Date: 3 November 2011

Dr. Dániel Apai

Date: 3 November 2011

Final approval and acceptance of this dissertation is contingent upon the candidate's submission of the final copies of the dissertation to the Graduate College.

I hereby certify that I have read this dissertation prepared under my direction and recommend that it be accepted as fulfilling the dissertation requirement.

Dissertation Director: Dr. George Rieke

Date: 3 November 2011

STATEMENT BY AUTHOR

This dissertation has been submitted in partial fulfillment of requirements for an advanced degree at The University of Arizona and is deposited in the University Library to be made available to borrowers under rules of the Library.

Brief quotations from this dissertation are allowable without special permission, provided that accurate acknowledgment of source is made. Requests for permission for extended quotation from or reproduction of this manuscript in whole or in part may be granted by the head of the major department or the Dean of the Graduate College when in his or her judgment the proposed use of the material is in the interests of scholarship. In all other instances, however, permission must be obtained from the author.

SIGNED: András Gáspár

ACKNOWLEDGMENTS

The path one walks down to reach the stage in life where they can actually sit down to write an acknowledgment for their doctoral thesis is extremely long, full of curves and obstacles. Along the way, I have met so many people that have influenced, guided, and helped me that listing them all is mere impossible and would over-tower the thesis itself.

The credit for teaching me how to write properly goes out to my Mother, who put a lot of effort into teaching me about languages and literature. Obviously, the biggest influence was that of my Father, who being a physical-chemist himself, always bestowed the logic of a scientist on me and allowed me to pursue and nurtured all of the interests I developed over the years. My elementary and high school physics teachers, Mihály Kotormán and Dr. Ervin Szegedi, were also invaluable in opening my eyes to the wonderful world of physics.

I have great deal of appreciation for all my previous advisors who took upon the task of advising me. If it were not for Dr. László L. Kiss, I would definitely not have started doing research as early as I have and maybe not even in astronomy. He taught me all the initial tools an astronomer needs to know and that I still use today. Dr. Zoltán Balog was not only a great advisor, but also a friend who I could and still can count on. It was absolutely his influence that I started working in infrared astronomy and that I applied to the University of Arizona later on. I am also thankful for Dr. Melvin G. Hoare for giving me an opportunity to work on the Science Verification phase of the UKIDSS project in Leeds, in the summer of 2005. I also thank Kate Su for the help she gave with my first two papers at Steward. I am grateful to Dr. Dimitrios Psaltis and Dr. Feryal Özel for teaching me how to correctly and professionally approach a numerical coding project and for devoting all the time they did to the final part of my thesis. Without their help this thesis would have turned out differently.

I do have many people to thank and acknowledge. One special person however, my advisor Dr. George Rieke, does stand out from the crowd. He has, next to his vast amount of duties, somehow always found time to advise me. He always gave just the right amount of a push to get me going and always took interest in my personal problems. He is someone who genuinely cares how his students are doing. He always has and always will inspire me.

Last, but not least, I thank all my friends who have been part of my life and supported me over the years. Zoltán Makai, Suresh Sivanandam, Dennis Just, Alan Cooney and many others, thank you for all the fun times! And thank you, my best friend, my dear wife, Bori, for everything, for your support, your understanding and all the joy I have gotten over the years. You make all this work and invested time have a meaning. Thank you.

DEDICATION

I dedicate this thesis to my past, my present and my future.

My past being my grandparents, who have all taught me so many valuable lessons in life and how to be a good person. They will always be an example to follow.

My present being my mother, Irén, my father, Vilmos, my sister, Judit and my wife, Bori. You have been with me throughout the struggles and the joyous moments. You have encouraged me and given me goals to reach.

And my future being our little baby, whom I don't even know yet, but cannot wait to see in February. You and Mommy are the single reason this is all worth doing.

TABLE OF CONTENTS

LIST OF FIGURES	9
LIST OF TABLES	11
ABSTRACT	12
CHAPTER 1 INTRODUCTION	14
1.1 Motivation	14
1.2 Extrasolar planets	15
1.3 Star and planet formation	18
1.4 Circumstellar debris disks	24
1.5 The solar system's debris disk	26
1.6 Outline of the thesis	27
CHAPTER 2 FALSE SIGNS OF DEBRIS DISKS	29
2.1 Introduction	29
2.2 Observations and Data Reduction	32
2.3 The Bow Shock Model	37
2.3.1 Physical description of the model	38
2.3.2 Model Geometry and Parameters	40
2.3.3 Results	42
2.4 Discussion	50
2.4.1 Bow Shock Model Results	50
2.4.2 ISM Interactions	52
2.4.3 Implications for Diffusion/ Accretion Model of λ Boötis Phenomenon	54
2.5 Summary	55
CHAPTER 3 DEBRIS DISK STUDY OF PRAESEPE	57
3.1 Introduction	58
3.2 Observations, data reduction, and photometry	61
3.3 Catalog surveys and the final sample	64
3.4 Results	74
3.4.1 Color-color selection	74
3.4.2 The SED fit selection	81
3.4.3 Praesepe white dwarfs	81
3.4.4 Debris Disk Candidates	81
3.5 Discussion	84
3.5.1 Calculating errors on debris disk fractions	85
3.5.2 The decay of the debris disk fraction in early-type stars	86
3.5.3 The decay of the debris disk fraction for solar-type stars	89

TABLE OF CONTENTS — *Continued*

3.5.4	Evolutionary differences between the debris disks around early- and solar-type stars	92
3.5.5	The results in context with the Late Heavy Bombardment	95
3.6	Summary	97
CHAPTER 4 MODELING COLLISIONAL CASCADES IN DEBRIS DISKS		102
4.1	Introduction	102
4.2	The physical and numerical challenges of modeling debris disks	105
4.2.1	Collisional outcomes	110
4.2.2	Incorporating the complete redistribution integral	112
4.2.3	The effect of radiation forces	112
4.3	The collisional model	113
4.3.1	The evolution equation	114
4.3.2	The collisional term	118
4.3.3	Collision outcomes	120
4.3.4	The initial distribution and fiducial parameters	125
4.4	Simplified Dynamics	125
4.4.1	Collisional velocities	128
4.4.2	Reduced collisional probabilities of β critical particles	129
4.4.3	Reduced collisional probabilities of the largest particles	131
4.5	Results	132
4.5.1	Comparison to Thébault et al. (2003)	133
4.5.2	Comparison to Löhne et al. (2008) and Wyatt et al. (2011)	137
4.6	Conclusions	145
CHAPTER 5 STEEP DUST-SIZE DISTRIBUTIONS		146
5.1	Introduction	146
5.2	Numerical modeling	147
5.2.1	Evolution of the reference model	148
5.2.2	The dependence of the steady-state distribution function on the collision parameters	152
5.2.3	The dependence of the steady-state distribution function on system variables	156
5.2.4	The dependence of the steady-state distribution function on numerical parameters	157
5.2.5	The time to reach steady-state	158
5.2.6	The robustness of the solution	159
5.3	Synthetic Spectra	160
5.4	Relation between the particle mass distribution and the SED	163
5.5	Comparison to observations	165
5.6	Conclusions	167

TABLE OF CONTENTS — *Continued*

CHAPTER 6	THESIS CONCLUSIONS	171
6.1	Summary	171
6.2	Future Work	174
6.2.1	Evolution of the particle size distribution slope	175
6.2.2	Warm debris disk models	175
6.2.3	Stochastic events and debris disk evolution	176
6.2.4	Debris disk haloes	179
APPENDIX A	AGE AND DISTANCE ESTIMATE OF PRAESEPE	180
APPENDIX B	STRENGTH CURVES	188
APPENDIX C	MASS CONSERVATION OF THE COLLISIONAL MODEL	191
APPENDIX D	NUMERICAL EVALUATION OF THE COLLISIONAL MODEL AND VERIFICATION TESTS	193
D.1	Taylor series expansion of T_I	193
D.2	Verification of the numerical precision of T_I	197
D.3	Numerical evaluation of T_{II}	199
D.4	Convergence tests	201
D.5	The ODE solver	203
REFERENCES	205

LIST OF FIGURES

1.1	The distribution of known extrasolar planets in the mass/semi-major axis phase space	16
1.2	The early evolutionary stages of planets and planetary systems . .	19
1.3	The decay of planetary circumstellar primordial disks	21
1.4	The Fomalhaut debris disk	24
1.5	The β Pic debris disk	25
2.1	The $24\ \mu\text{m}$ images of δ Velorum	36
2.2	The $70\ \mu\text{m}$ images of δ Velorum	37
2.3	Nomenclature of angles	43
2.4	Morphology of the bow shock at δ Velorum.	44
2.5	Constrainment of the model parameters	45
2.6	The avoidance distance as a function of grain size	46
2.7	Constraining the dynamical parameters of interaction	47
2.8	Determining the density of the ISM	49
2.9	Model images of δ Velorum	50
2.10	Calculated temperature distribution of the bow shock	51
2.11	Model subtracted images	52
2.12	Spectral energy distribution of the model	53
2.13	λ Boötis spectral comparison	55
3.1	Praesepe Observed field	62
3.2	The $24\ \mu\text{m}$ photometry errors of Praespe	63
3.3	Spatial distribution and CMD position of sources	66
3.4	Completeness limit of the $24\ \mu\text{m}$ sample	67
3.5	Determining the K_S -24 zero point	68
3.6	The color-color plot of Praesepe	76
3.7	Images for the debris disk candidate stars	80
3.8	SED fits of excess candidate sources	82
3.9	Decay of excess	99
3.10	Excess decay in binned data set	100
3.11	Probability of LHB like event	101
4.1	Illustration of the possible outcome scenarios of collisions	108
4.2	Values for the radiation-force parameter β around stars	115
4.3	Radiation force blowout vs. Poynting-Robertson drag timescales . .	117
4.4	The outcome possibilities as a function of colliding masses	121
4.5	Collision probabilities as a function of particle mass and eccentricity	130
4.6	Distribution evolution compared to Thébault et al. (2003)	135
4.7	Mass evolution compared to Thébault et al. (2003)	136

LIST OF FIGURES — *Continued*

4.8	Distribution evolution compared to Löhne et al. (2008) and Wyatt et al. (2011)	138
4.9	Mass evolution compared to Löhne et al. (2008) and Wyatt et al. (2011)	138
4.10	Binned mass evolution compared to Löhne et al. (2008)	139
4.11	The effects of varying collisional weights in the Löhne et al. (2008) runs on the distribution evolution	140
4.12	The effects of varying collisional weights in the Löhne et al. (2008) runs on the mass evolution	141
4.13	Evolution of the particle size distribution compared to the Löhne et al. (2008) and Wyatt et al. (2011) models.	142
5.1	Evolution of the reference model	150
5.2	The model's dependence on η_0 and M_{tot}	151
5.3	The model's dependence on α and b	153
5.4	The model's dependence on Q_{sc}, S and s	154
5.5	The model's dependence on R	157
5.6	The model's dependence on δ	158
5.7	The compiled effects of the variables	159
5.8	Silicate absorption efficiencies	161
5.9	Synthetic SEDs	162
5.10	Observed SEDs in the submillimeter and millimeter	168
A.1	Isochrone fitting	185
A.2	Isochrone fitting 2.	186
A.3	Best fitting isochrone of Praesepe	187
D.1	The values of $G(m, m')$ as a function of the colliding masses	194
D.2	The largest X fragment produced by collisions	198
D.3	The error in the integration of T_I	200
D.4	Iso-size contours for the produced Y fragments as a function of the colliding body sizes and interaction velocities	201
D.5	Description of the integration method used for T_{II}	202
D.6	Convergence test results of our code	203
D.7	Numerical accuracy and speed of our ODE solver	204

LIST OF TABLES

2.1	The parameters of δ Velorum	35
3.1	Photometry of Praesepe members in the [24] band	69
3.2	The probabilities of chance alignments for excess sources	79
3.3	The field star sample excess ratios for early-type stars	87
3.4	The cluster star sample excess ratios for early-type stars	88
3.5	The field star sample excess ratios for solar-type stars	90
3.6	The cluster star sample excess ratios for solar-type stars	91
3.7	The percent of debris disks in rebinned distributions, as a function of spectral-types.	94
4.1	The variables used in the model and their fiducial values	126
4.2	Parameters used for comparison models	132
5.1	The variables used in the reference model	149
5.2	Observational data of debris disks	166
A.1	The distance-modulus of Praesepe in the literature.	181
A.2	The solutions for the fitting of isochrones	184

ABSTRACT

In my thesis I investigate the occurrence of mid-infrared excess around stars and their evolution. Since the launch of the first infrared satellite, *IRAS*, we have known that a large fraction of stars exhibit significant levels of infrared emission above their predicted photospheric level. Resolved optical and infrared images have revealed the majority of these excesses to arise from circumstellar disk structures, made up of distributions of planetesimals, rocks, and dust. These structures are descriptively called debris disks.

The first part of my thesis analyzes the *Spitzer Space Telescope* Observations of δ Velorum. The $24\ \mu\text{m}$ *Spitzer* images revealed a bow shock structure in front of the star. My analysis showed that this is a result of the star's high speed interaction with the surrounding interstellar medium. We place this observation and model in context of debris disk detections and the origin of λ Boötis stars.

The second part of my thesis summarizes our observational results on the open cluster Praesepe. Using $24\ \mu\text{m}$ data, I investigated the fraction of stars with mid-infrared excess, likely to have debris disks. I also assembled all results from previous debris disk studies and followed the evolution of the fraction of stars with debris disks.

The majority of debris disks systems are evolved, few hundred million or a Gyr old. Since the dissipation timescale for the emitting dust particles is less than the age of these systems, they have to be constantly replenished through collisional grinding of the larger bodies. The last two chapters of my thesis is a theoretical analysis of the collisional cascade in debris disks, the process that produces the constant level of dust particles detected. I introduce a numerical model that takes into account all types of destructive collisions in the systems

and solves the full scattering equation. I show results of comparisons between my and other published models and extensive verification tests of my model. I also analyze the evolution of the particle size distribution as a function of the variables in my model and show that the model itself is quite robust against most variations.

CHAPTER 1

INTRODUCTION

1.1 Motivation

The genuine curiosity of mankind to understand the universe we live in has always been the driving force for our cognitive and technological evolution. We want to understand how the world around us formed and how we in it came to be. From the very early Greek philosophers, such as Epicurus (*"There are infinite worlds both like and unlike this world of ours"*), to modern luminaries, such as Kant, all intellectual thinkers have wondered about the possibility of life occurring elsewhere in this Universe. Our perspective of our place in the Universe has been constantly reevaluated over the centuries, from Geocentric through Heliocentric to a non-specifiable location, diminishing our special centrally located position. We now understand that the single thing that makes Earth, the solar system and the Milky Way special, is that we are in it. Our Sun is just one of $\sim 1 \times 10^{23}$ other stars in the world, making us absolutely insignificant and the possibility of other life forms existing not insignificant. The quest to know whether we are alone and to map the extent of our world is an ancient driving force that has led to the discovery of the New World over five hundred years ago and to humankind's greatest technical achievement so far, the Moon landings.

We have proposed the existence of life even within the solar system already, under the ice shelves of Europa, in the old dried out water flows of Mars, on the surface of Titan, and have been conducting endless endeavors to find it. We have also been increasing ambitious in searching for habitable planets around other stars, so far with slim results, to keep the idea alive that other intelligent life forms can also exist. We have found over 700 planets orbiting other stars (or

extrasolar planets), and their numbers keep rising. However, majority of them are gas giants in close orbits, some in further orbits, and only a very few of them are Super Earths. We are yet to detect an Earth mass planet orbiting in the habitable zone of a late spectral type star, the types of stars that live long enough to support the evolution of an intelligent life form on one of their planets. Human kind has embarked on one of its likely endless and final quests, to find another habitable planet and possibly intelligent life somewhere else in the Universe.

1.2 Extrasolar planets

When Galileo Galilei turned his spyglass to Jupiter, he was stunned to see four moons orbiting the planet. Almost 400 years later, Marois et al. (2008) imaged three planets orbiting HR 8799 and Kalas et al. (2008) imaged a planet orbiting Fomalhaut. We are finally able to image large planets on distant orbits around other stars. The very first extrasolar planet was discovered almost two decades ago (Wolszczan & Frail, 1992), orbiting the billion year old 6.2 ms pulsar 1257+12, by calculating the timing variations of the pulsar. The most successful technique, however, in detecting extrasolar planets, has been the radial velocity variation method. The first extrasolar planet around a main sequence star was detected with this technique (Mayor & Queloz, 1995), as well as over 500 of the almost 700 planets found to date. By nature, this technique is selective to large planets on close orbits.

Another successful technique, which is selective towards low inclination systems, is the transit method. Almost 200 planets have been detected (not all discovered) by this technique and many more are to be added to this list once the Kepler Space Telescope's detections are confirmed (Borucki et al., 2010). The transiting method is in theory not as selective towards close orbits as the radial ve-

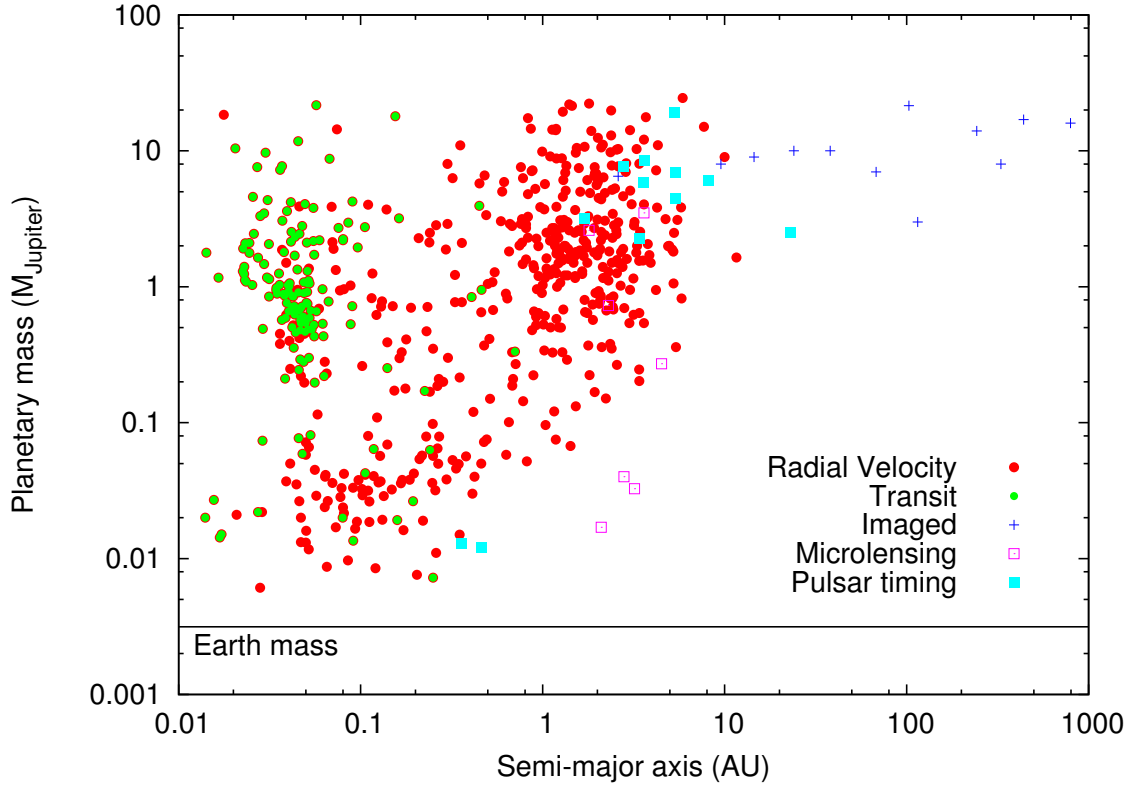


Figure 1.1 The distribution of known extrasolar planets in the mass vs. semi-major axis phase space. Our detections are mostly limited to large mass and close orbit systems (data collected from <http://exoplanet.eu>).

locity method is, but for it to detect large orbit systems long baselines in time are required, which can render the observations impossible. As with the radial velocity method, it is biased towards larger planets. In Figure 1.1, I show the distribution of known extrasolar planets in the planetary mass vs. semi-major axis phase space. The plot clearly shows that the majority of planets discovered to date have large masses and are located in close orbits, meaning their systems are very different from ours. This is most likely all due to observational biases and is no surprise.

The direct detection of Earth size planets with our current technology is im-

possible (Woolf & Angel, 1998; Perryman, 2000). The resolutions of our ground based telescopes are limited by the atmosphere of our planet by the Fried parameter (the maximum size of an atmospheric isothermal patch that introduces one radian of wavefront aberration) to $\sim \lambda/r_0$, equaling roughly 1'' in the optical. At higher altitudes the Fried parameter increases, enabling better resolutions, down to even 0.6'' in the infrared wavelengths. Adaptive Optics (AO) systems can improve the resolution down close to the theoretical limit of the telescope. For an 8 m telescope in the near infrared this can be as good as 60 milliarcseconds. This corresponds to a radial distance of 1.6 AU for a star at 10 pc. With AO systems and the James Webb Space Telescope (JWST), we are just at the limit to be able to resolve the Earth-Sun distance for a nearby star, where we hope to have terrestrial planets located. However, the diffraction halo of the stars will still be significant, especially when one considers that planets do not emit light. Any light we can detect from any planet will be scattered or reprocessed. The light from the star will still outshine the light from any possible planets.

Our observations have widened our imaginations as to what types of extrasolar planetary systems can exist, and given rise to new questions as to their origin and the frequency of planetary systems similar to ours. They have also demanded new methods to be explored to detect other types of systems. The high frequency of planetary systems shows that planets may be a necessary by-product of star formation. To detect planets, we must understand how they form, for which we have to understand how stars form. Below, I give a short review of our current understanding of star and planet formation, which will lead us to understand our extrasolar planetary system detection method and model.

1.3 Star and planet formation

The formation of stars and planets cannot be separated from each other. The formation of planets is a necessary by-product of the formation of stars, so we must understand the basic steps that lead to the formation of a star. In Figure 1.2, I show the stages of star formation, given by Shu et al. (1987), which starts off with a clump of gas and dust in a molecular cloud. In the left panels of the Figure, I show the observable spectral energy distributions of the system, while in the right panels I show simple sketches of the system itself as it goes through the formation phases. While in the pre-stellar phase, the pre-stellar core only emits in the submillimeter and mm wavelengths. The protostellar object is formed when the pre-stellar core settles in hydrostatic equilibrium, which is considered to be the time of birth for a star (Palla & Stahler, 1993). It is now called a Class 0 object. The core is surrounded by the infalling envelope of dust and gas, which start to form an accretion disk around the central object, as a result of the conservation of angular momentum.

As the protostellar object starts fusing deuterium, it also starts emitting first in the near-IR and later in the optical wavelengths, while heating the circumstellar disk, which starts to thermally emit in the mid- and far-IR wavelengths. At these stages, the disk still has a significant amount of gas in it and can be easily detected from its emission lines and near-to-far infrared excess continuum emission. This is also known as the T Tauri phase. The stellar wind, driven by convection, breaks out along the rotational axis of the pre-main sequence star, resulting in collimated jets from the poles, while the system is accreting matter from the disk. The accretion from the disk onto the star is terminated via viscous spreading in the inner (Hartmann et al., 1998) and via photoevaporation in the outer regions of the disk (Hollenbach et al., 1994; Gorti & Hollenbach, 2009), with stellar wind also speed-

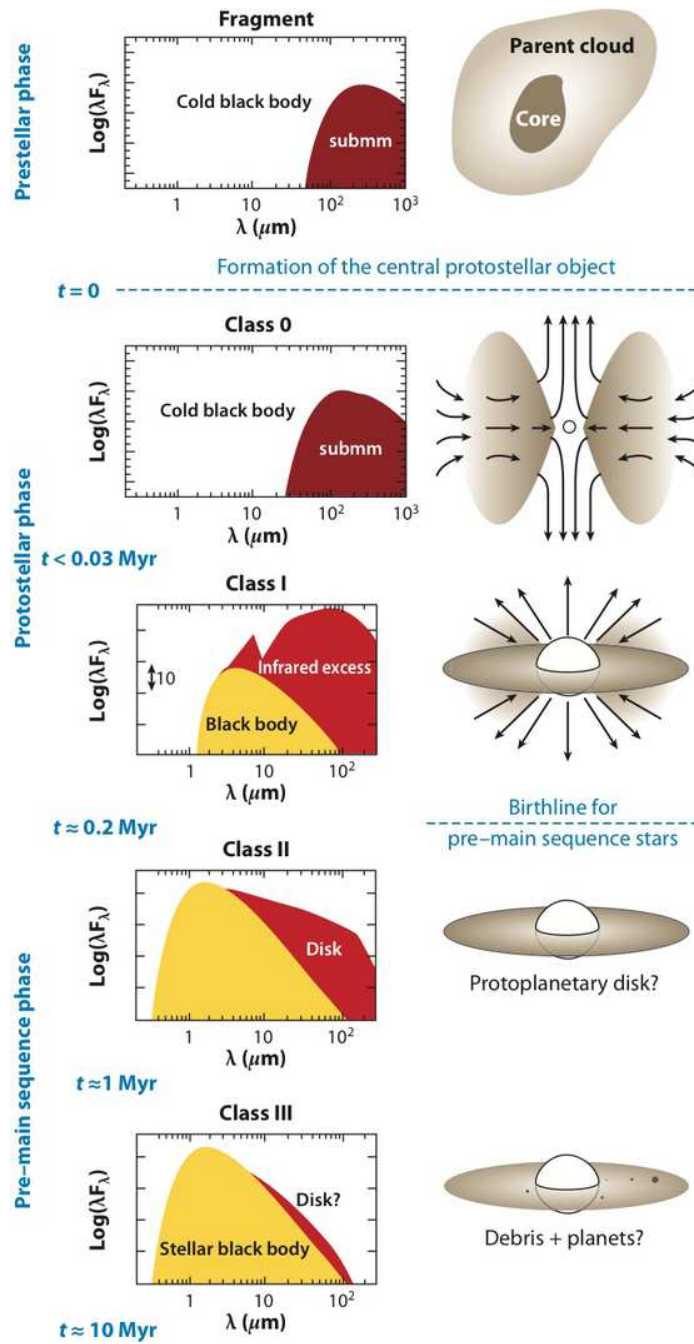


Figure 1.2 The early evolutionary stages of planets and planetary systems (fig. from Dauphas & Chaussidon, 2011).

ing the process (Matsuyama et al., 2009). The disk is continuously hollowed out from the inside, while external sources sometime also play a role via photoevaporation (Balog et al., 2007). This phase, called the transition phase, is defined when the disk itself does not produce significant excess emission in the near-IR wavelengths. The pre-main sequence phase of the star ends when it starts fusing hydrogen, however, leftover material in the disk will still contain both gas and dust that are in the process of forming planets. The excess emission of the disk is now strongest in the mid- and far-IR wavelengths, as its near-IR excess fades.

As the gas in the protoplanetary disk is accreted onto the planetesimals outside of the ice-line, and into the central star and also blown out of the system and photoevaporated from the inner regions of the system, the excess emission in the near-IR fades. In Figure 1.3, I show the decay in the measured fraction of stars with circumstellar protoplanetary disks in stellar clusters detected by their near-IR excess as a function of time (figure from Wyatt, 2008). This was originally observed by Haisch et al. (2001). It is in this early stage of stellar evolution when planetesimals and planetary cores start to form.

The processes that build planets are more complicated than those that build the stars. From observations, we see that the gas rich disk disappears within 10 Myr (Figure 1.3). Since the gas giant planets have to acquire the elements to build them, it is certain that they are formed in the first 3 Myr of a star's life. By nature gas giants are formed somewhat differently from terrestrial planets. We also know that they keep the majority of the angular momentum in the planetary systems, so they have great influence on the dynamical evolution of their planetary systems.

There are two different theories for the formation of giant planets. The first, core accretion, starts off with the same physics that is used to build terrestrial

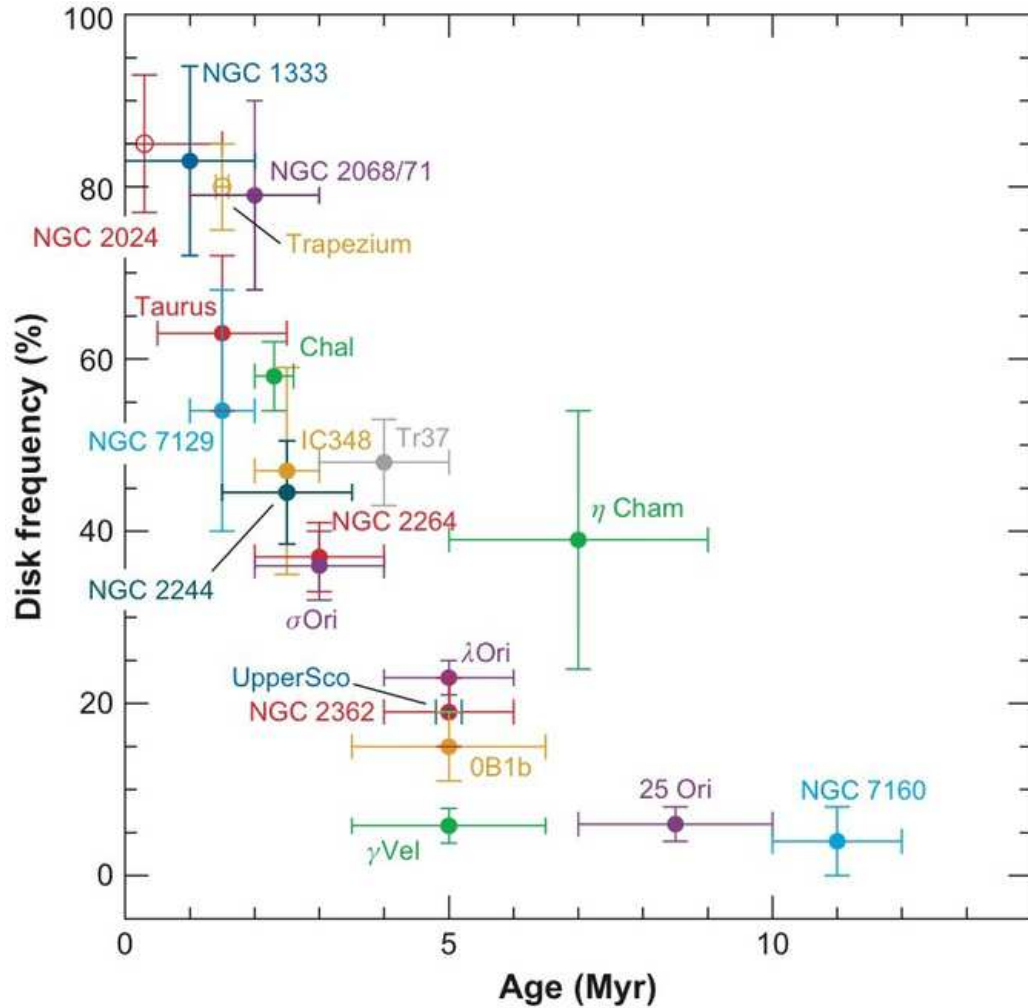


Figure 1.3 The decay of circumstellar primordial disks (Haisch et al., 2001; Wyatt, 2008; Williams & Cieza, 2011).

planets and later builds the gas giant on the core (D'Angelo et al., 2010). As dust and small grains coagulate into larger particles, they settle in the midplane of the protoplanetary disk. Here, they aggregate and form the larger planetesimals. The exact method they do this by is extremely complicated and not that well understood. The so called "meter size barrier" makes it hard to build planetesimals larger than a meter in size, as the collision of particles on this scale is always de-

structive and bodies of this size are also heavily affected by gas drag and quickly brought inward to the central star. However, if a particle is able to grow larger, then it is able to accumulate enough material to first form a planetary embryo and then a protoplanet. Once this protoplanet is large enough that the escape velocity from its surface exceeds the thermal speed of the surrounding gas, it starts to accrete gas onto the solid core. Since the planet's surface and the gas is constantly heated by the infall of planetesimals, the amount of gas it is able to accrete is limited. With the ever increasing core mass, however, after a certain point the core and gas envelope contract, allowing more gas to be accreted. This phase, known as runaway gas accretion, is only limited by the amount of the surrounding gas. The second, disk instability, assumes a similar core contraction to that of a star via the gravitational instability (GI) in the protoplanetary disk (Boss, 1997). While the first method is a bottom-up initially slow process, GI is a top down an initially rapid process.

The formation of the terrestrial size planets is still not a completely resolved problem. Radioactive isotope measurements suggest that the terrestrial bodies in the solar system took less than 200 Myr to form. Adding this to their average age of 4.5 Gyr, we match the age of the Sun, based on stellar evolution models. The surfaces of the non-eroding terrestrial bodies, such as that of the Moon, Mercury, and asteroids show never ending fields of impact craters. The ages of these craters suggest that impacts were much more common in the early solar system. Traditionally, there are two scenarios that have been considered for the formation of these large rocky planets. Either they form via pairwise collisions between dust grains, or rapidly via gravitational instability in the midplane of the protoplanetary disk. Unfortunately the effects of turbulence causes difficulties for the models. For the planetesimal theory, the large collisional velocities

make it difficult to build up objects larger than a meter in size. Due to turbulence, the collisional velocities between large, meter size objects is high enough to produce destructive collisions. Small particles on the other hand are too hard to merge with them. This is called the "meter-size barrier." For the GI model, turbulence does not allow the larger dust and meter size particles to settle in the disk midplane, thus the system cannot achieve gravitational instability. Two alternate models have recently been suggested to overcome these issues. Cuzzi et al. (2001) proposed that small particles are able to stay for longer periods of time between turbulent eddies. The probability of forming high density clumps is small, but they can become gravitationally bound. As the sub-Keplerian orbital velocity of the gas in the disk places ram pressure on the clumps, there is likely a minimum mass needed for the survival of these clumps, which models place at the mass of a solid planetesimal with a radius of 10-100 km. The second alternate theory (Johansen et al., 2006) assumes that the planetesimal theory has already produced a large number of meter sized objects. These meter size objects are affected by gas drag and move to pressure maxima points with short timescales. Once a large number of the meter size planetesimals are gathered in the pressure maxima, they start dragging the gas along and the radial drift is slowed. The resulting streaming instability produces gravitationally bound clumps of meter size objects, which then contract to form larger planetesimals/asteroids.

With either model, kilometer-size planetesimals are built within a few million years, with the planets possibly reaching Earth-size in 10-100 Myr. A smaller, Mars-size, planet can be built within 10 Myr. The final stage in planetary system formation is the removal of the leftover material. As the asteroid belt and Kuiper belt in the solar system show, this isn't an absolute process. Asteroids are able to remain in rings and haloes in the systems, and when undergoing gravitational

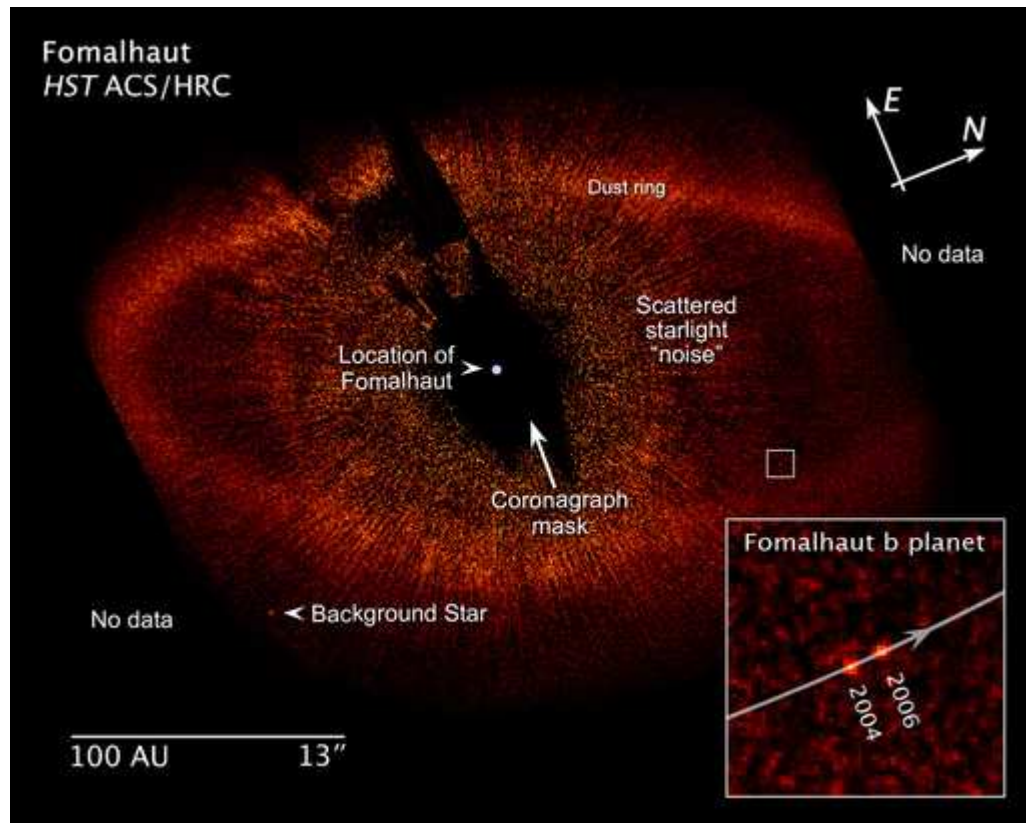


Figure 1.4 The Fomalhaut debris disk and its planet Fomalhaut b (Kalas et al., 2008).

instabilities they can once again take part in massive collisions with each other.

1.4 Circumstellar debris disks

Almost three decades ago, the serendipitous discovery of IR excess around Vega during routine calibration measurements came as a big surprise (Aumann et al., 1984). Similar excess was found around other main sequence stars, such as β Pictoris and Fomalhaut. Later, optical images showed an extended disk structure around β Pictoris (Smith & Terrile, 1984). The SEDs and the optical images were all consistent with originating from a distribution of dust particles heated to temperatures between 80-100 K orbiting at significant distances (50-200 AU) from

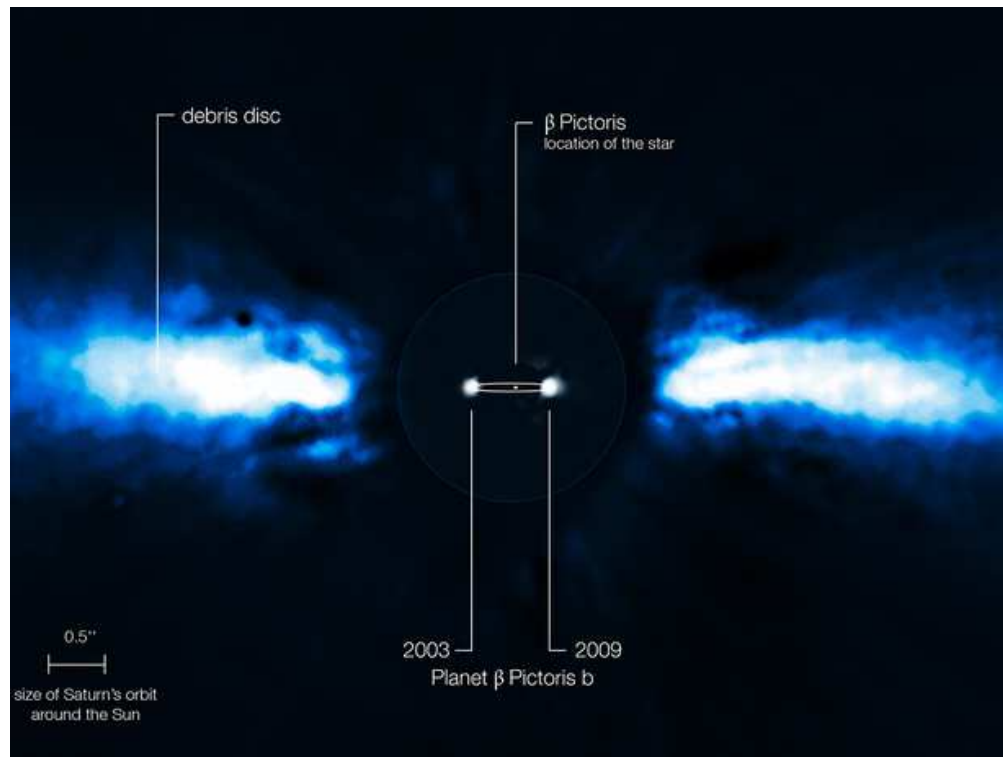


Figure 1.5 The β Pic debris disk and its planet β Pic b (Lagrange et al., 2010).

the stars. Later analysis of *IRAS* data revealed over a 100 systems with similar excesses (Mannings & Barlow, 1998) around stars of all ages and spectral types. These circumstellar disks are the third type of disk class, after primordial planetary and transitional disks, called debris disks. With the *Spitzer Space Telescope* we have detected many hundreds of them, both in the field (Rieke et al., 2005; Su et al., 2006; Trilling et al., 2008; Carpenter et al., 2008, 2009; Moór et al., 2006) and in stellar clusters, and up to many hundreds of parsecs.

What differentiates debris disks from the first two classes of circumstellar disks, is that they are completely deficient in gas. Since they are found around stars of all ages, and because the dissipation time of dust is significantly shorter than the ages of the systems (Gillett, 1986), they are not primordial interstel-

lar grains left over from the formation of the system, but produced from massive collisional cascades between the planetesimals. Since collisional cascades are likely initiated via dynamical instabilities in a disk due to planetary motions/migrations, the existence of these disks hint at the existence of planets in these systems. Inner clearings, such as that at Fomalhaut, are even stronger evidence for the case. The later, successfully imaged planets at the inner edges of the debris disks at Fomalhaut (Figure 1.4; Kalas et al., 2008) and β Pic (Figure 1.5; Lagrange et al., 2010) have confirmed this model.

As the Kuiper belt traces the solar system's dynamical history, so do the resolved systems of debris disks. To deduce the evolution of a debris disk, which is one of our main goals, the age of the system has to be known. This is not an easy task (Moór et al., 2006). We also have to understand the outcomes of planetesimal/asteroid collisions. In Chapter 3, I introduce my *Spitzer Space Telescope* observations on the open cluster Praesepe and deduced trends for the decay in debris disk fractions as a function of the central stars' spectral type. In Chapter 4, I detail my numerical model that solves the collisional evolution of the particle size distribution in debris disks. Knowing the particle size distribution lets us model the spectral energy distribution of the system and to analyze its evolution. More introductory details on debris disks can be found in the introductions of Chapter 3 and 4.

1.5 The solar system's debris disk

Our interest in extrasolar debris disks is rooted in our own solar system's debris disk. Astronomers have known for a while that our solar system has a ring of dust, seen as the zodiacal cloud at sunset and dawn, produced by these belts, comets and also composed of interstellar grains, constantly brought inward to

the Sun. However, unlike extrasolar debris disks, ours is low density, not observable from other stars. As it is low density, the collision rates are low, resulting in low production rates of small dust particles that could be blown out of the system. Instead, the dominant removal mechanism for the larger grains in our solar system is the Poynting-Robertson drag, which brings the dust grains inward to the the Sun. Over the 4.5 Gyr of our solar system's evolution, the majority of dust and planetesimals were removed via radiation pressure forces and due to dynamical interactions. According to lunar crater counts, the inner parts of the solar system underwent an intense period of planetesimal collisions roughly 3.8 Gyr ago (Tera et al., 1973, 1974). This could have been a result of such a dynamical instability, possibly caused by dynamical interactions of Jupiter and Saturn (Gomes et al., 2005). The importance of dynamical effects can be also seen today, with the resonant trapping of the asteroids in the Main Asteroid Belt in the Kirkwood zones, the warp in the zodiacal cloud (Dermott et al., 1999), and the asymmetric component that co-orbits with Earth (Dermott et al., 1994).

1.6 Outline of the thesis

In the past thirty years our understanding of how extrasolar planetary systems form and evolve has expanded by a great amount. We have imaged all stages of it, detected many hundred of planets, and built up physical models to explain the vast majority of observations. However, our knowledge is not yet complete, with gray and white areas to be filled, mostly in the field of understanding terrestrial planets and our own solar system. Observations and consequent models of debris disks will help us fill in many of these areas. Data from the *Spitzer Space Telescope* and *Herschel* has and will reveal to us many new details. The goal of my thesis is to understand certain aspects of debris disk evolution via observations

and models.

In Chapter 2, I present observations of a nearby star, δ Velorum. *Spitzer* images revealed a stunning bow shock structure in front of the star. Originally the mid-IR excess around the star was contributed to a debris disk. Although the topic of this chapter does not tie in directly to the wider theme of the thesis, it is meant to present alternate ways of producing debris disk like excesses around stars and to emphasize the existence of these systems. I model the bow shock as a result of the star's interaction with the Local Interstellar Cloud (LIC) in the Local Bubble. The mere presence of the bow shock is surprising, as the density of the Interstellar Medium is considerably lower in the Local Bubble, compared to other nearby regions in the Milky Way. In Chapter 3, I present *Spitzer* observations of the nearby open stellar cluster Praesepe. It is a good example of an older cluster, but with rich membership. It is also relatively nearby (~ 180 pc), meaning the cluster could be observed to high completeness even for later spectral type stars. The cluster's age coincides with the age of the solar system, when it underwent the Late Heavy Bombardment. I compile all available cluster and field star disk fraction in the paper and analyze the decay of the [24] disk fraction. In Chapter 4, I present a detailed numerical model of the collisional cascades in debris disks. My numerical model solves the full scattering equation and takes into account both destructive collision types, erosive and catastrophic. I compare the model to already published models in the literature and detail its strengths. In Chapter 5, I use my numerical model to calculate the evolution of the mass distribution slope in a collisional system. I show that the classic distribution function (Dohnanyi, 1969) produces a somewhat shallower slope than is yielded in our more accurate numerical modeling. In the final chapter I conclude my results and give goals for future work.

CHAPTER 2

FALSE SIGNS OF DEBRIS DISKS

My advisor, Kate Su, discovered a bow shock shaped mid-infrared excess region in front of δ Velorum using $24\ \mu\text{m}$ observations obtained with the Multiband Imaging Photometer for *Spitzer* (MIPS). The excess has been classified as a debris disk from previous infrared observations. Although the bow shock morphology was only detected in the $24\ \mu\text{m}$ observations, its excess was also resolved at $70\ \mu\text{m}$. I show that the stellar heating of an ambient interstellar medium (ISM) cloud can produce the measured flux and morphology. Since δ Velorum was classified as a debris disk star previously, our discovery may call into question the same classification of other stars. I model the interaction of the star and ISM, producing images that show the same geometry and surface brightness as is observed. The modeled ISM is ~ 15 times overdense relative to the average Local Bubble value, which is surprising considering the close proximity (24 pc) of δ Velorum.

The abundance anomalies of λ Boötis stars have been previously explained as arising from the same type of interaction of stars with the ISM. Low resolution optical spectra of δ Velorum show that it does not belong to this stellar class. The star therefore is an interesting testbed for the ISM accretion theory of the λ Boötis phenomenon.

2.1 Introduction

Using *IRAS* data, more than a hundred main-sequence stars have been found to have excess emission in the $12 - 100\ \mu\text{m}$ spectral range (Backman & Paresce, 1993). Many additional examples have been discovered with *ISO* and *Spitzer*. In most

cases the spectral energy distributions (SEDs) can be fitted by models of circumstellar debris systems of thermally radiating dust grains with temperatures of 50 to 200 K. Such grains have short lifetimes around stars: they either get ground down into tiny dust particles that are then ejected by radiation pressure, or if their number density is low they are brought into the star by Poynting-Robertson drag. Since excesses are observed around stars that are much older than the time scale for these clearing mechanisms, it is necessary that the dust be replenished through collisions between planetesimals and the resulting collisional cascades of the products of these events both with themselves and with other bodies. Thus, planetary debris disks are a means to study processes occurring in hundreds of neighboring planetary systems. *Spitzer* observations have revealed a general resemblance in evolutionary time scales and other properties to the events hypothesized to have occurred in the early Solar System.

Although the planetary debris disk hypothesis appears to account for a large majority of the far infrared excesses around main-sequence stars, there are two alternative possibilities. The first is that very hot gas around young, hot, and luminous stars can be responsible for free-free emission (e.g., Cote, 1987; Su et al., 2006). The second possibility is that the excesses arise through heating of dust grains in the interstellar medium around the star, but not in a bound structure such as a debris disk. Kalas et al. (2002) noticed optical reflection nebulosities around a number of stars with Vega-like excesses. These nebulosities show asymmetries that would not be typical of disks, they have complex, often striated structures that are reminiscent of the Pleiades reflection nebulosities, and they are much too large in extent to be gravitationally bound to the stars (see Gorlova et al., 2006).

Dynamical rather than stationary interactions with the ISM are more interest-

ing (Charbonneau, 1991). Originally, it was proposed that ISM dust grains could interact directly with material in debris disks (Lissauer & Griffith, 1989; Whitmire et al., 1992). However, it was soon realized that photon pressure from the star would repel interstellar grains, resulting in grain-free zones with possible bow-shock geometry around luminous stars (Artymowicz & Clampin, 1997).

This scenario has been proposed to account for the abundance anomalies associated with λ Boötis stars. These are late B to early F-type, Population I stars with surface underabundances of most Fe-peak elements and solar abundances of lighter elements, such as C, N, O and S. In the diffusion/accretion model (Venn & Lambert, 1990; Kamp & Paunzen, 2002; Paunzen et al., 2003), it is suggested that the abundance anomaly occurs when a star passes through a diffuse interstellar cloud. The radiation pressure repels the grains, and hence much of the general ISM metals, while the gas is accreted onto the stellar surface. While the star is within the cloud, a mid-infrared excess will result from the heating of the interstellar dust; however, after the star has left the cloud the abundance anomalies may persist for $\sim 10^6$ yr in its surface layers (Turcotte & Charbonneau, 1993) without an accompanying infrared excess.

There have been few opportunities to test the predictions for dynamical interactions of main-sequence stars with the ambient interstellar medium. France et al. (2007) have studied a bow shock generated by the O9.5 runaway star HD 34078. Ueta et al. (2006) describe the bow shock between the mass loss wind of the AGB star R Hya and the ISM. Noriega-Crespo et al. (1997) identified 58 runaway OB stars with an observable bow shock structure using high resolution *IRAS* 60 μm emission maps. Rebull et al. (2007) discovered that the young B5 star HD 281159 is interacting with the ISM, producing spherical shells of extended IR emission centered on the star with a spike feature pointing from the star into the shells.

None of these cases correspond to the type of situation that might be mistaken for a debris disk, nor which would be expected to produce a λ Boötis abundance pattern.

δ Velorum is a nearby (~ 24 pc) stellar system (at least five members)¹, with modest excess in the *IRAS* data. It has been classified as an A-type star with a debris disk system (e.g., Aumann, 1985, 1988; Cote, 1987; Chen et al., 2006; Su et al., 2006). Otero et al. (2000) observed a drop in the primary component's brightness ($\sim 0^m.3$) and showed that it is an eclipsing binary with probably two A spectral type components. With the available data, Argyle et al. (2002) computed the system's parameters. They suggested that the eclipsing binary (Aa) consists of two A dwarfs with spectral types A1V and A5V and masses of 2.7 and 2.0 M_{\odot} and with separation of 10 mas. The nearby B component is a G dwarf with mass around 1 M_{\odot} and separation of $0''.6$ from the main component. There is also another binary (CD component) at $78''$ from the star.

In §2.2, I report measurements demonstrating that this star is producing a bow shock as it moves through an interstellar cloud as hypothesized by Arty-mowicz & Clampin (1997). In §2.3, I model this behavior using simple dust grain parameters and show satisfactory agreement with expectations for the ISM and properties of the star. I discuss these results in §2.4, where I show that the star is most likely not part of the λ Boötis stellar class. Thus, δ Velorum provides a test of the diffusion/accretion hypothesis for λ Boötis behavior.

2.2 Observations and Data Reduction

I present observations of δ Velorum at 24 and 70 μm obtained with the Multiband Imaging Photometer for *Spitzer* (MIPS) as part of three programs: PID 57 (2004

¹It is a complex multiple system: Otero et al. (2000); Hanbury Brown et al. (1974); Horch et al. (2000); Argyle et al. (2002); Tango et al. (1979); Kellerer et al. (2007)

Feb 21), PID 20296 (2006 Feb 22, Apr 3) and PID 30566 (2006 June 12). For PID 57, 3 second exposures at four dither positions were taken, with a total integration time of 193 seconds. The other observations at $24\ \mu\text{m}$ (PID 20296) were done in standard photometry mode with 4 cycles at 5 sub-pixel-offset cluster positions and 3 sec integrations, resulting in a total integration of 902 sec on source for each of the two epochs. The star HD 217382 was observed as a PSF standard (AOR ID 6627584) for PID 57, with the same observational parameters. The observation at $70\ \mu\text{m}$ (PID 30566) was done in standard photometry default-scale mode with 10 sec integrations and 3 cycles, resulting in a total integration of 335 sec on source.

The binary component Aa was not in eclipsing phase according to the ephemeris equations by Otero et al. (2000) at either epoch. The period of the eclipse is ~ 45.16 days, and the system was ~ 13 days before a primary minimum at the first, ~ 3 days before one at the second and ~ 7.7 days before one at the third epoch for the $24\ \mu\text{m}$ observations. The $70\ \mu\text{m}$ observation was 2.53 days before a secondary minimum.

The data were processed using the MIPS instrument team Data Analysis Tool (DAT, Gordon et al., 2005) as described by Engelbracht et al. (2007) and Gordon et al. (2007). Care was taken to minimize instrumental artifacts.

Fitting the model described later demands flux measurements within a constant large external radius (see details in §2.3). Therefore, photometry for the target was extracted using aperture photometry with a single aperture setting. The center for the aperture photometry at both 24 and $70\ \mu\text{m}$ was determined by fitting and centroiding a 2-D Gaussian core. A radius of $56''.025$ was used for both wavelengths, with sky annulus between $68''.95$ and $76''.34$. The aperture size was chosen to be large enough to contain most of the flux from the bow shock, but small enough to exclude the CD component to avoid contamination. The CD

component was bright at $24\ \mu\text{m}$ at a distance of $78''$ from the AaB components, but could not be detected at $70\ \mu\text{m}$. Aperture corrections were not applied because of the large size of the aperture. Conversion factors of 1.068×10^{-3} and $1.652 \times 10^1\ \text{mJy arcsec}^{-2}\ \text{MIPS_UNIT}^{-1}$ were used to transfer measured instrumental units to physical units at 24 and $70\ \mu\text{m}$, respectively.

Faint extended asymmetric nebulosity offset from the central star is apparent at $24\ \mu\text{m}$, with the dark Airy rings partially filled in. Using standard aperture and point-spread-function (PSF) fitting photometry optimized for a point source, the total flux is $1420 \pm 42\ \text{mJy}$, ~ 1.12 times the expected photospheric flux, which was determined by fitting a Kurucz model (Castelli & Kurucz, 2003) to the optical and near infrared photometry and extrapolating it to 24 and $70\ \mu\text{m}$. The large aperture photometry value is greater by another factor of ~ 1.1 , which puts it above the expected photospheric flux by a factor of ~ 1.25 . The final photometry measurements (using the large aperture setting) are listed in Table 2.1. I also list the modeled photospheric flux of the star and the modeled value of the IR excess. Since the measured excess depends on the aperture used, to avoid confusion I do not give a measured excess value, only the photospheric flux which can be subtracted from any later measurements. The photospheric flux given in Table 2.1 does not include the contribution from the G dwarf (90 and $10\ \text{mJy}$ at 24 and $70\ \mu\text{m}$, respectively). The top left panel in Figure 2.1 shows the summed image from epochs 2 and 3, to demonstrate the asymmetry suggested even before PSF subtraction.

For the first epoch $24\ \mu\text{m}$ image, the reference star image was subtracted from the image of δ Velorum, with a scale factor chosen as the maximum value that would completely remove the image core without creating significant negative flux residuals. The deeper exposures from the second and third epochs were

Table 2.1. The parameters of δ Velorum

F_{24}^* (mJy)	F_{70}^* (mJy)	ρ_{ISM} ($10^{-24} \text{g cm}^{-3}$)	v_{rel} (km s^{-1})	$F_{\text{star}24}^\dagger$ (mJy)	$F_{\text{star}70}^\dagger$ (mJy)	$F_{\text{excess}24}^\ddagger$ (mJy)	$F_{\text{excess}70}^\ddagger$ (mJy)
1569 ± 42	237 ± 50	5.8 ± 0.4	36 ± 4	1277	147	174	141

*Observed fluxes with the large aperture

† Photospheric values - not including G star component

‡ Modeled excesses at large aperture

designed to reveal faint structures far from the star, where the observed PSF is difficult to extract accurately. Therefore, I used simulated PSFs (from STinyTim) and the MIPS simulator ². Because bright structures nearly in the PSF contribute to the residuals at large distances, I oversubtracted the PSF to compensate. The first epoch PSF subtracted 24 μm image is shown in the bottom panels of Figure 2.1 and the composite from epochs 2 and 3 in the upper right.

The PSF subtracted images in Figure 2.1 show that the asymmetry is caused by a bow shock. As shown in the lower left, the head of the bow shock points approximately toward the direction of the stellar proper motion. The bottom right panel shows the excess flux contours and that it consists of incomplete spherical shells centered on δ Velorum. Combined with the upper right image, there is also a parabolic cavity, as expected for a bow shock. The stagnation points (where photon pressure equals gravitational force) of the grains in the bow shock are within ~ 200 AU of the star, according to the sharp inner edges and the width of the bow shock. A notable feature in the upper right is the wings of the bow shock, which are detectable to ~ 1500 AU.

²Software designed to simulate MIPS data, including optical distortions, using the same observing templates used in flight.

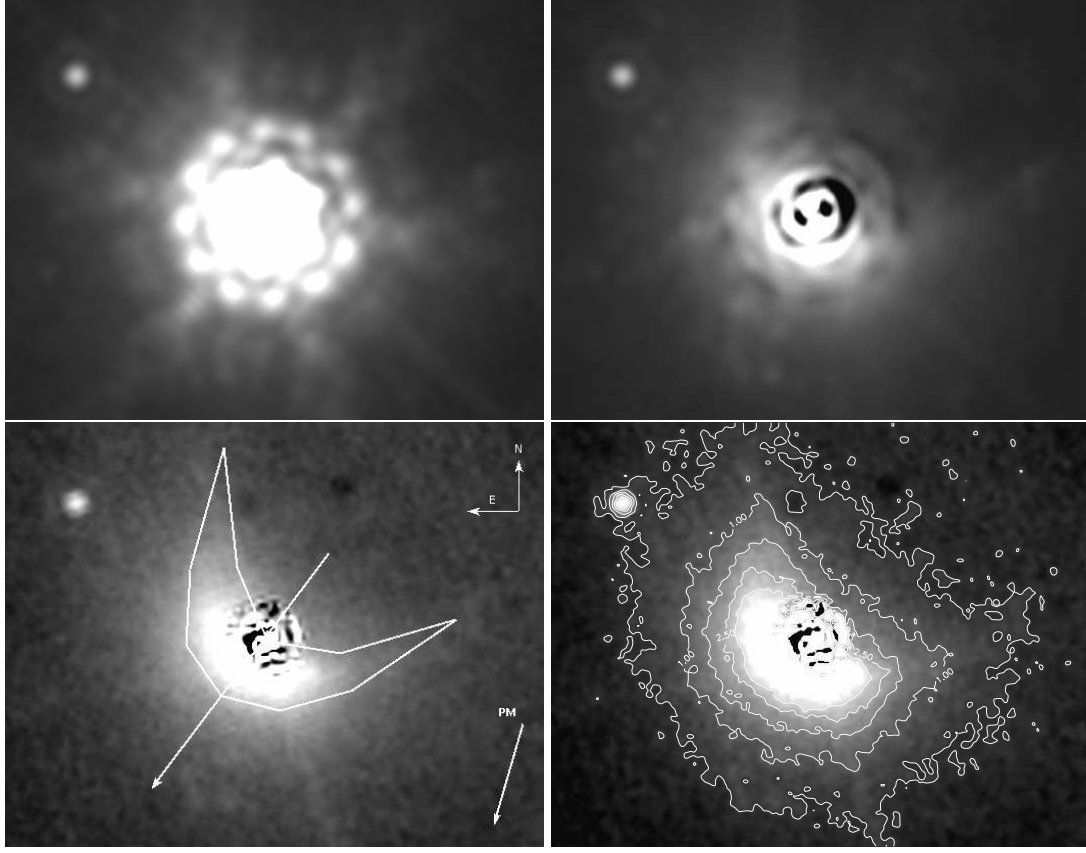


Figure 2.1 The panels show $24\ \mu\text{m}$ images of δ Velorum. All images are in logarithmic scaling, the FOV is $\sim 2.74 \times 2.34$. The scaling of the images are: $-0.5 - 4\ \text{MJy sr}^{-1}$. *Top-left panel*: The original observed composite image from the 2nd and 3rd epochs. *Top-right panel*: PSF oversubtracted image, which shows the bow shock structure far from the star. *Bottom-left panel*: The intensity scaled PSF subtracted image (first epoch), which shows the bow shock structure close to the star. This image shows the orientation of the images and the proper motion direction of the star. The arrow bisecting the bow shock contour shows the calculated direction of the modeled relative velocity. *Bottom-right panel*: Same image as the bottom-left panel, but with intensity contours plotted. The intensity contours are at $0.25, 1.0, 1.75, 2.5$ and $3.25\ \text{MJy sr}^{-1}$ from the faintest to the brightest, respectively. The contours show that the extended emission consists of incomplete spherical shells, centered on δ Velorum.

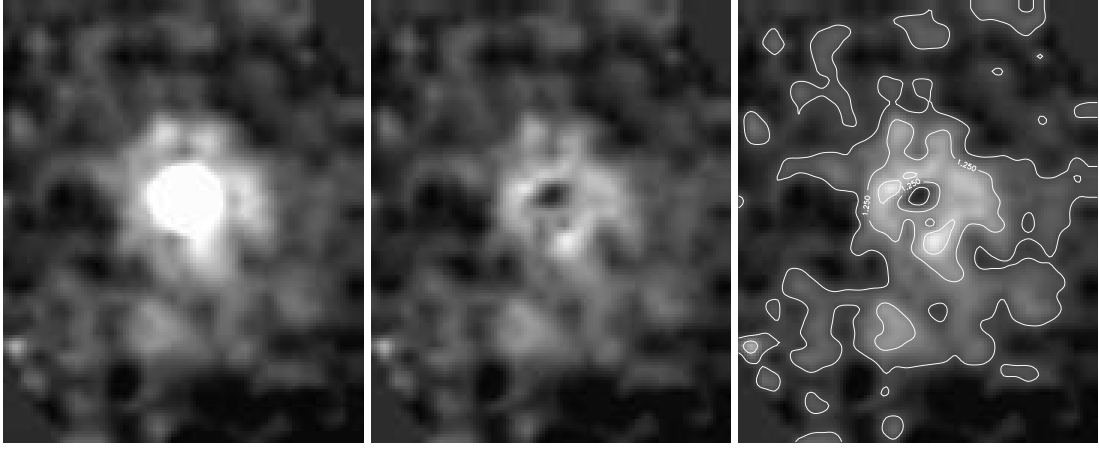


Figure 2.2 The panels show the $70\ \mu\text{m}$ image of δ Velorum. All images are scaled logarithmically from $-0.5 - 3\ \text{MJy sr}^{-1}$. The FOV is $\sim 2'46 \times 3'03$. The orientation of the images is the same as in Figure 2.1. *First panel*: the observed image. *Middle panel*: the PSF subtracted image. The residual flux seems close to being concentric. *Last panel*: the intensity contours. They suggest that there is a faint concentric $70\ \mu\text{m}$ excess further from the star that fades at the cavity region behind the star.

The $70\ \mu\text{m}$ observation is shown in Figure 2.2. The PSF subtraction (scaled to the point source flux of $125\ \text{mJy}$) does not reveal the bow shock structure at this wavelength, only that there is extended excess. The total flux of the residual of the PSF subtracted image is $119\ \text{mJy}$. The intensity contours (*last panel*) suggest that the $70\ \mu\text{m}$ excess fades at the cavity behind the star, but the effect is small. The geometry and direction of the bow shock are discussed in more detail in §2.3.2.

2.3 The Bow Shock Model

Based on a previous suggestion by Venn & Lambert (1990), Kamp & Paunzen (2002) proposed a physical model to explain the abundance pattern of λ Boötis stars through star-ISM interaction and the diffusion/accretion hypothesis. Their model is based on a luminous main-sequence star passing through a diffuse ISM cloud. The star blows the interstellar dust grains away by its radiation pressure,

but accretes the interstellar gas onto its surface, thus establishing a thin surface layer with abundance anomalies. So long as the star is inside the cloud, the dust grains are heated to produce excess in the infrared above the photospheric radiation of the star. Martínez-Galarza et al. (2009) have developed a model of this process and show that the global spectral energy distributions of a group of λ Boötis type stars that have infrared excesses are consistent with the emission from the hypothesized ISM cloud. Details of the model can be found in their paper. Here I adapt their model and improve its fidelity (e.g., with higher resolution integrations), and also model the surface brightness distribution to describe the observed bow shock seen around δ Velorum.

2.3.1 Physical description of the model

The phenomenon of star-ISM interactions generating bow shocks was first studied by Artymowicz & Clampin (1997). They showed that the radiative pressure force on a sub-micron dust grain can be many times that of the gravitational force as it approaches the star. The scattering surface will be a parabola with the star at the focus point of the parabolic shaped dust cavity. Since the star heats the grains outside of the cavity and close to the parabolic surface, an infrared-emitting bow shock feature is expected.

The shape of the parabola (for each grain size) can be given in terms of the distance between the star (focus) and the vertex. This so-called avoidance radius (or the $p/2$ parameter of the scattering parabola) can be calculated from energy conservation to be (Artymowicz & Clampin, 1997):

$$r_{\text{av}}^a = \frac{2(\beta^a - 1)GM}{v_{\text{rel}}^2}, \quad (2.1)$$

where a is the radius of the particle, M is the mass of the star and v_{rel} is the relative velocity between the star and the dust grains.

β^a is the ratio of photon pressure to gravitational force on a grain and it is given by (Burns et al., 1979):

$$\beta^a = 0.57 Q_{\text{pr}}^a \frac{L/L_{\odot}}{M/M_{\odot}} \left(\frac{a}{\mu\text{m}} \right)^{-1} \left(\frac{\delta}{\text{g cm}^{-3}} \right)^{-1}, \quad (2.2)$$

where δ is the bulk density of the grain material and Q_{pr}^a is the radiation pressure efficiency averaged over the stellar spectrum. $Q_{\text{pr}}^a(\lambda)$ can be expressed in terms of grain properties (absorption coefficient $Q_{\text{ab}}^a(\lambda)$, scattering coefficient $Q_{\text{sca}}^a(\lambda)$ and the scattering asymmetry factor $g = \langle \cos \alpha(\lambda) \rangle$, Burns et al., 1979; Henyey & Greenstein, 1938):

$$Q_{\text{pr}}^a(\lambda) = Q_{\text{ab}}^a(\lambda) + Q_{\text{sca}}^a(1 - g), \quad (2.3)$$

which gives

$$Q_{\text{pr}}^a = \frac{\int Q_{\text{pr}}^a(\lambda) B(T_*, \lambda) d\lambda}{\int B(T_*, \lambda) d\lambda}, \quad (2.4)$$

where $B(T_*, \lambda)$ is the Planck function. I adopted astronomical silicates in our model with $\delta = 3.3 \text{ g cm}^{-3}$ from Draine & Lee (1984) and Laor & Draine (1993). I considered a MRN (Mathis et al., 1977) grain size distribution in my model:

$$dn = C a^{-\gamma} da, \quad (2.5)$$

where C is a scaling constant and n is the number density of the cloud with $\gamma = 3.5$ and grain sizes ranging from $0.005 - 0.25 \mu\text{m}$.

With these equations I was able to model the avoidance cavity for a grain that encounters a star with known mass, luminosity and relative velocity. The model describes a situation where the expelled grains are instantly removed from the system rather than drifting away, but this only causes a minor discrepancy in the wing and almost none in the apex of the parabola compared to the actual case. In the actual scenario only those particles get scattered back upstream that encounter the central star with small impact parameter ($\sim r_{\text{av}}^a/2$). This means

that most of the grains will get expelled toward the wings, where the grains go further out and emit less infrared excess, thus their contribution to the total flux will be small.

The model determines the number density of certain grain sizes and the position of their parabolic avoidance cavity. Outside of the cavity I assumed a constant number density distribution for each grain size. To calculate the surface brightness of the system and its SED I assumed a thermal equilibrium condition, with wavelength dependent absorption and an optically thin cloud.

2.3.2 Model Geometry and Parameters

The model described in §2.3.1 gives the distribution and temperature for each grain size. This model was implemented in two ANSI C programs. The first program fits the SED of the system to the observed photometry points, while the second program calculates the surface brightness of the system. The fitted photometry included *uvby*, *UBV*, *HIPPARCOS* V band, *2MASS*, *IRAS* and *MIPS* (24 and 70 μm) data. I subtracted the 24 and 70 μm flux contributed by the G star (90 and 10 mJy, respectively) from the *MIPS* observations, because I wanted to model the system consisting of the two A stars and the bow shock.

The input parameters are: stellar radius, mass-to-luminosity ratio (MLR), relative velocity of cloud and star, ISM dust density, cloud external radius and the distance of the system. The stellar radius, MLR and the distance can be constrained easily. I determined the best-fit Kurucz model (Castelli & Kurucz, 2003) by fitting the photometry points at wavelengths shorter than 10 μm . Since the distance is known to high accuracy from *HIPPARCOS* I can determine the radius and thus the luminosity of the star precisely. The mass was adopted from Argyle et al. (2002). The G dwarf's luminosity is only 1% of the system, so leaving the star out does not cause any inconsistency. Its mass is only 17% of the total mass,

which can only cause minor changes in the determined final relative velocity, but none in the final surface brightness or the computed ISM density. The model then has three variable parameters: the density of the ISM grains (ρ_{dust} - does not include gas), the relative velocity between the cloud and the star (v_{rel}) and the external radius of the cloud (r_{ext}). The model should describe the total flux from exactly the area used for my photometry. The aperture radius of $56''.025$ (1366 AU at the stellar distance of 24.45 pc) was used as r_{ext} . Both programs calculate the $Q_{\text{pr}}^a, \beta^a, r_{\text{av}}^a, n$ values and then the temperature at r_{av}^a for each grain size.

The SED modeling program decreases the temperature value from the one at r_{av} by 0.01 K steps and finds the radius for that corresponding grain temperature. The program does not include geometrical parameters such as the inclination or the rotation angle of the system, since these are irrelevant in calculating the total flux. It calculates the contribution to the emitting flux for every grain size from every shell to an external radius (r_{ext}) and adds them up according to wavelength.

The program that calculates the surface brightness uses a similar algorithm as the SED program, but it calculates the temperature at 1 AU distance steps from r_{av}^a for every grain size and calculates the total flux in the line of sight in 1 AU^2 resolution elements.

The total inclination ι of the bow shock was not included as a parameter, since by eye the observed images seemed to show an inclination of $\iota \approx 90^\circ$ (a schematic plot of the angle nomenclature is shown in Figure 2.3). This approximation is strengthened by the radial velocity of the star, which is only $\sim 2 \text{ km s}^{-1}$ compared to the tangential velocity of $\sim 13 \text{ km s}^{-1}$. This assures that the motion of the system is close to perpendicular to the line of sight. However, I have found that the bow shock has similar appearance for a significant range of angles ($\pm 20^\circ$) relative to $\iota = 90^\circ$. I illustrate this in Figure 2.4. If the relative velocity vector

would have a 70° (or 110°) inclination it would only cause minor differences in the modeled velocity ($\Delta v_{\text{rel}} \approx 3 \text{ km s}^{-1}$) and ISM density ($\Delta \rho_{\text{ISM}} \approx 0.2 \times 10^{-24} \text{ g cm}^{-3}$). At an inclination of 50° , the “wings” spread out and the bright rim at the apex starts to become thin.

With interstellar FeII and MgII measurements Lallement et al. (1995) showed that the Local Interstellar Cloud (LIC) has a heliocentric velocity of 26 km s^{-1} moving towards the galactic coordinate $l_{II} = 186 \pm 3^\circ$, $b_{II} = -16 \pm 3^\circ$. Since δ Velorum is at $l_{II} \approx 272^\circ$, $b_{II} \approx -7^\circ$, the LIC is also moving perpendicular to our line of sight at the star and in the direction needed to reach a high relative velocity between the star and cloud. Crawford et al. (1998) showed a low velocity interstellar Ca K line component in the star’s spectrum with $v_{\text{helio}} = 1.3 \pm 0.4 \text{ km s}^{-1}$, which also proves that the ISM’s motion is perpendicular to our line of sight at δ Velorum. The offset of the proper motion direction of the star from the head direction of the bow shock by a few degrees could be explained by the ISM velocity. A simple vectorial summation of the star and the ISM velocities should give a net motion in the direction of the bow shock.

2.3.3 Results

I first tried to find the best fitting SED to the photometry points corresponding to wavelengths larger than $10 \mu\text{m}$ (MIPS, *IRAS*) with χ^2 minimization in the v_{rel} vs. ρ_{dust} phase space. I defined χ^2 as:

$$\chi^2 = \sum \frac{(F_{\text{obs}} - F_{\text{calc}})^2}{\sigma_{\text{obs}}^2} \quad (2.6)$$

The χ^2 phase space with $r_{\text{ext}} = 1366 \text{ AU}$ showed no minimum (Figure 2.5, *left panel*). The interpretation of the diagram is as follows: if the relative velocity is small, then the avoidance radius will be large. Consequently the grains will be at relatively low temperature and the amount of dust required to produce the

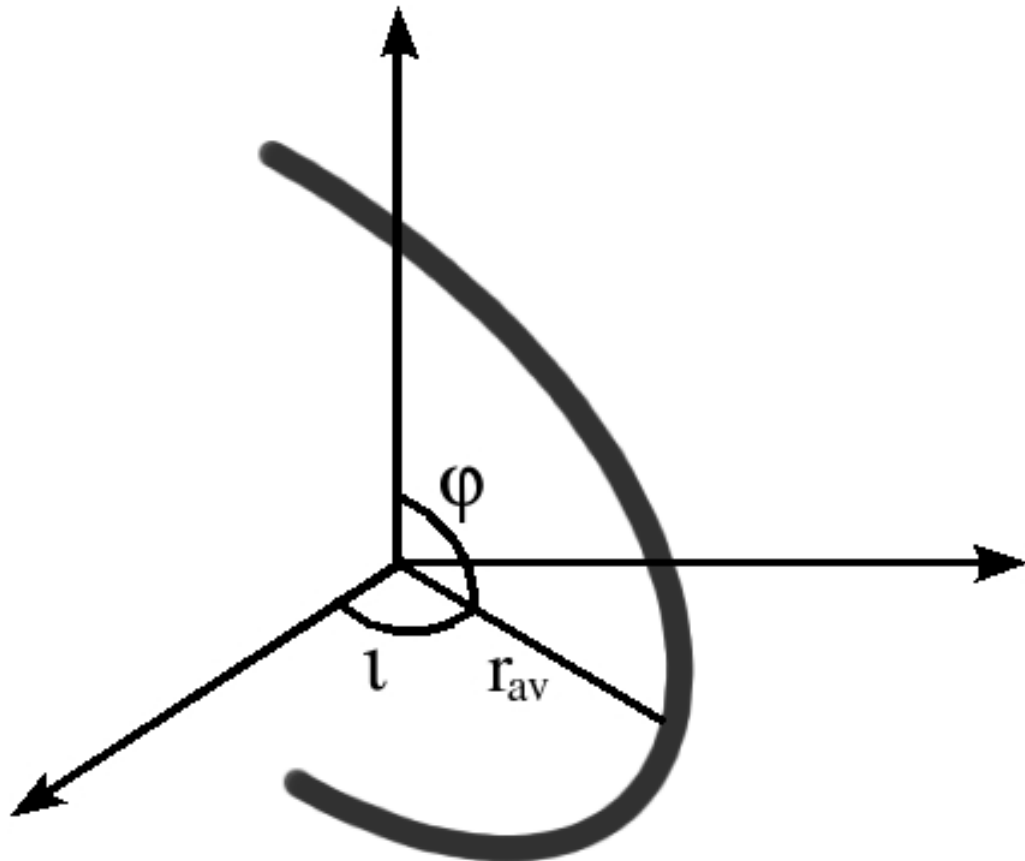


Figure 2.3 The nomenclature of the angles of the system. The heavy line is the grain avoidance parabola. φ is the rotation angle of the system on the plane of the sky (my initial guess was 4° N from the calculated direction of relative motion shown in Figure 2.1), ι is the inclination and r_{av} is an avoidance radius. The observer is viewing from the axis pointing to the bottom left.

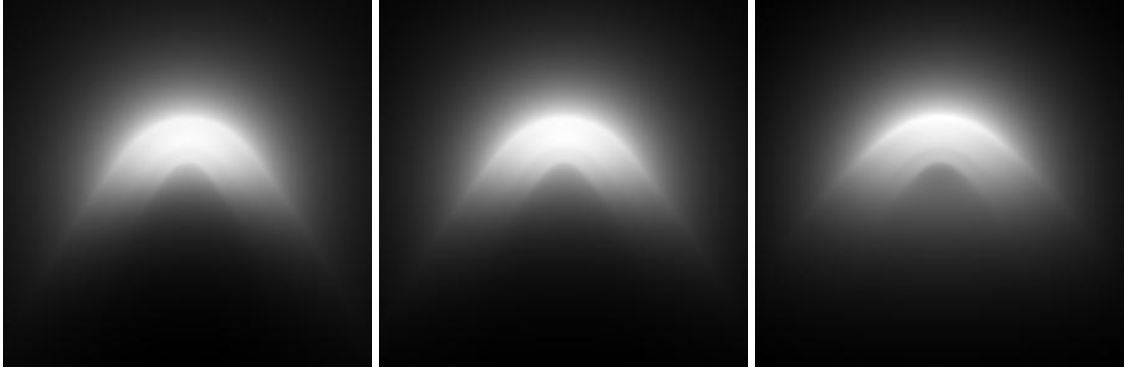


Figure 2.4 The panels show the $24\ \mu\text{m}$ morphology of the bow shock viewed at different inclinations, starting from 90° (left), 70° (middle) and 50° (right).

observed flux increases. On the other hand, if the relative velocity is large, then the grains can approach closer to the star and heat up to higher temperatures. As a result a smaller dust density is enough to produce the observed flux. Therefore, the combination of the density of the cloud and the relative velocity can be well constrained by the broad-band SED alone, but not each separately.

By using surface brightness values from the observations and the model calculations I was able to determine the v_{rel} parameter and thus eliminate the degeneracy of the model. Since the bow shock is a parabolic feature it has only one variable, the avoidance radius (r_{av}^a), which is the same as the $p/2$ parameter of the parabola (with p being the distance between the focus point and the vertex). The value of r_{av}^a does change as a function of grain size, but the head of the bow shock will be near the value where the avoidance radius has its maximum as a function of grain size. As can be seen in Figure 2.6, the avoidance radius has a maximum at $\sim 0.06\ \mu\text{m}$ grain size. The value of the avoidance radius on the other hand only depends on the relative velocity between the ISM cloud and the star. This way I can constrain the second parameter of the model (v_{rel}). The relative velocity has to be set so that the avoidance radius of the $\sim 0.06\ \mu\text{m}$ grain is around half the

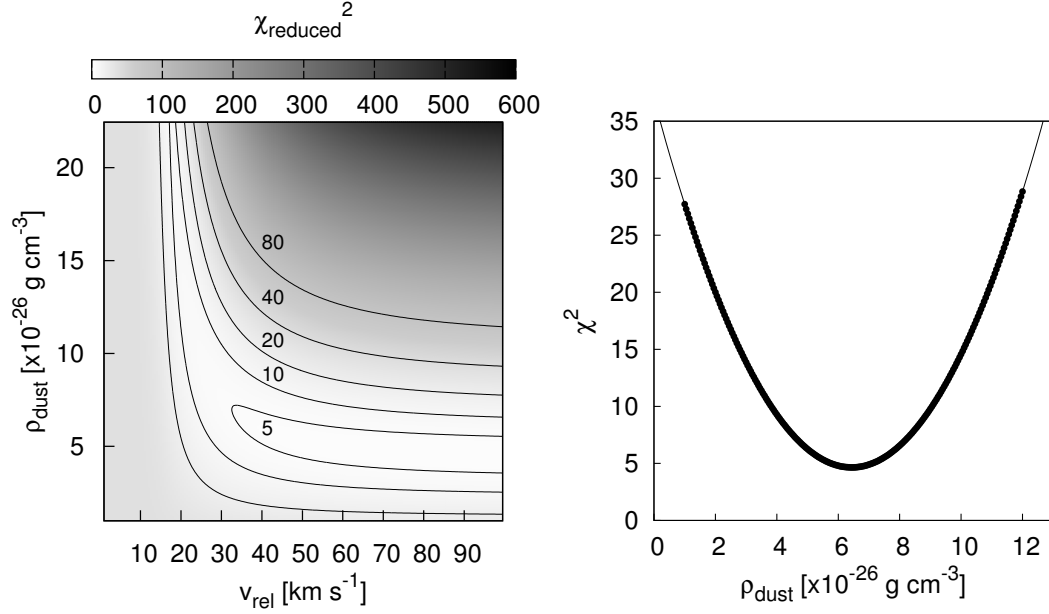


Figure 2.5 *Left panel:* The χ^2 phase space for ρ_{dust} vs. v_{rel} with constrained $r_{\text{ext}} = 1366$ AU. *Right panel:* The ρ vs. v_{rel} phase space (*left panel*) cut at $v_{\text{rel}} = 36$ km s $^{-1}$.

parabola parameter value. This method gives a value that only approximates the true one, but it can be used as an initial guess.

The v_{rel} parameter was constrained by comparing the PSF subtracted image “wings” with model images. Within a range of ± 6 km s $^{-1}$ of my initial guess ($v_{\text{rel}} = 35$ km s $^{-1}$) with 1 km s $^{-1}$ steps, I generated images of the surface brightness distribution to a radius of 2500 AU. The computational time for a total $5000 \times 5000 \times 5000$ AU data cube was long, so I only calculated to a depth of 250 AU, keeping the field of view (FOV) 5000×5000 AU. The fluxes of the generated images were normalized (to ensure that the geometry was the main constraint of the fit and not surface brightness variations) and rotated to angles $\varphi = \pm 20^\circ$ with 1° steps. After rotation, both the model images and the observed image were masked with zeros where there was no detectable surface brightness in the observed image.

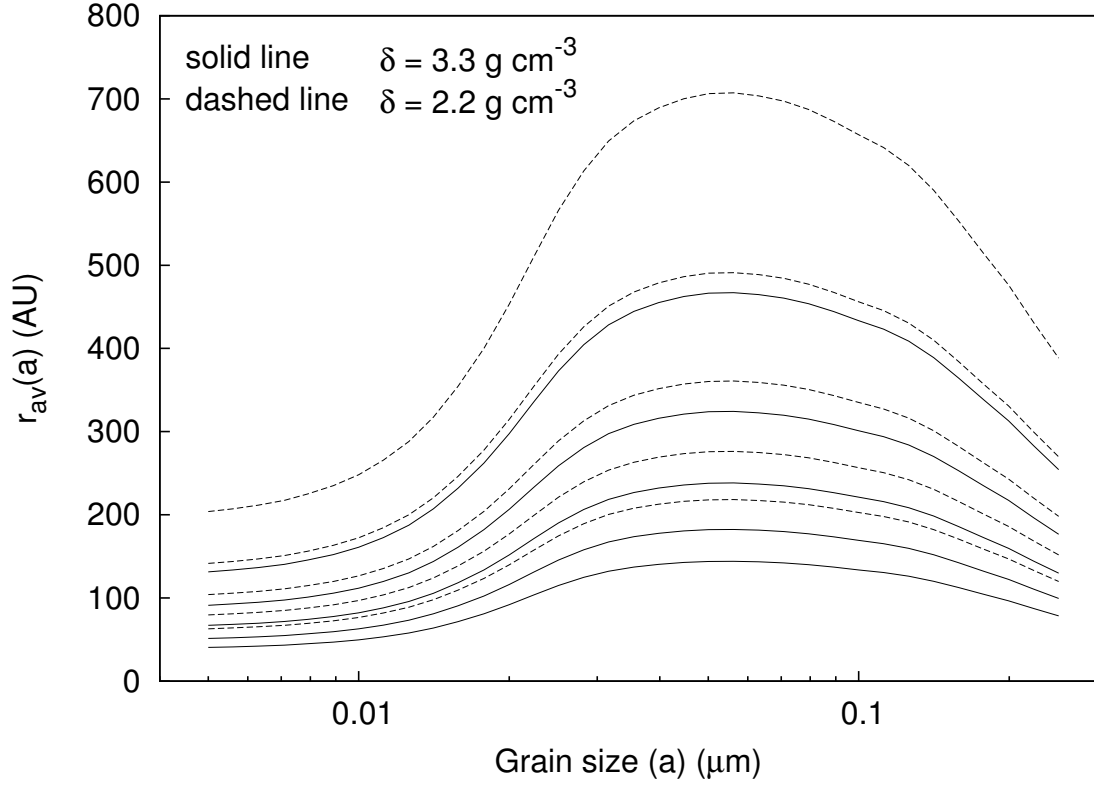


Figure 2.6 The value of r_{av} as a function of grain size. The solid lines are curves for a silicate bulk density of 3.3 g cm^{-3} , while the dashed ones are for 2.2 g cm^{-3} . The curves are for v_{rel} values of 25, 30, 35, 40 and 45 km s^{-1} from top to bottom, respectively.

The χ^2 of the deviations of the model from the observed image were calculated. I was able to constrain the rotation angle of the model and the relative velocity of the cloud to the star. The χ^2 values in the φ vs. v_{rel} phase space are shown in Figure 2.7 (*left panel*). The small values at large rotation angles are artifacts due to the masking. The best-fit rotation angle is at $\varphi = -4^\circ$ to my initial guess, which means that the direction of motion is 143° (CCW) of N. This is just 21° from the proper motion direction. The ISM velocity predicted from vectorial velocity summation to fit this angle is 24 km s^{-1} , which is close to the ISM velocity value calculated by Lallement et al. (1995). The tangential velocity direction of the ISM from the summation is $\sim 47^\circ$ CW of N, which is pointing only 4.5° south from the galactic plane.

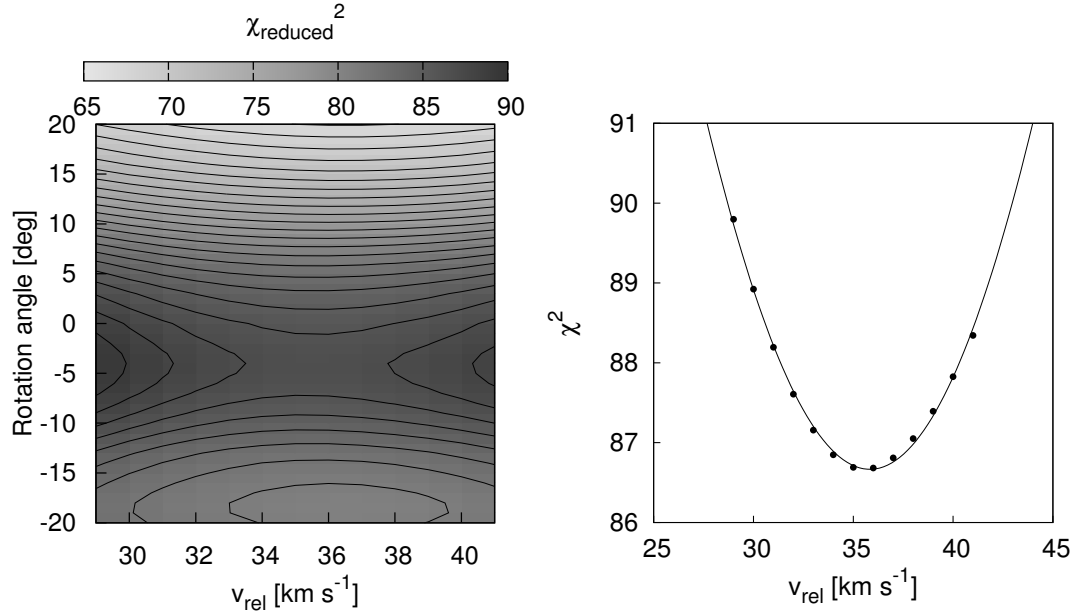


Figure 2.7 *Left panel*: χ^2 in the phase space of φ vs. v_{rel} . *Right panel*: The phase space cut at $\varphi = -4^\circ$, showing the best fit for v_{rel} .

The v_{rel} parameter and its error are calculated by fitting a Gaussian to the phase space values at $\varphi = -4^\circ$ (Figure 2.7, *right panel*). One σ errors are given by

values at $\Delta\chi^2 = 1$. The fits give $v_{\text{rel}} = 35.8 \pm 4.0 \text{ km s}^{-1}$. Figure 2.5 shows that if v_{rel} is constrained, then I can also determine the density of the cloud from simple SED modeling. The vertical cut of Figure 2.5 (*left panel*) at $v_{\text{rel}} = 36 \text{ km s}^{-1}$ is shown in the *right panel* of the same Figure. $\rho_{\text{dust}} = 6.43 \times 10^{-26} \text{ g cm}^{-3}$ is derived from this fit, which gives an original ISM density of $6.43 \times 10^{-24} \text{ g cm}^{-3}$ assuming the usual 1:100 dust to gas mass ratio. This ρ_{dust} is an upper estimate of the actual value, since the model computes what density would be needed to give the observed brightness using a r_{ext} radius sphere. Since the line-of-sight distribution of the dust is not cut off at r_{ext} , I used $\rho_{\text{dust}} = 6.43 \times 10^{-26} \text{ g cm}^{-3}$ as an initial guess; a range of density values was explored with model images.

Since the surface brightness scales with the density, only one image had to be computed, which could be scaled afterwards with a constant factor. The resultant χ^2 distribution is shown in Figure 2.8. The calculated best fitting ISM density is $5.8 \pm 0.4 \times 10^{-24} \text{ g cm}^{-3}$, assuming the average 1:100 dust to gas mass ratio. The error was calculated at $\Delta\chi^2 = 1$. This density ($n \sim 3.5 \text{ atoms cm}^{-3}$) is only moderately higher than the average galactic ISM density ($\sim 1 \text{ atom cm}^{-3}$). The calculated surface brightness images for the three MIPS wavelengths are shown in Figure 2.9. The closest stagnation point is for the $0.005 \mu\text{m}$ grains at 64 AU, while the furthest is at 227 AU for $0.056 \mu\text{m}$ grains. The temperature coded image in Figure 2.10 shows the surface brightness temperature of the bow shock (i.e. the temperature of a black body, that would give the same surface brightness in the MIPS wavelengths as observed). Table 2.1 shows good agreement between the model and the measured values.

The original observed images at $24 \mu\text{m}$ and $70 \mu\text{m}$ were compared to the model. I generated model images with high resolution that included the bow shock and the central star with its photospheric brightness value at the central

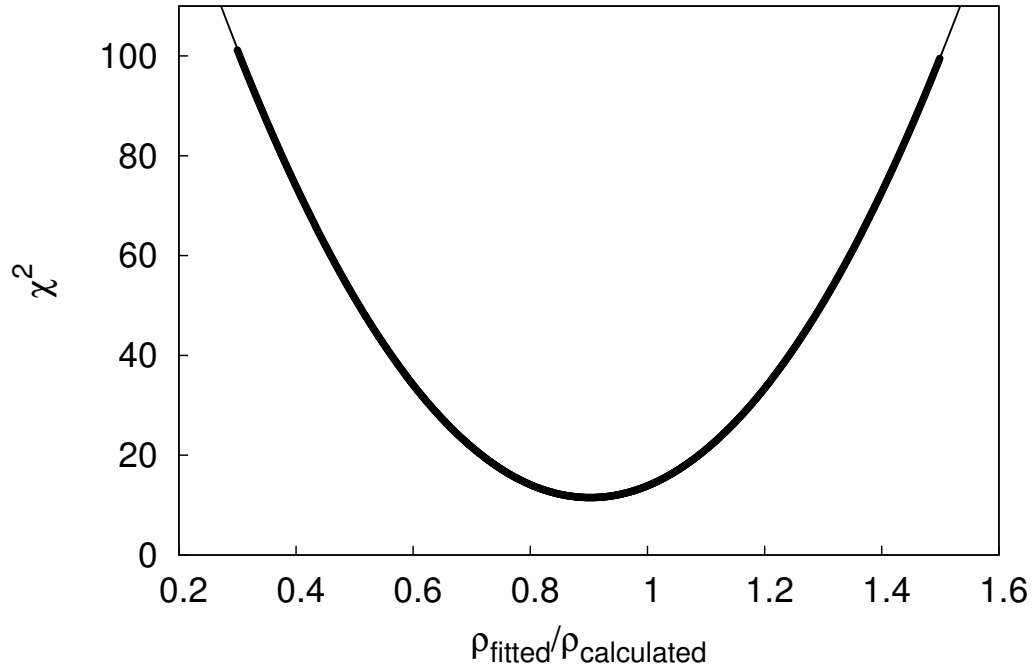


Figure 2.8 The final ISM density was determined from the best fitting surface brightness image. This plot shows the χ^2 of the fits of the model to the observed image, where $\rho_{\text{calculated}}$ is the initial guess from Figure 2.5 *right panel* and ρ_{fitted} is fitted density using surface brightness values.

pixel. I convolved these images with a 1.8 native pixel boxcar smoothed STiny-Tim PSF (see Engelbracht et al., 2007). These images were subtracted from the observed ones (Figure 2.11). The residuals are small and generally consistent with the expected noise. Finally, the best fitting SED of the system ($r_{\text{ext}} = 1366$ AU) is plotted in Figure 2.12. The total mass of the dust inside the $r_{\text{ext}} = 1366$ AU radius is $M_{\text{dust}} = 1.706 \times 10^{24}$ g ($0.023 M_{\text{Moon}}$).

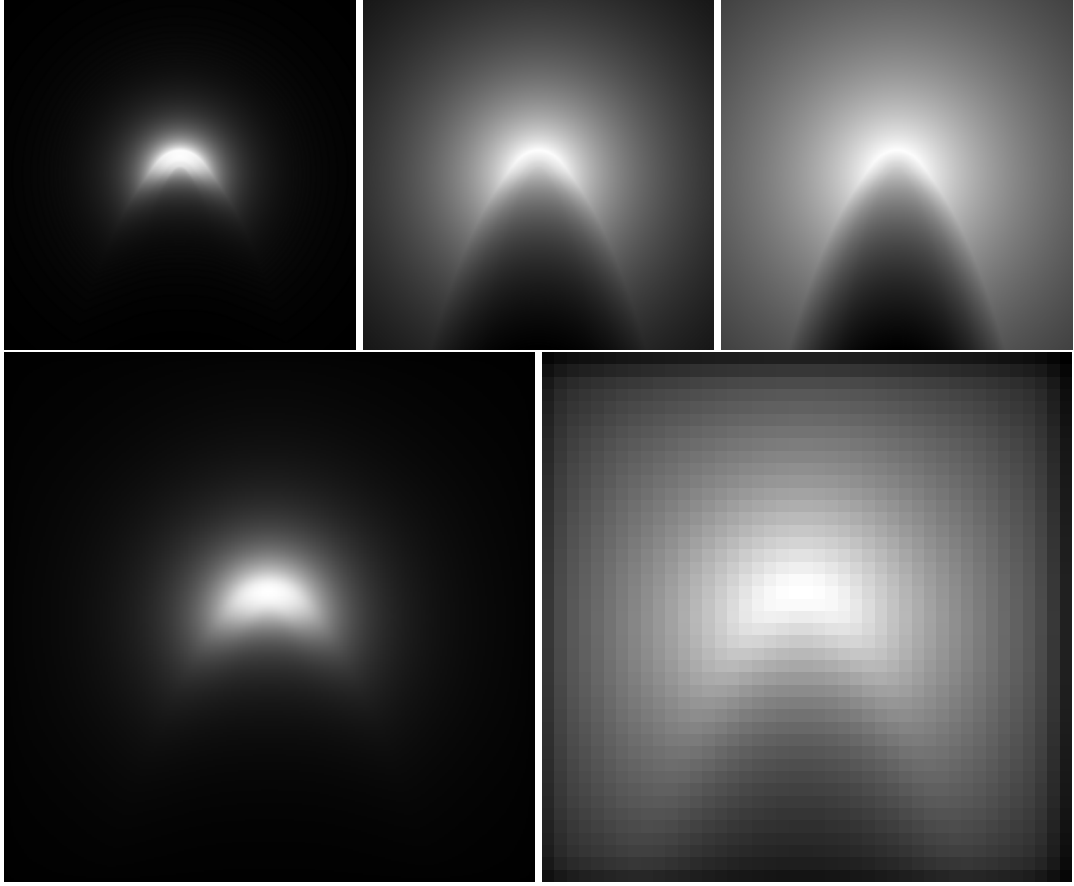


Figure 2.9 *Top panels:* Calculated high resolution surface brightnesses for 24, 70 and 160 μm , respectively. *Bottom panels:* The 24 and 70 μm image with MIPS resolution, convolved with STinyTim PSFs. The images are not rotated to the same angle as the observed bow shock.

2.4 Discussion

2.4.1 Bow Shock Model Results

My model gives a consistent explanation of the total infrared excess and the surface brightness distribution of the bow shock structure at δ Velorum. The question still remains how common this phenomenon is among the previously identified infrared-excess stars. Is it possible that many of the infrared excesses found around early-type stars result from the emission of the ambient ISM cloud? The



Figure 2.10 Image of the bow shock generated by the model computations. The image's FOV is 241×241 . The colorscale shows the integrated surface brightness temperature of the bow shock (and not the radial temperature gradient of the grains) in Kelvins.

majority of infrared excess stars are distant and cannot be resolved, so I cannot answer for sure. However the excess at δ Velorum is relatively warm between 24 and $70 \mu\text{m}$ ($F(24) \sim 0.17 \text{ Jy}$, $F(70) \sim 0.14 \text{ Jy}$), and such behavior may provide an indication of ISM emission. Another test would be to search for ISM spectral features. The ISM $9.7 \mu\text{m}$ silicate feature of the dust grains would have a total flux of $\sim 1 \text{ mJy}$ for δ Velorum. Since the $\sim 1 \text{ mJy}$ flux would originate from an extended region and not a point source that could fit in the slit of IRS, it would be nearly impossible to detect with *Spitzer*. Only a faint hint of the excess is visible in the

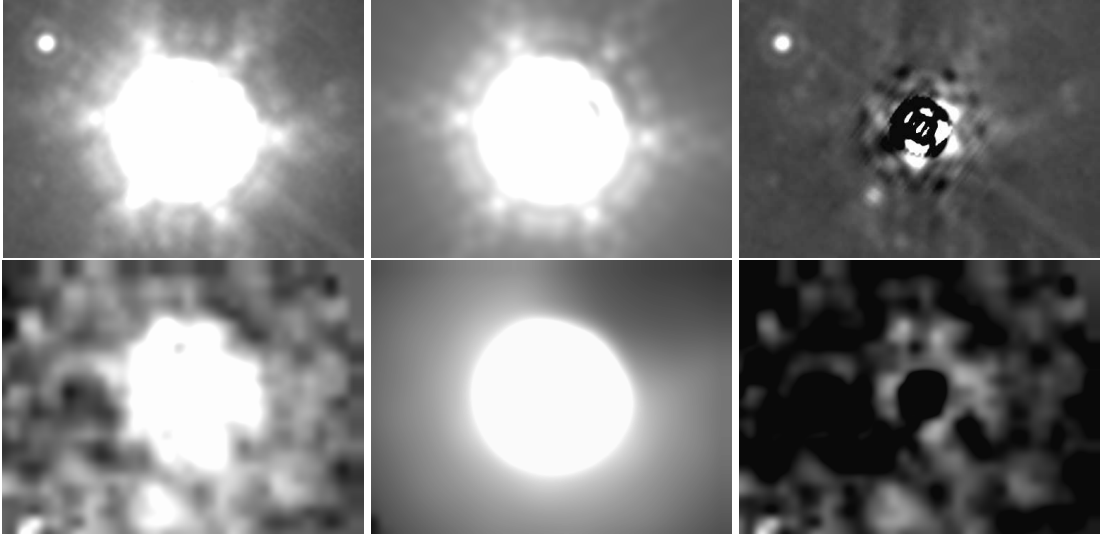


Figure 2.11 **Top row:** *Left panel:* Observed $24\ \mu\text{m}$ image. *Center panel:* Model $24\ \mu\text{m}$ image including both stellar photosphere and bow shock. *Right panel:* Model image subtracted from observed. **Bottom row:** *Left panel:* Observed $70\ \mu\text{m}$ image. *Center panel:* Model $70\ \mu\text{m}$ image including both stellar photosphere and bow shock. *Right panel:* Model image subtracted from observed. The FOV is $\sim 2.7 \times 2.1$, N is up and E to the left.

$8\ \mu\text{m}$ IRAC images, consistent with the small output predicted by my model.

2.4.2 ISM Interactions

To produce a bow shock feature as seen around δ Velorum, the star needs to be luminous, have a rather large relative velocity with respect to the interacting ISM, and be passing through an ISM cloud. A relative velocity of $\sim 36\ \text{km s}^{-1}$ is not necessarily uncommon, since the ISM in the solar neighborhood has a space velocity of $\sim 26\ \text{km s}^{-1}$ (Lallement et al., 1995) and stars typically move with similar speeds. If the ISM encountering the star is not dense enough the resulting excess will be too faint to be detected. The Sun and its close ($\sim 100\ \text{pc}$) surrounding are sitting in the Local Bubble ($n(\text{HI}) < 0.24\ \text{cm}^{-3}$, $T \approx 7500\ \text{K}$, Lallement, 1998; Jenkins, 2002). This cavity generally lacks cold and neutral gas up to $\sim 100\ \text{pc}$.

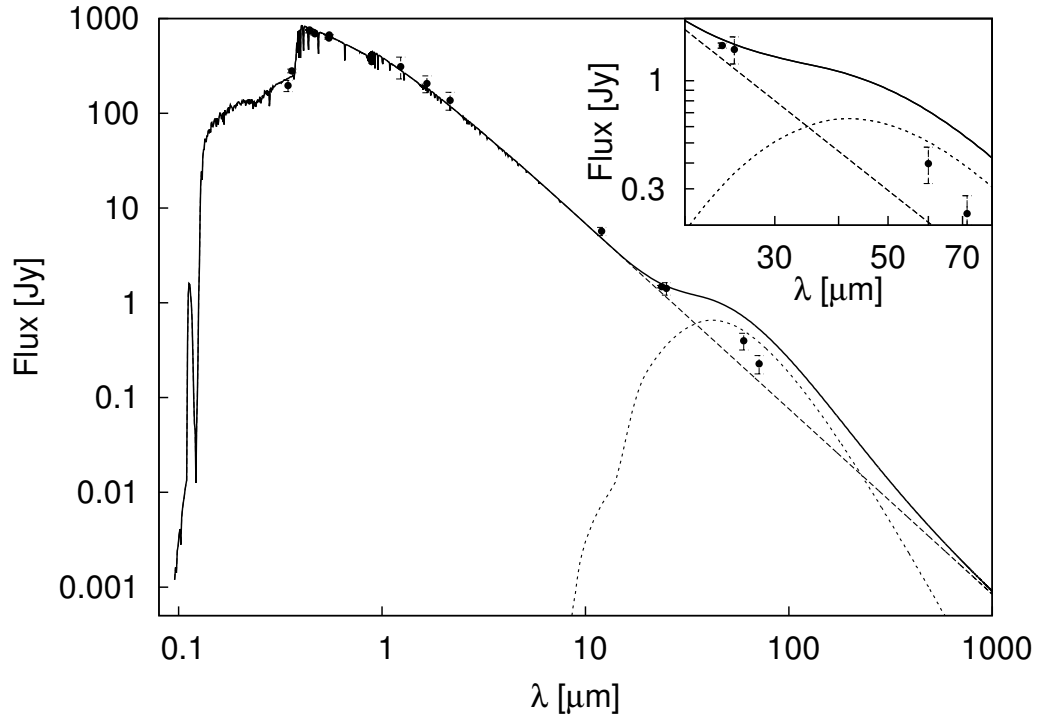


Figure 2.12 The best fit SED. The window in the upper-right corner is a magnified part of the SED between 20 and 80 μm . The plotted fluxes are 24 and 70 μm MIPS and 25 and 60 μm IRAS, with errorbars. The 9.7 μm silicate feature in the model SED of the ISM cloud is very faint and on a bright continuum. The flux from the G dwarf has been subtracted from the 24 and 70 μm MIPS observations.

The density I calculated at δ Velorum is ~ 15 times higher than the average value inside the Local Bubble. Observations over the past thirty years have shown that this void is not completely deficient of material, but contains filaments and cold clouds (Wennmacher et al., 1992; Herbstmeier & Wennmacher, 1998; Jenkins, 2002; Meyer et al., 2006). Talbot & Newman (1977) calculated that an average galactic disk star of solar age has probably passed through about 135 clouds of $n(\text{HI}) \geq 10^2 \text{ cm}^{-3}$ and about 16 clouds with $n(\text{HI}) \geq 10^3 \text{ cm}^{-3}$. Thus the scenario that I propose for δ Velorum is plausible.

2.4.3 Implications for Diffusion/Accretion Model of λ Boötis Phenomenon

Holweger et al. (1999) list δ Velorum as a simple A star, not a λ Boötis one. I downloaded spectra of the star from the Appalachian State University Nstars Spectra Project (Gray et al., 2006). The spectra of δ Velorum, λ Boötis (prototype of its group) and Vega (an MK A0 standard) are plotted in Figure 2.13. The metallic lines are generally strong for δ Velorum. One of the most distinctive characteristics of λ Boötis stars is the absence or extreme weakness of the MgII lines at 4481 Å (Gray, 1988). Although the MgII line seems to be weaker than expected for an A0 spectral type star, it still shows high abundance, which confirms that δ Velorum is not a λ Boötis type star (Christopher J. Corbally, private communication). The overall metallicity ratio for δ Velorum is $[M/H] = -0.33$, while for λ Boötis it is $[M/H] = -1.86$ (Gray et al., 2006). The G star's contribution to the total abundance in the spectrum is negligible, because of its relative faintness. I used spectra from the NStars web site to synthesize a A1V/A5V binary composite spectrum and found only minor differences from the A1V spectrum alone. Thus, the assigned metallicity should be valid.

These results show that at δ Velorum, where I do see the ISM interacting with a star, there is no sign of the λ Boötis phenomenon or just a very mild effect. Turcotte & Charbonneau (1993) modeled that an accretion rate of $\sim 10^{-14} M_{\odot} \text{ yr}^{-1}$ is necessary for a $T_{\text{eff}} = 8000$ K main sequence star to show the spectroscopic characteristics of the phenomenon. The λ Boötis abundance pattern starts to show at $10^{-15} M_{\odot} \text{ yr}^{-1}$ and ceases at $10^{-12} M_{\odot} \text{ yr}^{-1}$. To reach an ISM accretion of $10^{-15} M_{\odot} \text{ yr}^{-1}$ a collecting area of 2 AU radius would be needed with my modeled ISM density and velocity. For an accretion of 10^{-14} , 10^{-13} and $10^{-12} M_{\odot} \text{ yr}^{-1}$ collecting areas of 6.5, 20 and 65 AU radii are needed, respectively.

With the accretion theory of Bondi & Hoyle (1944), I get an accretion rate of

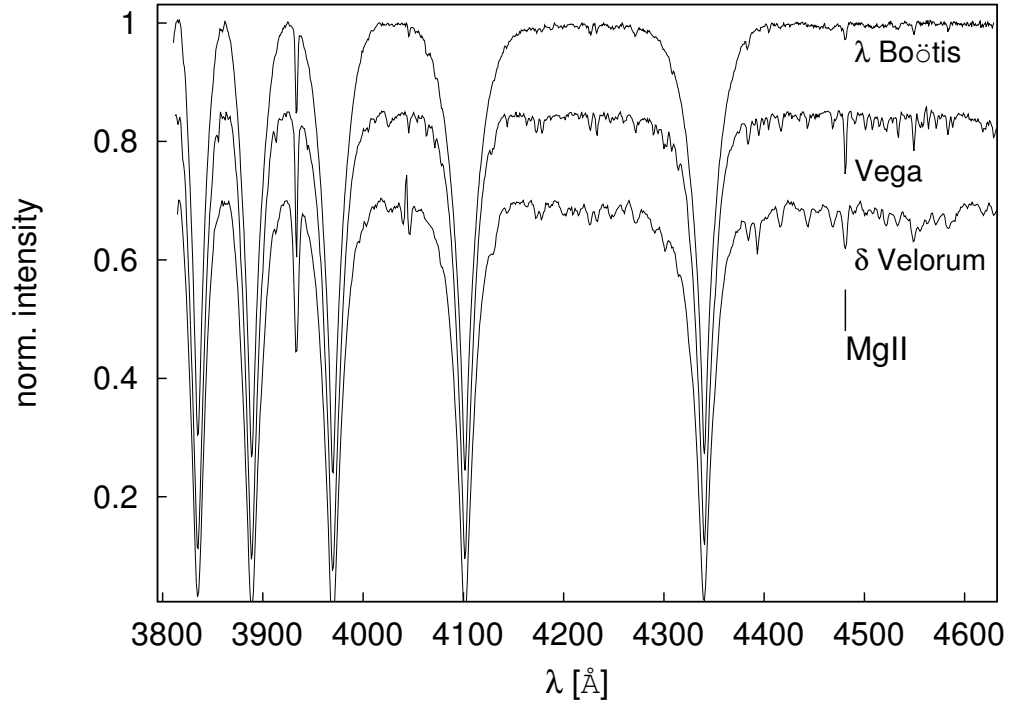


Figure 2.13 The spectra of δ Velorum (bottom line), Vega (middle line) and λ Boötis (top line).

$6.15 \times 10^{-15} M_{\odot} \text{ yr}^{-1}$ for δ Velorum. Thus, the accretion rate for this star is probably not high enough to show a perfect λ Boötis spectrum, but should be high enough for it to show some effects of accretion. This star is an exciting testbed for the diffusion/accretion model of the λ Boötis phenomenon.

2.5 Summary

I observe a bow shock generated by photon pressure as δ Velorum moves through an interstellar cloud. Although this star was thought to have a debris disk, its infrared excess appears to arise at least in large part from this bow shock. I present a physical model to explain the bow shock. My calculations reproduce the observed surface brightness of the object and give the physical parameters

of the cloud. I determined the density of the surrounding ISM to be $5.8 \pm 0.4 \times 10^{-24} \text{ g cm}^{-3}$. This corresponds to a number density of $n \approx 3.5 \text{ atoms cm}^{-3}$, which means a ~ 15 times overdensity relative to the average Local Bubble value. The cloud and the star have a relative velocity of $35.8 \pm 4.0 \text{ km s}^{-1}$. The velocity of the ISM in the vicinity of δ Velorum I derived is consistent with LIC velocity measurements by Lallement et al. (1995). My best-fit parameters and measured fluxes are summarized in Table 2.1.

Holweger et al. (1999) found that δ Velorum is not a λ Boötis star. The measurements from the Nstars Spectra Project also confirm this. Details regarding the diffusion/accretion time scales for a complex stellar system remain to be elaborated. Nevertheless, the *Spitzer* observations of δ Velorum provide an interesting testbed and challenge to the ISM diffusion/accretion theory for the λ Boötis phenomenon.

CHAPTER 3

DEBRIS DISK STUDY OF PRAESEPE

I present $24\ \mu\text{m}$ photometry of the intermediate-age open cluster Praesepe. I assemble a catalog of 193 probable cluster members that are detected in optical databases, the Two Micron All Sky Survey (2MASS), and at $24\ \mu\text{m}$, within an area of ~ 2.47 square degrees. Mid-IR excesses indicating debris disks are found for one early-type and for three solar-type stars. Corrections for sampling statistics yield a $24\ \mu\text{m}$ excess fraction (debris disk fraction) of $6.5 \pm 4.1\%$ for luminous and $1.9 \pm 1.2\%$ for solar-type stars. The incidence of excesses is in agreement with the decay trend of debris disks as a function of age observed for other cluster and field stars. The values also agree with those for older stars, indicating that debris generation in the zones that emit at $24\ \mu\text{m}$ falls to the older 1-10 Gyr field star sample value by roughly 750 Myr.

I discuss the results in the context of previous observations of excess fractions for early- and solar-type stars. I show that solar-type stars lose their debris disk $24\ \mu\text{m}$ excesses on a shorter timescale than early-type stars. Simplistic Monte Carlo models suggest that, during the first Gyr of their evolution, up to 15-30% of solar-type stars might undergo an orbital realignment of giant planets such as the one thought to have led to the Late Heavy Bombardment, if the length of the bombardment episode is similar to the one thought to have happened in our Solar System.

In Appendix A, I determine the cluster's parameters via bootstrap Monte Carlo isochrone fitting, yielding an age of 757 Myr (± 36 Myr at 1σ confidence) and a distance of 179 pc (± 2 pc at 1σ confidence), not allowing for systematic errors.

3.1 Introduction

Stars generally form with an accompanying circumstellar disk. Planets can grow from this primordial disk over a few to a few tens of Myr. The *Infrared Astronomy Satellite (IRAS)* detected infrared excess emission from disks around stars with ages much older than the clearing timescales of protoplanetary circumstellar disks (Aumann et al., 1984). These excesses arise from second-generation “debris disks” that are the results of collisional cascades initiated by impacts between planetesimals and of cometary activity (Backman & Paresce, 1993). The micron-sized dust grains in debris disks are heated by the central star(s) and reradiate the received energy at mid-infrared wavelengths. Studying this infrared emission lets us probe the frequency of formation of planetary systems and to track their evolution. For example, some of the relatively prominent disks may be analogs to that in the Solar System at the epoch of Late Heavy Bombardment (LHB; e.g. Gomes et al., 2005; Strom et al., 2005).

IRAS and *Infrared Space Observatory (ISO)* observations of debris disks suggest that the excess rate steadily declines with stellar age, indicative of stars losing these disks within a few hundred million years (Habing et al., 2001; Spangler et al., 2001). A theoretical model that involved delayed stirring was developed by Dominik & Decin (2003) to explain this phenomenon; however, a uniform evolutionary model could not be derived. There were a number of reasons. The sensitivity of these instruments was often inadequate for observations down to the photospheric levels. The large beam sizes also occasionally confused the excesses with background objects and/or the galactic cirrus. The Multiband Imaging Photometer for *Spitzer* (MIPS; Rieke et al., 2004) on the *Spitzer Space Telescope* has improved sensitivity and resolution in the mid-infrared and with it astronomers have been able to carry out more detailed statistical studies of debris disks at a

wide range of stellar ages and spectral types.

Rieke et al. (2005) observed a large sample of nearby A-type field stars with *Spitzer*, which combined with existing *IRAS* and *ISO* data definitively demonstrated that the frequency of debris disk excesses declines with age and that the disk properties vary at all ages. Even by probing excesses down to 25% above the photospheric level, Rieke et al. (2005) found that some stars at ages of only 10-20 Myr do not show any signs of excess. These results were confirmed by Su et al. (2006). This behavior implies a very fast clearing mechanism for disks around some of these stars, or perhaps that they form with only very low mass disks. The models of Wyatt et al. (2007) provided a first-order explanation in terms of a steady state evolution of the debris disks from a broad distribution of initial masses.

An important question for habitable planet search/evolution is whether the same processes occur for FGK-type stars. A number of surveys of solar-type stars have been conducted with *Spitzer*. The MIPS Guaranteed Time Observers (GTO) team has searched ~ 200 field stars for excesses (Trilling et al., 2008), plus many hundreds of open cluster members (e.g., Gorlova et al., 2006, 2007; Siegler et al., 2007). The legacy survey by the Formation and Evolution of Planetary Systems (FEPS) group has examined 328 stars (both field and open cluster members) (Mamajek et al., 2004; Meyer et al., 2004, 2008; Stauffer et al., 2005; Kim et al., 2005; Silverstone et al., 2006).

Trilling et al. (2008) showed that solar-type stars of age older than 1 Gyr have excess emission at $70\ \mu\text{m} \sim 16\%$ of the time. Excesses at this wavelength are expected to arise from Kuiper-Belt-like planetesimal regions, but with masses 10-100 times greater. Meyer et al. (2008) find that 8.5-19% of solar-type stars at ages < 300 Myr have debris disks detectable at $24\ \mu\text{m}$ and that this number gradually

goes down to $< 4\%$ at older ages, augmenting work by Gorlova et al. (2006), Siegler et al. (2007) and Trilling et al. (2008). Excesses at this wavelength around solar-type stars probe the 1-40 AU range, the asteroidal and planetary region in the Solar System.

The ideal laboratories to determine the stellar disk fractions with good number statistics are open clusters and associations. To investigate the fraction of solar-type excess stars, the observations have to be able to detect the photospheres of the non-excess stars. The range of distances to suitable clusters compromises the uniformity of the results. The survey of η and χ Persei (Currie et al., 2008) could only determine the early-type star excess fraction, while that of NGC 2547 (Young et al., 2004; Gorlova et al., 2007) could only detect photospheres down to early G due to similar limits. The observations in M47 (Gorlova et al., 2004) also yielded values to early G spectral type stars. The investigations of IC 2391 (Siegler et al., 2007) and the Pleiades (Gorlova et al., 2006) gave insights on debris disk evolution down as far as K spectral-type stars.

To study further the fraction of debris disks around solar-mass stars, I have observed the nearby Praesepe (M44, NGC 2632, Beehive) open cluster. My observations, along with those of Cieza et al. (2008) on the Hyades cluster, fill the gap in previous work on debris disk fractions in the age range of 600-800 Myr. This range is of interest because it coincides with the LHB in the Solar System. The close proximity of the cluster (~ 180 pc) and its large number of members ensured that good statistics would be achieved. Praesepe has been extensively studied by many groups (Klein Wassink, 1927; Jones & Cudworth, 1983; Jones & Stauffer, 1991; Hambly et al., 1995; Wang et al., 1995; Kraus & Hillenbrand, 2007), providing a nearly full membership list to the completeness limit of $[24] \sim 9$ mag (the brightness of a G4 V spectral-type star at the distance of the cluster). The

member stars have high proper motions ($\sim 39 \text{ mas yr}^{-1}$), clearly distinguishing them from field stars.

3.2 Observations, data reduction, and photometry

I used MIPS to observe Praesepe as part of the GTO program PID 30429 (2007 May 30). The center part of the cluster ($8^{\text{h}}40^{\text{m}}21^{\text{s}}$, $19^{\circ}38'40''$) was imaged using three scan maps (with 12 legs in a single scan map overlapping with half-array cross-scan). The map covers a field of $\sim 2.47 \text{ deg}^2$, as shown in Figure 3.1. Medium scan mode was used, resulting in a total effective exposure time per pixel of 80 s (at $24 \mu\text{m}$). All data were processed using the MIPS instrument team Data Analysis Tool (DAT, Gordon et al., 2005) as described by Engelbracht et al. (2007).

Although MIPS in scan-mode provides simultaneous data from all three detectors (at 24, 70 and $160 \mu\text{m}$), I base my study on the $24 \mu\text{m}$ channel data only. The 70 and $160 \mu\text{m}$ detectors are insensitive to stellar photospheric emissions at the distance of Praesepe. In retrospect, the rarity of excesses in the survey is consistent with the lack of detections at the longer wavelengths.

The initial coordinate list for the $24 \mu\text{m}$ photometry was assembled with the `daofind` task under IRAF¹. I later expanded this list by visually examining the images and manually adding all sources to the list that were missed by `daofind`. The final list for photometry contained 1457 sources. To achieve high accuracy, I performed point-spread function (PSF)–fitting photometry. The calibration star HD 173398 was adopted as a PSF standard, with the final PSF constructed from 72 individual observations, kindly provided to us by C. Engelbracht. The standard

¹IRAF is distributed by the National Optical Astronomy Observatories, which is operated by the Association of the Universities for Research in Astronomy, Inc. (AURA) under cooperative agreement with the National Science Foundation.

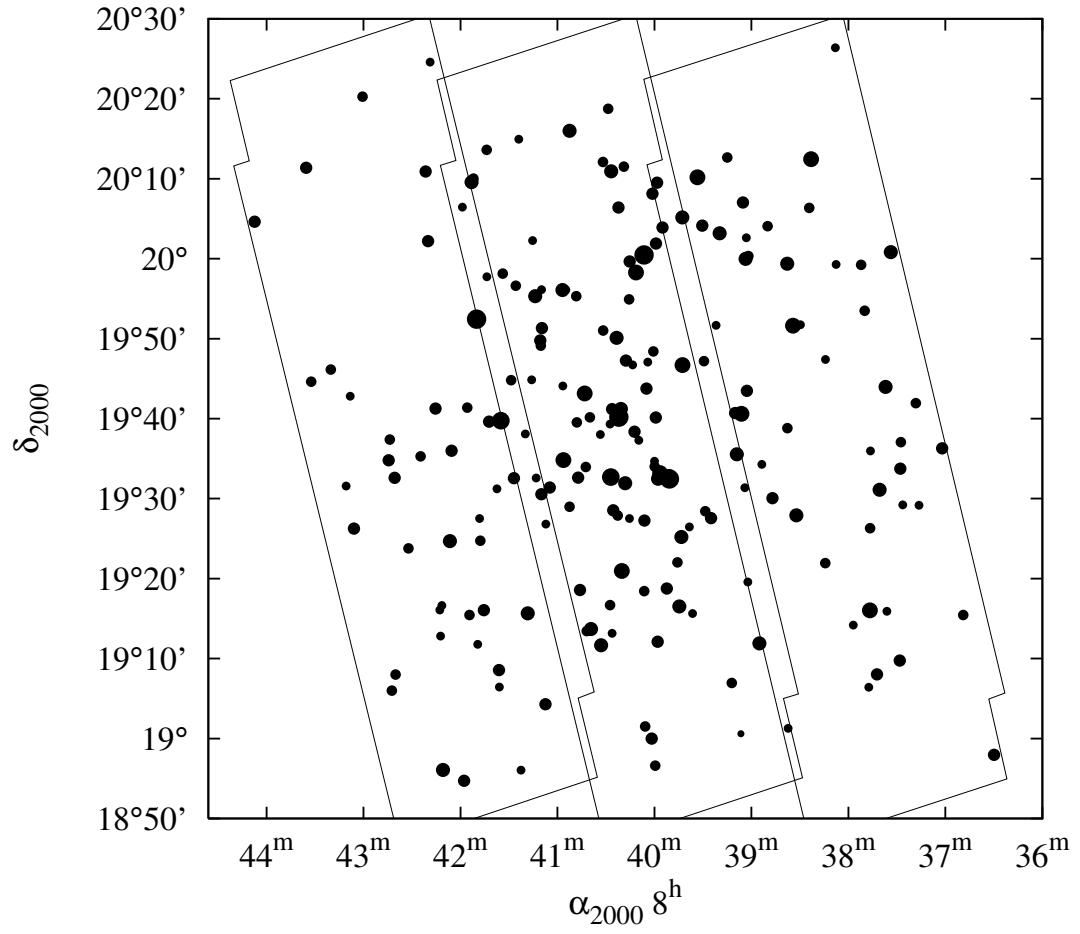


Figure 3.1 The observed field, showing the areas covered by three scanmaps and the observed cluster member stars with sizes proportional to their brightness in [24].

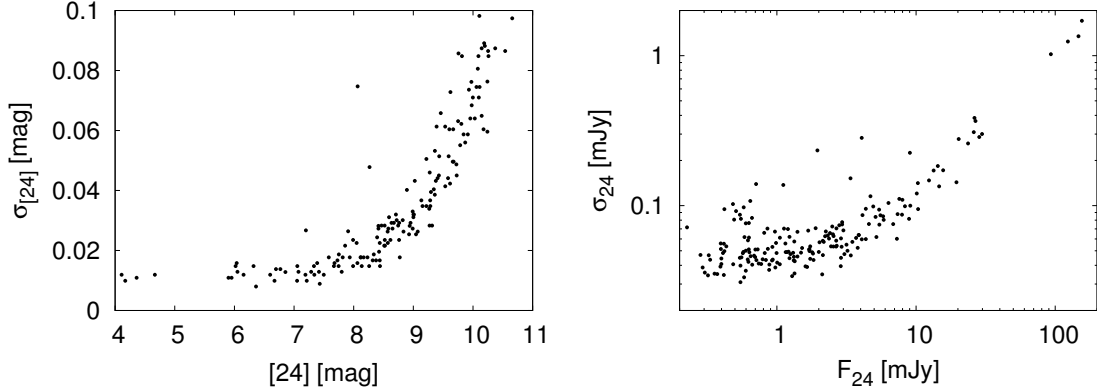


Figure 3.2 The error of the 24 μm photometry is plotted as a function of brightness for cluster member sources. The *left panel* shows the flux and its error on the magnitude scale, while the *right panel* shows them in mJy flux values. All points have less than 0.1 magnitude error and nearly all stars brighter than 9th magnitude have errors less than 0.04 magnitude.

IRAF tasks `phot` and `allstar` of the `daophot` package were used.

The observed field is free of nebulosity and stellar crowding, so I was able to use a large PSF radius of $112''$, with fitting radius of $5.7''$. The large PSF radius ensured us that the aperture correction was negligible. The instrumental number counts were converted to flux densities with the conversion $1.068 \times 10^{-3} \text{ mJy arcsec}^{-2} \text{ MIPS_UNIT}^{-1}$ (Engelbracht et al., 2007). I then translated these values to 24 μm magnitudes taking 7.17 Jy for the [24] magnitude zero point, which has error of $\pm 0.11 \text{ Jy}$ (Rieke et al., 2008). I show the photometric error vs. brightness plots of the measurements in Figure 3.2. Almost all sources brighter than 9th magnitude ($\sim 1.8 \text{ mJy}$) have errors less than 0.04 mag ($\sim 0.07 \text{ mJy}$) and all sources remain below errors of 0.1 mag; the average error is $\sim 5\%$. As a check, I performed independent PSF photometry with `StarFinder` under IDL, obtaining photometry values within the errors of the IRAF photometry and with errors similar to the ones given by `daophot`.

3.3 Catalog surveys and the final sample

I compiled a complete catalog for all sources in the field of view, including their optical, near infrared, and 24 μm data. I expanded this catalog with all known cluster members outside of the field of view (naturally without [24] data). This enabled us to plot a full cluster optical color-magnitude diagram (CMD), which I used to confirm the cluster's age and distance (see Appendix A).

Optical data for the sources were obtained from the 5th data release of the Sloan Digital Sky Survey (SDSS), while 2MASS provided J, H, and K_s magnitudes. The SDSS photometry is generally unreliable for bright sources, the ones mostly detected in the MIPS survey. To ensure I had good photometry for these sources, I collected BV data (for 356 stars altogether) using the Webda database², providing an ensemble of data for high probability cluster members from various papers (Johnson, 1952; Anthony-Twarog, 1982; Dickens et al., 1968; Lutz & Lutz, 1977; Upgren et al., 1979; Castelaz et al., 1991; Mermilliod et al., 1990; Weis, 1981; Stauffer, 1982; Andruk et al., 1995; Mendoza, 1967; Oja, 1985). The data downloaded from the Webda database cover the brightest magnitude range of the cluster, including stars avoided by modern CCD observations or where they are saturated. I converted the BV magnitudes to SDSS r and g values by averaging the conversion slopes of Jester et al. (2005); Jordi et al. (2006); Zhao & Newberg (2006) and Fukugita et al. (1996) and obtained

$$g = (0.607 \pm 0.016)(B - V) - (0.1153 \pm 0.0095) + V \quad (3.1)$$

$$r = (-0.453 \pm 0.028)(B - V) + (0.1006 \pm 0.0131) + V. \quad (3.2)$$

²<http://www.univie.ac.at/webda/>

Where the calculated r or g brightnesses for the Webda catalog members differed from the SDSS data by more than 0.5 magnitude, I replaced the SDSS data with the calculated one.

Cluster membership was determined by compiling all accessible databases. The largest membership lists are those of Wang et al. (1995) and Kraus & Hillenbrand (2007), which were supplemented by the Webda catalog search results. Wang et al. (1995) give a list of 924 stars, out of which I chose only 198 that are high probability members of the cluster according to the proper motion data in the paper. The list of Kraus & Hillenbrand (2007) is much more robust with 1130 stars, all of which have membership probability $> 50\%$; 1010 of them have $> 80\%$ membership probability. The databases (SDSS, 2MASS, Webda, Wang et al. (1995), Kraus & Hillenbrand (2007)) were cross-correlated with a maximum matching radius of $3.6''$. The closest member within this radius is matched as a pair and all others are added to the catalog as new sources. The program excluded pairing members from the same catalog. The final cluster member list contains 1281 candidates, of which 493 were in the observed field.

After plotting the color-magnitude diagram and doing an initial isochrone fit on cluster members, I tested for bad photometry. I generated a list of all the member stars that were further from the isochrone sequence than 0.3 magnitude, examined all these stars for anomalies on SDSS images, and searched for BV magnitudes in Simbad. If the star was saturated or a calculated r , g magnitude differed from the SDSS r , g value by 0.5 magnitude or more (the same criteria as used before), I used the calculated value.

In Figure 3.3, I show how the selection criteria narrow the CMD, and where sources with different selection characteristics are distributed in the field. From the 1457 sources identified in the $24\ \mu\text{m}$ survey, 201 were cataloged as cluster

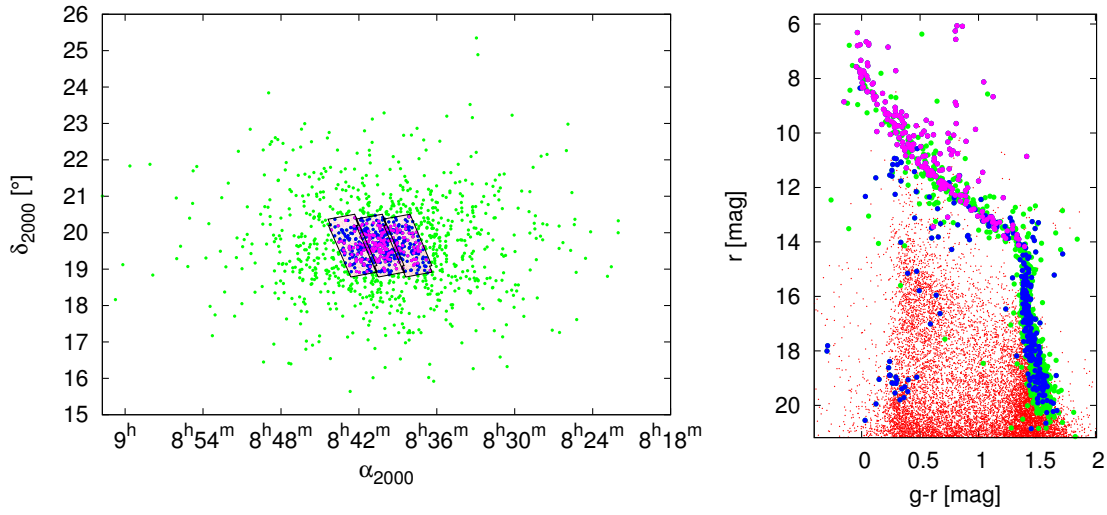


Figure 3.3 The spatial and CMD position of the selected sources. *Red dots*: The combined list for all sources in the observed field; *Green dots*: All cluster members outside the observed field; *Blue dots*: All cluster members in the observed field that could not be identified in the $24\ \mu\text{m}$ survey; *Magenta dots*: All cluster members that were identified in the $24\ \mu\text{m}$ survey.

members by previous work. Of these, 193 also have data in the optical and near infrared. The survey's completeness limit compared to 2MASS is at $J = 10$ mag ($[24] \sim 9$ mag), as is shown in Figure 3.4. This limit corresponds to a G4 V star at the distance of Praesepe. The completeness limit for the cluster member sources is also shown in Figure 3.4. Between 10^{th} and 11^{th} magnitude in J I achieve 75% completeness for cluster members.

For the $[24]$ magnitude values to be comparable to the 2MASS K_S photometry, I fitted a Gaussian to the binned number distribution of the $K_S - [24]$ values of all member sources with $r - K_S < 0.8$ (\sim A stars). I derived a general correction factor of -0.032 ± 0.002 magnitude ($\sim 3\%$) for the $[24]$ values. The Gaussian fits are shown in Figure 3.5. This same method has been used by Rieke et al. (2008) to obtain the average ratio of K_S to $24\ \mu\text{m}$ flux densities. By optimizing the fit of

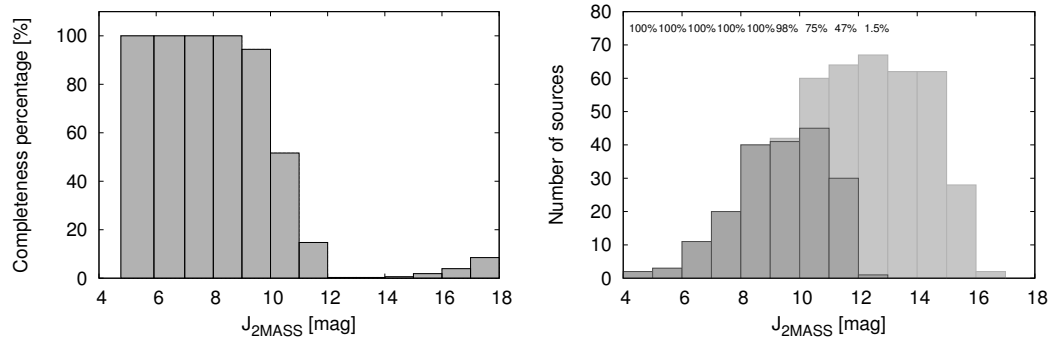


Figure 3.4 *Left Panel:* The completeness limit of the survey is shown as a function of 2MASS J magnitude. I detect almost all sources brighter than 10th magnitude, corresponding to a \sim G4 V star. For sources fainter than 14th magnitude random associations begin to occur. *Right Panel:* The total number of cluster members within the field of view (light gray) and the number of members detected (dark gray) at [24] are shown as a function of J magnitude.

the [24] data to the 2MASS K_S data, I eliminated any absolute calibration offsets. The average variance of the fitted gaussians is $\sigma = 0.047$ mag, consistent with the average [24] error value of ~ 0.05 mag.

I summarize the [24] photometry results for the 193 cluster members that were identified in all wavelength regions in Table 3.1. The first column of the table gives the designated number, while the coordinates are that of the 24 μ m flux source. As a source/coordinate comparison I also list the 2MASS source associated with the 24 μ m emission. The table contains the K_S adjusted [24] magnitude, the original flux values (in mJy) and the "best" r and g photometry value. Cluster membership probability is shown by either the proper motion of the source or by the Wang et al. (1995) catalog number of the source. Sources that are missing both values were listed as cluster members either in the Webda database or in Kraus & Hillenbrand (2007).

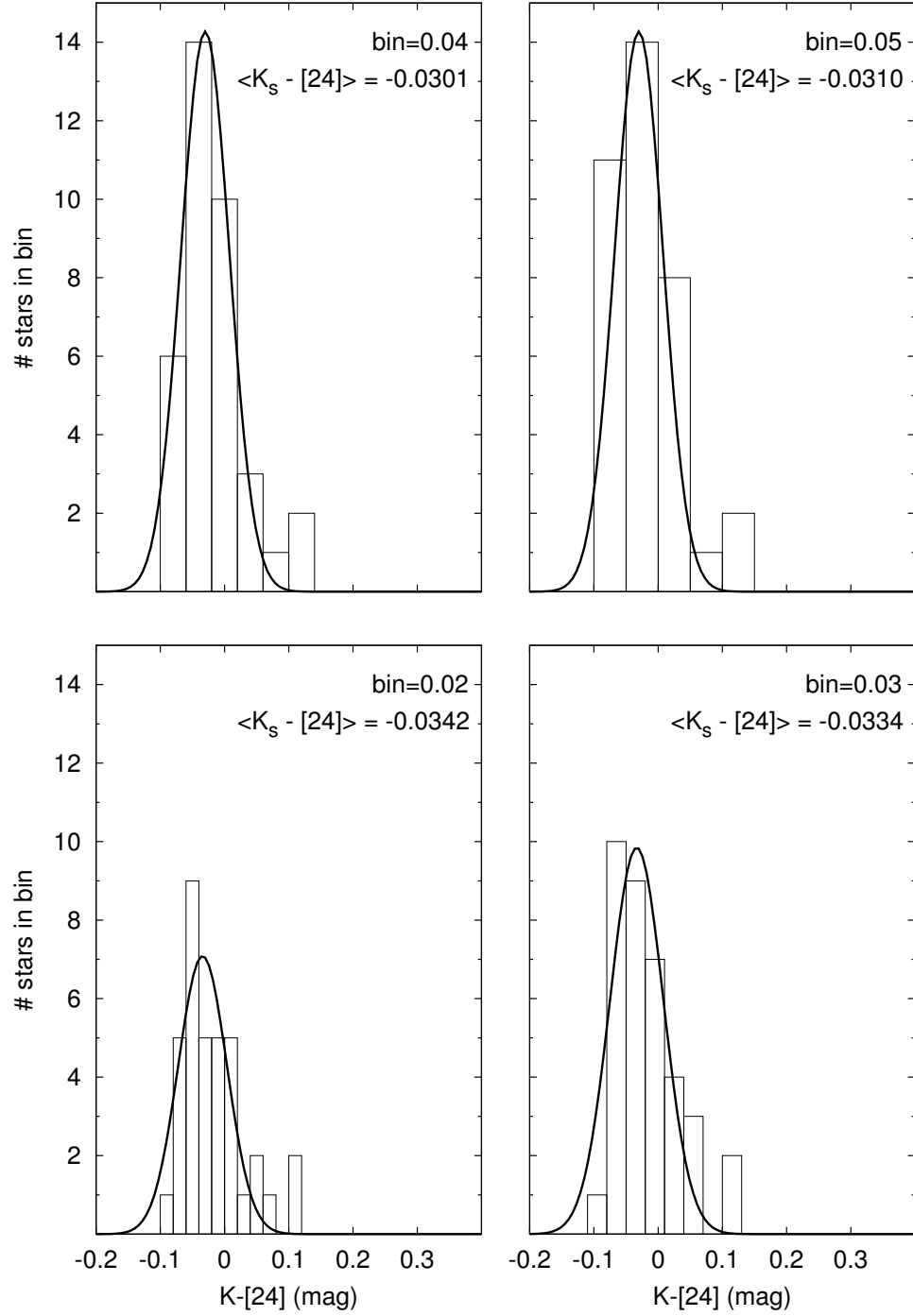


Figure 3.5 The panels show the Gaussian fits to the number distribution of A type stars, within certain $K_S - [24]$ bins.

Table 3.1. Photometry of Praesepe members in the [24] band

#	α_{2000} [h:m:s]	δ_{2000} [°:′:″]	g^* [mag]	r^* [mag]	K_{2MASS} [mag]	[24] [†] [mag]	F_{24}^{\dagger} [mJy]	μ_{α} [mas yr ⁻¹]	μ_{δ} [mas yr ⁻¹]	$W\#^{\ddagger}$	2MASS
1	8:36:29.83	18:57:56.52	9.57	9.33*	8.30±0.01	8.23±0.05	3.54± 0.15	-34.60	-12.60	-	08362985+1857570
2	8:36:48.95	19:15:26.06	11.54*	10.92*	9.69±0.02	9.35±0.06	1.26± 0.07	-36.30	-12.80	-	08364896+1915265
3	8:37:02.04	19:36:17.42	9.34	9.06*	8.06±0.01	8.01±0.02	4.32± 0.09	-34.30	-13.00	-	08370203+1936171
4	8:37:16.35	19:29:11.58	14.67	13.38	10.47±0.02	10.06±0.07	0.65± 0.04	-34.70	-15.40	267	08371635+1929103
5	8:37:18.29	19:41:56.33	11.75	11.23	9.80±0.02	9.69±0.05	0.93± 0.04	-37.20	-15.20	268	08371829+1941564
6	8:37:26.51	19:29:13.06	14.48	13.33	10.83±0.02	10.77±0.15	0.34± 0.05	-42.70	-14.40	274	08372638+1929128
7	8:37:27.58	19:37:03.29	11.97	11.40	9.81±0.02	9.75±0.06	0.87± 0.04	-34.10	-12.60	277	08372755+1937033
8	8:37:27.95	19:33:45.25	9.91*	9.64	8.46±0.02	8.48±0.02	2.80± 0.06	-36.60	-13.20	2	08372793+1933451
9	8:37:28.22	19:09:44.32	9.65	9.37*	8.40±0.01	8.39±0.02	3.06± 0.05	-36.20	-13.40	3	08372819+1909443
10	8:37:33.84	20:00:49.39	8.76*	8.66*	7.95±0.03	7.95±0.02	4.57± 0.10	-35.70	-13.10	5	08373381+2000492
11	8:37:36.33	19:15:53.96	14.05*	13.05*	10.76±0.02	10.34±0.09	0.51± 0.04	-35.30	-11.20	288	08373624+1915542
12	8:37:37.00	19:43:58.69	7.77*	7.79*	7.29±0.01	7.30±0.01	8.31± 0.09	N/A	N/A	6	08373699+1943585
13	8:37:40.71	19:31:06.38	8.29	8.20*	7.66±0.01	7.63±0.01	6.14± 0.08	-34.80	-12.50	10	08374070+1931063
14	8:37:42.36	19:08:01.57	10.05*	9.75*	8.58±0.02	8.58±0.02	2.57± 0.05	-36.60	-13.50	12	08374235+1908015
15	8:37:46.35	19:35:57.26	12.75	12.04	10.24±0.02	10.14±0.06	0.61± 0.03	-37.80	-9.40	295	08374640+1935575
16	8:37:46.64	19:26:18.10	10.85*	10.50	9.28±0.02	9.32±0.04	1.29± 0.04	-36.10	-13.40	13	08374660+1926181
17	8:37:46.77	19:16:02.03	6.75*	6.76*	6.17±0.01	6.12±0.01	24.79± 0.26	N/A	N/A	14	08374675+1916020
18	8:37:47.30	19:06:24.01	12.71	11.96*	10.20±0.02	10.07±0.07	0.65± 0.04	-35.60	-15.10	299	08374739+1906247
19	8:37:49.99	19:53:28.75	11.78*	11.13	9.33±0.02	9.10±0.04	1.59± 0.05	-31.80	-19.20	304	08374998+1953287
20	8:37:52.08	19:59:13.85	11.54	11.07	9.69±0.02	9.55±0.04	1.05± 0.04	-38.80	-14.60	310	08375208+1959138
21	8:37:57.06	19:14:09.67	12.23	11.59	10.04±0.02	10.11±0.09	0.63± 0.05	-35.40	-13.70	325	08375703+1914103
22	8:38:07.63	19:59:16.40	12.48	11.82	9.90±0.02	10.02±0.07	0.68± 0.05	-38.10	-13.50	346	08380758+1959163
23	8:38:08.08	20:26:20.83	12.08*	11.47*	9.93±0.02	10.03±0.17	0.68± 0.11	-36.40	-14.40	347	08380808+2026223
24	8:38:14.11	19:47:23.82	15.56	14.17	10.91±0.04	10.00±0.13	0.69± 0.08	N/A	N/A	358	08381421+1947234
25	8:38:14.28	19:21:55.37	11.20	10.31	9.19±0.02	9.12±0.03	1.56± 0.05	-35.00	-13.70	21	08381427+1921552
26	8:38:23.16	20:12:26.60	8.01*	7.71*	6.65±0.01	6.64±0.01	15.37± 0.13	N/A	N/A	-	08382311+2012263
27	8:38:24.31	20:06:21.92	10.80	10.40	9.18±0.02	9.23±0.03	1.41± 0.04	-36.30	-13.10	24	08382429+2006217
28	8:38:29.70	19:51:45.83	14.67*	13.53	10.93±0.02	10.56±0.14	0.41± 0.06	-40.10	-13.20	27	08382963+1951450
29	8:38:32.18	19:27:55.04	10.46*	9.65	7.54±0.01	7.46±0.01	7.18± 0.08	N/A	N/A	-	08383216+1927548
30	8:38:34.27	19:51:36.90	9.68	8.87	6.69±0.01	6.66±0.01	15.03± 0.18	N/A	N/A	-	08383425+1951369
31	8:38:37.43	19:01:14.81	14.45	13.27	10.61±0.01	10.16±0.18	0.60± 0.10	-37.70	-6.80	394	08383723+1901161
32	8:38:37.78	19:38:47.69	10.73*	10.43	9.22±0.02	9.24±0.05	1.40± 0.06	N/A	N/A	-	08383776+1938480
33	8:38:37.88	19:59:23.14	8.16*	8.16*	7.61±0.01	7.64±0.02	6.08± 0.08	-37.40	-13.60	35	08383786+1959231
34	8:38:46.97	19:30:03.53	9.08	8.95	8.22±0.02	8.08±0.02	4.06± 0.06	-34.80	-12.60	37	08384695+1930033
35	8:38:50.05	20:04:03.29	11.01	10.64	9.37±0.02	9.28±0.03	1.35± 0.03	-36.60	-15.40	423	08385001+2004035
36	8:38:53.57	19:34:17.90	14.82*	13.53*	10.96±0.02	10.92±0.17	0.30± 0.05	-40.90	-21.30	432	08385354+1934170

Table 3.1—Continued

#	α_{2000} [h:m:s]	δ_{2000} [°:′:″]	g^* [mag]	r^* [mag]	$K_{2\text{MASS}}$ [mag]	[24] [†] [mag]	F_{24}^{\dagger} [mJy]	μ_{α} [mas yr ⁻¹]	μ_{δ} [mas yr ⁻¹]	W# [‡]	2MASS
37	8:38:55.07	19:11:54.02	10.84	9.87	8.04±0.01	7.90±0.02	4.81±0.08	N/A	N/A	-	08385506+1911539
38	8:39:01.89	20:00:19.62	12.48*	11.45*	9.07±0.02	8.96±0.03	1.80±0.05	N/A	N/A	-	08390185+2000194
39	8:39:02.27	19:19:35.36	12.83	12.06	10.26±0.02	10.20±0.08	0.57±0.04	-36.60	-10.50	448	08390228+1919343
40	8:39:02.84	19:43:28.99	9.48	9.19*	8.12±0.01	8.08±0.02	4.06±0.06	-35.80	-11.20	46	08390283+1943289
41	8:39:03.24	20:02:35.12	15.18	13.86	11.05±0.02	10.88±0.13	0.31±0.04	-40.70	-14.30	47	08390321+2002376
42	8:39:03.60	19:59:59.24	8.33*	8.32*	7.77±0.01	7.71±0.02	5.69±0.09	-34.20	-13.30	48	08390359+1959591
43	8:39:04.09	19:31:23.20	14.40	13.28	10.86±0.01	10.46±0.13	0.45±0.05	-37.00	-14.60	450	08390411+1931216
44	8:39:05.25	20:07:01.92	9.51	9.31*	8.41±0.02	8.38±0.03	3.09±0.07	-35.70	-12.10	49	08390523+2007018
45	8:39:06.12	19:40:36.59	7.48*	7.43*	6.71±0.01	6.73±0.01	14.03±0.17	N/A	N/A	50	08390612+1940364
46	8:39:06.55	19:00:36.68	13.83	13.09	11.30±0.02	11.16±0.30	0.24±0.07	N/A	N/A	457	08390649+1900360
47	8:39:09.11	19:35:32.68	8.54*	8.49*	7.88±0.02	7.87±0.03	4.93±0.12	-35.30	-12.00	52	08390909+1935327
48	8:39:10.15	19:40:42.56	9.55*	9.32*	8.41±0.01	8.40±0.02	3.03±0.04	-36.10	-13.70	54	08391014+1940423
49	8:39:12.20	19:06:56.45	10.86	10.41	9.26±0.02	9.18±0.05	1.47±0.07	-37.00	-13.40	57	08391217+1906561
50	8:39:15.05	20:12:39.35	11.61	11.13	9.65±0.02	9.63±0.06	0.97±0.05	-35.20	-14.70	477	08391499+2012388
51	8:39:19.77	20:03:10.91	9.78	8.97	7.08±0.01	7.02±0.01	10.80±0.14	N/A	N/A	-	08391972+2003107
52	8:39:21.88	19:51:40.86	12.97*	12.20	10.37±0.02	10.07±0.10	0.65±0.06	-36.40	-8.80	65	08392185+1951402
53	8:39:24.99	19:27:33.70	10.75	10.01	9.00±0.01	8.89±0.03	1.92±0.04	-37.00	-14.90	66	08392498+1927336
54	8:39:28.63	19:28:25.00	12.07*	11.32*	9.53±0.02	9.40±0.05	1.21±0.06	-36.10	-10.80	506	08392858+1928251
55	8:39:29.42	19:47:11.51	13.09*	12.29	10.06±0.01	9.94±0.22	0.73±0.14	-38.90	-9.00	69	08392940+1947118
56	8:39:30.44	20:04:08.69	10.68*	10.11	8.81±0.01	8.74±0.02	2.22±0.03	-35.80	-13.40	70	08393042+2004087
57	8:39:33.44	20:10:10.52	9.79	8.67	6.13±0.01	6.00±0.02	27.56±0.38	N/A	N/A	-	08393342+2010102
58	8:39:36.35	19:15:39.67	15.10*	13.87	11.01±0.02	10.49±0.12	0.44±0.05	-33.30	-24.60	523	08393643+1915378
59	8:39:38.29	19:26:26.02	13.13	12.28	10.29±0.02	10.22±0.09	0.57±0.04	-33.00	-9.60	77	08393836+1926272
60	8:39:42.66	19:46:42.49	6.69*	6.65*	6.00±0.01	5.98±0.01	28.02±0.37	N/A	N/A	79	08394265+1946425
61	8:39:42.81	20:05:10.46	7.75*	7.73*	7.16±0.01	7.16±0.03	9.47±0.23	N/A	N/A	80	08394279+2005103
62	8:39:43.35	19:25:10.52	12.27	10.86	7.90±0.02	7.76±0.01	5.44±0.06	N/A	N/A	-	08394333+1925121
63	8:39:44.68	19:16:30.94	7.68*	7.69*	7.09±0.01	7.15±0.01	9.53±0.10	N/A	N/A	82	08394466+1916308
64	8:39:45.78	19:22:01.06	10.93	10.50	9.26±0.02	9.39±0.04	1.21±0.05	-35.40	-12.80	83	08394575+1922011
65	8:39:50.74	19:32:26.92	7.06*	6.26*	4.39±0.04	4.32±0.01	129.25±1.24	N/A	N/A	86	08395072+1932269
66	8:39:50.86	19:33:02.23	12.15*	11.56*	10.00±0.02	9.77±0.06	0.86±0.05	-36.10	-13.90	87	08395084+1933020
67	8:39:52.35	19:18:45.61	10.68	10.07	9.01±0.02	8.90±0.03	1.91±0.05	-34.80	-14.30	89	08395234+1918455
68	8:39:55.08	20:03:54.47	10.37	10.02	8.96±0.02	8.86±0.04	1.99±0.07	-37.50	-13.90	93	08395506+2003541
69	8:39:56.51	19:33:10.91	7.32*	7.33*	6.79±0.01	6.82±0.01	12.99±0.15	N/A	N/A	94	08395649+1933107
70	8:39:57.78	19:32:29.26	7.58*	7.53*	7.01±0.02	7.01±0.01	10.84±0.09	N/A	N/A	96	08395777+1932293
71	8:39:58.09	19:12:05.98	9.71	9.38	8.48±0.02	8.36±0.02	3.15±0.07	-37.40	-12.50	97	08395807+1912058
72	8:39:58.40	20:09:29.99	8.71	8.86	8.10±0.01	8.03±0.07	4.26±0.28	-36.00	-13.80	98	08395838+2009298

Table 3.1—Continued

#	α_{2000} [h:m:s]	δ_{2000} [°:′:″]	g^* [mag]	r^* [mag]	$K_{2\text{MASS}}$ [mag]	[24] [†] [mag]	F_{24} [†] [mJy]	μ_α [mas yr ⁻¹]	μ_δ [mas yr ⁻¹]	$W\#^\ddagger$	2MASS
73	8:39:59.10	20:01:53.15	9.35	9.15	8.21±0.02	8.22±0.01	3.56± 0.05	-36.40	-16.20	99	08395908+2001532
74	8:39:59.19	19:40:08.58	9.86	9.69	8.78±0.02	8.73±0.03	2.24± 0.06	N/A	N/A	-	08395915+1940083
75	8:39:59.58	18:56:35.30	10.08*	9.95	9.30±0.01	9.32±0.05	1.29± 0.06	N/A	N/A	-	08395957+1856357
76	8:39:59.84	19:34:00.55	12.41*	11.57*	9.48±0.02	9.31±0.04	1.31± 0.05	-33.80	-12.20	565	08395983+1934003
77	8:40:00.01	19:34:39.86	13.35*	12.51*	10.55±0.02	10.20±0.06	0.57± 0.03	-39.40	-4.20	100	08395998+1934405
78	8:40:00.64	19:48:23.44	10.49*	10.17*	9.08±0.02	8.97±0.03	1.80± 0.05	-36.30	-13.10	101	08400062+1948235
79	8:40:01.32	20:08:08.38	9.82*	9.57*	8.62±0.01	8.53±0.02	2.67± 0.05	-36.00	-14.50	102	08400130+2008082
80	8:40:01.72	18:59:59.17	10.47	9.93	8.70±0.02	8.48±0.03	2.81± 0.07	-36.50	-11.70	103	08400171+1859595
81	8:40:04.20	19:47:04.24	12.11	11.54	10.00±0.02	10.05±0.10	0.66± 0.06	-33.00	-13.70	576	08400416+1947039
82	8:40:04.92	19:43:45.48	9.95	9.67	8.65±0.02	8.54±0.03	2.65± 0.06	-36.10	-12.50	106	08400491+1943452
83	8:40:05.70	19:01:30.18	13.20	12.31	10.01±0.02	9.90±0.07	0.76± 0.05	-35.70	-12.20	578	08400571+1901307
84	8:40:06.28	19:27:14.80	10.55	10.10	8.87±0.02	8.80±0.03	2.10± 0.05	N/A	N/A	-	08400627+1927148
85	8:40:06.37	19:18:26.46	11.58*	10.76	9.23±0.02	9.23±0.03	1.40± 0.04	-34.30	-14.70	582	08400635+1918264
86	8:40:06.44	20:00:28.12	6.88*	6.06*	4.20±0.02	4.13±0.01	153.97± 1.35	N/A	N/A	111	08400643+2000280
87	8:40:09.74	19:37:17.83	12.54*	11.71	10.13±0.02	10.04±0.08	0.67± 0.05	-33.90	-10.50	114	08400968+1937170
88	8:40:11.46	19:58:16.21	6.78*	6.71	6.53±0.02	6.56±0.01	16.42± 0.17	N/A	N/A	115	08401145+1958161
89	8:40:12.32	19:38:22.78	10.07*	9.79*	8.67±0.02	8.56±0.03	2.62± 0.07	-36.90	-14.50	116	08401231+1938222
90	8:40:13.45	19:46:45.08	13.75*	12.79*	10.64±0.02	10.75±0.13	0.35± 0.04	-31.50	-14.40	117	08401345+1946436
91	8:40:15.36	19:59:39.66	8.88*	8.77*	8.04±9.99	8.03±0.02	4.27± 0.06	-35.80	-12.30	119	08401535+1959394
92	8:40:15.59	19:27:29.84	14.61	13.47	10.69±0.02	10.52±0.12	0.43± 0.05	-36.30	-8.50	601	08401549+1927310
93	8:40:15.72	19:54:54.07	13.15	12.29	10.01±0.02	9.92±0.06	0.75± 0.04	-38.00	-13.20	120	08401571+1954542
94	8:40:17.63	19:47:15.14	10.20	9.73*	8.58±0.02	8.60±0.03	2.52± 0.07	-35.50	-13.60	122	08401762+1947152
95	8:40:18.10	19:31:55.13	7.52*	7.57*	7.16±0.01	7.18±0.01	9.34± 0.08	N/A	N/A	123	08401810+1931552
96	8:40:18.97	20:11:31.16	13.59	12.38*	10.04±0.01	9.71±0.06	0.90± 0.05	-37.40	-14.00	607	08401893+2011307
97	8:40:20.16	19:20:56.44	6.83*	6.77*	6.04±0.01	6.01±0.01	27.23± 0.31	N/A	N/A	125	08402013+1920564
98	8:40:20.75	19:41:12.23	7.68*	7.69*	7.28±0.02	7.30±0.01	8.36± 0.11	N/A	N/A	127	08402075+1941120
99	8:40:22.09	19:40:11.82	6.95*	6.08*	4.18±0.03	4.07±0.01	162.87± 1.71	N/A	N/A	128	08402209+1940116
100	8:40:22.33	20:06:24.88	10.26	9.97	8.85±0.01	8.64±0.03	2.43± 0.06	-36.60	-12.20	129	08402231+2006243
101	8:40:22.73	19:27:53.46	10.94*	10.53*	9.34±0.02	9.25±0.04	1.39± 0.05	-37.80	-13.30	131	08402271+1927531
102	8:40:23.29	19:40:23.95	10.61*	10.20*	9.01±0.02	9.01±0.03	1.73± 0.04	-37.00	-11.80	132	08402327+1940236
103	8:40:23.48	19:50:06.04	8.09*	8.04	7.59±0.01	7.55±0.02	6.65± 0.10	N/A	N/A	133	08402347+1950059
104	8:40:25.55	19:28:32.92	9.75	9.37	8.76±0.02	8.71±0.03	2.28± 0.06	-36.80	-13.30	134	08402554+1928328
105	8:40:26.14	19:41:11.33	9.50*	9.27*	8.37±0.02	8.28±0.02	3.37± 0.05	-37.20	-11.90	135	08402614+1941111
106	8:40:26.30	19:13:11.06	13.40	12.50	10.46±0.02	10.56±0.13	0.42± 0.05	-38.40	-7.00	624	08402624+1913099
107	8:40:26.76	20:10:55.34	8.27*	8.17*	7.43±0.01	7.38±0.01	7.73± 0.09	N/A	N/A	136	08402675+2010552
108	8:40:27.03	19:32:41.42	6.27*	6.31*	5.88±0.01	5.92±0.01	29.83± 0.29	N/A	N/A	137	08402702+1932415

Table 3.1—Continued

#	α_{2000} [h:m:s]	δ_{2000} [°:′:″]	g^* [mag]	r^* [mag]	$K_{2\text{MASS}}$ [mag]	[24] [†] [mag]	F_{24} [†] [mJy]	μ_α [mas yr ⁻¹]	μ_δ [mas yr ⁻¹]	W# [‡]	2MASS
109	8:40:27.46	19:16:40.87	11.45	10.96*	9.65±0.02	9.58±0.04	1.02± 0.04	-33.30	-12.10	628	08402743+1916409
110	8:40:27.52	19:39:20.05	13.77*	12.83	10.69±0.02	10.84±0.12	0.32± 0.04	-33.40	-12.20	138	08402751+1939197
111	8:40:28.68	20:18:44.86	12.04*	11.35	9.46±0.02	9.42±0.07	1.18± 0.07	-37.40	-15.90	631	08402863+2018449
112	8:40:31.72	19:51:01.84	11.98*	11.38*	9.91±0.02	9.72±0.09	0.90± 0.07	-35.60	-12.90	640	08403169+1951010
113	8:40:31.85	20:12:5.98	11.85*	11.28	9.83±0.01	9.81±0.06	0.83± 0.04	-36.40	-13.90	641	08403184+2012060
114	8:40:32.97	19:11:39.59	8.72	8.55*	7.96±0.00	7.82±0.02	5.16± 0.10	-37.40	-14.20	141	08403296+1911395
115	8:40:33.48	19:38:00.42	12.63*	11.91*	10.17±0.02	10.05±0.08	0.66± 0.05	-38.90	-10.60	142	08403347+1938009
116	8:40:39.25	19:13:41.88	7.82*	7.80*	7.23±0.01	7.25±0.01	8.73± 0.10	N/A	N/A	150	08403924+1913418
117	8:40:39.94	19:40:09.37	11.44*	10.66	9.19±0.02	9.18±0.03	1.47± 0.05	-35.50	-11.30	151	08403992+1940092
118	8:40:41.91	19:13:25.68	10.86*	10.43*	9.06±0.02	9.04±0.03	1.68± 0.04	-35.90	-13.00	153	08404189+1913255
119	8:40:42.51	19:33:57.85	11.66*	11.11*	9.71±0.02	9.69±0.04	0.92± 0.04	-36.70	-13.80	154	08404248+1933576
120	8:40:43.22	19:43:09.62	7.07*	6.85	6.33±0.01	6.33±0.01	20.45± 0.14	N/A	N/A	156	08404321+1943095
121	8:40:46.09	19:18:34.67	9.79	9.45	8.53±0.02	8.49±0.02	2.79± 0.05	-37.10	-13.20	158	08404608+1918346
122	8:40:47.23	19:32:37.64	10.87	10.08	8.20±0.01	8.10±0.01	3.99± 0.05	N/A	N/A	-	08404720+1932373
123	8:40:48.01	19:39:31.57	11.56	10.79	9.25±0.02	9.25±0.03	1.39± 0.04	-37.60	-14.50	161	08404798+1939321
124	8:40:48.32	19:55:19.02	11.29	10.86	9.51±0.02	9.50±0.04	1.10± 0.04	-35.50	-13.00	162	08404832+1955189
125	8:40:52.52	20:15:59.87	8.52	8.47*	7.80±0.01	7.78±0.02	5.36± 0.08	-34.60	-12.70	166	08405247+2015594
126	8:40:52.53	19:28:59.77	10.55	10.15	9.05±0.02	8.97±0.03	1.79± 0.05	-37.00	-13.20	167	08405252+1928595
127	8:40:54.93	19:56:06.25	12.50*	11.80*	10.13±0.02	10.16±0.09	0.60± 0.05	-37.20	-14.90	677	08405487+1956067
128	8:40:56.29	19:34:49.26	6.76*	6.79*	6.28±0.01	6.28±0.01	21.23± 0.28	N/A	N/A	170	08405630+1934492
129	8:40:56.76	19:44:05.50	12.64*	11.94*	10.21±0.02	10.13±0.11	0.61± 0.06	-36.10	-11.10	171	08405669+1944052
130	8:40:56.95	19:56:05.57	8.79*	8.67*	8.05±0.02	7.95±0.01	4.57± 0.06	-36.10	-15.40	172	08405693+1956055
131	8:41:04.79	19:31:22.94	11.35	10.60	8.75±0.02	8.68±0.03	2.33± 0.06	N/A	N/A	-	08410478+1931225
132	8:41:07.34	19:26:48.08	13.01	12.12	10.29±0.02	10.30±0.20	0.53± 0.09	-43.70	-8.10	176	08410725+1926489
133	8:41:07.39	19:04:16.43	10.56	10.04	8.64±0.02	8.53±0.03	2.68± 0.06	-39.90	-14.10	177	08410737+1904164
134	8:41:09.61	19:51:18.32	11.01*	10.50*	8.94±0.02	8.61±0.03	2.48± 0.06	-36.70	-13.90	179	08410961+1951186
135	8:41:09.82	19:56:07.04	14.26*	13.19	10.76±0.02	10.67±0.10	0.37± 0.04	-42.40	-15.10	180	08410979+1956072
136	8:41:10.02	19:30:32.18	10.35*	9.98	8.91±0.02	8.83±0.13	2.04± 0.23	-36.90	-12.00	182	08411002+1930322
137	8:41:10.32	19:49:07.10	11.84*	11.29*	9.75±0.02	9.62±0.05	0.98± 0.04	-36.50	-13.20	183	08411031+1949071
138	8:41:10.70	19:49:46.38	9.06	8.86	8.19±0.01	8.19±0.02	3.66± 0.06	-37.80	-13.70	184	08411067+1949465
139	8:41:13.04	19:32:34.26	15.06	13.73	10.35±0.02	10.22±0.08	0.56± 0.05	-37.60	-9.70	709	08411319+1932349
140	8:41:13.80	19:55:19.24	8.35*	8.35*	7.77±0.01	7.69±0.02	5.82± 0.09	-36.90	-12.60	188	08411377+1955191
141	8:41:15.43	20:02:15.04	14.99*	13.78*	11.02±0.02	10.79±0.11	0.34± 0.03	-37.30	-11.90	189	08411541+2002160
142	8:41:16.04	19:44:54.13	14.06	13.44	11.71±0.02	10.50±0.09	0.44± 0.03	N/A	N/A	190	08411602+1944514
143	8:41:18.42	19:15:39.38	7.95*	7.90*	7.29±0.02	7.04±0.01	10.61± 0.12	-37.40	-12.90	192	08411840+1915394
144	8:41:19.96	19:38:04.20	14.20	13.09	10.76±0.02	10.22±0.17	0.56± 0.09	-36.30	-12.00	721	08411992+1938047

Table 3.1—Continued

#	α_{2000} [h:m:s]	δ_{2000} [°:′:″]	g^* [mag]	r^* [mag]	$K_{2\text{MASS}}$ [mag]	[24] [†] [mag]	F_{24} [†] [mJy]	μ_α [mas yr ⁻¹]	μ_δ [mas yr ⁻¹]	W# [‡]	2MASS
145	8:41:22.48	18:56:00.17	13.49	12.60	10.54±0.02	10.20±0.15	0.58± 0.08	-34.00	-9.90	726	08412258+1856020
146	8:41:23.93	20:14:57.30	15.46*	14.11*	10.78±0.02	10.11±0.13	0.63± 0.08	N/A	N/A	194	08412390+2014572
147	8:41:25.89	19:56:36.85	10.92*	10.55	9.33±0.02	9.37±0.04	1.24± 0.05	-36.30	-13.70	195	08412584+1956369
148	8:41:26.98	19:32:32.71	10.05	9.73*	8.72±0.02	8.79±0.03	2.12± 0.06	-37.30	-12.40	196	08412698+1932329
149	8:41:28.65	19:44:49.13	11.43	10.76	9.47±0.02	9.44±0.13	1.16± 0.14	-39.00	-13.50	198	08412869+1944481
150	8:41:33.89	19:58:08.83	12.07	11.47*	9.93±0.01	9.94±0.07	0.73± 0.05	-39.40	-14.40	201	08413384+1958087
151	8:41:35.09	19:39:45.04	9.17*	8.12	5.96±0.02	5.86±0.01	31.26± 0.30	N/A	N/A	-	08413506+1939449
152	8:41:35.90	19:06:25.16	14.84	13.59	10.98±0.02	10.55±0.11	0.42± 0.04	-31.10	-9.60	751	08413599+1906255
153	8:41:36.20	19:08:33.58	9.57	9.23	8.35±0.02	8.34±0.02	3.21± 0.05	-36.00	-14.30	204	08413620+1908335
154	8:41:37.43	19:31:13.08	14.19	13.09	10.73±0.01	10.50±0.14	0.44± 0.06	-40.90	-12.00	758	08413741+1931140
155	8:41:42.31	19:39:37.98	9.72*	9.50*	8.48±0.02	8.38±0.03	3.09± 0.08	-37.30	-13.80	206	08414229+1939379
156	8:41:43.68	19:57:43.85	12.73	12.05	10.26±0.02	10.15±0.10	0.60± 0.10	-40.50	-13.10	769	08414368+1957437
157	8:41:43.85	20:13:37.06	10.69	10.34	9.14±0.01	8.99±0.04	1.76± 0.07	-37.40	-15.70	771	08414382+2013368
158	8:41:45.49	19:16:02.17	10.35	9.98*	8.93±0.02	8.92±0.03	1.88± 0.05	-38.10	-13.20	208	08414549+1916023
159	8:41:47.74	19:24:43.88	11.66*	11.28	10.10±0.02	9.96±0.07	0.72± 0.05	-30.30	-9.50	-	08414776+1924439
160	8:41:48.24	19:27:30.49	14.28*	13.24	10.73±0.01	10.62±0.10	0.39± 0.04	-40.80	-9.80	774	08414818+1927312
161	8:41:49.34	19:11:47.51	15.24	13.90	10.83±0.01	10.55±0.11	0.42± 0.04	-33.90	-10.80	776	08414934+1911471
162	8:41:50.09	19:52:27.19	7.37*	6.56*	4.68±0.00	4.63±0.01	97.51± 1.02	N/A	N/A	212	08415008+1952270
163	8:41:51.98	20:10:01.99	12.44*	11.76*	10.09±0.02	9.78±0.08	0.85± 0.07	-40.60	-15.70	213	08415199+2010013
164	8:41:53.16	20:09:34.16	8.61*	8.51*	7.79±0.01	7.71±0.01	5.71± 0.07	-38.20	-13.70	214	08415314+2009340
165	8:41:54.37	19:15:27.14	11.65	11.03	9.64±0.02	9.56±0.05	1.04± 0.05	-34.80	-13.20	215	08415437+1915266
166	8:41:55.90	19:41:22.96	11.39	10.86	9.54±0.01	9.59±0.07	1.02± 0.07	-37.60	-12.10	217	08415587+1941229
167	8:41:57.84	18:54:42.08	9.66*	9.35	8.43±0.02	8.43±0.03	2.94± 0.07	-34.30	-11.10	218	08415782+1854422
168	8:41:58.86	20:06:26.82	13.77*	12.83	10.60±0.01	10.32±0.16	0.52± 0.08	-40.30	-11.80	792	08415884+2006272
169	8:42:05.50	19:35:57.95	11.07	10.33*	8.38±0.03	8.30±0.02	3.32± 0.05	N/A	N/A	-	08420547+1935585
170	8:42:06.51	19:24:40.72	7.96*	7.97*	7.43±0.02	7.39±0.01	7.64± 0.06	-38.40	-12.10	223	08420650+1924405
171	8:42:10.79	18:56:03.62	7.92*	7.93*	7.35±0.01	7.35±0.02	7.95± 0.11	-34.10	-12.10	224	08421080+1856037
172	8:42:11.50	19:16:36.37	12.57*	11.85*	10.17±0.01	9.99±0.06	0.70± 0.04	-37.60	-10.00	817	08421149+1916373
173	8:42:12.34	19:12:48.20	14.32	13.20	10.83±0.01	10.56±0.10	0.41± 0.04	-33.50	-9.60	822	08421233+1912488
174	8:42:12.85	19:16:03.79	14.10*	13.07	10.48±0.01	10.11±0.06	0.63± 0.04	-33.00	-11.70	824	08421285+1916040
175	8:42:15.50	19:41:15.47	10.12	9.78	8.77±0.01	8.72±0.02	2.24± 0.05	-37.60	-15.00	226	08421549+1941156
176	8:42:18.85	20:24:36.22	12.59	11.91	10.19±0.02	10.05±0.12	0.66± 0.08	N/A	N/A	839	08421883+2024350
177	8:42:20.16	20:02:11.72	9.91	9.56	8.41±0.02	8.40±0.02	3.03± 0.06	-35.70	-15.60	228	08422012+2002117
178	8:42:21.62	20:10:53.72	9.32	9.13	8.28±0.01	8.13±0.02	3.89± 0.06	-36.80	-14.40	229	08422162+2010539
179	8:42:24.74	19:35:17.27	11.21	10.83*	9.48±0.01	9.34±0.04	1.27± 0.05	N/A	N/A	-	08422471+1935175
180	8:42:32.27	19:23:46.25	11.38	10.84	9.46±0.01	9.50±0.06	1.10± 0.06	-36.50	-12.50	232	08423225+1923463

3.4 Results

In this section I present the results on the debris disk fraction I observed in Praesepe and place it in context with previous results on the evolution of debris disks. There are two basic methods to detect $24\ \mu\text{m}$ excess. The first is to use a color-color diagram, with one of the colors determining the stars' spectral type and the other being K_S -[24]. The r - K_S color is ideal to differentiate spectral types, while the K_S -[24] color depends only weakly on the spectral type of the star since both wavelengths fall on the Rayleigh-Jeans part of the spectral energy distribution (SED) for all sources hotter than early M type ($T_{\text{eff}} > 3200\ \text{K}$) (Gautier et al., 2007). For non-excess stars the K_S -[24] color should stay close to zero. Any excess measured in K_S -[24] is most likely caused by circumstellar material.

The second method is to fit the observed optical and near-infrared photometry with theoretical SEDs based on stellar photosphere models. Excesses are revealed if the $24\ \mu\text{m}$ flux density is significantly greater than the predicted flux.

3.4.1 Color-color selection

I used the color-color diagram shown in Figure 3.6 as the primary method to identify sources as excess candidates. I plot all cluster members that have magnitude values in r , K_S , and [24], 193 sources altogether.

Gautier et al. (2007) show the trend of K_S -[24] photospheric color with spectral type for stars of low effective temperature. The empirical locus of stars on the color-color plot in Figure 3.6 was derived by fitting a curve to a sample of field stars (from Gautier et al. (2007) and Trilling et al. (2008)). I then converted the fitted V - K_S colors to r - K_S colors through conversion tables in Cox (2000) and Kraus & Hillenbrand (2007). The final color-color curve for r - K_S vs. K_S -[24] for

Table 3.1—Continued

#	α_{2000} [h:m:s]	δ_{2000} [°:′:″]	g^* [mag]	r^* [mag]	K_{2MASS} [mag]	[24] [†] [mag]	F_{24}^{\dagger} [mJy]	μ_{α} [mas yr ⁻¹]	μ_{δ} [mas yr ⁻¹]	W^{\ddagger}	2MASS
181	8:42:40.19	19:07:58.87	12.55*	11.86*	10.19±0.01	9.83±0.06	0.81± 0.04	-35.30	-10.90	863	08424021+1907590
182	8:42:40.73	19:32:35.34	10.03	9.66	8.72±0.02	8.67±0.03	2.36± 0.07	-38.40	-12.70	235	08424071+1932354
183	8:42:42.51	19:05:59.78	12.04*	11.38	9.88±0.02	9.88±0.06	0.78± 0.04	-37.40	-13.50	236	08424250+1905589
184	8:42:43.72	19:37:23.52	12.76	11.76	9.80±0.02	9.64±0.05	0.97± 0.04	-36.40	-14.20	868	08424372+1937234
185	8:42:44.44	19:34:48.11	10.09	9.53	8.63±0.02	8.48±0.02	2.82± 0.05	-38.20	-13.50	238	08424441+1934479
186	8:43:00.59	20:20:15.79	11.76	11.24	9.77±0.02	9.57±0.06	1.03± 0.06	-37.30	-16.00	887	08430055+2020161
187	8:43:05.96	19:26:15.36	10.25	9.65	8.46±0.02	8.40±0.01	3.02± 0.04	-36.60	-13.80	248	08430593+1926152
188	8:43:08.24	19:42:47.59	13.92	12.89	10.67±0.01	10.15±0.09	0.60± 0.05	-33.70	-11.60	899	08430822+1942475
189	8:43:10.82	19:31:33.64	12.20	11.58	10.01±0.02	10.49±0.22	0.44± 0.09	-38.50	-17.50	902	08431076+1931346
190	8:43:20.20	19:46:08.58	11.05	10.62	9.36±0.02	9.26±0.04	1.37± 0.05	-39.40	-13.40	255	08432019+1946086
191	8:43:32.42	19:44:38.00	12.92	12.01	10.22±0.02	9.94±0.08	0.73± 0.05	-40.10	-16.50	919	08433239+1944378
192	8:43:35.56	20:11:22.63	10.29	9.99	8.92±0.02	8.95±0.03	1.82± 0.05	-39.30	-14.70	257	08433553+2011225
193	8:44:07.37	20:04:36.23	10.30	10.05	9.06±0.01	8.95±0.03	1.82± 0.04	N/A	N/A	-	08440734+2004369

*The r and/or g magnitudes marked with a star were calculated from B and V magnitudes as described in §3.3, while the rest are the original SDSS values.

[†]The [24] magnitudes are the ones that were calibrated to the 2MASS K_S magnitudes, while the mJy values in the F_{24} column are the original flux values.

[‡]The numbers in this column represent the numbering of Wang et al. (1995).

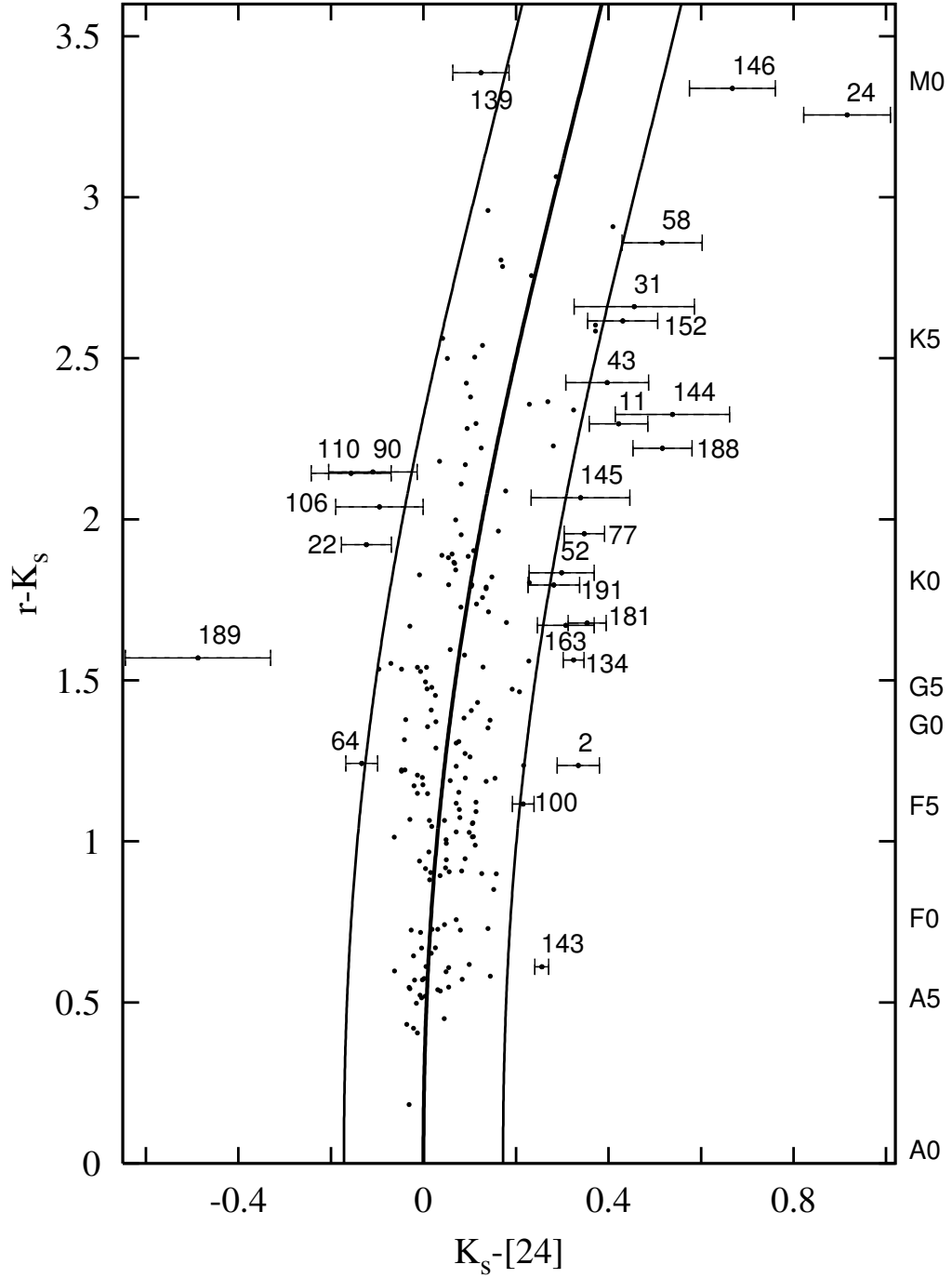


Figure 3.6 The color-color plot for the cluster members with photometric measurements in r , K_s , and $[24]$. The 1σ measurement error in $[24]$ is plotted for stars that are outside of the trend curve. The nomenclature is from Table 3.1.

main-sequence (MS) stars is:

$$K_S - [24] = 3.01 \times 10^{-5}(r - K_S) + 0.0233(r - K_S)^2 + 0.0072(r - K_S)^3 - 0.0015(r - K_S)^4. \quad (3.3)$$

In Figure 3.6, I plot this curve and the 3σ average confidence level for the photometry in [24] (~ 0.15 mag) (the errors of the curve itself are minor compared to the photometric errors). The majority of the stars ($> 86\%$) lie within this band. The errors plotted for the stars outside of the MS fitted curve are the 1σ errors in the [24] photometry. To use the K_S -[24] color as an excess diagnostic tool, one must make sure that the K_S magnitude is truly photospheric. I examined the J, H, and K_S fits to theoretical SEDs (Castelli & Kurucz, 2003) and concluded that all K_S magnitudes are truly photospheric; the largest difference (from the debris disk candidate sample introduced later) is in the case of star 143, where the measured value is above the predicted SED value by 5.6%.

As Figure 3.6 shows, I have 7 stars in the "blue" region of the color-color plot, which I used to establish a selection rule to clean the excess region of the plot of possible spurious detections. I only accepted stars as true excess stars that: 1) lie at least $3\sigma_{24}$ (their own σ and not the average [24] error) from the trend line; 2) have [24] data at least $3\sigma_{24}$ from the best fitting SED solution also; and 3) are point sources on the images and have no noise anomalies. All stars in the "blue" region failed these criteria. From the 19 stars that lie in the excess ("red") region of the color-color diagram, fifteen were eliminated as debris disk candidates for the following reasons. Only 8 were $3\sigma_{24}$ from the trend line: 181, 143, 100, 77, 134, 188, 24, and 2 (in the nomenclature of Table 3.1 and Figure 3.6). Star 188 turned out to be contaminated by a minor planet, which was identified by comparing scanlegs separately. Stars 24 and 2 are resolved doubles on the higher resolution 2MASS and SDSS images, so I excluded them from the list.

Star 100 is contaminated by a faint background galaxy, which was visible as a faint nebulosity next to the star. The probability for other sources of a $24\ \mu\text{m}$ excess arising through a chance alignment with distant galaxies can be determined from galaxy counts (Papovich et al., 2004). The ~ 0.15 mag [24] excess criterion results in different flux values identified as excesses as a function of source brightness. I estimated the probability of chance alignments by dividing the sample into 1 magnitude bins and running a Monte Carlo code with the number of sources in the bin and the number of extragalactic sources corresponding to 0.15 magnitude excess value for the specific bin. The matching radius for the chance alignment was chosen to be $r = 3.6''$ and the code was ran to 10000 simulations per magnitude bin. I summarize the simulation numbers with the probabilities of at least n number of chance alignments in each bin in Table 3.2. The probability that star 143 with [24] = 7.04 mag is a chance alignment with a background galaxy is very low ($< 3\%$), so it is very likely to be a true debris disk star. The probability that at least two sources (star 100 and 134) are contaminated by a background galaxy in the 8-9 magnitude bin is also very low ($< 4\%$), and since star 100 is already contaminated, I classify star 134 as a real debris disk star also. The likelihood that stars 77 and 181 are contaminated within $3.6''$ is high ($\sim 90\%$). However, there is no indication of any positional offset between K_S and [24], even at the $1''$ level, so this likelihood is probably overestimated.

I determine stars 143 and 134 to be definite debris disk stars in Praesepe and list stars 77 and 181 as possible debris disk stars. I show these sources in Figure 3.7 and detail their properties in §3.4.4. Figure 3.7 shows that the fields are clean and that the sources are point-like. The PSFs were centered on the $24\ \mu\text{m}$ sources with *IRAF*'s centroid algorithm. As Table 3.1 shows, the coordinate center of the excesses is closer than $1''$ to the 2MASS coordinates for the debris disk candidates.

Table 3.2. The probabilities of chance alignments for the sources with background galaxies as a function of [24] brightness.

[24] bin [mag]	N _* [#]	Flux [mJy]	Excess [mJy]	N _{galaxies} [sr ⁻¹]	<i>P</i> of at least <i>n</i> chance alignments				
					[0]*	[1] [†]	[2] [†]	[3] [†]	[4] [†]
4-5	4	125.900	16.245	2×10 ⁴	99.99%	0.01%	~0%	~0%	~0%
5-6	2	50.122	6.467	7×10 ⁴	99.98%	0.02%	~0%	-	-
6-7	11	19.954	2.575	4×10 ⁵	99.54%	0.46%	~0%	~0%	~0%
7-8	26	7.944	1.025	1×10 ⁶	97.46%	2.54%	0.04%	~0%	~0%
8-9	48	3.162	0.408	7×10 ⁶	72.35%	27.65%	3.80%	0.01%	~0%
9-10	53	1.259	0.162	4×10 ⁷	12.60%	87.40%	60.26%	31.93%	13.14%
10-11	48	0.501	0.065	8×10 ⁷	2.47%	97.53%	87.34%	69.30%	47.06%
11-12	1	0.199	0.026	1×10 ⁸	91.20%	8.80%	-	-	-

*The probability that none of the cluster member sources are chance aligned with a background galaxy in the appropriate magnitude range.

[†]The probability that at least 1, 2, 3 or 4 cluster member sources are chance aligned with a background galaxy in the appropriate magnitude range.

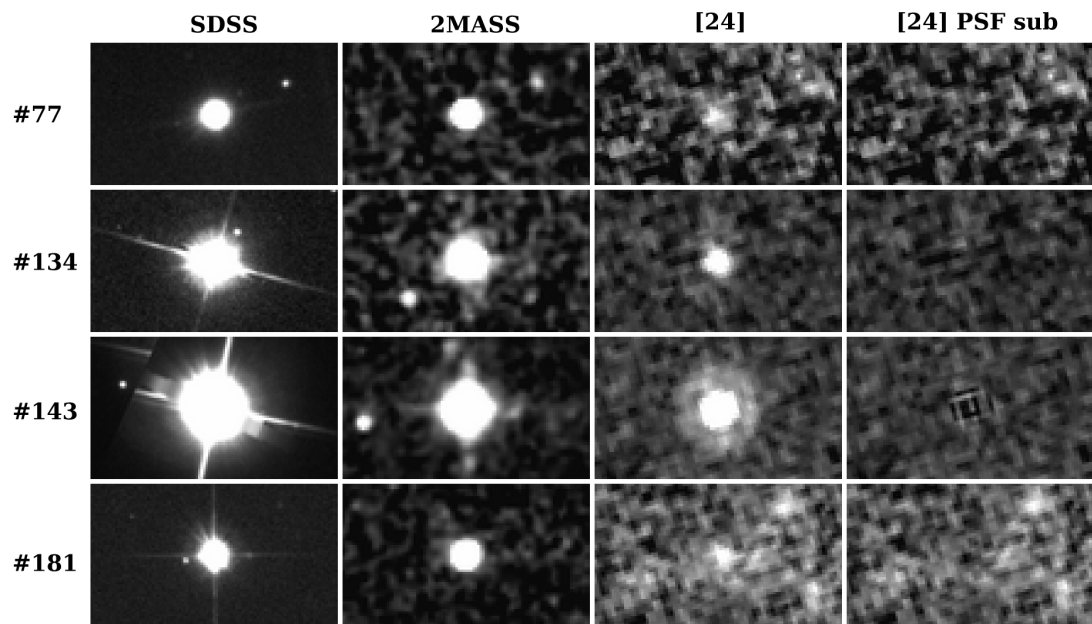


Figure 3.7 SDSS, 2MASS, 24 micron, and 24 micron PSF subtracted images for stars 77, 134, 143, and 181. The fields of view (FOV) for the images are $69.9'' \times 37.97''$ and they have linear flux scaling.

3.4.2 The SED fit selection

The 2MASS data are only useful in selecting debris disk candidates if the K_S magnitude is photospheric. Since the threshold of the K_S -[24] color above which a star is selected to be a debris disk candidate depends on the spectral type (the determination of which depends on correct r band photometry), I also fit the photometric data for all stars within the trend curves with model spectra to look for excess candidates. To be considered a debris disk candidate in this region required even stronger selection criteria than in the case of the "excess region stars." Stars were selected to be candidates from this region if their [24] photometry was at least $3\sigma_{24}$ from the fitted SED and if the star was $3\sigma_{24} + 10\%$ (0.1 mag) from the trend line in the color-color plot. The 10% is an allowance for systematic errors. None of the stars within the trend curves passed these criteria.

3.4.3 Praesepe white dwarfs

I also checked whether any of the known eleven Praesepe white dwarfs (Dobbie et al., 2006) were detected, indicating a possible white dwarf debris disk. WD 0837+199 showed a strong signal in [24]. The UKIRT Infrared Deep Sky Survey (UKIDSS) survey team (Sarah Casewell, private communication 2008) have found that this signal originates from a background galaxy a few arcseconds north of the WD.

3.4.4 Debris Disk Candidates

I discuss the four debris disk candidate stars in this section. None of these stars show extended emission (resolved disk), implying that the excess is confined to the radius of the MIPS beam of $6''$ (Rieke et al., 2004), which is ~ 1000 AU at the distance of Praesepe. This is consistent with the sizes of already resolved mid-IR debris disks (Stapelfeldt et al., 2004; Su et al., 2005, 2008; Backman et al., 2009).

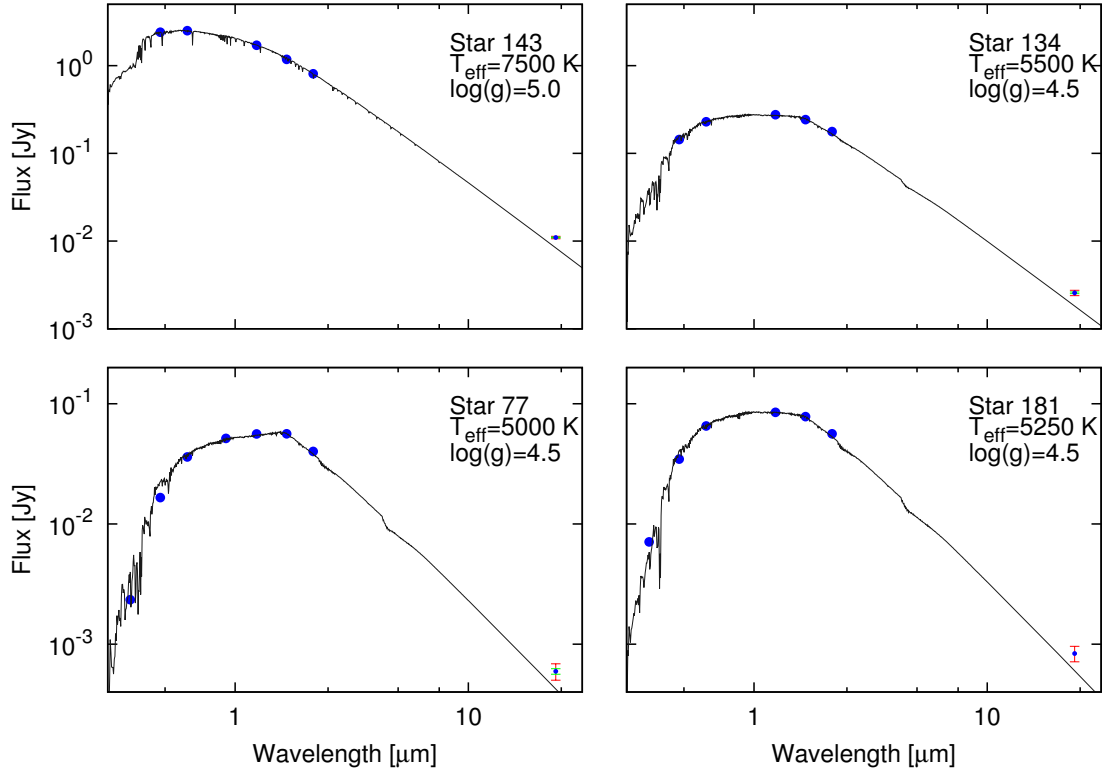


Figure 3.8 The best fitting SEDs of the debris disk candidate stars with available optical, 2MASS, and [24] photometry. The [24] photometry is plotted with 1 and 3σ errors.

The best fitting SEDs of the debris disk candidate stars are plotted in Figure 3.8.

3.4.4.1 Star #77

This star was identified on three separate scanlegs, with no contamination by minor planets. It is rather faint with $m_V = 12.88$ mag. Its optical and NIR photometry was best fitted by the $T_{\text{eff}} = 5000$ K and $\log g = 4.5$ (K3 V) Kurucz model (Castelli & Kurucz, 2003). Franciosini et al. (2003) used XMM-Newton to detect X-ray emission from it with a flux of $L_X = 1.67 \times 10^{28} \text{ erg s}^{-1}$ in the *ROSAT* 0.1-2.4 keV band. They point out that the flux measured by *ROSAT* (Randich & Schmitt, 1995) is a magnitude higher than theirs. The star is a cluster member cataloged in

many papers (Wang et al., 1995; Klein Wassink, 1927; Jones & Cudworth, 1983).

3.4.4.2 Star #134

Star #134 (WJJP 179, KW 367) is a bright cluster member, with $m_V = 10.71$ mag. It was imaged on two scanlegs with high S/N. Its optical and NIR photometry was best fitted by the $T_{\text{eff}} = 5500$ K and $\log g = 4.5$ (G8 V) Kurucz model (Castelli & Kurucz, 2003) and I detect no extent to the stellar PSF core (Figure 3.7). North of it by $6''$, a fainter extended source is visible on both scanlegs. It has been found to be a triple system by Mermilliod et al. (1994) and the mass of the components was estimated by Halbwachs et al. (2003) using CORAVEL radial velocity measurements. The system consists of a wide pair, one of which is a spectroscopic binary with a period of 3.057 days. It is also a definite cluster member (Wang et al., 1995; Klein Wassink, 1927; Jones & Cudworth, 1983).

3.4.4.3 Star #143

This is the brightest of all debris disk stars I observed, with $m_V = 8.04$ mag. Its optical and NIR photometry was best fitted with a $T_{\text{eff}} = 7500$ K, $\log g = 5.0$ (A7 V) Kurucz model (Castelli & Kurucz, 2003). The PSF subtraction was very clean, with no hint of any extended emission (Figure 3.7). The star was discovered to be a δ Scuti type of pulsating variable by Paparo & Kollath (1990) (HI Cnc, HD 73890, BD+19 2078). It has been cataloged as a definite cluster member in many papers (Wang et al., 1995; Klein Wassink, 1927; Jones & Cudworth, 1983). With high-resolution imaging surveys, Mason et al. (1993) found it to be a single star.

3.4.4.4 Star #181

The star was identified on three separate scanlegs. The best fit to its photometry points was with a $T_{\text{eff}} = 5250$ K, $\log g = 4.5$ (K0 V) Kurucz model (Castelli & Kurucz, 2003). It has been identified as a cluster member in many catalogs (Wang

et al., 1995; Hambly et al., 1995; Klein Wassink, 1927; Jones & Stauffer, 1991). It was not identified as a close binary star in the surveys of Bouvier et al. (2001) and Mermilliod & Mayor (1999). No extended emission is seen in the PSF subtracted image (Figure 3.7).

3.5 Discussion

I have found 4 sources out of 193 in the spectral range from A0 to K3 showing excess at $24\ \mu\text{m}$. One of the sources (star 143) is an A7 type star (out of 29 early-type stars), while the remaining three are G8, K0, and K3 (out of 164 solar-type stars), based on their photometric colors and fitted SEDs. Although the probability of chance alignments with faint background galaxies within $3.6''$ are rather high for the K0 and K3 spectral-type sources, since the peaks of their emission are well within $1''$ of the 2MASS coordinates they are likely excess sources. However, the statistics are incomplete to their spectral limit. In the field of view there are 106 stars within F0 and G8 spectral-type, of which I detected 98, meaning I have an almost complete sample of sources within this spectral band. I use the excess fraction of $1/106$ for the solar-type star sample.

The excesses found around early type stars (B8-A9) are usually dealt with separately in the literature from the ones found around solar-type stars (F0-K4), because the dominant grain removal processes in the debris disks may not be the same and the $24\ \mu\text{m}$ excesses probe significantly different distances from the stars. These populations are also separated observationally, by the natural detection limits.

In the following sections I analyze the results in the context of previous debris disk fractions observed around early- and solar-type stars. The errors on the debris disk fractions are given by Bayesian statistics detailed in the following

§3.5.1. I contrast the results for early- and solar-type stars in §3.5.2 and §3.5.3 and discuss the implications for debris disk decay time scales in §3.5.4. In §3.5.5, I compare these results with a simple model for the incidence of episodes like the LHB around other stars.

3.5.1 Calculating errors on debris disk fractions

Due to the small number of observations, I estimated the debris disk fractions and associated uncertainties using a Bayesian approach, which I outline in this section.

If the fraction of objects with disks is f_{disk} , derived from the observed number of disks (n) from a sample size of N , then the posterior probability that f_{disk} has a certain value will be

$$P(f_{\text{disk}}|n, N) \propto P(f_{\text{disk}})P(n|f_{\text{disk}}, N). \quad (3.4)$$

Here, $P(f_{\text{disk}}|n, N)$ is the probability distribution for f_{disk} , given that n and N are known. $P(f_{\text{disk}})$ is the prior distribution of f_{disk} and $P(n|f_{\text{disk}}, N)$ is the probability of observing that n of N sources have a disk, assuming a certain value of f_{disk} . $P(f_{\text{disk}}|n, N)$ will be the posterior probability distribution for f_{disk} and $P(n|f_{\text{disk}}, N)$ is the likelihood function. If no prior assumption is made on the value of f_{disk} , then the prior will be uniform, i.e. $P(f_{\text{disk}}) = 1$. This will be assumed, so that all information on f_{disk} originates from the data itself. The likelihood function, $P(n|f_{\text{disk}}, N)$, is a binomial distribution, therefore

$$P(f_{\text{disk}}|n, N) \propto f_{\text{disk}}^n (1 - f_{\text{disk}})^{N-n}, \quad (3.5)$$

where the binomial coefficient has been dropped because of its non-dependence on f_{disk} , making it irrelevant in the posterior distribution.

This equation is equivalent to a Beta (B) distribution with parameters $\alpha = n+1$ and $\beta = N - n + 1$. The expectation value (posterior mean) of the B distribution

is simply

$$E(f_{\text{disk}}) = \frac{\alpha}{\alpha + \beta} = \frac{n + 1}{N + 2}, \quad (3.6)$$

while its mode gives the regular ratio of n/N (if $n > 1$ and $N > 2$). The 1σ confidence region can be found by integrating the central region that contains 68.3% of the probability for the B distribution. This was done here by Monte Carlo-type calculations. I simulated 10^7 random variables from a B distribution and searched for the bottom and upper limits at the 15.85% and 84.15% percentiles.

I give the results with the expectation values and the upper and lower errors from the 1σ limits. I decided to use expectation values (posterior mean) over mode averages based on that the fractions are usually low making the distributions skewed. In such cases, they are better described by their mean. For example, this will give an expected debris disk fraction of

$$E(f_{\text{disk}}) = \frac{1 + 1}{106 + 2} = 1.85\% \quad (3.7)$$

for the solar-type stars.

3.5.2 The decay of the debris disk fraction in early-type stars

A-type stars are well suited to search for excess emission originating from debris disks. The extended surveys of Rieke et al. (2005) and Su et al. (2006), probed the excess fraction for A-type stars in the field and in associations between the ages of 5 and 850 Myr. Numerous observations have also determined the excess fraction for early-type stars in open clusters and associations (e.g. Young et al., 2004; Gorlova et al., 2004, 2006; Siegler et al., 2007; Cieza et al., 2008).

I compared the early spectral type excess fraction to the ones in the literature. I combined the data of Rieke et al. (2005) and Su et al. (2006), removing cluster and association members. Sources that were listed in both catalogs were adopted from Su et al. (2006), due to the improved reduction methods and photospheric

Table 3.3. The field star sample excess ratios at $24\ \mu\text{m}$ at certain age bins for early type stars (Rieke et al., 2005; Su et al., 2006).

Age [Myr]	Excess fraction	
	[#]	[%]
3.16 - 10.....	6/10	58.3 ± 14.2
10 - 31.6.....	3/4	$66.7^{+18.7}_{-19.1}$
31.6 - 100.....	4/10	41.7 ± 14.2
100 - 316.....	13/39	34.2 ± 7.4
316 - 1000.....	3/31	12.1 ± 5.5

model fits in the latter paper. Sources were counted as excess sources if their relative excess exceeded 15%. IRAS and ISO sources from the Rieke et al. (2005) sample were removed, due to their higher – 25% – excess thresholds. The final age bins from the combined catalogs are listed in Table 3.3.

I also compared the results to those from open cluster (and OB association) surveys by other groups. I list these clusters, their excess fraction, age and the references for these parameters in Table 3.4. The majority of these clusters are from MIPS group papers, that used the same 15% excess level threshold as I did in my study of Praesepe. The few others used similar thresholds, or as in the case of the β Pic MG study (Rebull et al., 2008), all excess sources that were identified exceeded their 20% threshold with no sources between 15 and 20%. I plot the excess fractions from all surveys with the field star samples in the *top left* panel of Figure 3.9.

The fifteen open clusters and associations follow the same trend as the field star sample, with the exception of IC 2602 (Su et al., 2006) and IC 2391 (Siegler et al., 2007). Possible explanations for this deviation are explored in Siegler et al. (2007) and they conclude that the most likely cause is the lack of a statistically

Table 3.4. The excess fraction at 24 μm for early type stars in clusters/associations.

Name	Age [Myr]	Excess fraction [#]	Excess fraction [%]	Excess Reference	Age
Upper Sco	5 \pm 1	0/3	36.9*	1,2	11
Orion OB1b	5 \pm 1	6/22	29.2 \pm 9.2	3	12
Orion OB1a	8.5 \pm 1.5	8/21	39.1 \pm 10.2	3	12
β Pic MG	12 $^{+8}_{-4}$	3/5	57.1 $^{+18.6}_{-18.7}$	4	13
Upper Cen	25 \pm 5	7/17	42.1 \pm 11.3	1,2	14
NGC 2547	30 \pm 5	8/18	45.0 \pm 11.1	5,6	5,6
IC 2602	30 \pm 5	1/8	20.0 $^{+12.3}_{-12.0}$	1	15
IC 2391	50 \pm 5	1/10	16.7 $^{+10.4}_{-10.1}$	7	16
α Per	65 \pm 15	2/5	42.9 $^{+18.7}_{-18.6}$	1,2	17,18
Pleiades	115 \pm 10	2/7	33.3 $^{+15.6}_{-15.5}$	1	18,19,20
Pleiades	115 \pm 10	5/20	27.3 $^{+9.5}_{-9.4}$	6	18,19,20
NGC 2516	145 \pm 5	13/51	26.4 \pm 6.0	2	19,21
Ursa M	400 \pm 100	1/7	22.2 $^{+13.5}_{-13.2}$	1	22,23,24
Coma Berenices	500 \pm 50	0/5	26.4*	1,2	25
Hyades	625 \pm 50	1/12	14.3 $^{+9.0}_{-8.8}$	1	26
Hyades	625 \pm 50	2/11	23.1 $^{+11.5}_{-11.4}$	9	26
Praesepe	757 \pm 114	1/29	6.5 \pm 4.1	10	10
Praesepe	757 \pm 114	0/5	26.4*	1	10

*Upper limit

References. — (1) Su et al. (2006); (2) Rieke et al. (2005); (3) Hernández et al. (2006); (4) Rebull et al. (2008); (5) Young et al. (2004); (6) Gorlova et al. (2007); (7) Siegler et al. (2007); (8) Gorlova et al. (2006); (9) Cieza et al. (2008); (10) This work; (11) Preibisch et al. (2002); (12) Briceño et al. (2005); (13) Ortega et al. (2002); (14) Fuchs et al. (2006); (15) Stauffer et al. (1997); (16) Barrado y Navascués et al. (2004); (17) Song et al. (2001); (18) Martín et al. (2001); (19) Meynet et al. (1993); (20) Stauffer et al. (1998); (21) Jeffries et al. (2001); (22) Soderblom & Mayor (1993); (23) Castellani et al. (2002); (24) King et al. (2003); (25) Odenkirchen et al. (1998); (26) Perryman et al. (1998)

large sample. The peak near ~ 12 Myr observed by Currie et al. (2008) is suggested. Thereafter, the excess fraction shows a steady decline to the age of Praesepe (~ 750 Myr). Although the single A7 debris disk star I observed is not a statistically high number, the sample of 29 stars it was drawn from is high enough to indicate a real lack of debris disks around early-type stars at ~ 750 Myr.

3.5.3 The decay of the debris disk fraction for solar-type stars

Detailed studies of the frequency of debris disks as a function of system age are useful tools to characterize belts of planetesimals and their collisions around solar-type stars. They provide important proxies for comparisons between the Solar System and exoplanetary systems in terms of planetary system formation and evolution. For example, observations at $70\ \mu\text{m}$ show that Kuiper-belt-like planetesimal systems around solar-type stars can be rather common ($\sim 16\%$; Trilling et al., 2008)($\sim 14\%$; Hillenbrand et al., 2008), but are not necessarily accompanied by $24\ \mu\text{m}$ excess, which would be indicative of terrestrial planet formation.

To provide a large sample, I merged the $24\ \mu\text{m}$ data of Trilling et al. (2008), Beichman et al. (2006) and that of the FEPS group (Carpenter et al., 2008, 2009; Meyer et al., 2008) resulting in a database of 425 solar-type field stars with age estimates in the range from 3.16 Myr to 10 Gyr. The tables in Trilling et al. (2008) include the results of Bryden et al. (2006) and Beichman et al. (2005) with their photometry data reevaluated with the same procedures as the newer Trilling et al. (2008) sample. I divided this database into the same logarithmic age bins as I did for the early-type field star sample and calculated the debris disk fraction in these bins using the 15% threshold in excess emission at $24\ \mu\text{m}$. The debris disk fractions are summarized in Table 3.5.

I also compiled results at $24\ \mu\text{m}$ from the literature on debris disk fractions

Table 3.5. The field star sample excess ratios at $24\ \mu\text{m}$ for solar-type stars at certain age bins from the compiled sample of Trilling et al. (2008), Beichman et al. (2006) and the FEPS collaboration (Carpenter et al., 2008, 2009; Meyer et al., 2008).

Age		Excess fraction	
		[#]	[%]
3.16 - 10	Myr.	2/12	$21.4^{+10.8}_{-10.6}$
10 - 31.6	Myr.	2/8	$30.0^{+14.4}_{-14.2}$
31.6 - 100	Myr.	2/38	7.5 ± 4.0
100 - 316	Myr.	7/48	16.0 ± 5.1
316 - 1000	Myr.	7/58	13.3 ± 4.3
1 - 3.16	Gyr.	2/94	3.1 ± 1.7
3.16 - 10	Gyr.	6/167	4.1 ± 1.5

around solar-type stars in open clusters and associations. They are summarized in Table 3.6. The excess fractions for the combined sample of solar-type stars are plotted in the *top right* panel of Figure 3.9. The plots show a significantly larger scatter in the excess fractions for solar-type than for early-type stars. A second interesting feature is a possible environmental effect on the fraction of debris disks around solar-type stars. Although not pronounced – and possibly strongly effected by sampling biases – there seems to be higher fraction of debris disk stars in clusters/associations than in the field.

In Praesepe, the few debris disk candidate stars (from a statistically large sample of 106 stars) implies that the planetary systems in the 1-40 AU zones around solar-type stars have generally reached a quiescent phase. This behavior can be compared with that of the field star sample, which levels off at a few percent at ages > 1 Gyr. This result may seem surprising given the LHB period of the Solar System, but it is actually consistent with the models of Gomes et al. (2005) and Thommes et al. (2008). The LHB was modeled in these papers to be a result

Table 3.6. The excess fraction in [24] for solar-type stars in clusters/associations.

Name	Age [Myr]	Excess fraction [#]	Excess fraction [%]	Excess Reference	Age
Orion OB1b	5±1	7/12	57.1±13.2	1	11
Upper Sco	5±1	5/16	33.3 ^{+11.1} _{-11.0}	2	12
Upper Sco	5±1	2/5	42.9 ^{+18.7} _{-18.6}	3	12
η Cha	8 ⁺⁷ ₋₄	8/13	60±12.6	4	13,14
Orion OB1a	9±2	4/5	71.4 ^{+16.4} _{-16.9}	1	11
β Pic MG	12 ⁺⁸ ₋₄	5/25	22.2±7.9	5	15
Lower Cen C . . .	16±1	11/24	46.2±9.8	3	16
Lower Cen C . . .	16±1	5/14	37.5 ^{+12.1} _{-12.0}	2	16
Upper Cen L . . .	17±1	3/11	30.8 ^{+12.7} _{-12.6}	3	12
Upper Cen L . . .	17±1	1/23	8.0 ^{+5.1} _{-5.0}	2	12
NGC 2547	30±5	8/20	40.9±10.5	6	6
Tuc-Hor	30±5	1/7	22.2 ^{+13.5} _{-13.2}	5	17
IC 2602	30±5	1/5	28.6 ^{+16.9} _{-16.4}	2	18
IC 2391	50±5	5/16	33.3 ^{+11.1} _{-11.0}	7	19
α Per	65±15	2/13	20.0 ^{+10.1} _{-10.0}	2	20,21
Pleiades	115±10	5/53	10.9±4.1	8	21,22,23
Pleiades	115±10	5/20	27.3±9.4	2	21,22,23
Hyades	625±50	0/67	2.7*	9	24
Hyades	625±50	0/22	7.7*	2	24
Praesepe	757±114	1/106	1.9±1.2	10	10

*Upper limit

References. — (1) Hernández et al. (2006); (2) Carpenter et al. (2008); (3) Chen et al. (2005); (4) Gautier et al. (2008); (5) Rebull et al. (2008); (6) Gorlova et al. (2007); (7) Siegler et al. (2007); (8) Gorlova et al. (2006); (9) Cieza et al. (2008); (10) This work; (11) Briceño et al. (2005); (12) Preibisch et al. (2002); (13) Mamajek et al. (1999); (14) Lyo et al. (2004); (15) Ortega et al. (2002); (16) Mamajek et al. (2002); (17) Rebull et al. (2008), with arbitrary errors adopted from similar age clusters; (18) Stauffer et al. (1997); (19) Barrado y Navascués et al. (2004); (20) Song et al. (2001); (21) Martín et al. (2001) (22) Meynet et al. (1993); (23) Stauffer et al. (1998); (24) Perryman et al. (1998)

of instability in the planetary system, caused by either strong interaction at the mean motion resonances of Jupiter and Saturn or that of Uranus and Neptune. In both cases the outer planetary disk is destabilized, causing planetesimals to migrate inward and initiate a collisional cascade. The models of Gomes et al. (2005) show a wide range of ages (192 Myr – 1.1 Gyr) when the LHB can occur, but they are more likely to be initiated at the earlier ages. The timing of the cascade depends on a few initial conditions that can be set to realistic parameters to give any of the solutions. The paper by Strom et al. (2005) also agrees that the LHB was a catastrophic event, lasting between 10 and 150 Myr, however they argue that the characteristics of the craters found on the inner planets originating from that epoch are more likely to be from main belt asteroids.³ The collisional cascade or “terminal cataclysm” model is also supported by recent studies of Hadean-era zircons on Earth (Trail et al., 2007).

3.5.4 Evolutionary differences between the debris disks around early- and solar-type stars

To illustrate the differences between the evolution of debris disks around early- and solar-type stars, I combined the top panel plots in Figure 3.9 in the bottom panel of the same figure. There appears to be an upper envelope to the excess fraction as a function of age, as if there were a theoretical maximum number of debris disks possible at any age. There is substantial scatter below this envelope.

Figure 3.9 shows that there is a subtle difference between the evolution of debris disks around early- and solar-type stars. To reduce the effects of observational biases (such as detection thresholds) and sampling differences (number

³Hartmann et al. (2000) and Morbidelli et al. (2001) argued that the LHB was the tail end of a monotonically decreasing impactor population. This theory was questioned by Bottke et al. (2007), who computed the probability of the cratering records being created by it, and could rule it out at a 99.7% (3σ) confidence level.

of stars in clusters), I rebinned all the data to a more homogeneous sampling. I used the same logarithmic age bins as I did for the field star samples: 3.16-10, 10-31.6, 31.6-100, 100-316 Myr, and 0.316-1, 1-3.16, and 3.16-10 Gyr. The result is shown in Figure 3.10, along with a second plot that shows the decay trends for A, F and G spectral-type stars separately. The data for all rebinned decay trends are summarized in Table 3.7. The “rise-and-fall” characteristics for early-type stars is confirmed (Currie et al., 2008), but with a quick drop-off at later ages. The solar-type stars show a monotonic decaying trend that reaches a constant of a few percent at later ages. The most important feature though is that the trends have different timescales.

The fraction of infrared excesses at a given age range is set by the interplay of the occurrence rate of the collisional cascades for each system, the longevity of the dust produced in these cascades, and my ability to detect the debris at the distance of the given cluster. Detailed modeling of these processes is required to interpret the different rate of decline in the debris disk fraction between early- and solar-type stars. Although such modeling is beyond the scope of this work, three possible explanations can be invoked to explain qualitatively the faster decline of excess fraction around solar-type stars. First, the dust must be in the $24\ \mu\text{m}$ emitting regions and solar-type stars have about $50\times$ smaller disk surface area in which a collisional cascade can produce warm enough dust. Second, the orbital velocity of planetesimals in the $24\ \mu\text{m}$ emitting zone will be higher around solar-type than the early-type stars, possibly accelerating the evolution of their debris disks. Third, the dust size distributions and lifetimes are different for the two groups of stars.

Table 3.7. The percent of debris disks in a rebinned distribution, as a function of stellar spectral-type.

Age		Early-type stars		Solar-type stars		A-type stars		F-type stars		G-type stars	
		Excess fraction		Excess fraction		Excess fraction		Excess fraction		Excess fraction	
[yr]		[#]	[%]	[#]	[%]	[#]	[%]	[#]	[%]	[#]	[%]
3.16 - 10	M	20/56	36.2 ± 6.3	28/63	44.6 ± 6.2	19/35	54.05 ± 8.2	12/20	59.09 ± 10.5	3/15	$23.5^{+10.1}_{-10.2}$
10 - 31.6	M	22/52	42.6 ± 6.7	37/137	27.3 ± 3.8	11/20	54.55 ± 10.6	19/42	45.45 ± 7.5	7/39	19.5 ± 6.1
31.6 - 100	M	7/25	$29.6^{+8.8}_{-8.7}$	9/67	14.5 ± 4.2	4/6	$62.50^{+17.1}_{-16.9}$	2/8	$30.00^{+14.2}_{-14.4}$	2/29	9.7 ± 5.1
100 - 316	M	33/117	28.6 ± 4.1	17/121	14.6 ± 3.2	13/44	30.43 ± 6.8	2/11	$23.08^{+11.4}_{-11.5}$	10/42	25.0 ± 6.5
316 - 1000	M	8/100	8.8 ± 2.8	8/253	3.5 ± 1.1	5/62	9.38 ± 3.6	4/30	15.62 ± 6.3	3/70	5.6 ± 2.6
1 - 3.16	G	-	-	2/94	3.1 ± 1.7	-	-	2/52	5.56 ± 3.0	0/37	$2.6^{+2.1}_{-2.2}$
3.16 - 10	G	-	-	6/167	4.1 ± 1.5	-	-	2/57	5.08 ± 2.7	0/85	1.2 ± 1.0

3.5.5 The results in context with the Late Heavy Bombardment

The cratering record of all non geologically active rocky planets and moons in the inner Solar System reveal a period of very intense past bombardment. Geochronology of the lunar cratering record shows that this bombardment ended abruptly at ~ 700 Myr (see e.g. Tera et al., 1973, 1974; Chapman et al., 2007), but the scarcity of the lunar rock record prior to this event hinders accurate assessment of the temporal evolution of the impact rates or the length of the bombardment period. Dynamical simulations of different possible impactor populations show that an unrealistically massive impactor population would be required to maintain the impact rate measured at the end of the bombardment for a prolonged period, thus convincingly arguing for the bombardment being a short-duration spike in the impact rate (Bottke et al., 2007). A possible explanation for this is that a dynamical instability initiated by the migration of the giant planets caused minor planetary bodies to migrate inwards from the outer region of the Solar System, bombarding the inner planets. Modeling shows that this scenario can occur over a wide range of ages (Gomes et al., 2005). Strom et al. (2005) show that it is possible instead that main belt asteroids bombarded the planetary system.

I performed a Monte Carlo simulation to evaluate the observed debris disk fraction in the context of the evidence from the LHB. The goal was to constrain the fraction of the solar-type stars that undergo LHB (or fine dust generation) and the duration of these events. I presumed in my models that all LHB events could be detected in the existing debris disk surveys and that they had an equal probability of occurring once from 100 Myr to 1 Gyr. Both of these are strong assumptions. There is significant uncertainty on how much dust was generated and under what time scales during the LHB, making it difficult to relate the LHB

unambiguously to debris disks. However, given that *Spitzer* measurements of $24\ \mu\text{m}$ excess emission are typically sensitive to a collisional cascade involving mass on the order of a few lunar masses, and that such an episode has clearing time scale $\gtrsim 2\ \text{Myr}$ (Grogan et al., 2001), it seems plausible that the destruction of a few large asteroids can be detected in most observed systems. In my code I modeled clusters with 135 (106+29) members in 20000 simulations. I varied the overall percentage of stars that will ever generate a debris disk from 0 to 100 % and the duration of their bombardment episodes from 0 to 500 Myr. If the number of disks at 750 Myr were within my measured excess fraction of 1-3%, the simulation was tagged as being consistent with the measurements, else it was tagged inconsistent. The overall probability of a given parameter pair is given by dividing the number of consistent simulations at a certain total disk fraction and duration timescale by the number of simulations (20000).

The calculated probability map is shown in Figure 3.11. The plot shows that the results are degenerate in the parameter space of dt and p_d , with dt being the duration of a bombardment episode and p_d the percentage of stars to ever undergo such an event. Between the extremes of a very large percentage of the stars undergoing debris disk generation, but with a very short lifetime ($\sim 5\text{-}10\ \text{Myr}$) and a very small percentage ($< 5\%$), with a long ($> 300\ \text{Myr}$) lifetime there is a continuous set of solutions.

My simple model allows the quantitative assessment of the probability of different types of LHB-like episodes. For example, I can exclude at a 3 % significance level that 60% of the stars undergo major orbital rearrangements, if this leads to debris production over 100 Myr. Similarly, very short debris producing events are unlikely, because they would not produce observable disks, inconsistent with the results.

If we seek to evaluate the probability of strictly LHB-like debris producing episodes, we can fix the length of the episode to 75 Myr, consistent with the duration estimated for the inner Solar System and the other timescales discussed in §3.5.3. In this case my results show that up to 15-30 % of the stars should undergo such a major orbital reorientation during the first Gyr of their evolution to be consistent with the modeling.

3.6 Summary

I conducted a 24 μm photometric survey for debris disks in the nearby (~ 180 pc) relatively old (750 Myr) Praesepe open cluster. The combined sample of SDSS, Webda, and 2MASS gave us a robust highly probable cluster member list. With simultaneous fitting of cluster distance and age I derived a series of solutions for both parameters as a function of metallicity (see Appendix A). The derived age for Praesepe is 757 Myr (± 114 Myr at 3σ confidence) and a distance of 179 pc (± 6 pc at 3σ confidence)

Out of the 193 cluster members that I detected at all wavelengths in the combined catalog, 29 were early (B5-A9) and 164 later (F0-M0) spectral types. I found one star in the early and three in the later spectral type groups that show excess emission. Up to near the completeness limit, with one debris disk star, there are 106 sources in the later spectral-type sample. This result shows that only $6.5 \pm 4.1\%$ of early- and $1.9 \pm 1.2\%$ of solar-type stars are likely to possess debris disks in the 1-40 AU zones. These values are similar to that found for old (> 1 Gyr) field stars.

I place my results in context with the Late Heavy Bombardment theory of the Solar System. With simple Monte Carlo modeling I show that the observations are consistent with 15-30% of the stars undergoing a major re-arrangement of the

planetary orbits and a subsequent LHB-like episode once in their lifetime, with a duration period of 50-100 Myr.

I also summarize the results in the literature on the decay timescales of debris disks around early- and solar-type stars. I find that the decay timescale for solar-type stars is shorter than for earlier-type stars.

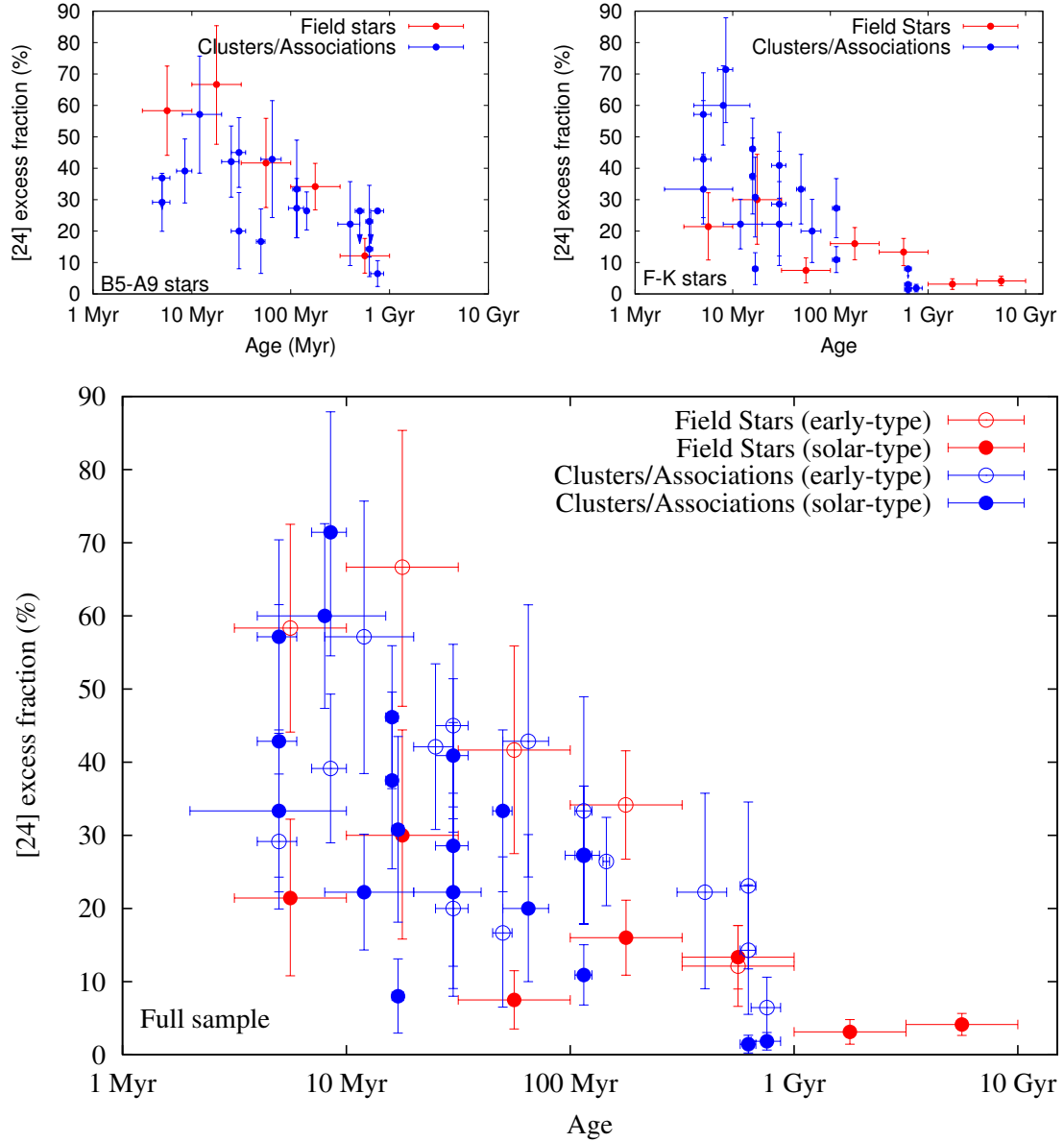


Figure 3.9 *Top Left Panel:* The decay of the debris disk fraction for early type stars. *Top Right Panel:* The decay of the debris disk fraction for solar-type stars. *Bottom Panel:* The combined plot of all excess fractions. The errors in excess fraction are the 1σ errors from the beta distribution calculations (§3.5.1) while the age errors are from the literature. The age "errors" for the field star sample show the age bins.

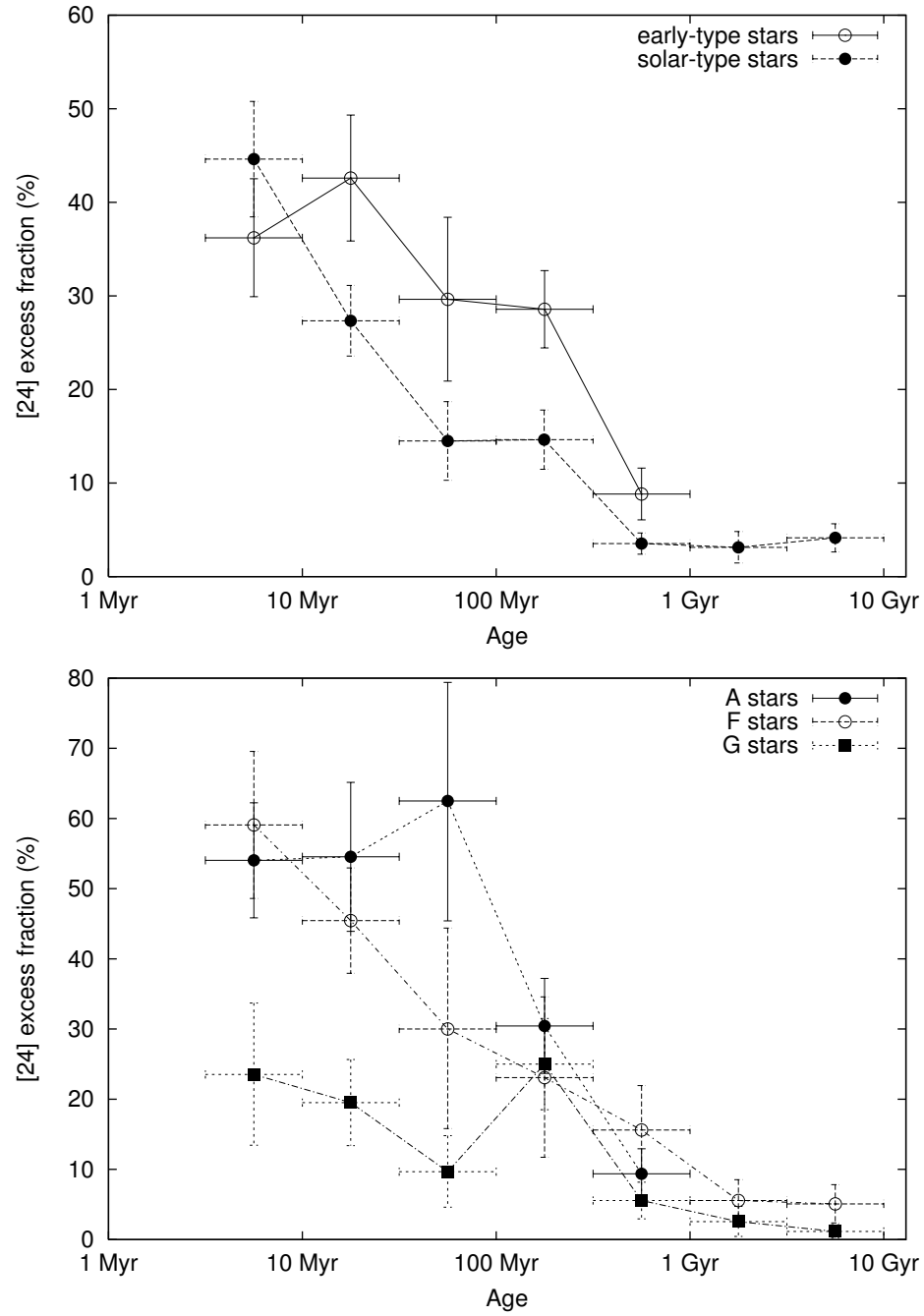


Figure 3.10 *Top panel:* The difference between the decaying trend for early- and solar-type stars, in a binned data plot. *Bottom panel:* The difference between the decaying trend for A, F and G spectral-type stars, in a binned data plot. The errors in the excess fraction are from beta distribution calculations (§3.5.1), while the "error bars" in the ages show the age bins. The numerical values for the data points are summarized in Table 3.7.

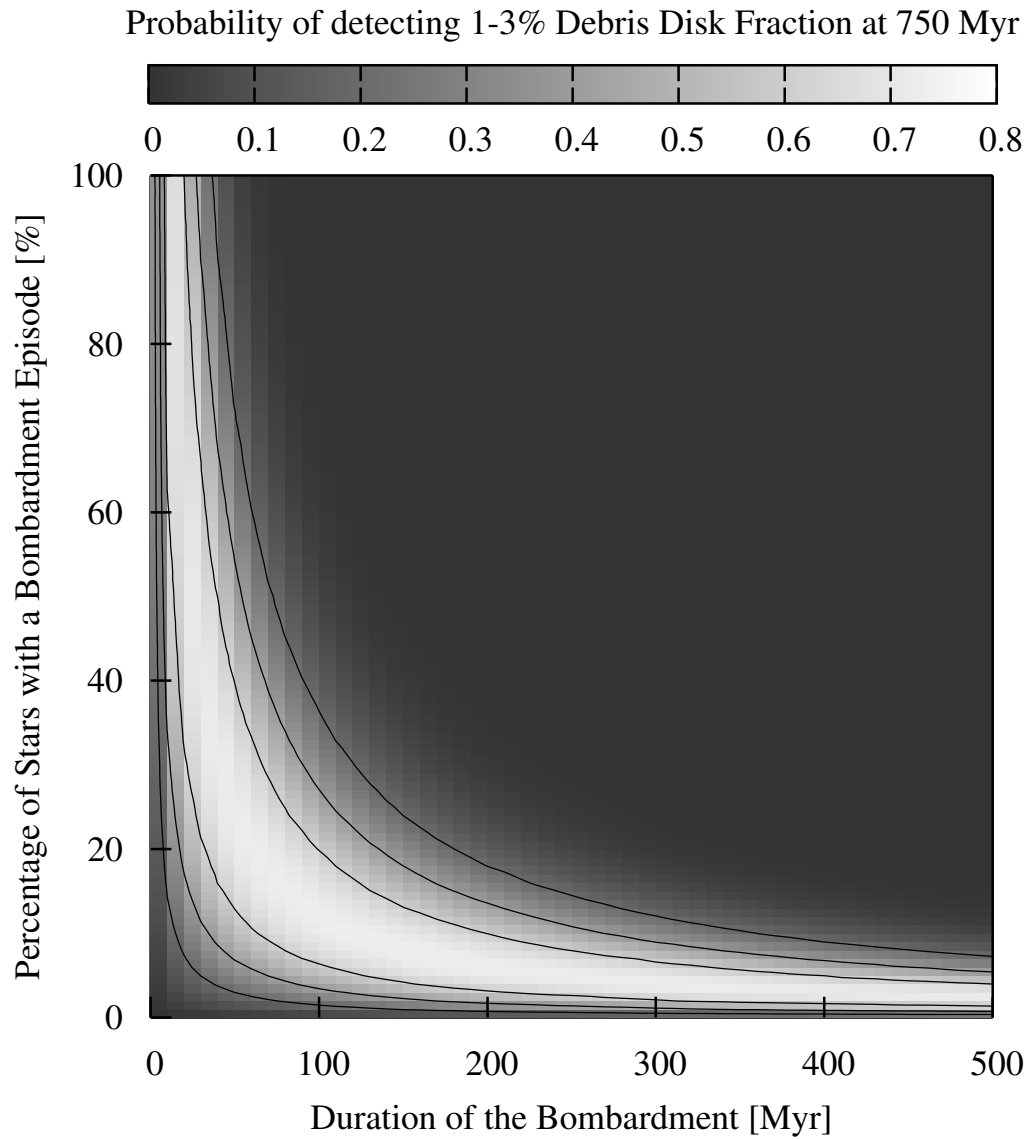


Figure 3.11 The probability of detecting the 1-3% ($2/(106+29)$) debris disk fraction observed at Praesepe, as a function of the percentage of stars that undergo LHB type debris disk generation and the duration of the events. The contour lines are at 20, 40 and 60% probability.

CHAPTER 4

MODELING COLLISIONAL CASCADES IN DEBRIS DISKS

I develop a new numerical algorithm to model collisional cascades in debris disks. Because of the large dynamical range in particle masses, I solve the integro-differential equations describing erosive and catastrophic collisions in a particle-in-a-box approach, while treating the orbital dynamics of the particles in an approximate fashion. I employ a new scheme for describing erosive (cratering) collisions that yields a continuous set of outcomes as a function of colliding masses. I demonstrate the stability and convergence characteristics of my algorithm and compare it with other treatments. I show that incorporating the effects of erosive collisions results in a decay of the particle distribution that is significantly faster than with purely catastrophic collisions.

4.1 Introduction

More than 500 extrasolar planets have been identified to date in over 400 planetary systems.¹ Most of these planets were discovered via radial velocity measurements. As a result, only a handful of them are less than 10 Earth masses; the vast majority are gas giants resembling Jupiter. They are also in extremely close orbits to their host stars, making these systems dramatically different from ours. A large number of additional candidate systems have been found recently with the Kepler mission (Borucki et al., 2010).

In contrast to the great majority of known exoplanet systems, our own solar system has a complex configuration with gas giants at significant distances from their central star and rocky planets/asteroids within the giant planet zone. The

¹<http://exoplanet.eu>

detection of rocky planets and planetesimals around other stars is difficult. One of the most productive approaches is indirectly via the thermal emission of their planetary debris dust belts. Ever since the discoveries with IRAS, we know that extrasolar systems harbor disks of dust/debris that are generated by planetesimal collisions and are similar to our Kuiper belt but much more massive (Aumann et al., 1984; Backman & Paresce, 1993). The dust reprocesses the stellar light and emits it as thermal radiation in the infrared, submillimeter and radio wavelength regime. A prototypical example of such a system is Fomalhaut, where a planet is shepherding the star's debris disk resolved in both scattered light (Kalas et al., 2008) and in infrared emission (Holland et al., 2003; Stapelfeldt et al., 2004; Marsh et al., 2005). Debris disks highlight the constituents of planetary systems that are many to hundreds of AU away from their stars.

With the launch of the *Spitzer Space Telescope*, many observations have been obtained to detect and possibly to resolve debris disks in the infrared regime. Debris disks have been probed around all types of stars, both in stellar clusters and in the field. These observations showed that even though debris disks are common around stars of all spectral types, they are more likely to be detected in the earlier stages of stellar evolution (Wyatt, 2008). We have also learned that debris disks may be located close to or far from their central stars (Morales et al., 2011), that there are systems with multiple debris rings (Hillenbrand et al., 2008, such as our solar system), and that there can be wide varieties of mineralogical compositions within the disks (Weinberger et al., 2003; Currie et al., 2011). Debris disk studies are now a major component of the Herschel observing program (Matthews et al., 2010; Eiroa et al., 2010), which will provide substantial advances in our understanding of their outer zones.

Interpreting these results demands theoretical insights in a variety of areas.

For example, attempts have been made to understand the evolution of debris disks as a function of stellar type by studying them in stellar clusters of different ages. As concluded in Gáspár et al. (2009), solar-type stars in the field (Beichman et al., 2006; Trilling et al., 2008; Carpenter et al., 2008, 2009) and in clusters (Gorlova et al., 2006, 2007; Siegler et al., 2007) may show a faster decay trend compared to that observed for earlier-type stars (Rieke et al., 2005; Su et al., 2006), although the difference is subtle and needs confirmation. The decay trends of the fractional luminosity ($f_d = L_{\text{exc}}/L_*$) show a large range in values. Spangler et al. (2001) find a decay $\propto t^{-1.76}$ when fitting ISO/IRAS data, while Greaves & Wyatt (2003) get a much shallower decay $\propto t^{-0.5}$. The majority of surveys however find a decay $\propto t^{-1}$ (Liu et al., 2004; Moór et al., 2006; Rieke et al., 2005). A better theoretical understanding is needed to sort out these results and to provide testable hypotheses that can be compared with the observations.

Only a handful of debris disks have been resolved; for the majority, we only know the integrated infrared excess emission. Finding the underlying spatial distribution of the debris in these disks is not straightforward, as any spectral energy distribution (SED) can be modeled with a degenerate set of debris rings at different distances. Although much of the uncertainty is associated with the optical constants of the grains, another under-appreciated issue is the grain size distribution. Collisional models can reduce the number of free parameters in the SED models by determining the stable size distribution of particles in the disks.

Observations of resolved debris disks also have raised questions that can best be addressed by theoretical models. For example, Spitzer MIPS images have shown a significant extended halo of dust around Vega (Su et al., 2005), both at 24 and 70 μm . Initial calculations hypothesized the halo around Vega to be a result of a high outflow of dust due to radiation pressure from a recent high-mass

collisional event (Su et al., 2005), while Müller et al. (2010) model it as a result of weakly bound particles on highly eccentric orbits. Further modeling and deep observations of additional systems will help distinguish these two possibilities.

In this chapter, I describe a new algorithm for modeling debris disks, in which I refine the physics and numerical methods used in collisional cascade models. In §4.2, I briefly outline previous models and introduce the basics of my algorithm. In §4.3, I detail my numerical methods, followed in §4.4 by my approach for including simplified dynamics. In the last section, I compare my numerical algorithm to previous ones and discuss in detail the differences between the codes and the effects those differences have on the outcome of the collisional cascades. I also supplement the work with an extended appendix that covers the numerical methods and the verification tests of the code.

4.2 The physical and numerical challenges of modeling debris disks

Collisional cascades have been studied both analytically and using collisional integro-differential numerical models. The classic analytic models of Dohnanyi (1969), Hellyer (1970), and Bandermann (1972) took into account both erosive and catastrophic collisional outcomes, assumed a material strength that was independent of the particle mass, a particle mass distribution with no cut-offs, and a constant interaction velocity. They yielded steady state power-law mass distribution indices of $-11/6$. This result was in general agreement with the measured size distribution of asteroids in the solar system. More recently, analytic models by Dominik & Decin (2003) and Wyatt et al. (2007) showed that the fractional infrared luminosity in a collision-dominated steady-state system decays following a t^{-1} power-law, in agreement with most observations. Wyatt et al. (2007) also derived a maximum mass and fractional luminosity as a function of age and dis-

tance from the central star, which they then used to classify systems with possible recent transient events.

However, numerical models are needed to expand on these results. In the particular case of our Solar System, sophisticated numerical models were developed to track the evolution of the largest asteroids (Greenberg et al., 1978). They have been further improved to reproduce the observed wavy structure in the size distribution at the very highest masses (e.g., O’Brien & Greenberg, 2005; Bottke et al., 2005). These models yield power-law distributions that deviate from the classic solution of Dohnanyi (1969), with certain regions steeper than it and others shallower. Using a steeper or shallower distribution and extrapolating it to dust sizes can result in substantial offsets in the number of particles and thus in the infrared emission originating from them for a given planetesimal mass. Conversely, the particle size distribution affects the underlying disk mass calculated from the observed infrared emission.

A complete numerical model of collisional cascades would follow outcomes from all types of collisions, include a kinematic description of the system, incorporate coagulation below certain thresholds, and do all this with high numerical fidelity. Although such a model has not yet been built because of its complexity, there are a number of approaches in the literature that model collisional cascades down to particles of micron size, each with distinctive strengths and weaknesses.

Dullemond & Dominik (2005) modeled the coagulation of dust particles to study the formation of planetesimals in protoplanetary systems. They show that fragmentation is important even at early ages. A purely coagulating system loses all of its dust in less than a million years, which is inconsistent with observations. Their models suggest that protoplanetary disks reach an equilibrium between grain growth and fragmentation, which maintains their infrared signatures for a

few million years.

The collisional code `ACE` has been used in many studies (Krivov et al., 2000, 2005, 2006, 2008; Löhne et al., 2008; Müller et al., 2010). It follows the evolution of the particle size distributions as well as the spatial distribution of the dust in debris disks. The code initially only accounted for collisions resulting in catastrophic outcomes, while the latest version (Krivov et al., 2008; Müller et al., 2010) includes erosive (cratering) events as well. The collisional outcome prescriptions are based on the Dohnanyi (1969) particle-in-a-box model, but with a more elaborate description of material strengths in collision outcomes as well as the radiation force blowout. The strength of the code is that it calculates the dynamical evolution of the systems, as well. Since following the dynamical evolution of a system makes large demands on computer memory space and CPU speed, the code can only model the size distribution with a low number of mass grid points; it originally used a first order Euler Ordinary Differential Equation (ODE) solving algorithm, but has been modified to include a more precise one (A. Krivov, priv. comm.). Krivov et al. (2006) and Müller et al. (2010) applied this algorithm to debris disks in general and to the specific example of the Vega system. They followed the orbital paths of fragments and placed special emphasis on radiation effects. Löhne et al. (2008) modeled debris disk evolution around solar-type stars and found, both with analytic and numerical analysis, that the majority of physical quantities, such as the mass and the infrared luminosity, decrease with time as $t^{-0.3}$ to $t^{-0.4}$. This is in contrast with the observed t^{-1} decay found by some observations (Liu et al., 2004; Moór et al., 2006; Rieke et al., 2005). However, the population synthesis verification tests in Löhne et al. (2008) yield good agreement with the latest Spitzer observations.

Thébault et al. (2003, 2007) study the evolution of extended debris disks with a

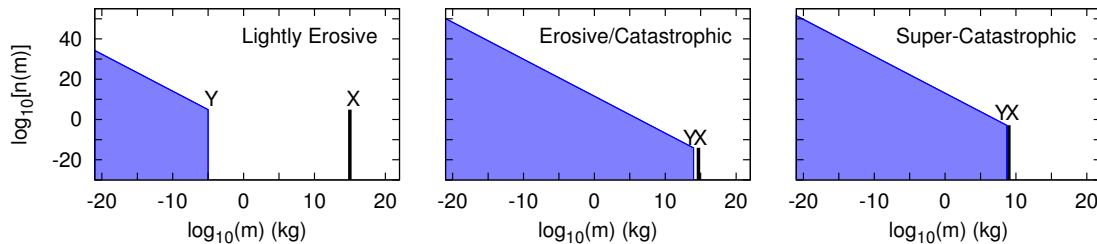


Figure 4.1 Illustration of the possible outcome scenarios of collisions. In all collisions, a single largest X fragment is created as well as a power-law distribution of fragments with a largest mass of Y .

particle-in-a-box algorithm. They include both catastrophic and erosive collisions and employ resolution and numerical methods similar to the ones implemented in the ACE code. They model the extended disk structure by dividing the disk into separate, but interacting rings. Their model does not include dynamics.

Campo Bagatin et al. (1994) showed that a series of wave patterns is produced in the mass distribution of particles when a low-mass cutoff is enforced, such as in the case of a radiation force blowout limit. This signature is produced by the other debris disk numerical models as well (Thébault et al., 2003; Thébault & Augereau, 2007; Krivov et al., 2006; Löhne et al., 2008; Wyatt et al., 2011). However, the conditions under which these waves are produced have not been completely analyzed. Wyatt et al. (2011) do show that the amplitude and wavelength of the waves is collisional velocity dependent. Such strong features in the particle size distribution are not observed in the dust collected within the solar system. The interplanetary dust flux model of Grün et al. (1985), which used in situ satellite measurements of the micro-meteoroid flux in the solar system, and the terrestrial particle flux measurements of the LDEF satellite (Love & Brownlee, 1993)

only show a single peak at $\sim 100\mu\text{m}$ in the dust distribution. However, these measurements detected particles that were brought inward from the outer parts of the solar system via Poynting-Robertson drag and particles removed from the inner parts of the solar system via radiation force blowout. Their results are reflections of more than a single parent distribution and of multiple physical effects.

The dynamical code of Kuchner & Stark (2010) models the evolution and 3D structure of the Kuiper belt, with a Monte Carlo algorithm and a simple treatment of particle collisions. Their models predict that grain-grain collisions are important even in a low density debris ring such as our Kuiper belt.

Kuchner & Stark (2010) and Dullemond & Dominik (2005) both emphasize the strong effects of fragmentation in their models. Müller et al. (2010) point out that including erosive (cratering) events is necessary for their models to reproduce the observed surface brightness profiles of Vega. Thébault & Augereau (2007) also show that a complete collisional treatment will result in significant deviations from the classic power-law solution.

My goal is to set up a numerical model that places special emphasis on investigating these issues. My new empirical description of collisional outcomes avoids discontinuities between erosive and catastrophic collisions and thus enables a more stable and accurate calculation. I also solve the full scattering integral, thus ensuring mass conservation and the propagation of the largest remnants of collision outcomes. Finally, I use second order integration and fourth order ODE solving methods to improve the numerical accuracy. Below, I outline the physical and numerical techniques I will employ. In the Appendix, I present verification tests of these treatments.

4.2.1 Collisional outcomes

In collision theory, two types of outcomes are generally distinguished: catastrophic and erosive (the latter also known as cratering). In the case of a catastrophic collision (CC), both colliding bodies are completely destroyed and their masses are redistributed in a power-law distribution. In the case of an erosive collision (EC), the projectile is much smaller than the target, resulting in one big fragment whose mass is close to the original target mass. The cratered mass plus the original projectile mass is redistributed also in a power-law distribution. The boundary between these two classifications is drawn by convention at the point where the largest fragment mass is half of the original target mass. I illustrate these outcomes in Figure 4.1.

In the first panel of Figure 4.1, I plot the outcome distribution of an erosive collision, where there is a single large X fragment and a distribution of dust at much lower masses. The X fragment is over half the mass of the original target mass M . The redistributed mass is equal to the cratered mass plus the projectile mass. The largest fragment in the distribution, Y , is arbitrarily set to be 20% of the cratered mass. In §4.3.3 I elaborate on the validity of this arbitrary value.

In the second panel of Figure 4.1, I plot the outcome at the boundary case between catastrophic and erosive collisions, where the single largest fragment X is exactly half of the original target mass M . The redistributed mass is equal to the other half of the target mass M plus the projectile mass. The largest fragment in the distribution, Y , is arbitrarily set to be 20% of the cratered mass here as well (10% of the target mass).

Finally, in the third panel of Figure 4.1, I plot the outcome of a super-catastrophic collision, where the target and projectile masses are equal. The mass of the single largest fragment X is given by the relation of Fujiwara et al. (1977).

The redistributed mass is equal to $M - X$ plus the projectile mass. The largest fragment in the distribution, Y , is arbitrarily set to be at $0.5X$.

In reality, there is no strict boundary between catastrophic and erosive collisions (Holsapple et al., 2002). The outcomes between these two extreme scenarios should be continuous. In laboratory experiments, however, it is easier to test the extreme outcomes. In my model, I use the laboratory experiments to describe the extreme solutions and connect them with simple interpolations throughout the parameter space. I revise the currently used models to include an X fragment for both erosive and catastrophic collisions as a separate new gain term, thus avoiding a discontinuous mathematical assumption. In this treatment, the placement of the X fragments is grid size independent, further improving precision and guaranteeing the accurate downward propagation of these fragments. I am able to express the loss term in a much simpler form, including collisions from both regimes. Previous models only included a full loss term for catastrophic collisions and removed fractions of particles for erosive collisions.

The slope of the power-law particle redistribution has been studied extensively. Dohnanyi (1969) used a single power-law value from the largest mass to the smallest. Later experiments have shown that a double (or even a triple) power-law distribution is a more likely outcome (see, e.g., Davis & Ryan, 1990). This has led to the widespread use of a double power-law for the redistribution in numerous collision models. I conducted numerical tests that demonstrated that there is negligible difference in using a wide range of slopes with a single power-law. Therefore, I have used the simplest method of redistributing the fragmented particles with a single power-law slope from the second largest Y fragment downwards, scaled to conserve mass. As a nominal value, I will use the classic $-11/6$ redistribution slope.

4.2.2 Incorporating the complete redistribution integral

The classic solution to the collisional evolution of an asteroid system involves solving the Smoluchowski (1916) integro-differential equation. This was first done by Dohnanyi (1969). Because erosive collisions remove only a small part of the target mass in a collision, Dohnanyi (1969) expressed the erosive removal term in a differential form. This is not appropriate for my case. My system has well defined boundaries; thus a continuity equation cannot be used. The locality of the collisional outcomes in phase space is not certain either.

Therefore, to solve the Smoluchowski equation for the problem at hand, I need to solve the full scattering integral. This is complicated numerically, as the integrations must extend over the entire dynamical range of ~ 40 orders of magnitude in mass. To be able to perform accurate integrations over such a large interval, I need to use a large number of grid points and sophisticated numerical methods. To achieve this in a reasonable time, I drop the radial dependence of the various quantities and to solve the equations under a “particle-in-a-box” approximation. With this approach, I lose radial and velocity information but gain accuracy.

4.2.3 The effect of radiation forces

Poynting-Robertson drag can be an effective form of removing particles from the disk, so I include it in my model. However, the strongest and most dominating radiation effect is the removal of particles via radial radiation forces. These act on orbital timescales and can remove or place particles on extremely eccentric orbits. This gives rise to the challenge of incorporating a radial dependent removal term into a particle-in-a-box model that does not carry radial information. In §4.3.1.1 and §4.3.1.2, I discuss my approach for incorporating these radiation effects.

Stellar wind drag is an important dust removal effect for very late-type stars,

such as in the case of AU Mic (Augereau & Beust, 2006; Strubbe & Chiang, 2006), which is an M1 spectral-type star. I concentrate on modeling debris disks in early- and solar-type systems, so I chose to neglect the effects of stellar wind drag. I do not take into account the Yarkovsky effect either, as it is small in high-density debris disks compared to the other radiation effects.

4.3 The collisional model

I now discuss my collisional code (CODE-M - COLLISIONAL Disk Evolution Model), which solves a system of integro-differential equations that describe the evolution of the number densities of particles of different masses. The code includes outcomes from erosive (cratering) collisions and catastrophic collisions and qualitatively follows the effects originating from radiation forces and Poynting-Robertson drag.

The system-dependent parameters are: the spectral-type of the central star (which defines the stellar mass M_* and the magnitude of the radiation effects it will have on the particles), the minimum and maximum particle masses (m_{\min} and m_{\max} , respectively), the radius, width, and height of the debris ring (R , ΔR , and h , respectively), the total mass within the ring (\mathcal{M}_{TOT}), and the slope of the initial size distribution of the particles (η). I estimate the total volume of the narrow ring, \mathcal{V} , as

$$\mathcal{V} = 2\pi h R \Delta R, \quad (4.1)$$

which together with \mathcal{M}_{TOT} defines a mass density.

4.3.1 The evolution equation

In general, the change in the differential number density $n(m, t)$ at any given time for a particle of mass m is given by (Smoluchowski, 1916)

$$\frac{d}{dt}n(m, t) = T_{\text{PRD}} + T_{\text{coll}} , \quad (4.2)$$

where T_{PRD} is the Poynting-Robertson drag (PRD) term and T_{coll} is the sum of the collisional terms. I define the differential number density of particles such that

$$N(t) = \int n(m, t) dm \quad (4.3)$$

is the time-dependent total number density of particles within the ring.

Effects such as radiation force blowout and Poynting-Robertson drag are able to deplete the low-mass end of the distribution, which in turn alters the evolution of the disk and more importantly, its infrared signature. Because I do not follow the radial profile of the various debris disk quantities in my algorithm, I can only capture the effects of radiation forces in a simplified way.

4.3.1.1 Poynting-Robertson drag term

Poynting-Robertson drag has an important effect on the orbits of particles around stars. A complete analysis is given by Burns et al. (1979), who correct many errors made in previous work.

Poynting-Robertson drag arises from the fact that particles re-radiate the energy they absorb from the central star preferentially in their direction of motion. This eventually causes the particles to slow in their orbit and follow an inward spiral. Burns et al. (1979) show that the change in the orbital distance due to Poynting-Robertson drag can be written as

$$\frac{dR(m)}{dt} = -\frac{2GM_*\beta(m)}{cR} , \quad (4.4)$$

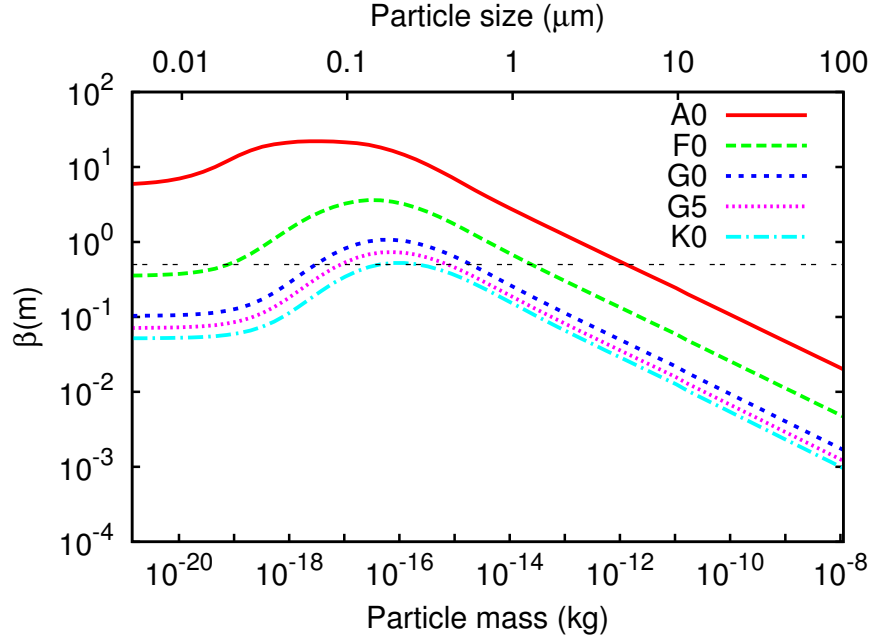


Figure 4.2 Calculated values for the radiation-force parameter β around stars of spectral-type A0, F0, G0, G5 and K0. The thin double-dashed black line is at the critical value $\beta=0.5$, above which radiation forces are able to remove particles from circular orbits.

where G is the gravitational constant, c is the speed of light, and $\beta(m)$ is a parameter for a particle of mass m that measures the ratio of radiation to gravitational force the particle experiences.

I calculate the $\beta(m)$ values as a function of the particle masses, optical constants, and the spectral type of the central star following Gáspár et al. (2008). For the calculations I assume a silicate composition for the particles and a bulk density of 2.7 g cm^{-3} . I show the calculated $\beta(m)$ values for a few different spectral type stars in Figure 4.2.

I use equation (4.4) to derive an approximate term that captures the effect of

Poynting-Robertson drag as (see eq. [4.2])

$$T_{\text{PRD}} = -\frac{n(m, t)}{\tau_{\text{PRD}}(m)}, \quad (4.5)$$

where

$$\tau_{\text{PRD}}(m) = \frac{c}{2GM_*\beta(m)} R\Delta R. \quad (4.6)$$

The mass dependence of the timescale comes from the mass dependence of the parameter β . In principle, once a particle is removed from the collisional system it still radiates in the IR; it just does not take part in the collisional cascade. I keep track of the removal rate of these particles, but do not follow the total amount removed or their infrared emission.

4.3.1.2 Radiation force blowout

The effects of the radiation force blowout are incorporated in my code with the simplified dynamics treatment introduced in §4.4, and not by the inclusion of a separate term in the differential equation as are the effects of Poynting-Robertson drag.

Removing a particle from the collisional system via radiation force blowout requires roughly an orbital timescale

$$\tau_{\text{RFB}} = 2\pi\sqrt{\frac{R^3}{GM_*}}. \quad (4.7)$$

As I will show in §4.4, under my assumptions a newly created particle of mass m gets removed via radiation force blowout if $\beta(m) \geq 0.5$ and is unaffected by radiation forces when $\beta(m) < 0.5$.

Although the radiation force blowout timescale is not used in my code, in Figure 4.3 I compare it to the Poynting-Robertson drag timescale around an A0 spectral-type star, assuming a disk width-to-radius ratio of 0.1. The plot shows that within reasonable disk radii estimates, radiation force blowout will always

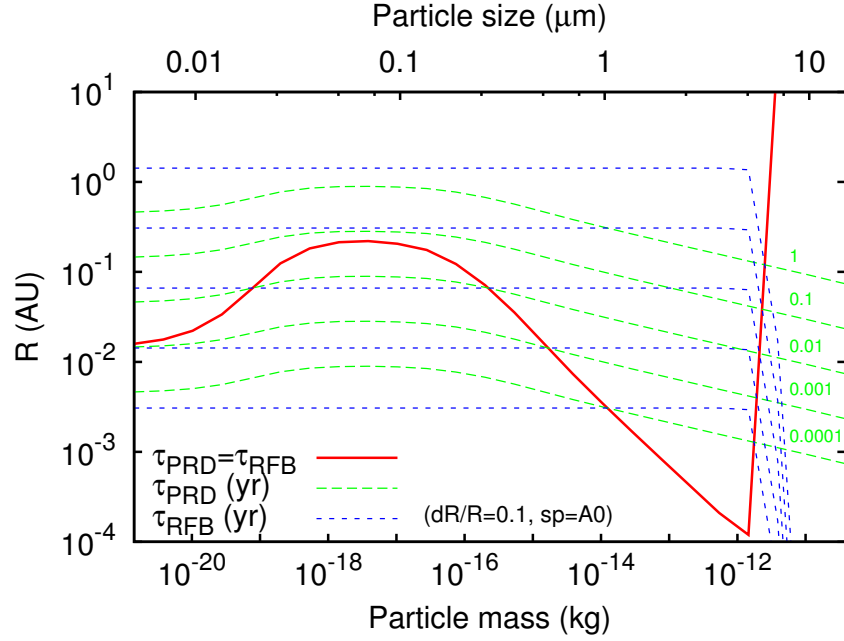


Figure 4.3 Comparison of the radiation force blowout (RFB) to the Poynting-Robertson drag (PRD) timescales for an A0 spectral-type star, as a function of particle mass and distance from the star, with a disk width of $dR/R = 0.1$. The dashed lines give the orbital distances as a function of particle size, where the Poynting-Robertson drag and blowout timescales are 0.1, 0.01, 0.001 and 0.0001 years. The solid red line gives the distance where the timescale for Poynting-Robertson drag is equal to the radiation force blowout timescale. Above the solid red line, radiation force blowout dominates, while below it Poynting-Robertson drag does. The plot shows that within reasonable disk radii estimates, radiation force blowout will always dominate in the $\beta(m) > 0.5$ domain, while outside of it Poynting-Robertson drag will be the stronger effect.

dominate in the $\beta(m) > 0.5$ domain, while outside of it Poynting-Robertson drag will be the stronger effect. Whether Poynting-Robertson drag is an effective form of removal in the $\beta(m) < 0.5$ domain depends on the number density of particles

in the ring, i.e., the collisional timescale of the system (Wyatt et al., 2005). The outcomes are similar for all spectral type stars and for realistic $\Delta R/R$ values.

4.3.2 The collisional term

The probability of a collision between two particles is a function of their number densities and their collisional cross section. I express the collisional cross section for particles of mass m and m' as

$$\sigma(m, m') = \pi [r(m) + r(m')]^2, \quad (4.8)$$

where $r(m)$ is the radius of each particle. I express the differential rate of collisions between the two masses as

$$\begin{aligned} P(m, m'; t) &= n(m, t)n(m', t)V\sigma(m, m') \\ &= n(m, t)n(m', t)V\pi[r(m) + r(m')]^2 \\ &= \kappa n(m, t)n(m', t)V\pi\left(m^{\frac{1}{3}} + m'^{\frac{1}{3}}\right)^2 \end{aligned} \quad (4.9)$$

where V is their characteristic collisional velocity, $n(m, t)$ and $n(m', t)$ are the differential number densities for particles of mass m and m' ,

$$\kappa \equiv \left(\frac{3}{4\pi\rho}\right)^{\frac{2}{3}}, \quad (4.10)$$

and ρ is the bulk mass density of the particles. The number densities in the problem are naturally all time dependent. However, for brevity, hereafter I drop the time dependence from my notation.

The decrease or increase in number density at a certain mass will be determined by three separate events: the removal of particles caused by their interaction with all other particles, the addition of the X particles from the interactions of other particles (see §4.2.1 and Figure 4.1), and the addition of particles from the redistribution of smaller fragments originating from collisions of other particles.

I express the first event, which describes the removal of particles, as

$$\left. \frac{d}{dt} n(m) \right|_{\text{rem}} = - \int_{m_{\min}}^{m_{\max}} dm' P(m, m') . \quad (4.11)$$

I completely remove all particles from all grid points if they take part in a collision, even if they are the target objects in erosive collisions.

The second event to be described is the addition of the large X fragments. To this end, I need to calculate the mass M that will produce a particle of mass $m = X$ when interacting with a particle of mass m' . I achieve this with a root finding algorithm from the collisional equations presented in the following sections and calculate it only once in the beginning of each run. In equation form,

$$\left. \frac{d}{dt} n(m) \right|_{m \equiv X(m', M)} = \int_{m_{\min}}^{\mu_X(m)} dm' P(M, m') . \quad (4.12)$$

The lower limit of the integration is the minimum mass in the distribution. I denote the largest mass m' that can create a particle of mass m as the X fragment as $\mu_X(m)$. Its value can also be calculated via root finding algorithms and has to be calculated for each value of m once in the beginning of each run (see Figure D.2 in the Appendix).

These first two integrals may catastrophically cancel, meaning that the difference between the two terms may be significantly smaller than the absolute value of each, causing the former to be artificially set to zero when evaluated numerically. It is therefore useful to combine these terms into a single integral in a way that will lessen the probability of catastrophic cancellation:

$$\begin{aligned} T_I(m) = & -V\pi\kappa \left\{ \int_{m_{\min}}^{\mu_X(m)} dm' n(m') \left[n(m) \left(m^{\frac{1}{3}} + m'^{\frac{1}{3}} \right)^2 - n(M) \left(M^{\frac{1}{3}} + m'^{\frac{1}{3}} \right)^2 \right] \right. \\ & \left. + \int_{\mu_X(m)}^{m_{\max}} dm' n(m') n(m) \left(m^{\frac{1}{3}} + m'^{\frac{1}{3}} \right)^2 \right\} , \end{aligned} \quad (4.13)$$

Unfortunately T_I can still suffer from catastrophic cancellation (when m' is much smaller than m , and by definition only for the first integral). I overcome this issue by employing a Taylor-series expanded form of T_I , as given in the Appendix.

The third event in the collisional term is the addition of the power-law fragments back to the distribution. The description of this process is quite simple; however, its precise calculation is not. I write in general

$$T_{II}(m) = \int_{m_{\min}}^{m_{\max}} d\mu \int_{\mu}^{m_{\max}} dM P(\mu, M) A(\mu, M) \times H[Y(\mu, M) - m] m^{-\gamma}, \quad (4.14)$$

where μ is the projectile mass, M is the target mass, A is the scaling of the power-law distribution, and H is the Heaviside function. The total redistributed mass is

$$M_{\text{redist.}}(\mu, M) = \int_0^{Y(\mu, M)} A(\mu, M) m^{-\gamma+1} dm, \quad (4.15)$$

where Y is the largest fragment within the redistribution (i.e., the second largest fragment in the collision, after X ; see §4.2.1). This gives the scaling factor

$$A(\mu, M) = \frac{(2 - \gamma) M_{\text{redist.}}(\mu, M)}{Y^{2-\gamma}(\mu, M)}. \quad (4.16)$$

The precision of this integration depends strongly on the resolution of the grid points, due to the integration limits set by the Heaviside function. I discuss in detail the integration methods I used in the Appendix.

4.3.3 Collision outcomes

The collisional equations can be integrated if the values of $X(\mu, M)$, $Y(\mu, M)$, and $M_{\text{redist.}}(\mu, M)$ are known as a function of the colliding masses. Their values are strongly dependent on the outcome of the collision they originate from, which is determined by the energies of the colliding parent bodies. I show the domains of erosive, interpolated erosive (explained later in the section), and catastrophic collisions as a function of the colliding body masses in Figure 4.4 for collisional

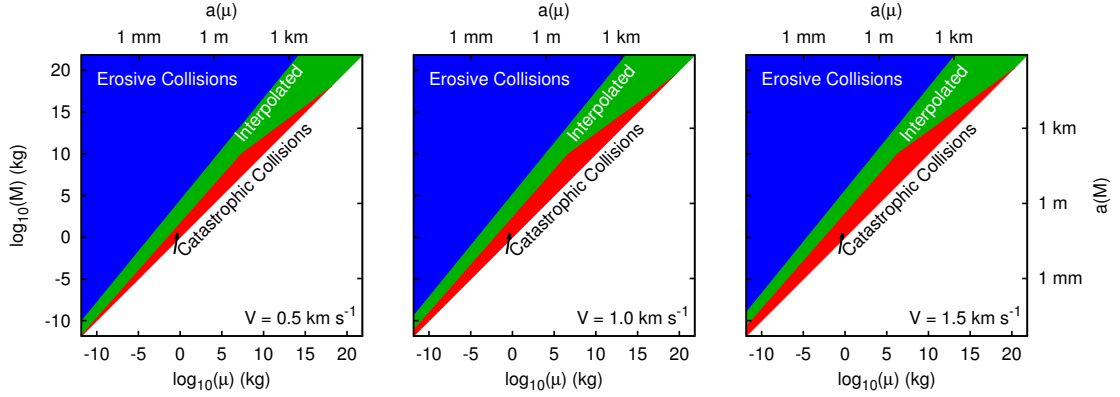


Figure 4.4 The outcome possibilities as a function of colliding masses plotted for collisional velocities of 0.5, 1 and 1.5 km s^{-1} . These collisional velocities roughly correspond to debris ring radii of 100, 25 and 10 AU around an A spectral type star, respectively (see §4.4). I note that higher collisional velocities can occur in some systems.

velocities of $V = 0.5, 1.0$ and 1.5 km s^{-1} . I introduce the method for calculating collisional velocities from orbital velocities in §4.4, but it is a good general approximation that the collisional velocity is roughly an order of magnitude smaller than the orbital velocity. These collisional velocities will then correspond to debris ring radii of 100, 25 and 10 AU around an A spectral type star, respectively.

A collision is considered to be catastrophic if

$$Q(\mu, M)_{\text{impact}} \equiv \frac{\mu V^2}{2M} \geq Q^*(M) , \quad (4.17)$$

where $Q^*(M)$ is the dispersion strength parameter of the target mass M , μ is the projectile mass, and V is the relative velocity of the projectile compared to the parent ring (§4.3.1). I use the dispersion strength description of Benz & Asphaug (1999) and discuss my choice in the Appendix. Note that, in a more accurate treatment, I would redistribute the relative kinetic energy to both masses and

not just to the target mass (i.e., divide by $\mu + M$ instead of M). I am, however, using the original definition of Q_{impact} (as opposed to using the relative kinetic energy) because the $Q^*(M)$ values that I will be comparing it to were defined the same way (Benz & Asphaug, 1999) and this definition makes the problem more tractable numerically. I note that some work has indicated that the tensile strength curve itself may be collision velocity dependent (Holsapple et al., 2002; Stewart & Leinhardt, 2009), which I currently do not take into account.

In catastrophic collisions both particles are completely destroyed. Based on experimental evidence (Fujiwara et al., 1977; Matsui et al., 1984; Takagi et al., 1984; Holsapple et al., 2002), I will assume that apart from the largest fragment $X(\mu, M)$, the total mass is redistributed as a power-law distribution of particles up to a mass that I denote as $Y(\mu, M)$. I calculate the largest single mass created using the relation (Fujiwara et al., 1977)

$$X(\mu, M) = M \frac{1}{2} \left[\frac{\mu V^2}{2MQ^*(M)} \right]^{-\beta_X}. \quad (4.18)$$

At the separatrix between catastrophic and erosive collisions, $Q(\mu, M)_{\text{impact}} = Q_D^*(M)$, and $X(\mu, M) = M/2$, which is exactly what I expect. The β_X factor is measured to be 1.24 by Fujiwara et al. (1977) and this is the fiducial value that I use. Some experiments have shown that the shape and material of the target have an effect on the exact value of β_X (Matsui et al., 1984; Takagi et al., 1984).

The second largest fragment, Y , is always a fraction ($0 < f_Y < 1.0$) of the cratered mass, M_{cr} , in the erosive collision domain up to the erosive/catastrophic collision boundary. In the catastrophic collision domain, Y is a fraction (f_X) of the X fragment. I interpolate f_X from its value defined by f_Y at the separatrix (where $f_Y = f_X$, as $X = M_{\text{cr}}$) to a specified value f_X^{max} at the super catastrophic

collision case of $\mu = M$ as

$$f_X = \exp \left\{ \ln(f_Y) + \ln \left(\frac{f_X^{\max}}{f_Y} \right) \frac{\ln \left[\frac{\mu}{2Q^*(M)MV^{-2}} \right]}{\ln \left[\frac{M}{2Q^*(M)MV^{-2}} \right]} \right\} . \quad (4.19)$$

My fiducial values for these fractions are $f_Y = 0.2$ and $f_X^{\max} = 0.5$. I express the remaining mass in catastrophic collisions as

$$M_{\text{redist}}(\mu, M) = \mu + M - X(\mu, M) , \quad (4.20)$$

which is redistributed as a large number of smaller particles.

I can check the plausibility of the $f_Y = 0.2$ value by taking the asteroid family Eunomia as an example. Its largest member is said to be 70% of the original parent body's (meaning that the collision generating the family was erosive). The asteroid family's largest member is 264 km in diameter, while the second is 116 km (Leliwa-Kopystyński et al., 2009). Assuming equal densities, the second ranked body therefore accounts for 20% of the mass removed from the parent body. Since this is a single case, I cannot be sure that this is a good description in every case.

Erosive collisions are more complicated and less well understood. A collision will be erosive if

$$Q(\mu, M)_{\text{impact}} \equiv \frac{\mu V^2}{2M} < Q_D^*(M) . \quad (4.21)$$

As described in §4.3, an erosive collision will result in a single large fragment, which will be a remnant of the target body, and a distribution of smaller particles. I use the formula of Koschny & Grün (2001a,b), i.e.,

$$M_{\text{cr}} = \alpha \left[\frac{\mu V^2}{2} \right]^b , \quad (4.22)$$

to calculate the total mass cratered from the target, where α and b are constants, with fiducial values of $\alpha = 2.7 \times 10^{-6}$ and $b = 1.23$. This formula is only valid for small cratered masses; it can lead to artificially high values for the cratered

masses (much larger than the target mass) even in the erosive collision domain. When the cratered mass given by this formula is larger than an arbitrarily set fraction f_M of the target mass, I use the following interpolation formula

$$M_{\text{cr}} = M \times \exp \left\{ \ln(f_M) + \ln \left(\frac{0.5}{f_M} \right) \frac{\ln \left(\frac{\mu V^2}{2M} / Q_l \right)}{\ln [Q_D^*(M) / Q_l]} \right\} , \quad (4.23)$$

where

$$Q_l = \left(\frac{f_M}{\alpha} M^{1-b} \right)^{1/b} . \quad (4.24)$$

I choose an arbitrary fiducial value for f_M of 10^{-4} .

In erosive collisions, the single large fragment is expressed as

$$X = M - M_{\text{cr}} . \quad (4.25)$$

As defined before, the largest fragment of the redistributed mass is a fraction f_Y of the cratered mass

$$Y(\mu, M) = f_Y M_{\text{cr}}(\mu, M) , \quad (4.26)$$

while the redistributed mass is

$$M_{\text{redist}}(\mu, M) = \mu + M_{\text{cr}} . \quad (4.27)$$

Thus, the $X(\mu, M)$, $Y(\mu, M)$, and $M_{\text{redist}}(\mu, M)$ parameters can be summarized as

$$X(\mu, M) = \begin{cases} M^{\frac{1}{2}} \left[\frac{\mu V^2}{2M Q^*(M)} \right]^{-\beta_X} & \text{in CC} \\ M - M_{\text{cr}}(\mu, M) & \text{in EC} \end{cases} \quad (4.28)$$

$$Y(\mu, M) = \begin{cases} f_X(\mu, M) X(\mu, M) & \text{in CC} \\ f_Y M_{\text{cr}}(\mu, M) & \text{in EC} \end{cases} \quad (4.29)$$

$$M_{\text{redist}}(\mu, M) = \begin{cases} \mu + M - X(\mu, M) & \text{in CC} \\ \mu + M_{\text{cr}}(\mu, M) & \text{in EC} \end{cases} \quad (4.30)$$

The M_{redist} is redistributed as a large number of smaller particles in both collision types, with a slope of $\gamma = 11/6$ and a scaling given by equation (4.16). I choose a redistribution slope of $\gamma = 11/6$, which is a value close to that given by experimental results (Davis & Ryan, 1990) and is the same as used by Dohnanyi (1969).

I give a list of the variable collisional parameters of my model and their fiducial values in Table 4.1.

4.3.4 The initial distribution and fiducial parameters

I use the Dohnanyi (1969) steady-state solution of $\eta = 11/6$ as the initial distribution, where η is the slope of the initial distribution and yields an initial number density of $n(m) = Cm^{-\eta}$, where C is an appropriate scaling constant for the distribution. The exact value of this slope is unknown for all real systems. Fortunately, the convergent solutions and the timescales of reaching a convergent solution are fairly insensitive to this value.

4.4 Simplified Dynamics

For the smallest particles, which I am particularly interested in modeling, radiation forces lead to effects such as reduced collisional probabilities in thin ring disks and increased collisional velocities in extended disks. In this section, I describe my approximate treatment of these effects.

The radiation originating from the central star effectively modifies the mass of the star seen by the particles; the orbits themselves remain conic sections. I calculate the particle orbits using

$$m\ddot{\mathbf{R}} = F_{\text{rad}}(m) + F_{\text{grav}}(m) = -\frac{[1 - \beta(m)]GM_*m}{R^2} \cdot \frac{\mathbf{R}}{R} \quad (4.31)$$

If $\beta(m) < 1$, then the net force is still attractive, so all conic sections are possible

Table 4.1. The numerical, collisional and system parameters used in my model and their fiducial values

Variable	Description	Fiducial value	Notes
Numerical variable			
δ	Neighboring grid point mass ratio	1.1	§B
System variables			
ρ	Bulk density of particles		Eq. (4.10)
m_{\min}	Mass of the smallest particles in the system		§4.3, Eq. (4.13)
m_{\max}	Mass of the largest particles in the system		§4.3, Eq. (4.13)
M_{tot}	The total mass within the debris ring		§4.3
η	Initial power-law distribution of particle masses		§4.3
R	The distance of the debris ring from the star		Eqs. (4.1, 4.6, 4.7, 4.42, 4.46)
ΔR	The width of the debris ring		Eqs. (4.1, 4.6, 4.42, 4.46)
h	The height of the debris ring		Eqs. (4.1, 4.43)
Sp	The spectral-type of the star		§4.4
Collisional variables			
γ	Redistribution power-law	11/6	Eqs. (4.14, 4.15, 4.16)
β_X	Power exponent in X particle equation	1.24	Eqs. (4.18, 4.28)
α	Scaling constant in M_{cr}	2.7×10^{-6}	Eqs. (4.22, 4.24)
b	Power-law exponent in M_{cr} equation	1.23	Eqs. (4.22, 4.24)
f_M	Interpolation boundary for erosive collisions	10^{-4}	Eqs. (4.23, 4.24)
f_Y	Fraction of Y/M_{cr}	0.2	Eq. (4.19, 4.26, 4.29)
f_X^{\max}	Largest fraction of Y/X at super catastrophic collision boundary ...	0.5	Eq. (4.19)
Θ	Constant in smoothing weight for large-mass collisional probability.	$10^6 m_{\max}$	Eq. (4.48)
p	Exponent in smoothing weight for large-mass collisional probability	16	Eq. (4.48)
Q_{sc}	The total scaling of the Q^* strength curve	1	Eq. (B.1)
S	The scaling of the strength regime of the Q^* strength curve	$3.5 \times 10^7 \text{ erg/g}$	Eq. (B.1)
G	The scaling of the gravity regime of the Q^* strength curve	$0.3 \text{ erg cm}^3/\text{g}^2$	Eq. (B.1)
s	The power exponent of the strength regime of the Q^* strength curve	-0.38	Eq. (B.1)
g	The power exponent of the gravity regime of the Q^* strength curve .	1.36	Eq. (B.1)

as orbital paths. Reaching a hyperbolic orbit is possible as long as the specific orbital energy of a particle,

$$E = \frac{1}{2}mv_{\text{orb}}^2 - \frac{GM_*m}{R} \quad (4.32)$$

is positive, where v_{orb} is orbital velocity. According to equation (4.32), the velocity needed to obtain a positive specific orbital energy is

$$v_{\text{orb}}^2 \geq [1 - \beta(m)] \frac{2GM_*}{R} . \quad (4.33)$$

while the velocity the particle inherits from its parent body is approximately

$$v_{\text{orb}}^2 \approx \frac{GM_*}{R} , \quad (4.34)$$

assuming that both particles that collided were in circular orbits and they collided with a relative velocity significantly smaller than their orbital velocities. From the last two equations we see, that

$$\beta(m) \geq \frac{1}{2} \quad (4.35)$$

is required for a newly created particle to be put on a hyperbolic orbit, which I take as the requirement for radiation force blowout to occur. A more detailed analysis of the energetics can be found in Kresak (1976), Burns et al. (1979), and references therein.

The effects of dynamical evolution on the collisional cascade can be traced to the eccentricity of the orbits. To follow the orbital path of a dust grain that has been created in a collision, I assume that the parent bodies were on circular orbits at radius R and had $\beta(m) \approx 0$. I also assume that the produced grain will be created with very small relative velocity with respect to the parent bodies. The total energy per unit mass of the grain is

$$\frac{E(m)}{m} = -\frac{M_*G}{2R} + \frac{M_*G\beta(m)}{R} . \quad (4.36)$$

The first term of the RHS of the equation gives the total energy per unit mass before the collision (which I assume not to be affected by the radiation force) and the second part gives the decrease in potential energy per unit mass after the break-up. I can also write the total energy per unit mass as

$$\frac{E(m)}{m} = -\frac{M_* G [1 - \beta(m)]}{2a(m)}, \quad (4.37)$$

where $a(m)$ is the semi-major axis of the orbit the particle of mass m will acquire. Equating these two expressions I get

$$a(m) = \frac{1 - \beta(m)}{1 - 2\beta(m)} R. \quad (4.38)$$

As expected, at $\beta(m) = 0.5$ the semi-major axis becomes infinite while at $\beta(m) = 0$ it is equal to the semi-major axis of the colliding particles' original orbit. The eccentricity (e_β) of the orbit can be determined from the fact that the periapsis will equal the original orbital distance

$$a(m) [1 - e_\beta(m)] = R, \quad (4.39)$$

yielding

$$e_\beta(m) = \begin{cases} \beta(m) / [1 - \beta(m)] & \text{if } \beta \leq 0.5 \\ > 1 & \text{if } \beta > 0.5 \end{cases}. \quad (4.40)$$

At $\beta(m) = 0.5$, the eccentricity equals 1, and at $\beta(m) = 0$, it equals zero, consistent with my expectations. Similar derivations can be found elsewhere (e.g., Harwit, 1963; Kresak, 1976). A particle on an eccentric orbit will have a modified probability of interaction with other particles in the parent ring, which I address in §4.4.2.

4.4.1 Collisional velocities

Lissauer & Stewart (1993) give the velocity of a planetesimal relative to the other

planetesimals in the swarm (i.e., the collisional velocity), averaged over an epicycle and over a vertical oscillation as

$$V = v_{\text{orb}} \sqrt{\frac{5}{4} \left(\frac{e}{2}\right)^2 + \left(\frac{i}{2}\right)^2}, \quad (4.41)$$

where e is the maximum eccentricity and i is the maximum inclination in the system. This equation is valid for a swarm of particles in Rayleigh distributed equilibrium. This condition is true for a system in quasi-collisional equilibrium. I use this equation to estimate the collisional velocity of all particles, setting

$$e = \frac{\Delta R}{2R} \quad (4.42)$$

and

$$i = \frac{h}{2R}. \quad (4.43)$$

The smallest particles that are in highly eccentric orbits will have varying velocities along their trajectories. However, when at their periapsis, they will have their original orbital velocities, as by definition they are on eccentric orbits due to their original periapsis velocity. Because of this, in the simplified dynamical treatment I only use a single collisional velocity for all particles, which is described by equation (4.41).

4.4.2 Reduced collisional probabilities of β critical particles

Particles with $\beta(m)$ less than 0.5, but which are still non-zero, called β critical particles, are thought to produce halos around debris disks via the highly eccentric orbits radiation forces place them on (Thébault & Wu, 2008; Müller et al., 2010).

For a particle to go into an eccentric orbit, it must acquire a radial velocity component that is different than zero. In collisions, fragments will be ejected in all directions with a certain velocity distribution. Since the smallest fragments will tend to escape with the highest velocities (e.g., Jutzi et al., 2010), it is a fair

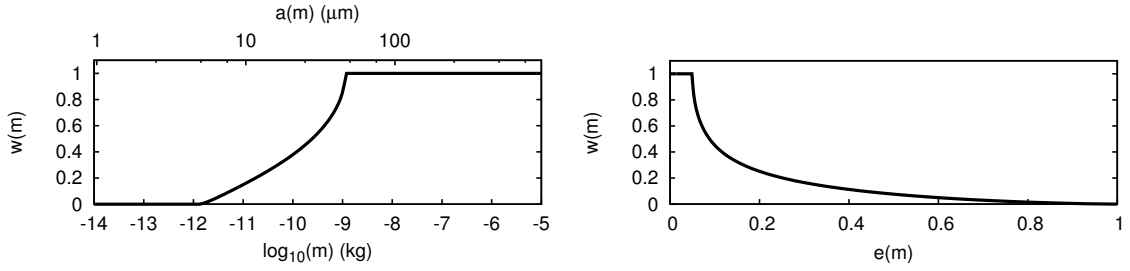


Figure 4.5 *Left Panel:* The weighted collisional probabilities of particles as a function of their mass m (and size). *Right Panel:* The weighted collisional probabilities of particles as a function of their eccentricity e . The particles are assumed to be within a narrow ($dR/R = 0.1$) ring at 25 AU from an A0 spectral-type star.

question to ask whether thermalization of velocity vectors and their high values is a stronger effect in placing dust particles on higher eccentricity orbits compared to radiation effects that reduce the effective stellar mass.

To answer this question, I need to examine the origin of the particles that contribute to the increase of the differential density in each mass grid point. I calculate T_{II} only integrating in μ space, thus calculating the rate of increase of the differential number density of particles with mass m that originate from collisions with a target of mass M . My calculations show that there is a pronounced peak from M masses roughly on the same scale (at most one order of magnitude higher) as m itself. Most particles originate from targets $\sim 3 - 5\times$ larger in size than the particle itself. The results of Jutzi et al. (2010) clearly show that the velocities acquired by collision fragments at $1/3$ sizes are more than an order of magnitude lower than the collisional velocities, meaning that, in the most extreme case, a fragment will receive up to a few tenths of a km s^{-1} radial velocity compared to its $10\text{-}30 \text{ km s}^{-1}$ orbital velocity. I can thus safely say that particles

that are created with $\beta(m)$ values similar to 0.5 tend to be placed on eccentric orbits by the radiation forces rather than being dispersed. These orbits will extend out from the initial debris disk ring, shielding the particles from being destroyed and from them creating other particles.

My approach to calculating a weighting factor for each particle mass, determined by the fraction of its orbital period it spends in the parent ring is similar to that of Thébault & Wu (2008). The orbital time of a particle in an elliptical orbit as a function of its distance from the center of mass is (Taff, 1985)

$$\cos^{-1} \left(\frac{a-l}{ae_\beta} \right) - e_\beta \sqrt{1 - \left(\frac{a-l}{ae_\beta} \right)^2} = (t - t_0) \sqrt{\frac{GM}{a^3}}, \quad (4.44)$$

where $t_0 = 0$ is the initial time at periapsis, l is its distance at time t from the center of mass, and I omit the m dependences of e_β and a for clarity. I estimate the semi-major axis as

$$a = \frac{R - \Delta R/2}{1 - e_\beta}, \quad (4.45)$$

and I calculate the time Δt needed for a particle to reach the outer edge of the disk at $l = R + dR/2$. Dividing Δt by the half of the orbital period gives the weighting factor for each mass m as

$$w = \frac{1}{\pi} \left\{ \cos^{-1} \left[\frac{\Delta R (2 - e_\beta) - 2Re_\beta}{e_\beta (\Delta R - 2R)} \right] - 2 \sqrt{\frac{\Delta R (e_\beta - 1) (\Delta R - 2Re_\beta)}{(\Delta R - 2R)^2}} \right\} \quad (4.46)$$

I plot these weighting factors as a function of the particle mass and orbital eccentricity in Figure 4.5. When analyzing the particle distributions, I only plot the number of particles within the parent ring, which I calculate as

$$n_{\text{ring}}(m) = n(m)w(m). \quad (4.47)$$

4.4.3 Reduced collisional probabilities of the largest particles

The very last grid point in the domain of solution will only reduce its number density, as it cannot gain from larger masses. The lack of a positive term for the

Table 4.2. Parameters used for comparison models

Variable	Comparison to Thébault (2003)	Comparison to Löhne (2008)
ρ (kg m ⁻³)	2700	2500
m_{\min} (kg)	1.42×10^{-21}	1.42×10^{-21}
m_{\max} (kg)	1.78×10^{18}	4.20×10^{18}
M_{tot} (M _⊕)	0.0030221	1.0
η	11/6	1.87
R (AU)	5	11.25
ΔR (AU)	1	7.5
h (AU)	0.5	3.4
Sp	A0	G5
PRD	off	off

last grid point causes its evolution time to become very small compared to all others and leads to a numerical instability. In order to avoid this, I multiply the collisional rates with a weight that smooths to zero for the largest particles

$$\sigma_w(m) = \left[\frac{1 - \exp\left(-\frac{m_{\max} - m}{\Theta}\right)}{1 - \exp\left(-\frac{m_{\max}}{\Theta}\right)} \right]^p, \quad (4.48)$$

for both the projectile and target particle. I chose Θ to be a number a few orders of magnitude larger than m_{\max} and use an arbitrary $p = 16$. The modified collisional rates, therefore, read

$$P(m, m') = V \pi \kappa n(m) n(m') w(m) w(m') \times \sigma_w(m) \sigma_w(m') \left(m^{\frac{1}{3}} + m'^{\frac{1}{3}} \right)^2. \quad (4.49)$$

I discuss the implications of the choice of the weight function and of its parameters in §4.5.2.

4.5 Results

As I discussed in §4.2, collisional cascades in debris disks have been studied extensively in the past decades, with many different analytic and numerical solu-

tions to the problem. To demonstrate the similarities and differences between my model and some earlier ones, I show in the following subsection the results of a few comparison tests. The system variables used by my code for these runs are summarized in Table 4.2.

I compare my numerical model to three previous well known algorithms, the particle-in-a-box code of Thébault et al. (2003), the dynamical code `ACE` (Krivov et al., 2000, 2005; Löhne et al., 2008; Müller et al., 2010), and the 1D steady-state solver code of Wyatt et al. (2011). Although I do make an effort to model their systems as accurately as possible, a true benchmark between the codes is impossible. This is due in part to the fact that all models have somewhat different collisional and dynamical prescriptions.

4.5.1 Comparison to Thébault et al. (2003)

A relatively straightforward comparison can be made between `CODE-M` and the Thébault et al. (2003) model. Although the initial Thébault et al. (2003) model has been subsequently improved in Thébault & Augereau (2007), I chose to compare my results with the former, as they are both particle-in-a-box approaches to the collisional cascade, with some dynamical effects included in a simplified manner.

Thébault et al. (2003) aimed to model the inner 10 AU region of the β Pictoris disk, with their reference model being a dense debris ring at 5 AU, with a width of 1 AU and height of 0.5 AU. I adopted their largest particle size of 54 km for the comparison run. However, I adopted a smaller minimum particle size than they did (in my case well below the blowout size), to be able to follow the removed particles more completely. This treatment does not have effects on the actual distribution within the ring. I also had Poynting-Robertson drag turned off. Although both of our models include erosive (cratering) collisions, the Thébault et al. (2003) prescription uses hardness constants (α) of much softer material than

that of my nominal case and a linear relationship between cratered mass and impact energy (the prescription for erosive collisions has been changed in their later paper Thébault & Augereau 2007). For a better agreement, I also model a modified cratered prescription case, where I set $b = 1$, $\alpha = 10^{-4}$ and $f_M = 0.01$. With these adjustments our cratering prescriptions agree better; however my interpolation formula is offset compared to Thébault et al. (2003). While ours has a continuous prescription at the CC/EC boundary (i.e., the cratered mass is $0.5M$), the Thébault et al. (2003) interpolation does not (i.e., the cratered mass is $0.1M$).

Figure 4.6 compares the evolution of the distribution of particles between the Thébault et al. (2003) nominal case and my runs. In the vertical axes I plot $n(m) \times m^2$, which is similar to the “mass/bin” value used by Thébault et al. (2003). To make them exact, I divide the Thébault et al. (2003) values by $(\delta-1)$, which places them on the same scale. A few similarities and a few significant differences can be noted. Generally both models show wavy structure - which is a well studied phenomenon (see e.g., Campo Bagatin et al., 1994; Wyatt et al., 2011) - but the exact structure of the waves differs.

My modified erosive (cratering) prescription model gives a much better agreement with the Thébault et al. (2003) results than my fiducial prescription, in the sense that it yields a deeper first wave in the distribution with a larger wavelength. The offset between the locations of the first dip and the subsequent peak in the two models could likely result from the higher collisional velocities that Thébault et al. (2003) calculate for the smallest particles. My modified erosion prescription gives a good agreement with the Thébault et al. (2003) results for particles larger than a km in size, which is a surprise as the Thébault et al. (2003) erosive constants are for much softer materials than my nominal values are for. Just above the blow-out regime my model becomes abundant in dust particles,

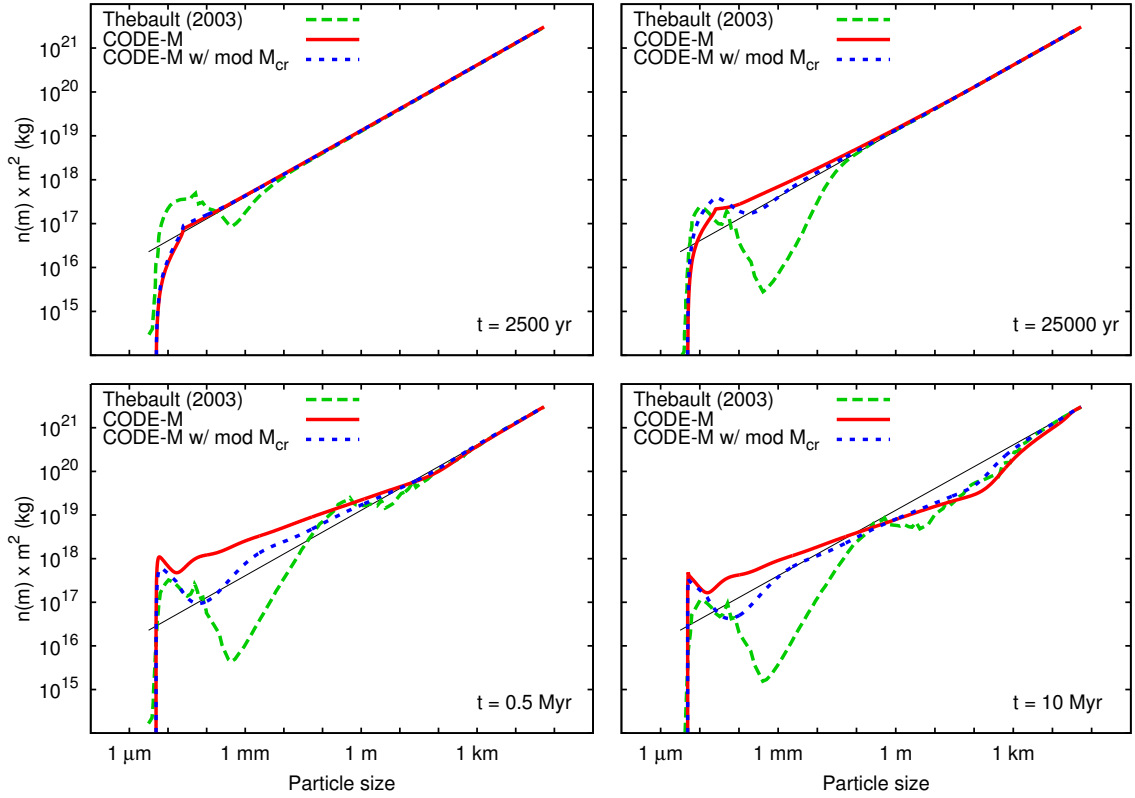


Figure 4.6 Comparison of the evolution of the dust distribution around the β Pictoris disk modeled by Thébault et al. (2003) and the model presented in this work. The thin solid line is the initial distribution. The modified cratered mass (M_{cr}) model uses an erosive collision prescription that is a closer analog to the original Thébault et al. (2003) soft material one. See text for more details.

as more and more dust is placed on highly eccentric orbits. Although some smoothing is expected in reality, I do expect the number of dust particles near the blowout limit to increase.

While both my distributions show the typical double power-law feature of quasi steady-state collisional cascades (see e.g., Wyatt et al., 2011) above and below the change in the strength curve, it is masked in the Thébault et al. (2003)

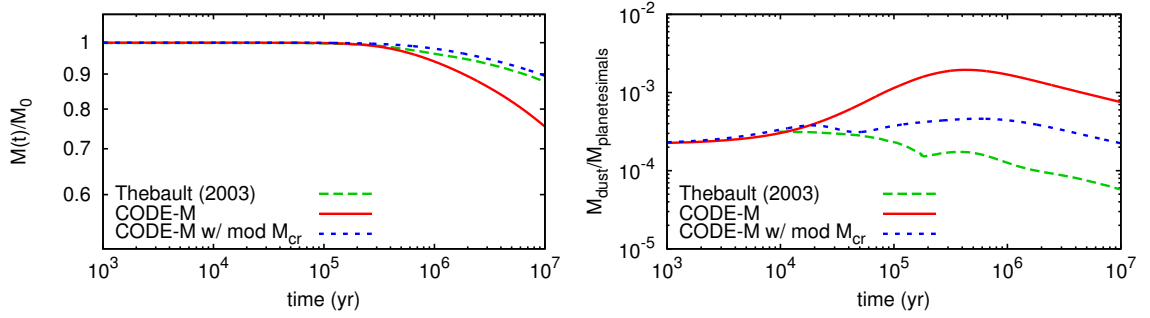


Figure 4.7 Comparison of the evolution of the total disk mass and the dust-to-planetesimal mass ratio around the β Pictoris disk modeled by Thébault et al. (2003) and the models presented in this work. The modified cratered mass (M_{cr}) model uses an erosive collision prescription that is a closer analog to the original Thébault et al. (2003) one. See text for more details.

model, due to the high amplitude wavy structures.

In Figure 4.7, I show the differences in the evolution of the disk mass between the nominal case of Thébault et al. (2003) and my models. The left panel shows the evolution of the total disk mass within the debris ring, while the right panel shows the evolution of the dust-to-planetesimal mass ratio. These figures are equivalent to Thébault et al. (2003) figures 2 and 3 (except that these are in plotted in logarithmic scales). My nominal model predicts a faster decay of the total disk mass, reaching 25% mass loss, while the modified erosive prescription agrees with the Thébault et al. (2003) model and loses $\sim 12\%$ of its initial mass. The evolution of the dust-to-planetesimal disk mass differs while the quasi steady-state is being reached, after which all models decay with the same slope. My nominal case model has an order of magnitude larger dust-to-planetesimal mass ratio at all times compared to the Thébault et al. (2003) model, while my modified erosive collision prescription case is close to it.

There are some easily identified differences between our models. Thébault et al. (2003) use the same Benz & Asphaug (1999) dispersive strength curve as I do, although they do average it to account for impact angle variations. This is an unnecessary step, as the Benz & Asphaug (1999) strength curve is already impact angle averaged, and is corrected in Thébault & Augereau (2007). However, I find that this scaling offset does not have a significant effect on the outcome of the distribution evolution. Thébault et al. (2003) use a double power-law for fragment redistribution, while I use only a single power-law. In Chapter 5, I will show that varying the slope of the single power-law does not have a significant effect on the evolution of the distribution either, so it appears that this difference is also likely not a significant contributing factor to our discrepancies. A noteworthy difference between our models is that Thébault et al. (2003) calculate fragment re-accumulation, while I do not. This is a possible explanation for our discrepancies at high masses, and the offsets I have in the total mass decay.

The most significant difference between the models is that ours uses a single interaction velocity, while Thébault et al. (2003) model the interaction velocity between the β critical elliptical orbit smallest particles and the parent ring. This is likely to account for some of the additional offsets for the smallest particles, as higher interaction velocities have been shown to initiate higher amplitude waves (Campo Bagatin et al., 1994; Wyatt et al., 2011). Thébault et al. (2003) also take into account the constant presence of particles smaller than the blowout limit within the parent ring, which I do not. Within denser disks this step may smooth out any features near the blowout limit.

4.5.2 Comparison to Löhne et al. (2008) and Wyatt et al. (2011)

As introduced in §4.2, the numerical code ACE (Krivov et al., 2000, 2005, 2006, 2008; Löhne et al., 2008; Müller et al., 2010) solves the dynamical evolution of the

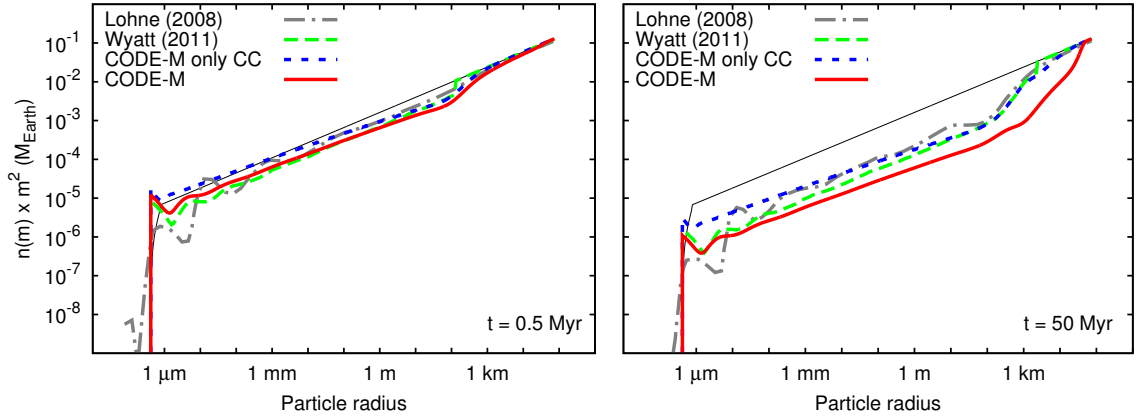


Figure 4.8 Comparison of the evolution of the particle distribution within a debris disk around a solar-type star modeled by Löhne et al. (2008), Wyatt et al. (2011) and the code presented in this work. The "only CC" CODE-M model uses only catastrophic collisions. The thin solid line is the initial distribution. See text for more details.

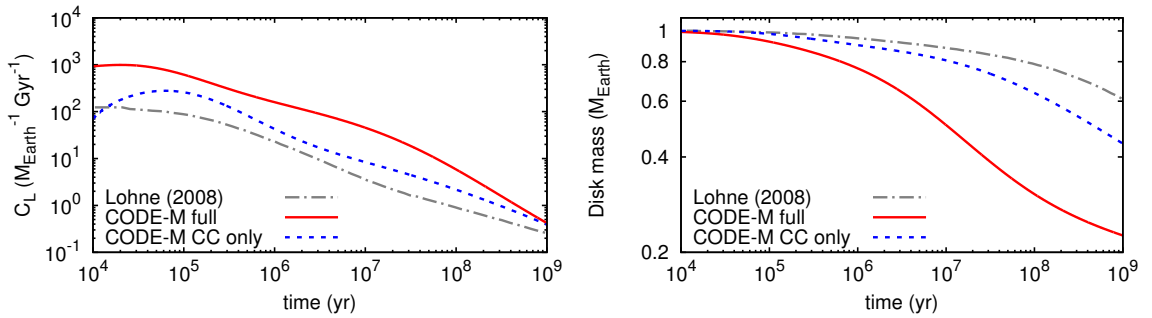


Figure 4.9 Comparison of the evolution of the dust mass within a debris disk around a solar-type star modeled by Löhne et al. (2008) and the model presented in this work. See text for details.

collisional system as well as the collisional fragmentation, thus a straight comparison to CODE-M cannot be performed. I use their `ii-0.3` model (Löhne et al.,

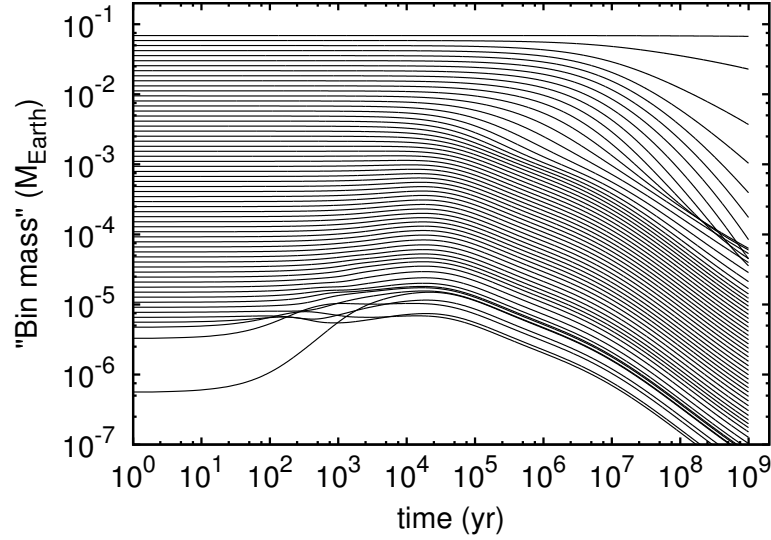


Figure 4.10 Evolution of the total mass within consecutive mass regions from the smallest to the largest particles in the system for the full collisional system, using the $\alpha=0.3$ parameters of Löhne et al. (2008). The plot can be compared to the top panel of Figure 4. of Löhne et al. (2008).

2008) for comparison, which is for a relatively wide (7.5-15 AU), extremely dense ($1 M_{\oplus}$ total mass with a largest planetesimal size of 74 km) debris ring. I turned off the effects of Poynting-Robertson drag for this comparison model. The initial parameters I assumed are summarized in Table 4.2. This same system was modeled by Wyatt et al. (2011), whose results I also use for comparison.

In Figure 4.8, I show the evolution of the dust distribution of the system given by CODE-M, ACE, and Wyatt et al. (2011). As the version of ACE used in Löhne et al. (2008) only modeled catastrophic collisions and the Wyatt et al. (2011) model uses catastrophic collision rates, I also include a CODE-M run in the plot that only models the outcomes of catastrophic collisions. Since the Löhne et al. (2008) values are already downscaled by $(\delta - 1)$, no additional scaling was required of their

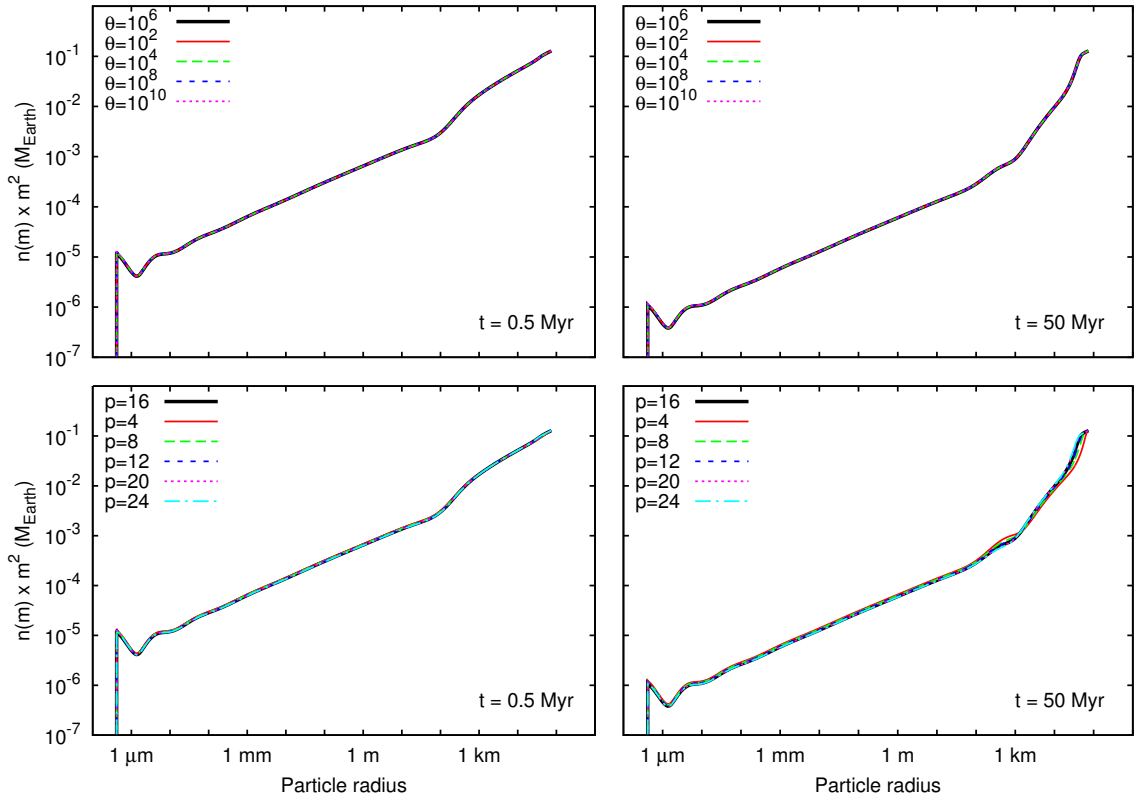


Figure 4.11 Comparison of the evolution of my model distribution using the Löhne et al. (2008) $\alpha=0.3$ parameters, when varying the parameters of the weights in the collision cross sections for large particles.

data. The Wyatt et al. (2011) data points are divided by $\delta - 1 = 0.0626$ to convert them to differential number densities. Qualitatively, all distributions agree much better than in the Thébault et al. (2003) comparison (Figure 4.6); however, there is some scaling offset between the full CODE-M and the other models, especially at large masses.

The wavelengths of the waves roughly agree between CODE-M and ACE, with the single difference being the absence of the strong offset of the first crest in my model; the agreement is also good between CODE-M and Wyatt et al. (2011).

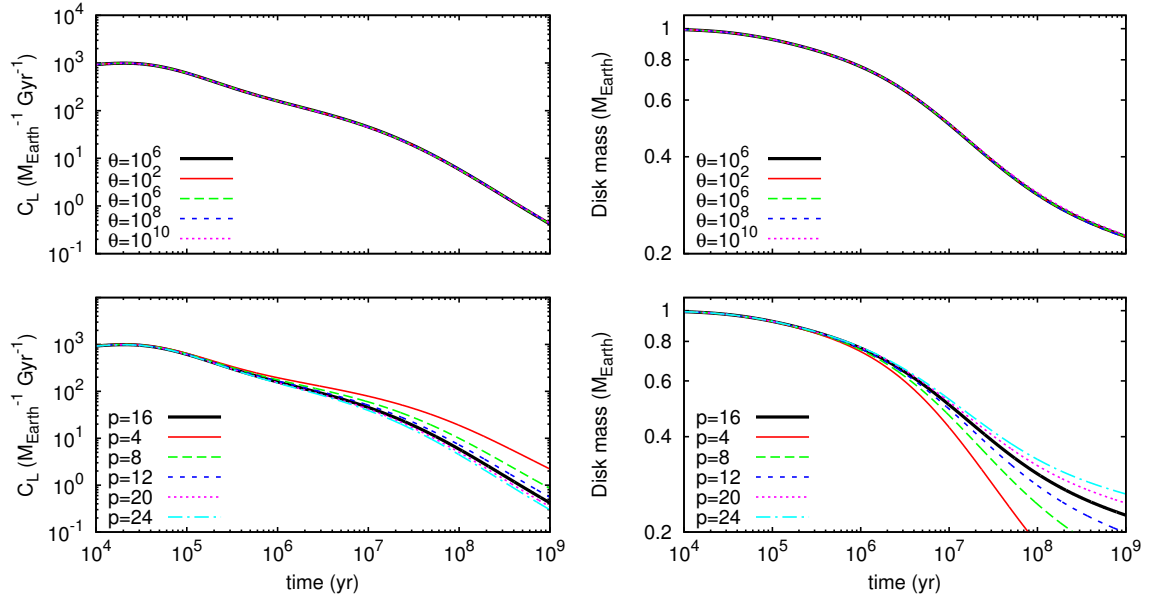


Figure 4.12 The change in the dust mass evolution when varying the parameters of the weights in the collision cross sections for large particles.

The double power-law distribution due to the change from strength to gravity dominated thresholds in the strength curve (Benz & Asphaug, 1999) can be distinguished in all three models, with roughly the same slopes. The ACE and the Wyatt et al. (2011) models maintain their initial -1.87 number density distribution slope, while CODE-M becomes somewhat steeper for the smallest particles.² My catastrophic-collision-only model has a smaller amplitude and wavelength wave structure than my full model or the other models. The most significant difference between the models is the scaling offset of the full CODE-M model, which I analyze below.

In Figure 4.9, I show a comparison to figures 1 and 2 of Löhne et al. (2008). In the left panel I show the evolution of C_L ($C_{\text{Löhne}}$), which is introduced in Equation

²In Figure 4.8, I plot in the y-axis the product $n(m)m^2$, so that a steeper number density slope will show up as a flatter distribution.

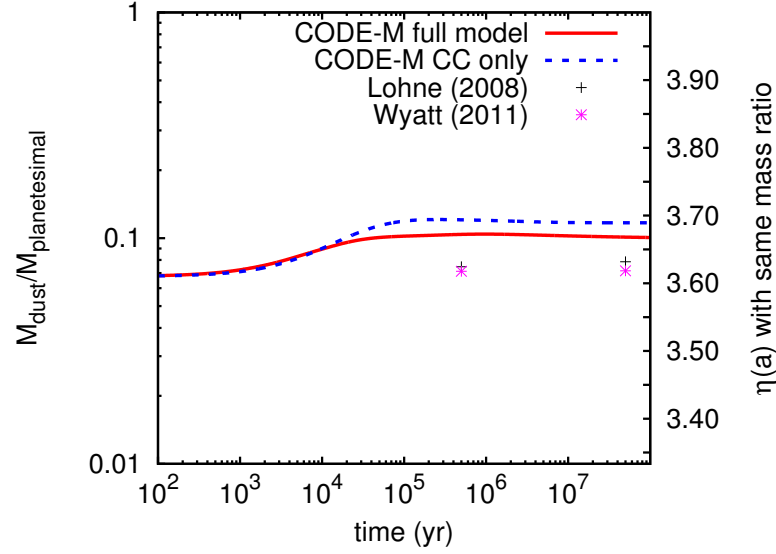


Figure 4.13 The evolution of the dust-to-planetesimal mass ratio of the CODE-M models and the values for the Löhne et al. (2008) and Wyatt et al. (2011) models at 0.5 and 50 Myr. I calculate the dust mass from 0.1 mm to 10 cm and the planetesimal mass from 10 cm to 100 m. On the right vertical axis I give the value of the slope of the power-law distribution that would give the same dust-to-planetesimal mass ratio.

(11) of Löhne et al. (2008) as

$$C_L = -\frac{\dot{M}_{\text{disk}}}{M_{\text{disk}}^2}, \quad (4.50)$$

This quantity is inversely proportional to the characteristic timescale of the system. As expected, since my system evolves faster, its characteristic timescale is shorter, so the C_L factor for my models is larger. This can be seen in the right panel as well, where I plot the decay of the total mass in my system and that given in figure 2 of Löhne et al. (2008). I adopted the exact strength curve of Löhne et al. (2008) in this run of my model, with the corrections given by Wyatt et al. (2011).

In Figure 4.10, I show a comparison to the top panel of figure 4 in Löhne et al. (2008), which shows the evolution of the total mass within each of their mass bins. In this plot, I show the evolution of the full collisional system, which includes erosive and catastrophic collisions. Since I do not use mass bins, but rather a differential number density gridding, I integrate the distribution between 14 grid points for each mass value, which roughly corresponds to a single mass bin of Löhne et al. (2008). Up to roughly a few hundred meters in size (where the strength curve has its minimum) all mass “bins” decay in close parallel slopes to each other after reaching their quasi steady-state around 10,000 yr. This is in contrast to the Löhne et al. (2008) results and agrees more with figure 2 of Wyatt et al. (2011), who model the same system. The intermediate size planetesimals (\sim km) show a steeper decay than that modeled by either Löhne et al. (2008) or Wyatt et al. (2011).

The obvious difference between `ACE` and `CODE-M`, is that `ACE` also evolves the dynamics in the system and takes into account the varying collisional velocities in the system from particles that are in elliptical orbits within the parent ring. This could easily explain the offset of the first wave given by `ACE` in Figure 4.8.

The increasing offset between the full `CODE-M` run and the other two models is likely due to the absence of erosive collisions by Löhne et al. (2008) and to using catastrophic collision rates in Wyatt et al. (2011). Kobayashi & Tanaka (2010) have shown earlier erosive (cratering) collisions to be the dominant effect for mass loss in collisionally evolving systems. This effect is demonstrated by the `CODE-M` model I run with only catastrophic collisions included, which scales exactly with the `ACE` and Wyatt et al. (2011) models. Since `CODE-M` does not include aggregation, the collisions of the smallest particles with the largest bodies is not modeled perfectly. I assume the realistic distribution decay to lie between

the two models given by `CODE-M`.

As introduced in §4.4.3, I artificially reduce the collision cross section of the largest particles in the system to zero in order to avoid numerical instabilities. However, as this is a completely arbitrarily defined numerical necessity, I investigate its effects on the total mass decay, where I expect it to be the strongest. I reproduce Figures 4.8 & 4.12, but with varying the values of Θ and p in the smoothing function, in Figures 4.11 & 4.12. As can be seen in these plots, the variable Θ does not affect either the evolution of the distribution or the total mass decay, as long as it is larger than one. Varying the values of p does have an effect on both the evolution of the distribution and the total mass decay. The effect is only on the largest bodies in the system; below a size of one hundred meters, the shapes of the distributions remain unchanged, with the only differences being scaling offsets.

Visual examination of the distributions in Figure 4.9 hint at a slightly steeper distribution slope for the `CODE-M` models than the Löhne et al. (2008) and Wyatt et al. (2011) ones. Since the distributions have wavy structures in them, this is difficult to show with a slope fit. Therefore, I calculate the dust-to-planetesimal mass ratios of the distributions. I define the dust sizes to be from 0.1 mm to 10 cm and the planetesimal sizes to be from 10 cm to 100 m. In Figure 4.13, I plot the evolution of the mass ratios of my models and the mass ratios for the Löhne et al. (2008) and Wyatt et al. (2011) models at 0.5 and 50 Myr. My models have significantly higher mass ratios than theirs. This is likely a result of the differences between our collisional equations.

4.6 Conclusions

In this chapter, I present a numerical model of the evolution of the distribution of dust in dense debris disks. I calculate my model with a new numerical code, `CODE-M`, which I extensively verify and test in the Appendix. I compare my code to the previously published numerical models of collisional cascades in debris disks, showing general agreement. Unlike previous codes, which include features such as a detailed treatment of particle dynamics and extended debris disks, `CODE-M` only models rings but with improved fidelity in this situation, because I solve the full scattering integral and use solvers that achieve high numerical accuracy.

My model shows faster decays than previously published ones (Thébault et al., 2003; Löhne et al., 2008; Wyatt et al., 2011) and also yields slightly higher dust-to-planetesimal mass ratios. I attribute these characteristics to be a result of the accurate treatment of collisional cascades.

CHAPTER 5

STEEP DUST-SIZE DISTRIBUTIONS

In this chapter, I explore the evolution of the mass distribution of dust in collision-dominated debris disks, using the collisional code introduced in the previous chapter. I analyze the equilibrium distribution and its dependence on model parameters by evolving over 100 models to 10 Gyr. With numerical models, I show that systems reach collisional equilibrium with a mass distribution that is steeper than the ones given by earlier analytic or current numerical methods. My model yields a steady state slope of $n(m) \sim m^{-1.88}$ [$n(a) \sim a^{-3.65}$]. This steeper solution has observable effects in the submillimeter and millimeter wavelength regimes of the electromagnetic spectrum. I assemble data for nine debris disks that have been observed at these wavelengths and, using a simplified absorption efficiency model, show that the predicted slope of the particle mass distribution generates SEDs that are in agreement with the observed ones.

5.1 Introduction

The total mass within debris disks as well as the infrared excess emission produced by their dust are generally calculated assuming the analytic estimate of the distribution of masses in the asteroid belt by Dohnanyi (1969). This solution predicts that the sizes follow a power-law, with their numbers increasing with decreasing size a as $n(a) \sim a^{-3.5}$. However, a number of recent efforts to model observations of debris disks have found it necessary to adopt steeper slopes (Krist et al., 2010; Golimowski et al., 2011).

Durda & Dermott (1997) showed that a steep tensile strength curve, i.e., the function that gives the minimum energy required to disrupt a body catastrophically,

cally (see, e.g., Holsapple et al., 2002; Benz & Asphaug, 1999; Gáspár et al., 2011), results in a steeper steady-state distribution than the traditional solution. Collisional models of the dust in circumstellar disks (Thébault et al., 2003; Krivov et al., 2005; Thébault & Augereau, 2007; Löhne et al., 2008; Müller et al., 2010; Wyatt et al., 2011) have also shown that the dust particles will settle with a distribution $n(a) \sim a^{-3.61}$, on top of which additional structures appear. This steeper distribution has readily observable effects at the far-IR and submm wavelengths. It also results in higher total dust mass and lower planetesimal mass estimates for the systems.

In this chapter, I investigate the slope of the mass distribution and the physical parameters that influence it with the numerical code, introduced in Chapter 4. My code has been developed to calculate the evolution of the particle mass distribution in collisional systems, taking into account both erosive and catastrophic collisions. In §5.2, I introduce models for the numerical analysis of the collisional cascades and give my findings. In §5.3, I generate a set of synthetic spectra in order to analyze the effects certain distribution parameters have on different parts of the SEDs. In §5.4, I introduce a simple relation between the Rayleigh-Jeans part of the spectral energy distributions and the particle size distribution. In §5.5, I compare the results to the observed far-IR and sub millimeter data for nine sources.

5.2 Numerical modeling

In this section, I analyze the steady-state dust distribution with the full numerical code. I run a set of numerical models to study the evolution of the slope of the steady-state distribution function and its dependence on the model parameters. I investigate the time required for the distribution to settle into its steady-state

and, with a wide coverage of the parameter space, I also examine the robustness of the solution.

5.2.1 Evolution of the reference model

I set up a reference debris disk as a basis for comparison to all other model runs. This model consists of a moderately dense debris disk situated at 25 AU around an A0 spectral-type star, with a width and height of 2.5 AU. This radial distance ensures a moderate evolution speed, but with a peak emission in the mid-infrared. It also guarantees a Rayleigh-Jeans tail in the far-infrared regime, which is the primary imaging window for the *Herschel Space Telescope*. The total mass in the debris disk is $1 M_{\oplus}$, distributed within minimum and maximum particle masses that correspond to radii of 5 nm and 1000 km, when assuming a bulk density of 2.7 g cm^{-3} . I summarize the disk parameters of the reference model in Table 5.1. I evolve the reference model for 10 Gyr.

In Figure 5.1, I show the evolution of the particle distribution, plotting it at six different points in time up to 10 Gyr. I plot $\log_{10} [n(m) \times m^2]$ on the vertical axis, which can be related to the “mass/bin” that is frequently used in other simulations. Even though the number densities decrease with increasing particle masses, the mass distribution increases towards the larger masses in this representation, as long as the mass distribution slope is smaller than 2.

The smallest particles reach collisional equilibrium first, roughly at 1 Myr, followed by larger particle sizes as the system evolves. After 50-100 Myr of evolution, the upper, gravity dominated part of the distribution ($m > 10^{13} \text{ kg}$) also reaches equilibrium. The distribution maintains its slope for masses below 10^{10} kg , which roughly corresponds to a planetesimal radius of 100 m. The kink in the distribution at the upper end is due to the change in the strength curve slope (O’Brien & Greenberg, 2005; Bottke et al., 2005).

Table 5.1. Numerical, Collisional, and System parameters of the reference model

Variable	Description	Fiducial value
System variables		
ρ	Bulk density of particles	2.7 g cm^{-3}
m_{\min}	Mass of the smallest particles in the system	$1.42 \times 10^{-21} \text{ kg}$
m_{\max}	Mass of the largest particles in the system	$1.13 \times 10^{22} \text{ kg}$
M_{tot}	Total mass within the debris ring	$1 M_{\oplus}$
η_0	Initial power-law distribution of particle masses	1.87
R	Distance of the debris ring from the star	25 AU
ΔR	Width of the debris ring	2.5 AU
h	Height of the debris ring	2.5 AU
Sp	Spectral-type of the star	A0
Collisional variables		
γ	Redistribution power-law	11/6
β_X	Power exponent in X particle equation	1.24
α	Scaling constant in M_{cr}	2.7×10^{-6}
b	Power-law exponent in M_{cr} equation	1.23
f_M	Interpolation boundary for erosive collisions	10^{-4}
f_Y	Fraction of Y/M_{cr}	0.2
f_X^{\max}	Largest fraction of Y/X at super catastrophic collision boundary ...	0.5
Q_{sc}	Total scaling of the Q^* strength curve	1
S	Scaling of the strength regime of the Q^* strength curve	$3.5 \times 10^7 \text{ erg/g}$
G	Scaling of the gravity regime of the Q^* strength curve	$0.3 \text{ erg cm}^3/\text{g}^2$
s	Power exponent of the strength regime of the Q^* strength curve ...	-0.38
g	Power exponent of the gravity regime of the Q^* strength curve	1.36
Numerical parameters		
δ	Neighboring grid point mass ratio	1.104
Θ	Constant in smoothing weight for large-mass collisional probability	$10^6 m_{\max}$
P	Exponent in smoothing weight for large-mass collisional probability	16

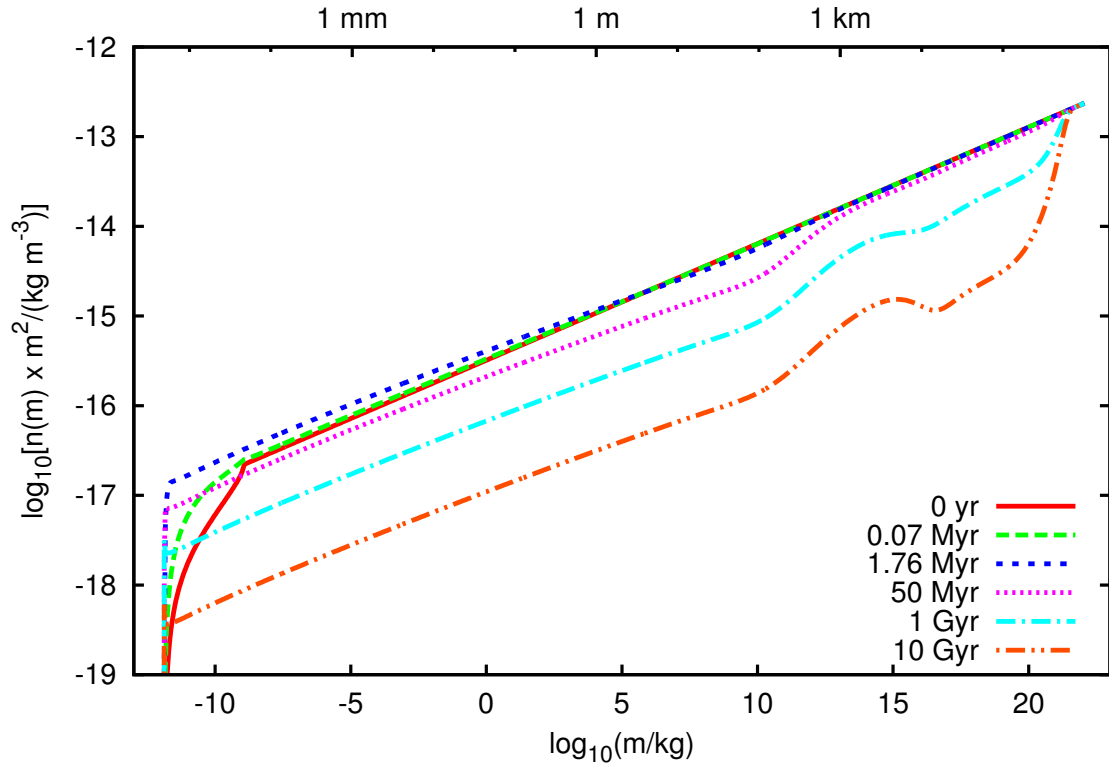


Figure 5.1 Particle mass distribution of the reference model plotted at various points in time.

Structures in the distribution slope, such as waves, may in principle occur at the low-mass end when assuming softer material properties or higher collision velocities. The distribution may also acquire some curvature (see Chapter 4). Because of these effects, I evaluate the average slope of the distribution by fitting a power-law over a large mass range, but one that remains below the kink in the distribution. Specifically, I fit the distribution between masses 10^{-8} and 10^4 kg, which roughly correspond to sizes of 0.1 mm and 1 m.

I examine the dependence of the steady-state distribution slope on the ad hoc initial conditions parametrized by the initial mass-distribution slope η_0 and the

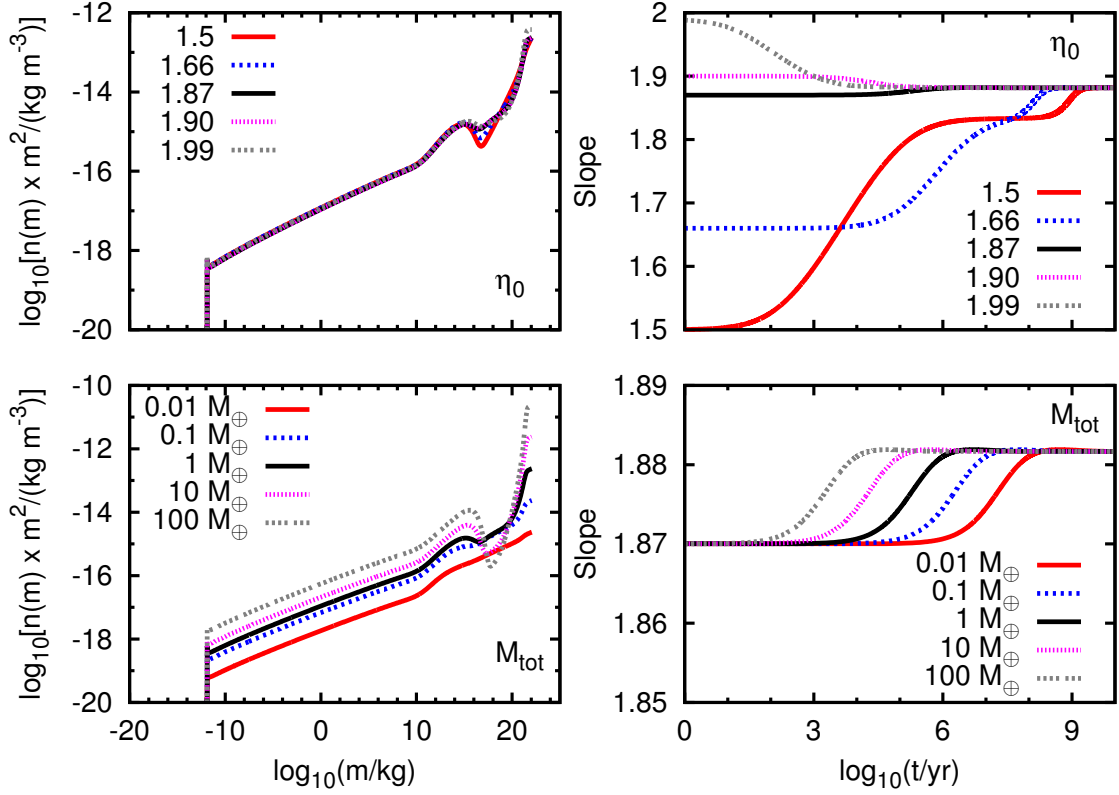


Figure 5.2 (*Left panels*) Particle mass distribution at 10 Gyr, when varying the initial mass distribution slope (top) and the total mass of the system (bottom). (*Right panels*) Evolution of the dust-mass distribution slopes when varying the initial mass distribution slope (top) and the total mass of the system (bottom). The steady-state distribution slope is practically independent of these initial conditions.

initial total mass in the disk M_{tot} . In Figure 5.2, I show the evolution of the particle mass distribution and its slope as a function of these parameters. The left panels show the dust distribution after 10 Gyr of evolution for different values of the two parameters, while the right panels show the evolution of the dust-mass distribution slope. The top right panel shows the evolution of the dust distribution

slope for varying initial mass-distribution slopes. Variations in η_0 do not affect the final dust distributions, although the high mass end evolves differently or reaches equilibrium at different timescales. A distribution with less dust initially ($\eta_0 < 1.87$) also takes more time to reach equilibrium. A shallow distribution with an initial slope of $\eta_0 = 1.5$ takes as much as ~ 1 Gyr to reach equilibrium, although such initial distribution slopes are unlikely. As shown by Löhne et al. (2008), the evolution of the particle mass distribution is scalable by the total mass (or number densities of particles), which is what we see in the bottom two panels of Figure 5.2. All systems with different initial masses reach the same equilibrium mass distribution, but on different timescales. More massive systems evolve on shorter timescales, thus reaching their equilibrium more quickly, while less massive systems evolve more slowly.

5.2.2 The dependence of the steady-state distribution function on the collision parameters

The parameters that describe the outcomes of collisions, in principle, should be roughly the same for all collisional systems. These are the fragmentation constants and the parameters of the strength curve (Benz & Asphaug, 1999). In order to investigate their effects on the evolution of the particle mass distribution, I vary their nominal values and evolve the models to the same 10 Gyr, as I did for the reference model.

I give here a detailed analysis of the effects of varying only five of the twelve parameters (α, b, Q_{sc}, s, S), as the remaining seven ($\gamma, \beta_X, f_Y, f_X^{\max}, f_M, g, G$) have no significant effects (see Table 5.1 for the description of these parameters).

In Figure 5.3, I plot the resulting mass distributions when varying the cratered mass parameters α and b (Koschny & Grün, 2001a,b). The parameter α is the total scaling and b is the exponent of the projectile's kinetic energy in the equation of

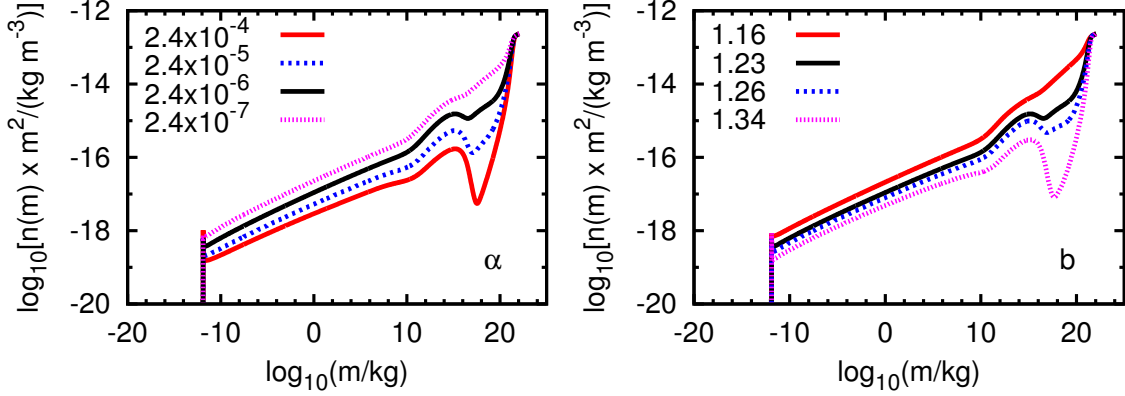


Figure 5.3 Particle mass distribution at 10 Gyr, when varying the parameters α (left) and b (right) of the cratered mass (equation 5.1).

the cratered mass

$$M_{\text{cr}} = \alpha \left(\frac{\mu V^2}{2} \right)^b. \quad (5.1)$$

As can be seen in Figure 5.3, the resulting mass distributions depend on the values of α and b only in the gravity dominated regime. At these larger masses, the model is incomplete, because I do not include aggregation. When increasing α , i.e., basically softening the materials or increasing the effects of erosions, the number of eroded particles in the gravity-dominated regime increases rapidly. A similar effect can be observed when increasing the value of b . However, within reasonable values of α and b , the variation of the equilibrium particle mass distribution slope in the dust mass regime is negligible.

In Figure 5.4, I plot the resulting distributions and the evolution of the dust distribution slope when I vary the parameters Q_{sc} , S , and s . These are all variables in the tensile strength curve, which is given as (Benz & Asphaug, 1999)

$$Q^*(a) = 10^{-4} Q_{\text{sc}} \left[S \left(\frac{a}{\text{cm}} \right)^s + G \rho \left(\frac{a}{\text{cm}} \right)^g \right] \frac{\text{J g}}{\text{erg kg}}. \quad (5.2)$$

The variable Q_{sc} is a global scaling factor, S is the scaling of the strength-doma-

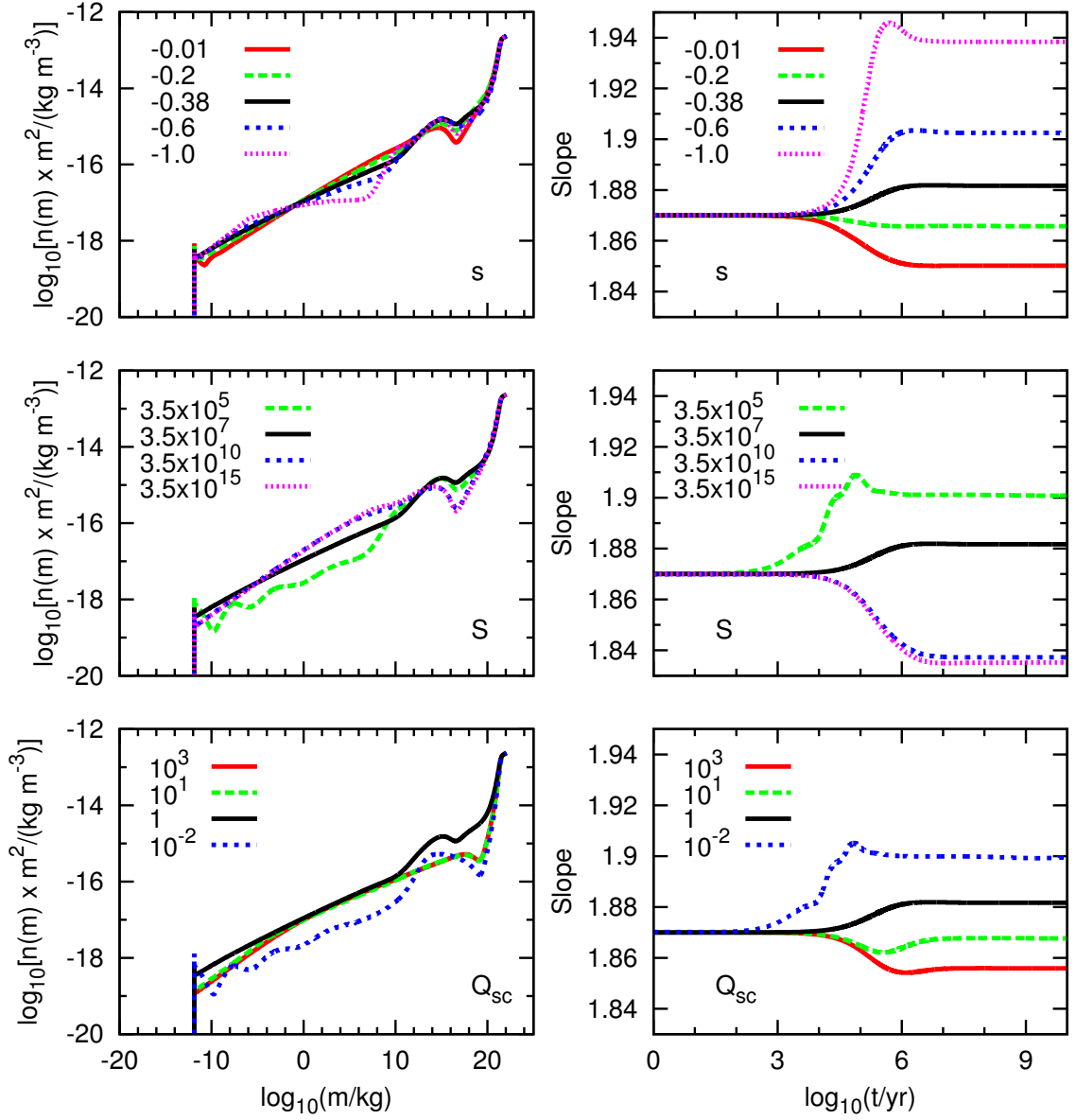


Figure 5.4 (*Left panels*) Particle mass distribution at 10 Gyr, when varying the values of the tensile strength curve parameters Q_{sc} , S and s . (*Right panels*) Evolution of the dust-mass distribution slopes when varying the values of the same parameters.

ted regime, s is the power dependence on particle size of the strength-dominated regime, G is the scaling of the gravity-dominated regime, and g is the power dependence on particle size of the gravity-dominated regime. The tensile strength curve has been extensively studied for decades. However, as it is dependent on various material properties and the collisional velocity (Stewart & Leinhardt, 2009; Leinhardt & Stewart, 2011), its parameters do not have universally applicable values. Determining the tensile strength curve at large and small sizes is also extremely difficult experimentally. However, because variations in the gravity-dominated regime of the curve (G and g) do not have significant effects on the equilibrium dust-mass distribution, I do not consider these parameters further in the following discussion.

The slope s of the strength curve in the strength-dominated regime depends on the Weibull flaw-size distribution. Its measured values range anywhere between -0.7 and -0.3 (Holsapple et al., 2002). Steeper values of s make smaller materials harder to disrupt, which results in a steeper dust distribution slope. At $s = 1.0$, the smallest particles are hard enough to resist catastrophic disruption even when the projectile mass equals the target mass. This results in a mass distribution with a slope equal to the redistribution slope $\gamma = 1.83$. At $s = 0.6$, the smallest particles are still able to destroy each other and generate a dust distribution slope that is close to 1.91.

The scaling constants of the tensile strength curve are the dominant parameters in the evolution toward the steady state distribution. When reducing the complete tensile strength curve scaling Q_{sc} , wave structures form more easily, as a particle becomes capable of affecting the evolution of particles much larger than itself (see Chapter 4). When upscaling the tensile strength curve, the steady-state distribution slope starts to resemble the redistribution slope, as it is the particle

redistributions that lead the evolution of the particle mass distribution. When varying the scaling of only the strength side of the curve S , similar effects can be seen.

I conclude that, for all reasonable values of the collisional parameters, the steady-state dust-mass distribution slope is larger or equal to 1.88.

5.2.3 The dependence of the steady-state distribution function on system variables

There are a number of parameters that can change from one collisional system to another: the material density ρ , the maximum and the minimum particle mass in the system m_{\min} and m_{\max} , the radial distance R , height h , and width ΔR of the disk, and the spectral type of the central star. All these parameters affect three properties of the collisional model: the blow-out mass, the collisional velocity, and the number density of particles. Varying these parameters will change the timescale of the evolution and affect the steady-state distribution slope. In this subsection, I analyze the effects of varying the radial distance, as it modifies the equilibrium mass distribution by setting the collisional velocity. Modifying either disk parameters ΔR and h or the spectral-type of the star would have similar effects. I do not discuss the variations in the timescales.

In the left panel of Figure 5.5, I show the effects of varying the radial distance, R , on the mass distribution evolved to 10 Gyr. Variations in the radial distance affect both the number density of particles and the collisional velocity, naturally changing the timescale of the evolution and also the outcome of the collisions. Decreasing the radial distance will increase the collisional velocity, resulting in the appearance of waves at the small-mass end of the distribution. It also generates a much more pronounced kink at the high mass end. On the other hand, when the velocity is decreased at large radii, the low mass end of the distri-

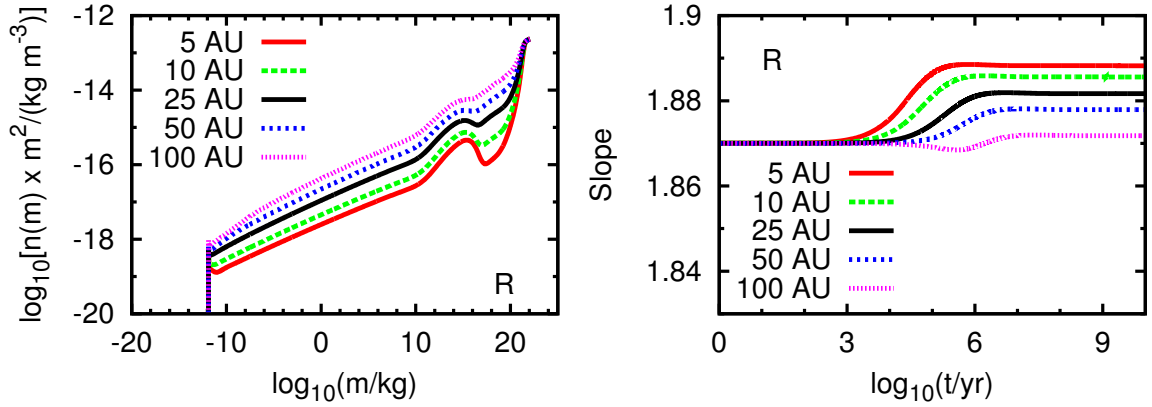


Figure 5.5 (*Left panel*) Particle mass distribution at 10 Gyr, when varying the value of the radial distance of the disk. (*Right panel*) Evolution of the dust-mass distribution slopes when varying the same parameter.

bution starts resembling the redistribution function, as smaller particles are not destroyed due to the lower energy collisions. Moreover, no kink is produced at the high mass end. In the right panel of Figure 5.5, I show the evolution of the particle-mass distribution slope as a function of the collisional velocity. For high velocity collisions, the waves render the fitting of a single mass distribution slope ill constructed but the underlying slope of the wavy mass distribution is slightly steeper than for the smaller collisional velocity case.

5.2.4 The dependence of the steady-state distribution function on numerical parameters

I discuss here the effects of three non-physical variables that appear in the numerical algorithm. They are: the mass ratio δ between neighboring grid points and the parameters of the large particle collisional cross-section smoothing formula, Θ and p (see Chapter 4). In Figure 5.6, I plot the distribution of the model with varying values of δ at 10 Gyr (left panel) and the evolution in the slope of the dust

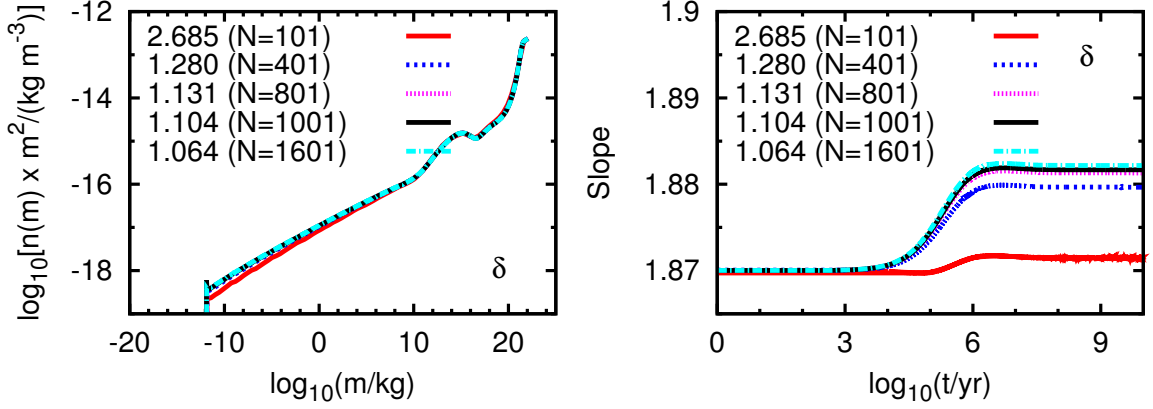


Figure 5.6 (*Left panel*) Particle mass distribution at 10 Gyr, when varying the resolution of the numerical model. (*Right panel*) Evolution of the dust-mass distribution slopes when varying the same parameter.

distribution (right panel). The evolution of the dust distribution is affected by the number of grid points used, converging at $\delta = 1.13$; this corresponds to 801 grid points between my m_{\min} and m_{\max} mass range. Using a lower number of grid points leads to errors in the numerical integration for the redistribution, leading to an offset larger than 7% for the smallest particles in the system, when only using half as many grid points. I find that the dust distribution slope is practically independent of the smoothing variables Θ and p .

5.2.5 The time to reach steady-state

In the model calculations, the dust distributions in the vast majority of cases reach steady state by 10-20 Myr and only in a few cases do they take somewhat longer. The characteristic time is less than 100 Myr for all realistic cases. This shows that, apart from second generation debris disks, the majority of debris disks around stars of ages over 100 Myr are most likely to be in collisional steady-state, at least for the smallest particles (< 1 cm). However, young and extended systems, such

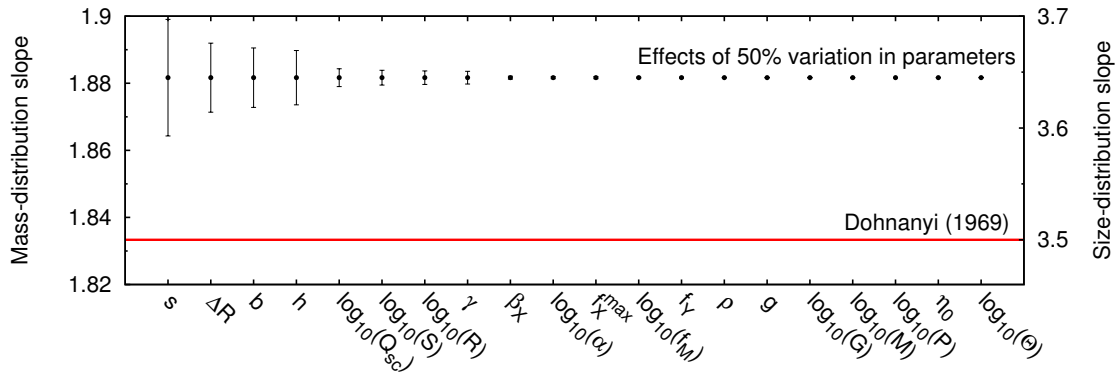


Figure 5.7 Effect on the equilibrium particle mass and size distributions of varying each collisional and system variable by 50%.

as β Pic (Smith & Terrile, 1984; Vandenbussche et al., 2010), might not be in complete steady-state at the outer parts of their disks, where interaction timescales are longer.

5.2.6 The robustness of the solution

One of the most surprising results from the wide range of numerical models computed is the robustness of the steady state distribution. Varying the values of the model parameters does not result in significant changes in the slope of the distributions. In Figure 5.7, I show the effect of varying each model parameter by 50% on the equilibrium slope of the dust-mass distribution function. I order the parameters on the horizontal axis as a function of decreasing magnitude of their effects. Note that I varied the parameters that typically span many orders of magnitude by 50% in log. The plot shows that the dominant parameter, by far, is the slope of the strength curve in the strength-dominated regime. This is followed by variables that affect the collisional velocity (ΔR and h) and the power b of the erosive cratered mass formula (equation [5.1]). The plot also shows that neither of

the arbitrarily chosen collision prescription constants have any significant effects on the outcome of the collisional cascade. The model runs predict an equilibrium dust mass distribution slope of $\eta = 1.88 \pm 0.02$ ($\eta_a = 3.65 \pm 0.05$), taking the maximum offsets originating from the 50% variation in the model parameters test as the error.

5.3 Synthetic Spectra

In the following sections, I compare the emission that results from the predicted particle-mass distributions to observations. As a first step, I generate an array of synthetic spectra using realistic astronomical silicate emission properties. I then analyze how the spectra are influenced by the particle mass distribution function.

The flux emitted by a distribution of particle masses at a certain frequency is equal to

$$F_\nu = \frac{\mathfrak{v}\pi}{D^2} \int_{\mathfrak{n}}^x da n(a) a^2 Q_{\text{abs}}(a, \nu) B_\nu(T) , \quad (5.3)$$

where Q_{abs} is the absorption efficiency coefficient, $B_\nu(T)$ is the blackbody function, and \mathfrak{v} is the total volume of the emitting region. Since in infrared astronomy it is customary to express the flux density as a function of wavelength, I rewrite this also as

$$F_\nu = \frac{\mathfrak{v}\pi\lambda^2}{D^2c} \int_{\mathfrak{n}}^x da n(a) a^2 Q_{\text{abs}}(a, \lambda) B_\lambda(T) . \quad (5.4)$$

The exact function of the absorption efficiencies of particles in the interstellar medium or in circumstellar disks is largely unknown. The most commonly used particle types for SED calculations are artificial astronomical silicate (the properties of which are adjusted to reproduce the typical $10 \mu\text{m}$ silicate feature and measured laboratory dielectric functions) and graphite (Draine & Lee, 1984). In Figure 5.8, I plot the absorption efficiency as a function of wavelength for a few astronomical silicate particle sizes. Particles larger than $10 \mu\text{m}$ have nearly con-

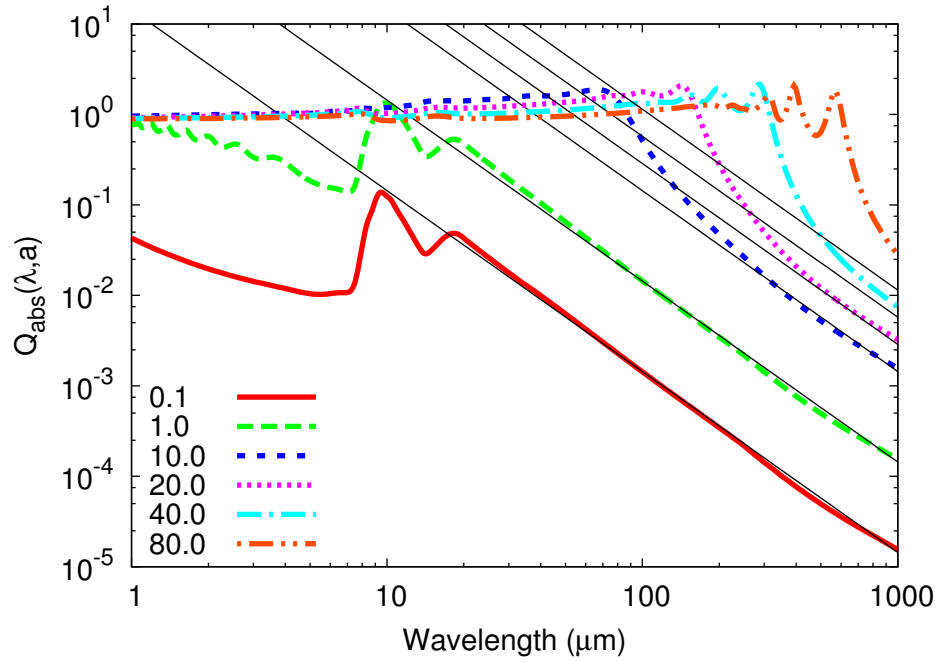


Figure 5.8 Absorption efficiency of astronomical silicates as a function of wavelength for a range of particle sizes between 0.1 and 80 μm . Solid lines are the $\sim \lambda^{-\beta}$ approximations to the long-wavelength regimes of the curves that I employ in this work.

stant absorption efficiency curves at shorter wavelengths ($\lambda < 2\pi a$, where a is the particle radius) with $Q_{\text{abs}} = 1$, which is followed by a power-law cut off. The slope of this power-law becomes constant for wavelengths larger than $\sim 8\pi a$, and is commonly denoted by the variable β . Astronomical silicates of all sizes have a typical value of $\beta = 2$ (Draine & Lee, 1984).

In Figure 5.9, I show synthetic SEDs, all scaled to the same flux level at 1000 μm . The top panel shows spectra calculated around an A0 spectral-type star, with debris rings placed at various distances between 2 and 292 AU. The minimum particle size cut-off was set at $\sim 5 \mu\text{m}$, in accordance with the model (see Chapter 4).

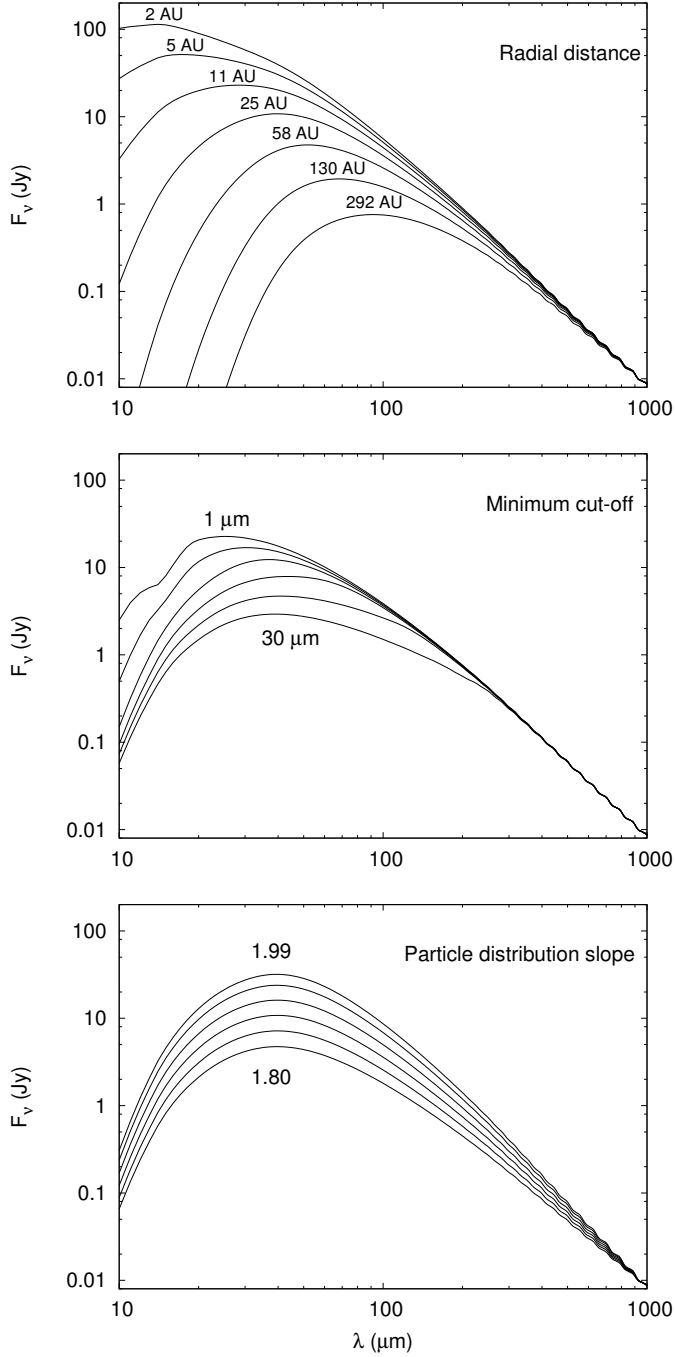


Figure 5.9 Synthetic SEDs for an array of model power-law particle mass distributions, with varied parameters. The fluxes are scaled to match at $1000\ \mu\text{m}$. In the top panel, I show the synthetic SEDs generated for a variety of radial distances; in the middle panel, I show synthetic SEDs generated for a variety of minimum cut-offs (1, 2, 4, 8, 15 and $30\ \mu\text{m}$); and in the bottom panel, I show synthetic SEDs generated for a variety of particle-mass distribution slopes (1.80, 1.84, 1.88, 1.92, 1.96 and 1.99). *Note:* In the middle-panel I vary the minimum cut-off of the particle mass distributions, even though it is a parameter inherently set by equations in the collisional model. Since in reality, the placement of the cut-off is set by the optical properties and structural build of the micron size particles, it is generally treated as a variable in SED models. In the plot, I show that such variations in the placement of the minimum cut-off do not affect the long-wavelength part of the SEDs.

All disks with radial distances below ~ 130 AU have a common slope for wavelengths larger than $250 \mu\text{m}$, and the furthest disk at 292 AU joins this common slope around $\sim 350 \mu\text{m}$.

The blow-out size in a system depends on grain structure (porosity) and the exact value of the optical constants for small grains (which is largely unknown and is a function of grain material). For this reason, I also calculated synthetic SEDs for a debris ring at 25 AU around an A0 spectral-type star, with the minimum particle size of the distribution artificially cut off at sizes between 5 and $30 \mu\text{m}$. (Note that I normally calculate the blow-out mass self-consistently as described in Chapter 4.) I plot these SEDs in the middle panel of Figure 5.9. The offsets between the SEDs become apparent for wavelengths shorter than $200 \mu\text{m}$, while for longer wavelengths, the emission profiles agree and have a common Rayleigh-Jeans slope.

Finally, I explore the dependence of the SED on the slope of the steady-state particle-mass distribution. The bottom panel of Figure 5.9 shows synthetic SEDs generated for a debris ring at 25 AU around an A0 spectral type star, with a minimum particle cut-off size at $5 \mu\text{m}$, but with particle mass distribution slopes between 1.81 and 1.99. These plots show that the slope of the Rayleigh-Jeans part of the emission is greatly influenced by the particle size distribution slope. In fact, they depend almost solely on it, with the temperature of the grains having mild effects at large orbital distances.

5.4 Relation between the particle mass distribution and the SED

The absorption efficiency curves can be simplified and described as

$$Q_{\text{abs}}(\lambda, a) \propto \begin{cases} 1 & \lambda < 4\pi a \\ \left(\frac{4\pi a}{\lambda}\right)^\beta & \lambda > 4\pi a \end{cases}$$

where x is a scaling constant for the power-law part of the function. Fitting the silicate absorption efficiency functions, I find

$$x = 12 \left(\frac{a}{\mu\text{m}} \right)^{-0.5}. \quad (5.5)$$

Using this simplified absorption efficiency model and assuming that all particles contribute to the Rayleigh-Jeans tail of the SED with their own Rayleigh-Jeans emission, I estimate the emitted flux density at long wavelengths as

$$F_\nu = \frac{2\nu\pi k_b T C_{\text{disk}}}{D^2 \lambda^2} \left[10^{-3} \left(\frac{12}{\lambda} \right)^\beta \int_0^{\frac{\lambda}{4\pi}} da a^{2+\frac{\beta}{2}-\eta_a} + \int_{\frac{\lambda}{4\pi}}^\infty da a^{2-\eta_a} \right]. \quad (5.6)$$

Here I assumed a β parameter that is independent of the particle size. The variable C_{disk} is the number density scaling (see Chapter 4), k_b is the Boltzmann constant, T is the temperature of the dust grains (which I also assume to be particle size independent), and D is the distance of the system from the observer. The quantity η_a is the steady state particle size distribution slope, and can be calculated from the mass distribution slope as $\eta_a = 3\eta - 2$. Integrating these functions, I get

$$F_\nu(\lambda) = C_1 \lambda^{1-\frac{\beta}{2}-\eta_a} + C_2 \lambda^{1-\eta_a}, \quad (5.7)$$

where

$$C_1 = \frac{2\nu\pi k_b T C_{\text{disk}}}{D^2} \times \frac{10^{-3} 12^\beta 2^{2\eta_a-5-\beta} \pi^{\eta_a-3-\beta/2}}{6 + \beta - 2\eta_a} \quad (5.8)$$

$$C_2 = \frac{2\nu\pi k_b T C_{\text{disk}}}{D^2} \times \frac{(4\pi)^{\eta_a-3}}{\eta_a - 3}. \quad (5.9)$$

Assuming $\beta = 2$, which is appropriate for astronomical silicates, I find that the slope of the SED is equal to $-\eta_a$ for the short wavelength part of the Rayleigh-Jeans tail of the SED and $1 - \eta_a$ for the long wavelength regime. Similar results have been found by Wyatt & Dent (2002).

The models yield a steady-state distribution slope of $\eta_a \approx 3.65$, meaning that the Rayleigh-Jeans tail end of the SEDs should be proportional to

$$F_\nu \propto \lambda^{-2.65}, \quad (5.10)$$

as long as the particles are in collisional steady state.

5.5 Comparison to observations

To compare the computed spectra of steady-state collisional disks to data, I assembled the available data for debris disks with far-IR and submillimeter observations. As a result of the analysis in §5.3, where I determined the wavelength range that is least sensitive to parameters, I use only data at wavelengths larger than $250 \mu\text{m}$. To fit a power-law to the Rayleigh-Jeans regime of the SEDs, I need a minimum of three data points above the wavelength cut-off. I found a total of only nine sources that fulfill these requirements. I present the far-IR/submillimeter fluxes for these sources in Table 5.2. Occasionally, published submillimeter measurements do not account for systematic errors. In these cases, I applied a total of 30% error to all ground based measurements at 350 and $450 \mu\text{m}$ and 15% for all Herschel data and measurements above $850 \mu\text{m}$. I also made sure that the data included all the flux from each source and applied an aperture correction estimate otherwise. All corrections are listed as notes in Table 5.2.

I perform individual power-law fits to the data of each source as well as a fit to all sources simultaneously with a common Rayleigh-Jeans slope. In Figure 5.10, I present the photosphere subtracted excess emissions for each source in the left panels and plot the best-fit power-law spectrum of the form

$$F_\nu = A \times \left(\frac{\lambda}{200 \mu\text{m}} \right)^{-l}, \quad (5.11)$$

obtained from individual fits. I show in the right panels of Figure 5.10 the error

Table 5.2. Observational data of debris disks

Star	λ (μm)	Flux (mJy)	Error (mJy)	Excess (mJy)	Reference
β Pic	250	1,900.0	285.0	1,897.5	Vandenbussche et al. (2010)
	350	720.0	108.0	718.7	Vandenbussche et al. (2010)
	500	380.0	57.0	379.4	Vandenbussche et al. (2010)
	800	115.0	30.0	114.8	Zuckerman & Becklin (1993)
	850	85.2	13.0	85.0	Holland et al. (1998)
	850	104.3	16.0	103.8	Holland et al. (1998)
	1200	24.3	4.0	24.2	Liseau et al. (2003)
	1200	35.9	5.0	35.8	Liseau et al. (2003)
	1300	24.9	4.0	24.8	Chini et al. (1991)
ϵ Eri	350	366.0	109.8	359.45	Backman et al. (2009)
	450	250.0	75.0	246.06	Greaves et al. (2005)
	850	37.0	5.55	35.92	Greaves et al. (2005)
	1300	24.2	4.0	23.74	Chini et al. (1991)
Fomalhaut	350	1,180.0	354.0	1,168.3	Marsh et al. (2005)
	450	595.0	200.0	587.8	Holland et al. (2003)
	850	97.0	14.55	95.1	Holland et al. (2003)
	1300	21.0	3.5	20.17	Chini et al. (1991)
HD 8907	450	22.0	11.0	21.87	Najita & Williams (2005)
	850	4.8	1.2	4.76	Najita & Williams (2005)
	1200	3.2	0.9	3.18	Roccatagliata et al. (2009)
HD 104860	350	50.1	15.0	50.0	Roccatagliata et al. (2009)
	450	47.0	14.0	46.9	Najita & Williams (2005)
	850	6.8	1.2	6.78	Najita & Williams (2005)
	1200	4.4	1.1	4.39	Roccatagliata et al. (2009)
	3000	1.35	0.67	1.35	Carpenter et al. (2005)
HD 107146	350	319.0	90.0	318.8	Roccatagliata et al. (2009)
	450	130.0	39.0	129.9	Najita & Williams (2005)
	850	20.0	3.2	19.96	Najita & Williams (2005)
	1300	10.4	3.0	10.39	Najita & Williams (2005)
	3000	1.42	0.3	1.41	Carpenter et al. (2005)
HR 8799	350	89.0	26.0	88.8	Patience et al. (2011)
	850	15.0	3.0	14.96	Williams & Andrews (2006)
	1200	4.0	2.7	3.98	Bockelée-Morvan et al. (1994)
Vega	250	1,680.0	260.0	1,617.6	Sibthorpe et al. (2010)
	350	610.0	100.0	578.5	Sibthorpe et al. (2010)
	500	210.0	40.0	194.8	Sibthorpe et al. (2010)
	850	45.7	7.0	40.5	Holland et al. (1998)
HD 207129	250	113.0	18.0	111.78	Marshall et al. (2011)
	350	44.3	9.0	43.68	Marshall et al. (2011)
	500	25.9	8.0	25.60	Marshall et al. (2011)
	870	5.1	2.7	5.00	Nilsson et al. (2010)

contours of the slope and normalization of the power-law at the 1, 2, and 3σ levels. The plots also indicate the $\chi^2_{\min}/\text{d.o.f.}$ (the minimum of the reduced χ^2) of each fit. The solid red line represents the Rayleigh-Jeans slope calculated from the Dohnanyi (1969) analytic solution, the green band represents the best slope given by the reference model calculation (including errors from 50% variations in the slope of the strength curve, see Figure 5.7), and the blue band yields the global fit solution of

$$l = 2.60 \pm 0.06 . \quad (5.12)$$

The global fit and the reference model agree within the errors of the prediction.

5.6 Conclusions

In this Chapter, I used the numerical model introduced in Chapter 4 to follow the evolution of a distribution of particle masses. I varied all twelve collisional, all six system, and all three numerical variables of my model and examined the effects of these variations on the evolution of the particle mass distribution. My numerical model has been built to ensure mass conservation and that the resulting distribution of particles is not artificially offset due to numerical errors, as the integrations of the model span over 40 orders of magnitude in mass. In §5.2.4 of this Chapter, I demonstrate that lower precision integrations can lead to shallower particle distributions.

The steady-state particle distribution of the collisional system is extremely robust against variations in its variables, with the strongest effects occurring from changes to the tensile strength curve (Holsapple et al., 2002; Benz & Asphaug, 1999). Even these variations have mild effects on the slope of the particle mass distribution, modifying it only between the values of 1.84 and 1.94 (3.52 and 3.82 in mass space, respectively). I find the dust distribution of the reference model to

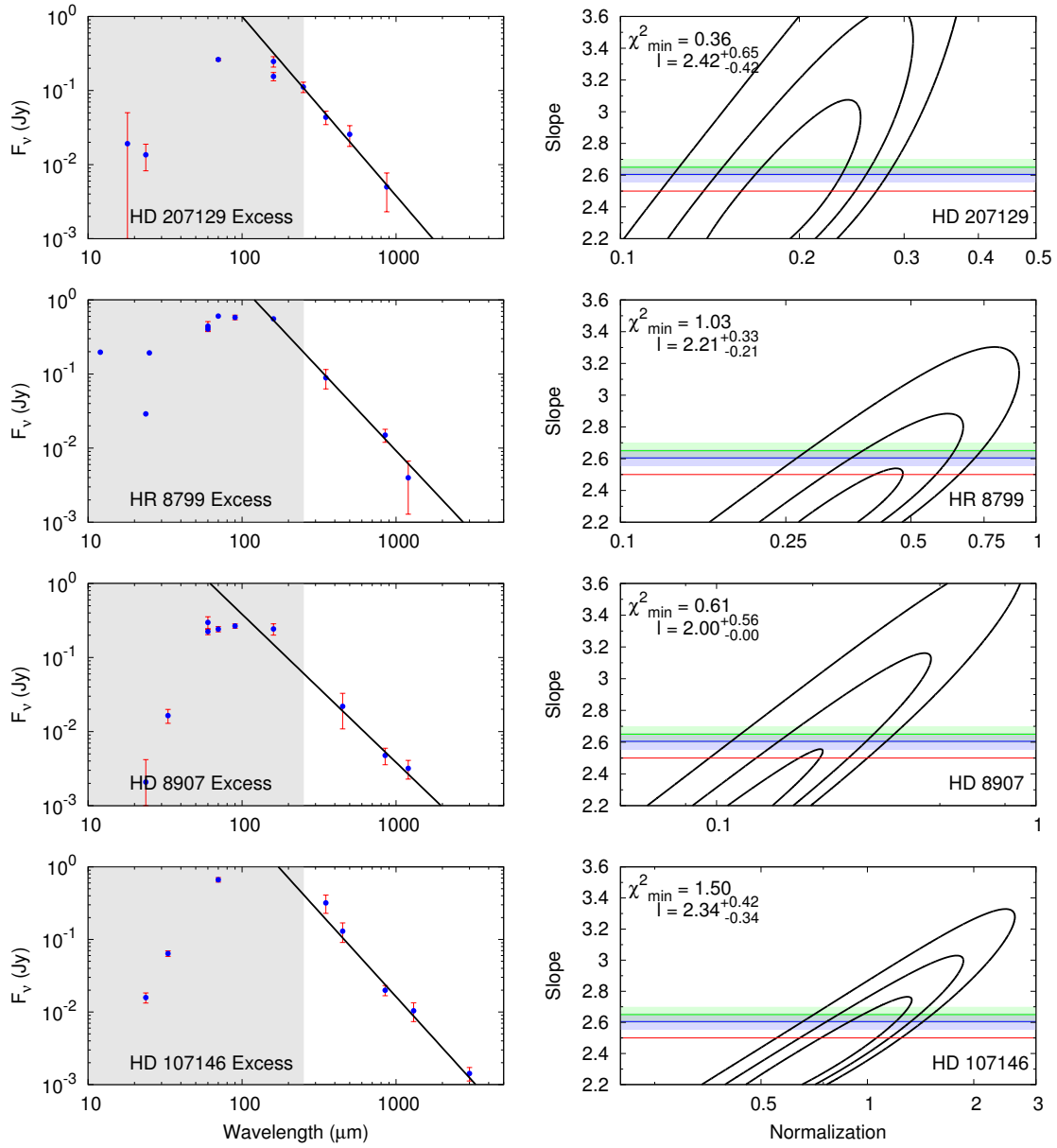


Figure 5.10 Observed SEDs of debris disks with submillimeter and millimeter data. The left panels are the photosphere-subtracted fluxes of the excess emissions with the best fitting slopes, while the right panels are the 68%, 95% and 99% confidence contours of the individual fits. The error contours also show the slope given by the Dohnanyi (1969) mass distribution function in red, the value predicted by the numerical code in the green band, and the best global fit with errors in the blue band.

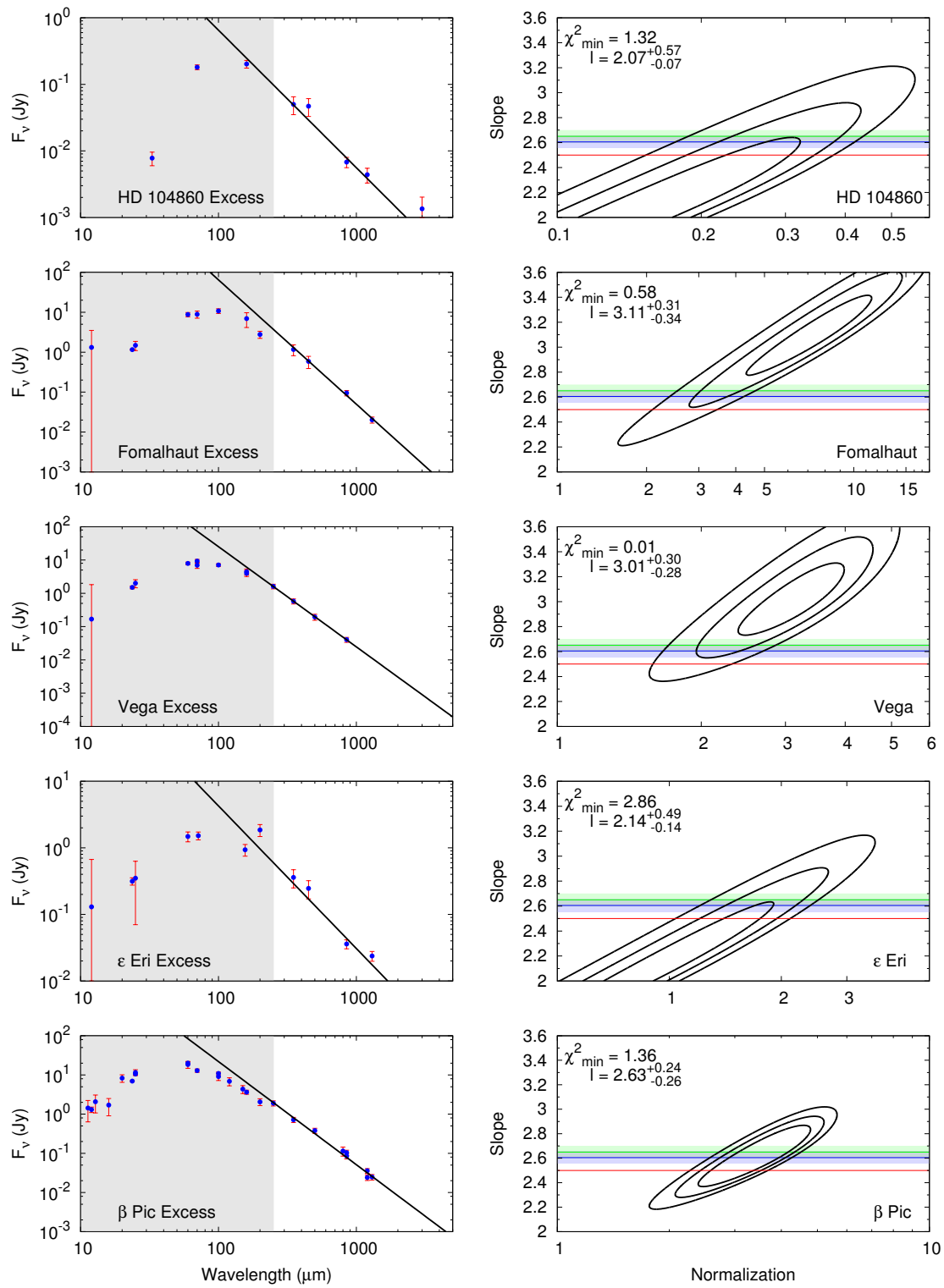


Figure 5.10. (Cont.)

be 1.88 (3.65 in size space). I find that waves occur when the collisional velocities are high or when particle strengths are low at the mass distribution cut-off, where the radiation force blowout dominates the dynamics.

The Rayleigh-Jeans tail of the debris disk SEDs is dominated by the medium sized particles, whose mass distribution is less affected by possible wavy structures. I derive a simple formula that gives the slope of the measured flux density in the Rayleigh-Jeans part of the SEDs as

$$F_\nu \propto \lambda^{1-\eta_a} .$$

This implies that the mass distribution slope itself could, in principle, be measured from long-wavelength observations. I assemble a list of nine debris disks that have been measured at the far-IR, submillimeter, and millimeter wavelengths and examine the Rayleigh-Jeans slope of their emissions. My predictions of a slope of $l = 2.65 \pm 0.05$ agrees well with the observations, which have a global slope fit of $l = 2.60 \pm 0.06$.

CHAPTER 6

THESIS CONCLUSIONS

This thesis gives an analysis of the nature of debris disk infrared signatures, using observational data obtained with the *Spitzer Space Telescope* and theoretical models. Below I give a brief summary of the results presented in the thesis followed by an outlook for future work.

6.1 Summary

In Chapter 2, I present an observational example for a false debris disk signature resulting from the thermal heating of the interstellar dust repelled and accumulated in front of the A spectral-type star δ Velorum. The star was originally assumed to have a debris disk based on its mid-IR excess emission. This was later revisited when precision PSF subtraction from $24\ \mu\text{m}$ *Spitzer MIPS* images revealed an impressive bow shock structure in front of the star. Assuming that this structure is produced by a dynamical interaction between the star and the surrounding interstellar medium, I introduce a model that calculates the geometry of the bow shock that expects the dynamics of the system to be dominated by the radiation and gravitational forces the interstellar dust particles experience from δ Velorum. I also calculate the total surface brightness emitted by the system, when assuming the particles to be in thermal equilibrium. My model gives a consistent explanation of the total infrared excess and the surface brightness distribution of the bow shock structure at δ Velorum. I determined the density of the surrounding ISM to be $5.8 \pm 0.4 \times 10^{-24}\ \text{g cm}^{-3}$. This corresponds to a number density of $n \approx 3.5\ \text{atoms cm}^{-3}$, which means a ~ 15 times overdensity relative to the average Local Bubble value. The cloud and the star have a relative velocity of

$35.8 \pm 4.0 \text{ km s}^{-1}$. The velocity of the ISM in the vicinity of δ Velorum I derived is consistent with LIC velocity measurements by Lallement et al. (1995). The question still remains how common this phenomenon is among the previously identified infrared-excess stars. Is it possible that many of the infrared excesses found around early-type stars result from the emission of the ambient ISM cloud? The majority of infrared excess stars are distant and cannot be resolved, so we cannot answer for sure. However the excess at δ Velorum is relatively warm between 24 and $70 \mu\text{m}$ ($F(24) \sim 0.17 \text{ Jy}$, $F(70) \sim 0.14 \text{ Jy}$), and such behavior may provide an indication of ISM emission.

In Chapter 3, I show the results of the *Spitzer* $24 \mu\text{m}$ survey of the nearby ($\sim 180 \text{ pc}$), relatively old (750 Myr) galactic open cluster Praesepe. I compiled a cluster member list using data from SDSS, Webda, and 2MASS. Out of the 193 cluster members detected at all wavelengths in the combined catalog, 29 were early (B5-A9) and 164 later (F0-M0) spectral types. I found one star in the early and three in the later spectral type groups that show excess emission. Up to near the completeness limit, with one debris disk star, there are 106 sources in the later spectral-type sample. This result shows that only $6.5 \pm 4.1\%$ of early- and $1.9 \pm 1.2\%$ of solar-type stars are likely to possess debris disks in the 1-40 AU zones. These values are similar to that found for old ($> 1 \text{ Gyr}$) field stars. This result can be placed in context with the Late Heavy Bombardment theory of the Solar System. With simple Monte Carlo modeling, I show that the observations are consistent with 15-30% of the stars undergoing a major re-arrangement of the planetary orbits and a subsequent LHB-like episode once in their lifetime, with a duration period of 50-100 Myr. I also summarize the results in the literature on the decay timescales of debris disks around early- and solar-type stars, and find that the decay timescale for solar-type stars is shorter than for earlier-type stars.

In Chapter 4, I present the main theoretical work of my thesis, which is the numerical modeling of the collisional cascades in debris disks. With my numerical code, I am able to follow the evolution of the distribution of particles in a collisionally evolving system. The collisional equation that I introduce in my thesis, unlike previous ones, solves the full scattering equation. The model includes both erosive and catastrophic collisions, but currently does not evolve the dynamical state of the system. In Chapter 4, I compare the code to the previously published similar numerical models, showing general agreement. My model does show faster decays than previously published ones (Thébault et al., 2003; Löhne et al., 2008; Wyatt et al., 2011) and also yields slightly higher dust-to-planetesimal mass ratios. I attribute these characteristics to be a result of the accurate treatment of collisional cascades. I place special emphasis on improving the fidelity of the code by using solvers that achieve high numerical accuracy. The numerical methods I use are extensively verified and tested in Appendix D.

In Chapter 5, I analyze the evolution of my numerical code and its dependence on the model variables. I vary all twelve collisional, all six system and all three numerical variables of the model and examine the effects of these variations on the evolution of the particle mass distribution. The collisional system is surprisingly extremely robust against variations in its variables, with the strongest effects occurring from changes to the tensile strength curve (Holsapple et al., 2002; Benz & Asphaug, 1999). Even significant variations seem to have only mild effects on the slope of the particle mass distribution. My reference model's dust mass distribution slope of $1.88\bar{3}$ (3.65 in size space) is a good average representation of the expected dust distribution slope. I also derive a simple formula, that gives the slope of the measured flux density in the Rayleigh-Jeans part of the

SEDs as

$$F_\nu \propto \lambda^{1-\eta_a} ,$$

where F_ν is the flux density λ is the wavelength, and η_a is the size distribution slope. This relationship shows that the flux density is only a function of the dust distribution slope. This in turn means that the distribution slope itself, in principle, can be measured from long wavelength observations. I assemble a list of nine debris disks that have been measured at the far-IR, submillimeter and millimeter wavelengths and examine the Rayleigh-Jeans slope of their emissions. My predictions of a R-J slope of $l = 2.65 \pm 0.05$ agrees well with the observations, which have a global slope fit of $l = 2.605 \pm 0.0645$.

6.2 Future Work

Debris Disk research has been ever expanding since their first discovery almost thirty years ago. We have been able to resolve debris disk in optical scattered and at thermal infrared and submillimeter wavelengths. Numerical models have attempted to understand the physical phenomena that keeps these systems alive at such old stellar ages and detailed analysis of their material composition have been tested by spectroscopic observations. With the latest launches of mid/far infrared satellites our sensitivity level to their excesses have significantly lowered and the prospect of future launches of satellites as *WFIRST* and the *JWST* give hope for new and exciting results to come.

Interpreting the high quality data requires evermore sophisticated numerical models and theoretical predictions. We still do not know how to interpret certain observational details, such as the extended halo around certain debris disks (like Vega), the necessary large-mass cutoff in particle size in warm debris disk spectral models, the variation in the predicted particle size distribution for various debris

disks, the timescale of stochastic events in debris disk evolution and the period of the re-birth of debris disk excesses. I plan on addressing these problems with my numerical code and elaborate on them below.

6.2.1 Evolution of the particle size distribution slope

In Chapter 4, I presented my numerical model of collisional cascades in Debris Disks and in Chapter 5, I made predictions for the equilibrium size distribution as a function of model parameters. I also showed that the Rayleigh-Jean tail of the spectral energy distribution emitted by debris disks is in direct correlation with the particle size distribution slope. A near-future plan I intend to execute expands on this idea. In a recently submitted *Herschel Space Observatory* OT2 proposal I aim at studying a number of young debris disks with the *SPIRE* detector at 250, 350 and 500 μm , in the hopes of detecting variations in the dust distribution when compared to older, more tranquil systems. In my proposed sample, I include systems with ages between 1 and 100 Myr, with more sources near the lower limit. With already available submillimeter and millimeter data on a number of older sources and more to appear in the *Herschel data* archive, I will be able to study the evolution of the particle size distribution directly via observations. This I will be able to compare with my model predictions.

6.2.2 Warm debris disk models

Our solar system has two remaining planetesimal belts, the asteroid and Kuiper belt. When searching for solar system like extrasolar planetary systems, we hope to find systems with similar components. The majority of the discovered debris disks have been of Kuiper belt like cold debris disks, however lately there have been successful observations of warmer components. These warm debris disks have been found around many different type and age stars. Well known debris

disks stars, like Vega (Su et al., 2005; Peterson et al., 2006), β Pic (Boccaletti et al., 2009), Fomalhaut (Absil et al., 2009), and η Tel (Smith & Wyatt, 2010) all show signs of a warm component to their infrared excess, and even the 10 Gyr old τ Ceti seems to have an inner, warm disk (di Folco et al., 2007). Observational data of these warm debris disks yield spectral energy distributions that can be modeled only with a narrow range of particle sizes, which poses a problem. A general property of collisional cascade numerical models is the formation of waves when collisions are energetic (Campo Bagatin et al., 1994; Thébault & Augereau, 2007; Löhne et al., 2008). This is a feature that my models show, which I present in Chapter 5. A possible resolution to the problem of limited particle size ranges seen in warm debris disks is the occurrence of waves in the particle size distribution in the higher orbital velocity and collisional system that forms in the close orbits. I plan on assembling a uniform catalogue of warm debris disks, in collaboration with Kate Su and George Rieke, and give predictions to the particle size distribution and observable SEDs of the systems. Comparison to actual observations will yield an opportunity to verify and fine tune my numerical model.

6.2.3 Stochastic events and debris disk evolution

All current observations and models agree that the timescale of terrestrial planet formation is between 10 - 50 Myr, with the excess dust and gas removed from the primordial circumstellar disk under the same timescale. It is within this timescale that the runaway growth first turns into a slower, oligarchic accretion process and then into a late-stage growth phase. Finally, planetesimal systems tranquilize. According to all dating methods, the planet formation process in the solar system ended completely after 200 Myr. However, as observational evidence shows, an older system, even a Gyr old system, is able to produce a significant debris disk signature, whilst the typical removal timescale for dust is on the order of a few

million years. We know that even our solar system underwent periods of intense bombardment, the latest being the Late Heavy Bombardment (LHB) 3.8 Gyr ago (Tera et al., 1974). All evidence shows that the "re-birth" of circumstellar dust disks is a common phenomenon, and more likely to occur at the earlier stages of stellar evolution, but certainly after 10 - 20 Myr (Kenyon & Bromley, 2004). The late episode of bombardment in our solar system, however, does not seem to be a common phenomena (Gáspár et al., 2009).

Continuing my research, I will expand my theoretical framework to include collisional dynamics, as it currently only solves the collisional Boltzmann equation for a system of interacting particles. This way, I will be able to follow the spatial and time evolution of debris disks. This is necessary for us to understand how a giant planet or planetary system initiates/effects the evolution of a collisional system and to understand if the debris disk systems we are detecting are actually terrestrial planet bearing or not.

I am not the first to propose a dynamical simulation of debris disks, and many interesting results have been published in the field. The collisional model ACE (Krivov et al., 2005; Löhne et al., 2008) solves the collisional Boltzmann equation like my current numerical model (Gáspár et al., 2011), but in a three dimensional system, with the orbital elements of the dust particles evolved, thus correctly accounting for the motion of β meteorites. A similar model was presented by Thébault & Augereau (2007), who divide the debris disks into rings. However, none of these models include individual large planets, just particle distribution functions, meaning that they are unable to follow or predict the actual dynamical formation and evolution of debris systems.

An opposite modeling philosophy was presented by Raymond et al. (2011), who follow the dynamical evolution of a system of massive planets and a distri-

bution of planetesimals, assuming a variety of initial system configurations. Assuming the traditional (and now outdated) Dohnanyi (1969) particle size distribution slope, they predict the evolution of the mid-infrared excess in their model systems. As intriguing as their models are, they employ a number of simplifications that question the validity of their results. They simplify their collisions as being only mergers, while debris disks are the result of collisional cascades. Their final spectral energy distributions are calculated by assuming that the planetesimal distribution particles are aggregates of a distribution of particles, that emit as black bodies with distributions that can be described by traditional models.

A synthesis of these models will be able to provide an adequate tool to analyze the formation and evolution of debris disks and to finally understand the connection between them and planetary systems. The model I am proposing will be a hybrid Monte Carlo/Boltzmann solver, with the dynamical evolution of the planets, and larger planetesimals followed by an orbital integrator, while the distribution of the dust produced via collisions would be estimated from my already existing numerical code. Since all the mass in collisions is in the largest fragments, only the few largest fragments from larger collisions need to be followed, while the dust distributions can be scaled, extrapolated and accumulated at certain orbital distances and also removed by their respective removal methods. This numerical code would properly fragment or merge planetesimals when they collide, depending on their collisional energy, follow the orbital evolution and location of the fragments, and predict the expected infrared signature of the debris disks, assuming realistic particle size distributions and emission efficiencies.

6.2.4 Debris disk haloes

The very first debris disk discovered (Aumann et al., 1984), the one around Vega, still presents unresolved problems for debris disk evolution models, as it harbors an extended halo. Similar, although not as impressive, halos have been found around other early spectral-type, debris disk host stars, like Fomalhaut (Espinoza, in prep.). The extended halo around Vega has initially been explained as a stream of micron sized particles being ejected from the system via radiation forces (Su et al., 2005). This has been questioned by later numerical models (Müller et al., 2010) that propose the halo to be a result of particles with sizes larger than the blow-out limit on highly eccentric orbits.

Although my numerical model currently does not model or evolve the dynamical state of the collisional systems, it does keep track of the particles on eccentric orbits and is able to predict their number densities on their respective orbits, meaning it is able to give a rough estimate for the surface brightness of the extended halo of the disk. I plan on investigating this matter in more detail as well.

APPENDIX A

AGE AND DISTANCE ESTIMATE OF PRAESEPE

The precise value of the cluster age is important in constraining the debris disk fraction as a function of stellar age. The age and distance of Praesepe have been a matter of debate, especially since it is an important step in the galactic distance ladder. The estimated ages spread from $\log t = 8.6$ all the way to $\log t = 9.15$ (400 Myr – 1.42 Gyr)¹. Most papers list it as a coeval cluster with the Hyades because of their similar metallicities and spatial motions (see, e.g., Barrado y Navascués et al., 1998). The Hyades on the other hand has a better defined age of $\log t \approx 8.8$ (625 ± 50 Myr) (Perryman et al., 1998; Lebreton et al., 2001). If the clusters are coeval, their ages should agree within close limits.

Aside from using pulsating variables (Tsvetkov, 1993) or stellar rotation (Pace & Pasquini, 2004) to estimate the age of the cluster, the only method is to fit theoretical stellar evolution turnoff points on the observed CMD. This procedure involves a precise simultaneous fitting of the cluster distance, reddening, metallicity and age.

The metallicity of Praesepe has been revisited many times. The value of Boesgaard & Budge (1988) of $[\text{Fe}/\text{H}] = 0.13 \pm 0.07$ is usually accepted. An et al. (2007), with new spectroscopic measurements, obtained a value of $[\text{Fe}/\text{H}] = 0.11 \pm 0.03$, also showing that the cluster is slightly metal rich. This fact has been overlooked in some studies that have used solar values for metallicity, and which therefore underestimate the cluster distance and overestimate its age.

The distance to Praesepe has been determined with many methods, yielding slight differences among the measured values. Gatewood & de Jonge (1994) used

¹Cox (2000); Vandenberg & Bridges (1984); Tsvetkov (1993); González-García et al. (2006)

Table A.1. The distance-modulus of Praesepe in the literature.

Reference	Method used	$m - M$ [mag]
Nissen (1988)	Photometric	6.05
Mermilliod et al. (1990)	Photometric	6.2
Hauck (1981)	Photometric ^a	6.26 ± 0.23
Vandenberg & Bridges (1984)	Photometric	5.85
An et al. (2007)	Photometric ^b	6.33 ± 0.04
Gatewood & de Jonge (1994)	Parallax	6.42 ± 0.33
Loktin (2000)	Geometric	6.16 ± 0.19
This paper	Photometric	6.267 ± 0.024

^aUsing Lutz-Kelker corrections (Lutz & Kelker, 1973).

^bUsing empirically corrected isochrones.

the Multichannel Astrometric Photometer (MAP) of the Thaw Refractor of the University of Pittsburgh to determine a weighted mean parallax of $\pi = 5.21$ mas for five cluster member stars. The geometric method used by Loktin (2000) determines the apparent variation of the angular diameter of the cluster as it moves along the line of sight and estimates the distance to the cluster from it. The basic idea of this method is very similar to that of the convergent point method. The photometric distances (main-sequence fitting) seem to show a large scatter. We summarize the previous distance measurements and the methods used to obtain the values in Table A.1.

We determined the distance and age of the cluster by simultaneously fitting the distance modulus and the age with isochrones. The photometry values we used were our best SDSS g and r band data, with the corrections explained in §??. We did not include reddening in our color values, because it can be neglected

towards Praesepe ($E(B-V)=0.027 \pm 0.004$ mag; Taylor (2006)). Since the plotted CMD of Praesepe clearly showed a vertical trend at the later spectral type stars at $g - r \approx 1.2$, we only fitted cluster member points with $g - r < 1.2$ (fitting the distance modulus to a vertical trend is impossible and only adds errors to the fit). The isochrones for the fit were obtained from the Padova group website², where isochrones of any age and metallicity can be generated for a large number of photometric systems, such as the SDSS system (Girardi et al., 2004). These isochrones are similar to the empirical isochrones produced by An et al. (2007).

Since the metallicity of the cluster is still debated, we fitted isochrone sets for all metallicities in the literature. Assuming that metallicities are solar scaled, we set $[Fe/H]=[M/H]$. We fitted the following: $[Fe/H]=0.13$ ($Z=0.025$; Boesgaard & Budge, 1988), $[Fe/H]=0.11$ ($Z=0.024$; An et al., 2007) and $[M/H]=0.2$ ($Z=0.03$; An et al., 2007). The two values from the An et al. (2007) paper are from $[Fe/H]$, determined from spectroscopy, and an $[M/H]$ value from isochrone fitting. We also fitted solar metallicity isochrones to show the errors they give in the age and distance determinations.

We calculated the best fit via Monte Carlo (i.e. bootstrap) method. We generated 10,000 new samples with the same number of sources as in the original cluster member list. As with the bootstrap method, the members in the new samples were randomly picked from the original, resulting in multiple picks of a few sources and null of others. The best fitting isochrones (as a function of age and distance) to these mock samples were found by χ^2 minimization. We computed χ^2 from each fit as

$$\chi^2 = \sum (\Delta r^2 + \Delta(g - r)^2), \quad (A.1)$$

where Δr^2 is the r magnitude difference while $\Delta(g - r)^2$ is the color difference

²<http://pleiadi.pd.astro.it/>

from the closest point of the isochrone model. By finding the closest point of the isochrones we not only fit the luminosity difference, but an actual distance from the isochrone, thus allowing points to be horizontally offset. We did not weight our fit by photometric errors, because the brightest members (that are most crucial in the age determination) did not have quoted errors, while the errors of the SDSS data cannot be trusted brighter than 14th magnitude. The means and errors in age and distance modulus of the best fitting isochrone (for all metallicities) were calculated from the distribution of solutions given by the bootstrap method. Following an initial fit, we removed stars that were further than $3\sigma_{m-M}$ magnitude from the best fitting isochrones and reran the Monte Carlo code. The best fit value is given as the arithmetic mean and its error as its standard deviation.

The 2D errors for the fits are shown in Figure A.1, both for the full and for the clipped samples. The histograms of the distance modulus and age fits are shown in Figure A.2, both for the full and for the clipped samples also. The results of the fitting for the $3\sigma_{m-M}$ clipped sample are summarized in Table A.2 quoting the 1σ errors. These errors are purely from the fitting procedure, and do not include possible systematic errors such as those from isochrone models, reddening, extinction and photometry.

The best fitting isochrones for the four metallicities are shown in Figure A.3. All isochrones seem to deviate from the observed trend at $g - r > 1.2$ magnitude. This is either due to errors in the calculated isochrones or to the membership criteria of Kraus & Hillenbrand (2007), who used estimated T_{eff} and luminosity values from photometry fitted SEDs and theoretical Hertzsprung-Russell diagrams.

We adopted the metallicity of $Z=0.03$ (An et al., 2007) to give a final estimate of the cluster's age and distance. We chose this metallicity to ensure comparability, since An et al. (2007) deduced it from isochrone fitting also. The distance modulus

Table A.2. The solutions for the fitting of isochrones via two parameters for solar and the metallicities found in the literature given with 1σ errors. These values are the ones determined after the 3σ clipping iteration.

Metallicity	$m - M$ [mag]	Age [log t]
[Fe/H] = 0.00	6.012 ± 0.020	8.952 ± 0.011
[Fe/H] = 0.13 ^a	6.153 ± 0.022	8.918 ± 0.018
[Fe/H] = 0.11 ^b	6.179 ± 0.022	8.908 ± 0.019
[M/H] = 0.20 ^b	6.267 ± 0.024	8.879 ± 0.020

^aBoesgaard & Budge (1988)

^bAn et al. (2007)

of our best fit for this metallicity is $m - M = 6.267 \pm 0.024$ at 1σ confidence, within errorbars of the value of An et al. (2007) ($m - M = 6.33 \pm 0.04$ mag). The errorbars on distance are small at 3σ and comparable to the diameter of the cluster's central region (~ 6 pc). The age of the cluster is determined to be $\log t = 8.879 \pm 0.020$ (757 ± 36 Myr) at 1σ confidence. The errorbars on cluster age are significantly smaller than in papers before and help to pin down the decay trend at ages between 0.5 and 1 Gyr. The bootstrap Monte Carlo isochrone fitting method we introduce here turned out to be a very effective and successful way to determine cluster distance and age, and to estimate the errors of these parameters.

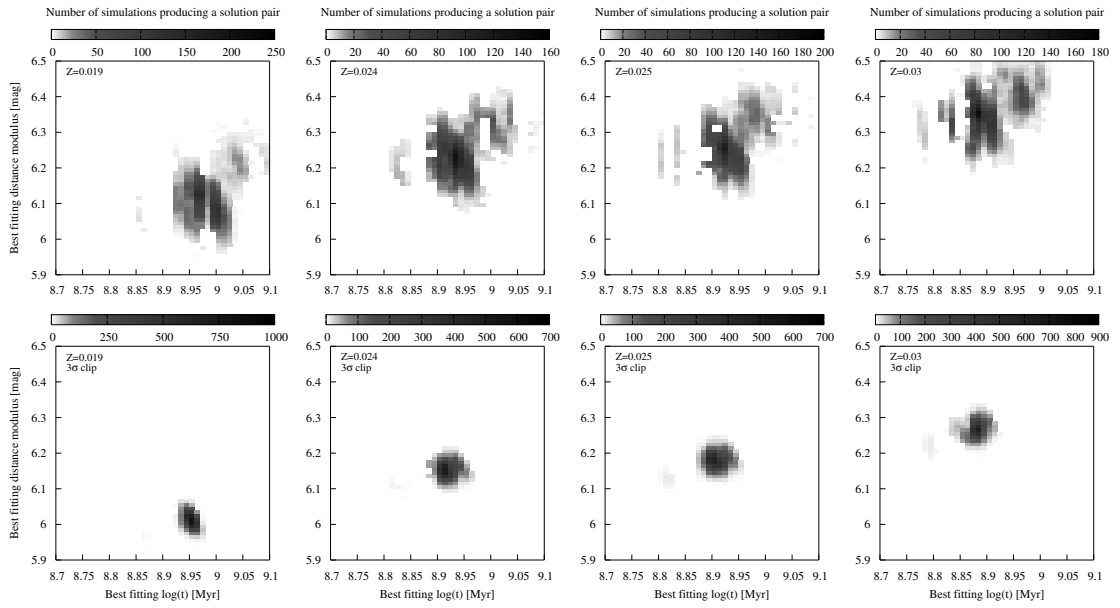


Figure A.1 The 2D probability maps show the number of solutions that were given for certain solution pairs by the Monte Carlo isochrone fitting algorithm. The top row shows the fitting for the full sample, while the bottom row gives the solutions after a 3σ clipping iterative step. The fitted metallicities are $Z = 0.019, 0.024, 0.025$ and 0.03 .

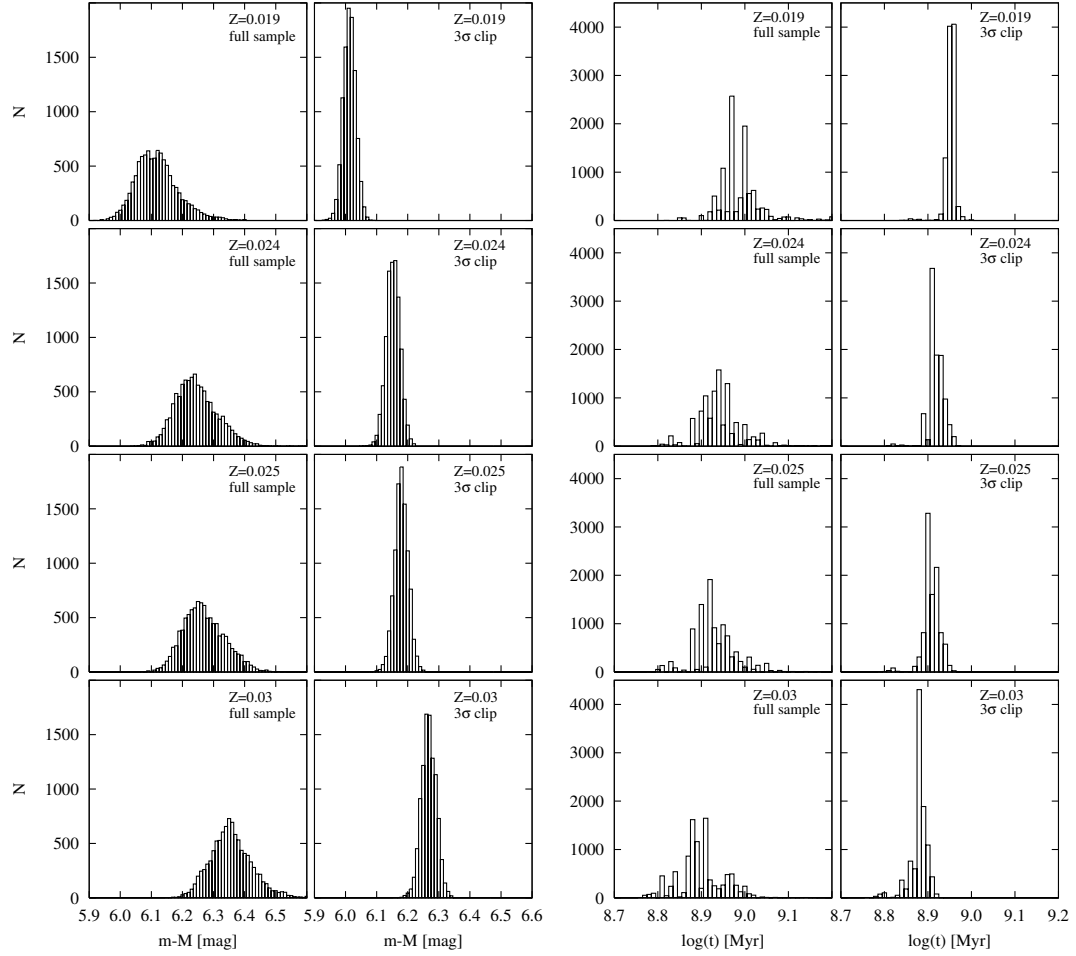


Figure A.2 These plots show the 1D representation of Figure A.1, separately for $m - M$ and $\log(t)$. The distributions get much narrower after the 3 σ clipping iterations. These plots clearly show that as you go to more metal rich isochrones, the best fitting isochrones will be younger and more distant.

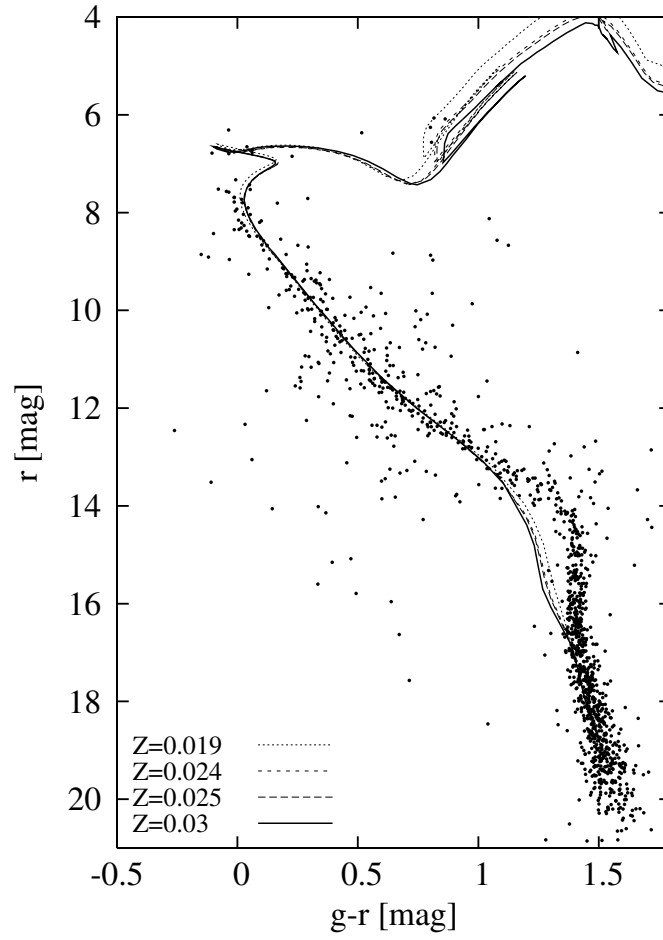


Figure A.3 The best fitting isochrones for all metallicities in the literature plus solar. The dotted line isochrone that deviates from the rest at high luminosities is the solar ($Z=0.019$) isochrone.

APPENDIX B

STRENGTH CURVES

The redistribution outcome of collisions depends almost solely on the energy of the impact and the colliding masses. In experiments it is common to specify the ratio of the kinetic energy of the projectile to the mass of the target. This ratio is known as the specific energy Q_{imp} of the impact. Gault & Wedekind (1969) already noticed that the fragment distribution of particles depends on Q_{imp} (which they called “rupture energy”) when firing aluminum projectiles into glass targets. Their experiments showed that the fragments will have a power-law distribution, with the largest fragment being a function of the specific energy of the impact. This relationship was first given in equation format in Fujiwara et al. (1977) for basalt targets. They note an offset from the Gault & Wedekind (1969) results, likely due to material strength differences.

Two specific values of Q_{imp} are used: Q_S^* (the shattering specific energy) and a somewhat larger Q_D^* (the dispersion specific energy). The value of Q_S^* gives the energy required to shatter the target so that the mass of the largest fragment is no more than half of the original target mass. However, if the target is large enough, then self gravity pulls the fragments back together, leaving a remnant larger than half of the original. The larger Q_D^* gives the value of Q_{imp} needed to disperse the fragments, so that the largest remaining piece is half of the original target mass. At lower target masses, where self-gravity can be neglected, $Q_D^* \approx Q_S^*$. We use Q_D^* in our code and refer to it as Q^* .

Determining the value of Q^* is difficult, especially for such a large range of particle sizes, from μm to km. The values for smaller bodies on the order of a few kilograms are mostly determined from laboratory experiments, while the values

for larger bodies are determined from under-surface explosions, observations of large asteroids and with experiments done under very high pressure (Holsapple et al., 2002). However, material strength varies greatly as a function of material type, object size, surface type and the number of shattering events an object has gone through over its lifetime. An object that has gone through many collisions in its lifetime, but still remains in one piece (descriptively called a “rubble pile”) can endure harder collisions, which can actually be absorbed and help to compact the object, rather than dispersing it into smaller particles. This may seem like an important parameter only for larger objects; however, the evolution of larger objects significantly influences the evolution of smaller particles, and thus is important in our study. We also lack experiments done with targets and impactors cooled down to space temperatures of 100-150 K, where one would assume that objects get more brittle and easier to shatter.

Experiments clearly show that Q^* is a function of the target mass M , meaning that different mass targets will get shattered (with a $0.5M$ largest fragment) by different specific energies. Holsapple et al. (2002) reviews experimental and theoretical results on collisions and strength curves. A common result for all of them is a minimum in the strength curve for bodies around 0.3 km in radius, where planetesimals are easiest to disperse (the number of cavities and cracks weakening the bodies increases, while self-gravitation is not dominant yet). As a result, there is a bump in the size distribution of minor planets in the solar system around this size. Smooth particle hydrodynamic (SPH) models give the Q^* strength curve for larger bodies, while experiments help to anchor the curve down to smaller rocks on the scale of a few cm in radius. It is still not clear whether the power-law shape of the curve can be extrapolated down to micron size particles, where experiments cannot be carried out. To study the col-

lisional evolution of the smallest particles, the exact value of the strength curve must be known. In the absence of any models/experiments currently at those sizes, the best that can be done is a simple extrapolation of the strength curve to those regimes. Stewart & Leinhardt (2009) introduce a velocity-dependent tensile strength curve, that is defined by variables such that it removes ambiguities over material density and projectile-to-target mass ratio. Their tensile strength curve is ideal for low-velocity ($1\text{-}300\text{ m s}^{-1}$) collisions, such as those found during planet formation or at large radii debris disks. However, their universal relationship does not hold for conditions that depart from the catastrophic disruption regime.

In our models we use the Benz & Asphaug (1999) dispersion strength curve. It is derived from SPH models, represents a reasonable average of all previous strength curves, and is impact angle averaged. This curve can be written as (all units are in SI)

$$Q^*(a) = 10^{-4} Q_{\text{sc}} \left[S \left(\frac{a}{1\text{ cm}} \right)^s + G\rho \left(\frac{a}{1\text{ cm}} \right)^g \right] \text{ J gerg}^{-1} \text{ kg}^{-1}, \quad (\text{B.1})$$

where the fiducial values in the equation are given in Table 5.1.

APPENDIX C

MASS CONSERVATION OF THE COLLISIONAL MODEL

A crucial test of any collisional code is for it to conserve the initial total mass of the system. Since particles are removed at the low mass end, this behavior can be complicated to verify. However, a system can only maintain its total mass numerically, if its collisional equations are mass conserving analytically. Here, we prove that our collisional equation is mass conserving.

The collisional equation can be written as

$$\begin{aligned} \frac{dn(m)}{dt} = & - \int_0^\infty dm' n(m) n(m') \sigma(m, m') \\ & + \int_0^\infty d\mu \int_\mu^\infty dM n(\mu) n(M) \sigma(\mu, M) \delta [X(\mu, M) - m] \\ & + \int_0^\infty d\mu \int_\mu^\infty dM n(\mu) n(M) \sigma(\mu, M) R(m; \mu, M) , \end{aligned} \quad (\text{C.1})$$

where $R(m; \mu, M)$ is the redistribution function to mass m from $\mu + M$ collisions, such that

$$\int_0^\infty dm R(m; \mu, M) m = \mu + M - X(\mu, M) , \quad (\text{C.2})$$

and δ is the Kronecker function. Multiplying Equation (C.1) by m and integrating over dm gives

$$\begin{aligned} \frac{dM}{dt} = & - \int_0^\infty dm \int_0^\infty dm' n(m) n(m') \sigma(m, m') m \\ & + \int_0^\infty d\mu \int_\mu^\infty dM n(\mu) n(M) \sigma(\mu, M) \int_0^\infty dm \delta [X(\mu, M) - m] m \\ & + \int_0^\infty d\mu \int_\mu^\infty dM n(\mu) n(M) \sigma(\mu, M) \int_0^\infty dm R(m; \mu, M) m , \end{aligned} \quad (\text{C.3})$$

where

$$\int_0^\infty dm \delta [X(\mu, M) - m] m = X(\mu, M) , \quad (\text{C.4})$$

resulting in

$$\begin{aligned} \frac{dM}{dt} = & - \int_0^\infty dm \int_0^\infty dm' n(m)n(m')\sigma(m, m')m \\ & + \int_0^\infty d\mu \int_\mu^\infty dM n(\mu)n(M)\sigma(\mu, M)(\mu + M) \end{aligned} \quad (C.5)$$

The first integral can be separated into two sections as

$$\begin{aligned} \int_0^\infty dm \int_0^\infty dm' n(m)n(m')\sigma(m, m')m = & \int_0^\infty dm \int_0^m dm' n(m)n(m') \times \\ & \sigma(m, m')m + \int_0^\infty dm \int_m^\infty dm' \times \\ & n(m)n(m')\sigma(m, m')m . \end{aligned} \quad (C.6)$$

Since $\sigma(\mu, M)$ is a symmetric function, we can swap the limits of integration for m and m' in the second integral of Equation (C.6) and, after making a change of variables of $m = \mu$ and $m' = M$ in the first and $m' = \mu$ and $m = M$ in the second integral, the full equation becomes

$$\frac{dM}{dt} = \int_0^\infty d\mu \int_\mu^\infty dM n(\mu)n(M) [\sigma(\mu, M)\mu + \sigma(M, \mu)M - \sigma(\mu, M)(\mu + M)] . \quad (C.7)$$

Since the collisional cross section is completely symmetric, the integral itself becomes zero, thus proving that our equation is mass conserving.

APPENDIX D

NUMERICAL EVALUATION OF THE COLLISIONAL MODEL AND VERIFICATION TESTS

The integro-differential equation presented in §4.3 must be integrated over 40 orders of magnitude in mass space, contains a double integral whose errors can easily increase if not evaluated carefully, and is bundled in a differential equation that evolves the number densities of dust grains and boulders within the same step. These characteristics demand attention in its numerical evaluation. In the following subsections we explain the numerical methods used to evaluate each integral and the ordinary differential equation (ODE). We also present verification and convergence tests for our code, which explain why such precisions are really necessary.

D.1 Taylor series expansion of T_I

First, we expand equation (4.13) to use a Taylor series when $m' \ll m$ and $m' < \mu_X(m)$. For this, we rewrite M in terms of m and m' as

$$M = m + m'G(m, m') , \quad (\text{D.1})$$

where $m'G(m, m')$ equals the cratered mass, m is the largest $X(M, m')$ particle created and $G(m, m')$ can be found by root finding algorithms. As written, $G(m, m')$ can be related to the Γ parameter used by Dohnanyi (1969), for which he used a constant value of 130 for 5 km s^{-1} collisions. We plot the value of $G(m, m')$ as a function of μ and M in Figure D.1, with the thicker solid line giving the contour of $G(m, m') = 100$. This contour lies at sizes reasonable for experiments in laboratory conditions, which is why Dohnanyi (1969) used a value close to it. The

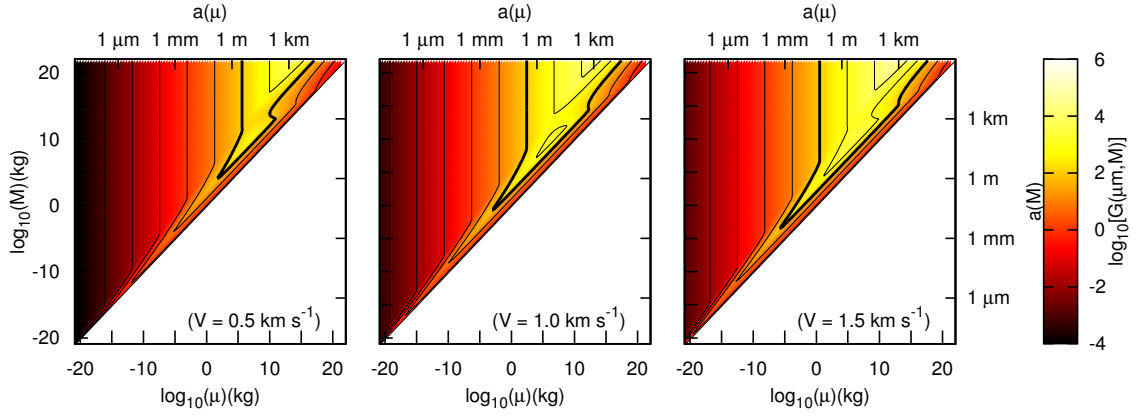


Figure D.1 The values of $G(m, m')$ as a function of the colliding masses. The thick contour is for $G(m, m') = 100$, which is roughly equal to the Γ value used in Dohnanyi (1969). The panels give the contours as a function of collision velocities. The collisional velocities of 0.5, 1.0, and 1.5 km s^{-1} correspond to debris ring radii of 100, 25, and 10 AU around an A spectral type star, respectively. The $G(m, m')$ parameter is strongly dependent on the collisional velocity.

positions of the contours are a strong function of the interaction velocities. The $m' < \mu_X(m)$ integrand can be written as

$$I(m, m') = f(m')w(m')\sigma_w(m')m'^{-\eta}a(m)^2 \left(f(m)w(m)\sigma_w(m)(1+Z)^2 - f(M) \times w(M)\sigma_w(M) [1 + G(m, m')Z^3]^{-\eta} \left\{ Z + [1 + G(m, m')Z^3]^{\frac{1}{3}} \right\}^2 \right) \quad (\text{D.2})$$

where $Z = a(m')/a(m)$ and $f(m)$ and $f(m')$ are dimensionless number densities that can be expressed as

$$f(m) = \frac{n(m)}{Cm^{-\eta}}. \quad (\text{D.3})$$

We rewrite this integrand as

$$I(m, m') = f(m')w(m')\sigma_w(m')m'^{-\eta}a(m)^2f(m)w(m)\sigma_w(m) \left((1+Z)^2 - \frac{f(M)}{f(m)} \times \frac{w(M)\sigma_w(M)}{w(m)\sigma_w(m)} [1 + G(m, m')Z^3]^{-\eta} \left\{ Z + [1 + G(m, m')Z^3]^{\frac{1}{3}} \right\}^2 \right) \quad (\text{D.4})$$

The Taylor series for the components are

$$\begin{aligned} (1+Z)^2 &= 1 + 2Z + Z^2 \\ &\equiv \mathfrak{T}_1 \end{aligned} \quad (\text{D.5})$$

and

$$\begin{aligned} [1 + G(m, m')Z^3] - \eta \left[Z + \sqrt[3]{1 + G(m, m')Z^3} \right]^2 &= 1 + 2Z + Z^2 \\ &\quad + \left[\frac{2G(m, m')}{3} - \eta G(m, m') \right] Z^3 \\ &\quad + \left[\frac{2G(m, m')}{3} - 2\eta G(m, m') \right] Z^4 \\ &\quad - \eta G(m, m')Z^5 \\ &\equiv \mathfrak{T}_1 + \mathfrak{T}_2 \end{aligned} \quad (\text{D.6})$$

Both $f(M)/f(m)$ and $w(M)/w(m)$ are close to 1, while $\sigma_w(M)/\sigma_w(m)$ deviates from 1 as m approaches m_{\max} . In those cases, the ratio can be expressed as

$$\frac{\sigma_w(M)}{\sigma_w(m)} = 1 + \frac{\partial \sigma_w(m)}{\partial M} \Big|_{M=m} (M - m) = 1 - P \frac{\text{Exp} \left(-\frac{m_{\max} - m}{\Theta} \right)}{\Theta \left[1 - \text{Exp} \left(-\frac{m_{\max} - m}{\Theta} \right) \right]} m' G(m, m') , \quad (\text{D.7})$$

since we know that $M - m = m' G(m, m')$. We write this ratio as

$$\frac{\sigma_w(M)}{\sigma_w(m)} = 1 - F . \quad (\text{D.8})$$

The integrand then takes the form

$$I(m, m') = f(m')w(m')\sigma_w(m')m'^{-\eta}a(m)^2f(m)w(m)\sigma_w(m) \times \left[\mathfrak{T}_1 - (\mathfrak{T}_1 + \mathfrak{T}_2) \frac{w(M)f(M)}{w(m)f(m)} (1 - F) \right] . \quad (\text{D.9})$$

Rearranging it gives us

$$I(m, m') = f(m')w(m')\sigma_w(m')m'^{-\eta}a(m)^2f(m)w(m)\sigma_w(m) \times \left\{ \mathfrak{T}_1 \left[1 - (1 - F) \frac{w(M)f(M)}{w(m)f(m)} \right] - \mathfrak{T}_2 \frac{w(M)f(M)}{w(m)f(m)} (1 - F) \right\} \quad (\text{D.10})$$

When

$$1 - \frac{w(M)f(M)}{w(m)f(m)} < 10^{-9}, \quad (\text{D.11})$$

we use the approximate formula

$$I(m, m') = f(m')w(m')\sigma_w(m')m'^{-\eta}a(m)^2f(M)w(M)\sigma_w(m) \times \left[\mathfrak{T}_1 F - \mathfrak{T}_2 (1 - F) \right]. \quad (\text{D.12})$$

We use the Taylor series of the components to write the integrand below the limit of $Z < 10^{-3}$ (i.e., $m'/m < 10^{-9}$). This means that our full integral for the first term (T_1) takes the final form

$$\begin{aligned} \frac{df_I(m, t)}{dt} = -V\pi C & \left\{ \int_{m_{\min}}^{\mu_X(m)} dm' \mathcal{I} \right. \\ & \left. + \int_{\mu_X(m)}^{m_{\max}} dm' f(m', t) (m')^{-\eta} f(m, t) (a(m) + a(m'))^2 \right\} \quad (\text{D.13}) \end{aligned}$$

where

$$\mathcal{I} = \begin{cases} f(m')w(m')\sigma_w(m')m'^{-\eta}a(m)^2f(m)w(m)\sigma_w(m) \times \\ \quad \left\{ \mathfrak{T}_1 \left[1 - (1-F) \frac{w(M)f(M)}{w(m)f(m)} \right] - \mathfrak{T}_2 \frac{w(M)f(M)}{w(m)f(m)} (1-F) \right\} \\ \quad \text{if } m' < m \times 10^{-9} \ \& \ 1 - \frac{w(M)f(M)}{w(m)f(m)} \geq 10^{-9} \\ f(m')w(m')\sigma_w(m')m'^{-\eta}a(m)^2f(M)w(M)\sigma_w(m) \times \left[\mathfrak{T}_1 F - \mathfrak{T}_2 (1-F) \right] \\ \quad \text{if } m' < m \times 10^{-9} \ \& \ 1 - \frac{w(M)f(M)}{w(m)f(m)} < 10^{-9} \\ f(m', t)(m')^{-\eta} \left[f(m, t) (a(m) + a(m'))^2 - f(M, t) \left(\frac{M}{m} \right)^{-\eta} (a(M) + a(m'))^2 \right] \\ \quad \text{if } m \times 10^{-9} \leq m' < \mu_X(m) \end{cases}$$

In Figure D.2, we show the mass of the X fragments created when particles of mass μ and M collide. The $m = X(\mu, M)$ regions are well defined in our single collisional velocity case. When using collisional velocity that depends on particle size, more than one $\mu_X(m)$ boundary may exist.

D.2 Verification of the numerical precision of T_I

To verify the precision of our integrator we set up an equation that is similar to T_I in behavior and that has an analytic solution and compare values given by our code to it. The integral we evaluate both analytically and numerically with our code is

$$TV_I(m) = \int_{m_{\min}}^{\mu_X(m)} dm' (m')^{-\eta} \left\{ \left(m^{\frac{1}{3}} + m'^{\frac{1}{3}} \right)^2 - \left[(m + m'\Gamma)^{\frac{1}{3}} + m'^{\frac{1}{3}} \right]^2 \times \right. \\ \left. \left(\frac{m + m'\Gamma}{m} \right)^{-\eta} \right\} + \int_{\mu_X(m)}^{m_{\max}} dm' (m')^{-\eta} \left(m^{\frac{1}{3}} + m'^{\frac{1}{3}} \right)^2, \quad (\text{D.14})$$

where we have removed all the constants and the dimensionless number densities. We have also replaced $G(m', m)$ with a constant Γ (which can be related to the Γ parameter used by Dohnanyi 1969) to enable an analytic solution. To verify

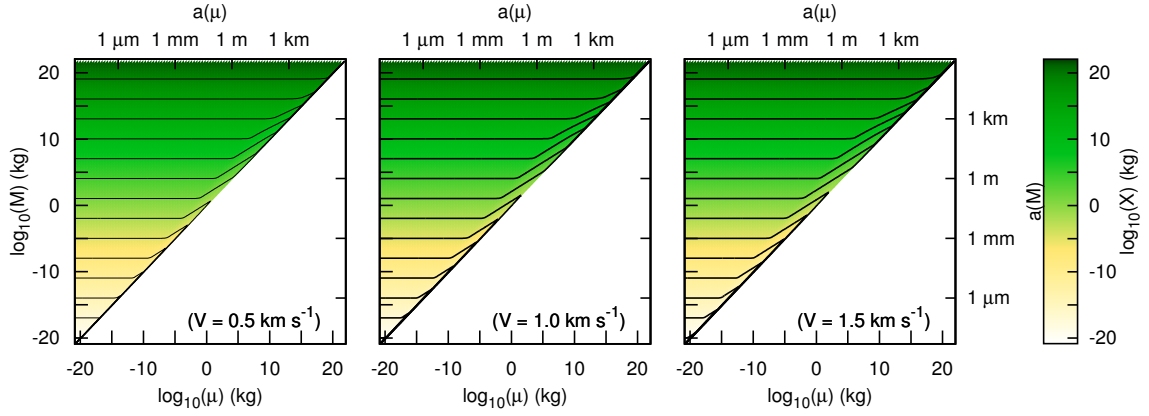


Figure D.2 The largest X fragment produced by collisions between particles μ and M as a function of collision velocities. The collisional velocities of 0.5, 1.0, and 1.5 km s^{-1} correspond to debris ring radii of 100, 25, and 10 AU around an A spectral type star, respectively.

our algorithm for the evaluation of this term we set the initial particle distribution to a power-law ($\eta=11/6$). The integration boundary can be evaluated as

$$\mu_X(m) = \begin{cases} \frac{m}{1-\Gamma} & \text{if } \Gamma < 1 \\ \frac{m_{\max}-m}{\Gamma} & \text{if } \Gamma \geq 1 \end{cases} \quad (\text{D.15})$$

The first integral is (setting $Z \equiv \frac{m'}{m}$)

$$\mathfrak{F} = -\frac{2}{5}Z^{-\frac{2}{3}}m'^{-\frac{1}{6}} \left\{ \left(15Z^{\frac{2}{3}} + 10Z^{\frac{1}{3}} + 3 \right) - (1 + \Gamma Z)^{\frac{1}{6}} \times \left[\frac{10Z^{\frac{1}{3}}(1 + 2Z\Gamma)}{(1 + Z\Gamma)^{\frac{2}{3}}} + \frac{3(1 + 6Z\Gamma)}{(1 + Z\Gamma)^{\frac{1}{3}}} + \frac{3Z^{\frac{2}{3}}(5 + 6Z\Gamma)}{1 + Z\Gamma} \right] \right\}. \quad (\text{D.16})$$

When $\frac{m'}{m} = Z < 10^{-9}$, the equation does not describe the analytic result correctly as the first three components completely cancel the last three components numerically; however, analytically the result is not zero and this non-zero component gets multiplied by a large number. This is the same catastrophic cancellation that

affects the numerical evaluation of $T_I(m)$. To overcome this and correctly represent the analytic result of the integral in such cases, we rewrote this to a Taylor series as well. The first three components cancel, and we are left with

$$\begin{aligned} \mathfrak{F} = & +\frac{2}{5}Z^{-2/3}m'^{-1/6}\left[\frac{35}{2}\Gamma Z + 15\Gamma Z^{4/3} + \frac{11}{2}\Gamma Z^{5/3} - \frac{65}{24}\Gamma^2 Z^2 \right. \\ & \left. - \frac{25}{4}\Gamma^2 Z^{7/3} - \frac{85}{24}\Gamma^2 Z^{8/3} + \frac{665}{432}\Gamma^3 Z^3\right]. \end{aligned} \quad (\text{D.17})$$

The second integrand has a much simpler anti-derivative

$$\mathfrak{F} = -\frac{6}{5}\frac{m^{2/3}}{m'^{5/6}} - 4\frac{m^{1/3}}{m'^{1/2}} - \frac{6}{m'^{1/6}} \quad (\text{D.18})$$

In Figure D.3, we show the computational error as a function of mass m , the Γ constant and the number of grid points used (neighboring grid point mass ratio). In the actual model Γ is not a constant, but equal to the variable $G(m, m')$ which, as shown in Figure D.1, varies from 10^{-4} to 10^6 . Figure D.3 shows that the errors do not improve much past $N=1000$ ($\delta = 1.1$) and that, in general, errors are smaller for large values of Γ . This shows that errors originating from T_I are most likely to affect the smallest particles in the system. We expect the errors to actually be completely symmetric, with the highest masses showing the same quantitative errors as the lowest masses near the boundary. Offsets are due to the fact that our analytic model includes targets larger than m_{\max} . The maximum error of 10^{-4} is not ideal, but acceptable. When running our code, we use $N=1000$ grid points, which corresponds to a $\delta = 1.1$.

D.3 Numerical evaluation of T_{II}

As a double integral, the second term, T_{II} , poses a larger challenge to achieve acceptable precision. A collision between masses μ and M will be able to produce a mass m in the redistribution power-law, if $m < Y(\mu, M)$. In Figure D.4 we

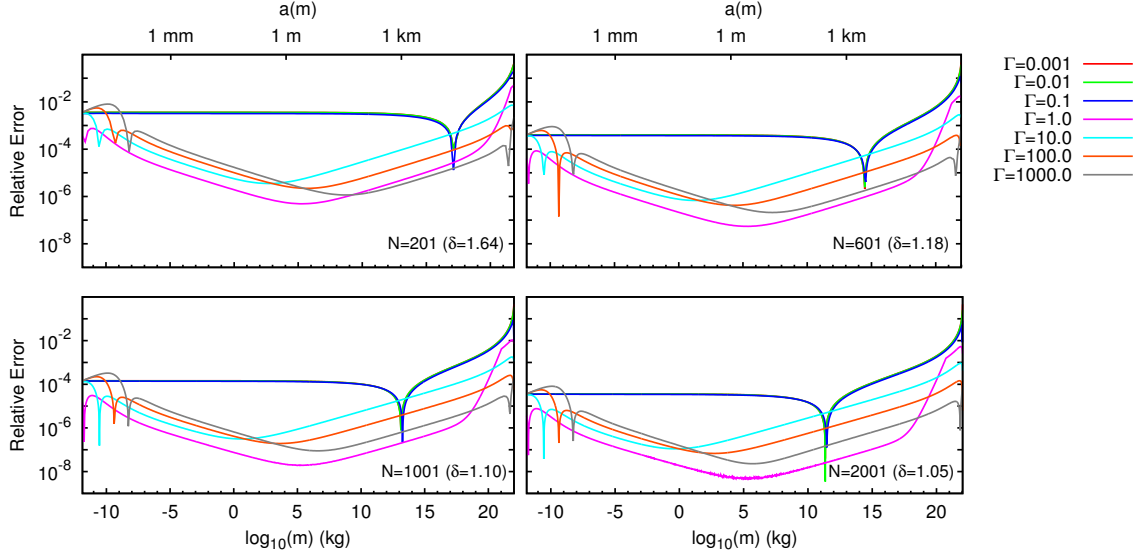


Figure D.3 The error in the integration of T_I as a function of the mass m and the value of the Γ constant for neighboring mass grid ratios of $\delta = 1.64, 1.18, 1.10$ and 1.05 .

plot the iso- Y contours in the μ vs. M phase space, which shows that integrating between exact boundaries is difficult for T_{II} , especially if the collisional velocity is not a constant but a function of the particle mass.

As a first step, we determine which m masses can be produced by the grid points (μ, M) and their neighbors. For a grid point to be able to produce a particle of mass m , $Y(\mu, M)$ has to be larger than m . We determine the limiting mass that is produced by each grid point and all of their neighbors as well. Up to that $\min(\mu, M)$ value, all m masses are produced with the full weight of the grid point. Between $\min(\mu, M)$ and $\max(\mu, M)$ - which is the largest m still produced by the (μ, M) grid point itself - we analyze the areas divided into quadrants, and assign integration weights appropriately. A simple plot is shown in Figure D.5 to explain the weights given to each grid point.

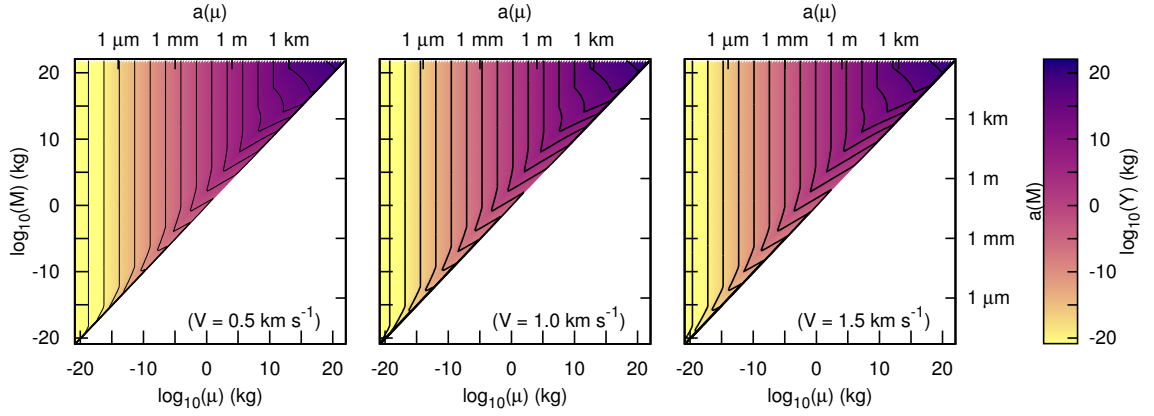


Figure D.4 Iso-size contours for the produced Y fragments as a function of the colliding body sizes and interaction velocities. Fragments of size $a(m)$ will be produced within regions where $a(m) < a(Y)$. The largest fragments produced are not heavily dependent on the interaction velocities. The collisional velocities of 0.5, 1.0 and 1.5 km s^{-1} correspond to debris ring radii of 100, 25 and 10 AU around an A spectral type star, respectively.

These minimum and maximum masses are usually at most 2-3 grid points apart. This means that on average 2-3 numbers have to be stored for all $(\mu; M)$ grid points, as below $\min(\mu, M)$ all m masses have the same weight. The final integration speed can be increased by factors of 5 as the integration loops can be run in non-redundant ways.

D.4 Convergence tests

We run convergence tests on our code for both terms to find the least number of grid points we can use and still keep an acceptable numerical accuracy. We calculate convergence to the value given using 4000 grid points. Our convergence plot for T_1 in Figure D.6 shows that, for such a large dynamic range in masses, one

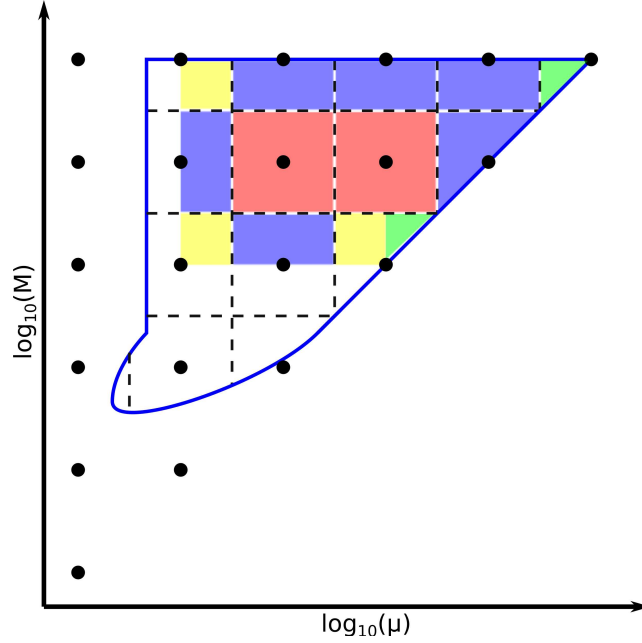


Figure D.5 Description of the integration method used for T_{II} . The blue line represents the boundary, within which collisions are able to produce a certain mass m in the redistribution power-law. Resolution elements capable of producing m on their full area are colored red. Boundary resolution elements (i.e., $\mu \equiv M$ or $M \equiv m_{\max}$) will be able to produce m on a “half” area, colored blue. The tip of the distribution (green) will be able to produce on an eighth of its full area. Partial quarter contributions are given by the yellow areas. Increasing the number of grid points used obviously increases not just the precision but the area used for the integration as well.

needs a neighboring grid mass ratio of at most $\delta = 1.1$ to reach a relative error of 10^{-5} .

Our convergence test for T_{II} does not reach the same level of accuracy, as at $\delta \approx 1.1$ we reach a relative error of 10^{-2} only. However, this error is driven by the resolution dependent integration limits and not the method itself. As such

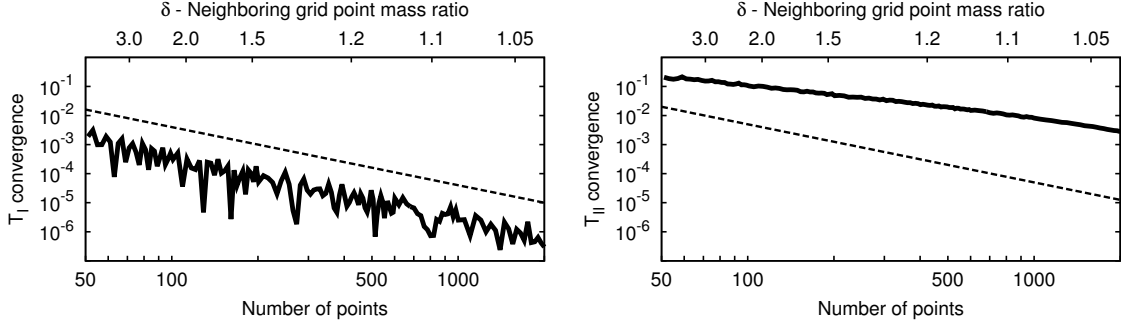


Figure D.6 Convergence test results of our code. The *left panel* gives the results for T_I , while the *right panel* for T_{II} . We also plot a N^{-2} curve with a dashed line, which is the effective accuracy of the trapezoid integration method. The accuracy of the first term follows this trend, however, that of the second term is shallower, due to the resolution dependent integration limits.

the number of particles added by T_{II} will always be underestimated by a small amount.

D.5 The ODE solver

Previous work (i.e., Thébault et al., 2003; Thébault & Augereau, 2007; Krivov et al., 2000; Löhne et al., 2008) used only a first order Eulerian algorithm to solve the differential equation. We are using a 4th order Runge-Kutta algorithm (RK4). To verify the ODE solver we simply evolve the Poynting-Robertson drag term, whose analytic solution is

$$n(m, t) = n(m, t = 0) \exp \left(-\frac{t}{\tau_{\text{PRD}}} \right). \quad (\text{D.19})$$

In the following, we verified the accuracy of the ODE integrator by setting $\beta \equiv 0.100$ for the particles and using the solar system timescale of 400 years.

Using the results from the code, we define the ratio of the particle density at some time t to the particle density at time zero, i.e., $R_{\text{code}} \equiv f(m, t)/f(m, t = 0)$,

and compare it to the analytic result, $R_{\text{exp}} = \exp(-t/\tau_{\text{PRD}})$. We then compute the fractional error between the numerical and the analytic solution. The left panel of Figure D.7 shows the fractional error as a function of the time step Δt , evaluated at a time roughly $t \approx \tau_{\text{PRD}}$ (4000 years) for both the RK4 and Euler method.

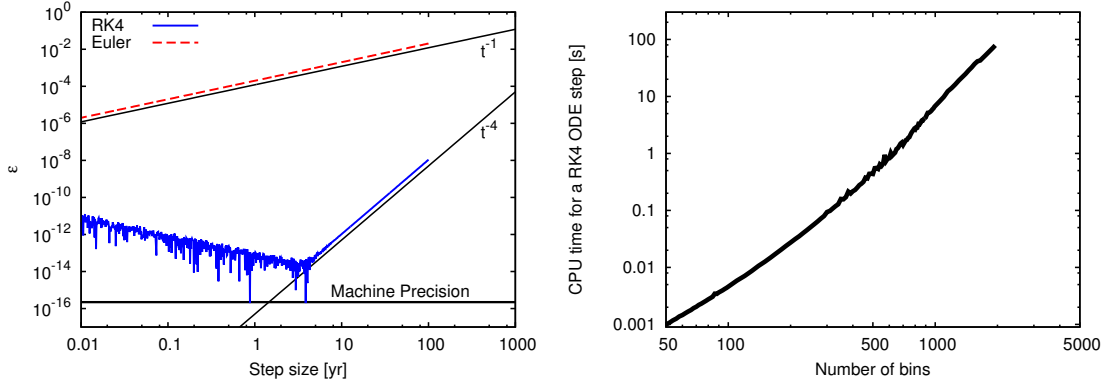


Figure D.7 *Left Panel*: The fractional difference between the numerical and analytical results at a time roughly equal to 4000 yr as a function of the time step used. We show errors for both an Euler ODE solver and for our RK4 algorithm. We also plot a t^{-1} and a t^{-4} curve to guide the eye. *Right Panel*: The amount of processor time needed by our code to complete an RK4 step as a function of the number of mass grid points used.

For this particular set-up, the optimal time step is ~ 4 yr for the RK4. However, the optimal time step depends on the time t at which the fractional difference is evaluated because of the accumulation of round-off errors. Finally, the right panel of Figure D.7 shows the amount of CPU time taken to calculate an RK4 step as a function of the number of mass grid points used on a Mac Pro4 with 2 2.26 GHz Quad Core Intel Xeon processors.

REFERENCES

- Absil, O., Mennesson, B., Le Bouquin, J.-B., Di Folco, E., Kervella, P., & Augereau, J.-C. 2009, *ApJ*, 704, 150
- An, D., Terndrup, D. M., Pinsonneault, M. H., Paulson, D. B., Hanson, R. B., & Stauffer, J. R. 2007, *ApJ*, 655, 233
- Andruk, V., Kharchenko, N., Schilbach, E., & Scholz, R. D. 1995, *Astronomische Nachrichten*, 316, 225
- Anthony-Twarog, B. J. 1982, *ApJ*, 255, 245
- Argyle, R. W., Alzner, A., & Horch, E. P. 2002, *A&A*, 384, 171
- Artymowicz, P., & Clampin, M. 1997, *ApJ*, 490, 863
- Augereau, J.-C., & Beust, H. 2006, *A&A*, 455, 987
- Aumann, H. H. 1985, *PASP*, 97, 885
- . 1988, *AJ*, 96, 1415
- Aumann, H. H., et al. 1984, *ApJL*, 278, L23
- Backman, D., et al. 2009, *ApJ*, 690, 1522
- Backman, D. E., & Paresce, F. 1993, in *Protostars and Planets III*, ed. E. H. Levy & J. I. Lunine, 1253–1304
- Balog, Z., Muzerolle, J., Rieke, G. H., Su, K. Y. L., Young, E. T., & Megeath, S. T. 2007, *ApJ*, 660, 1532
- Bandermann, L. W. 1972, *MNRAS*, 160, 321

- Barrado y Navascués, D., Stauffer, J. R., & Jayawardhana, R. 2004, *ApJ*, 614, 386
- Barrado y Navascués, D., Stauffer, J. R., & Randich, S. 1998, *ApJ*, 506, 347
- Beichman, C. A., et al. 2005, *ApJ*, 622, 1160
- . 2006, *ApJ*, 652, 1674
- Benz, W., & Asphaug, E. 1999, *Icarus*, 142, 5
- Boccaletti, A., Augereau, J.-C., Baudoz, P., Pantin, E., & Lagrange, A.-M. 2009, *A&A*, 495, 523
- Bockelée-Morvan, D., André, P., Colom, P., Colas, F., Crovisier, J., Despois, D., & Jorda, L. 1994, in *Circumstellar Dust Disks and Planet Formation*, ed. R. Ferlet & A. Vidal-Madjar, 341–+
- Boesgaard, A. M., & Budge, K. G. 1988, *ApJ*, 332, 410
- Bondi, H., & Hoyle, F. 1944, *MNRAS*, 104, 273
- Borucki, W. J., et al. 2010, *Science*, 327, 977
- Boss, A. P. 1997, *Science*, 276, 1836
- Bottke, W. F., Durda, D. D., Nesvorný, D., Jedicke, R., Morbidelli, A., Vokrouhlický, D., & Levison, H. 2005, *Icarus*, 175, 111
- Bottke, W. F., Levison, H. F., Nesvorný, D., & Dones, L. 2007, *Icarus*, 190, 203
- Bouvier, J., Duchêne, G., Mermilliod, J.-C., & Simon, T. 2001, *A&A*, 375, 989
- Briceño, C., Calvet, N., Hernández, J., Vivas, A. K., Hartmann, L., Downes, J. J., & Berlind, P. 2005, *AJ*, 129, 907

- Bryden, G., et al. 2006, *ApJ*, 636, 1098
- Burns, J. A., Lamy, P. L., & Soter, S. 1979, *Icarus*, 40, 1
- Campo Bagatin, A., Cellino, A., Davis, D. R., Farinella, P., & Paolicchi, P. 1994, *Planet. Space Sci.*, 42, 1079
- Carpenter, J. M., Wolf, S., Schreyer, K., Launhardt, R., & Henning, T. 2005, *AJ*, 129, 1049
- Carpenter, J. M., et al. 2008, *ApJS*, 179, 423
- . 2009, *ApJS*, 181, 197
- Castelaz, M. W., Persinger, T., Stein, J. W., Prosser, J., & Powell, H. D. 1991, *AJ*, 102, 2103
- Castellani, V., Degl’Innocenti, S., Prada Moroni, P. G., & Tordiglione, V. 2002, *MNRAS*, 334, 193
- Castelli, F., & Kurucz, R. L. 2003, in *IAU Symposium*, Vol. 210, *Modelling of Stellar Atmospheres*, ed. N. Piskunov, W. W. Weiss, & D. F. Gray, 20P—+
- Chapman, C. R., Cohen, B. A., & Grinspoon, D. H. 2007, *Icarus*, 189, 233
- Charbonneau, P. 1991, *ApJL*, 372, L33
- Chen, C. H., Jura, M., Gordon, K. D., & Blaylock, M. 2005, *ApJ*, 623, 493
- Chen, C. H., et al. 2006, *ApJS*, 166, 351
- Chini, R., Kruegel, E., Kreysa, E., Shustov, B., & Tutukov, A. 1991, *A&A*, 252, 220
- Cieza, L. A., Cochran, W. D., & Augereau, J.-C. 2008, *ApJ*, 679, 720

- Cote, J. 1987, *A&A*, 181, 77
- Cox, A. N. 2000, *Allen's astrophysical quantities*, ed. Cox, A. N.
- Crawford, I. A., Lallement, R., & Welsh, B. Y. 1998, *MNRAS*, 300, 1181
- Currie, T., Kenyon, S. J., Balog, Z., Rieke, G., Bragg, A., & Bromley, B. 2008, *ApJ*, 672, 558
- Currie, T., Lisse, C. M., Sicilia-Aguilar, A., Rieke, G. H., & Su, K. Y. L. 2011, *ApJ*, 734, 115
- Cuzzi, J. N., Hogan, R. C., Paque, J. M., & Dobrovolskis, A. R. 2001, *ApJ*, 546, 496
- D'Angelo, G., Durisen, R. H., & Lissauer, J. J. 2010, *Giant Planet Formation*, ed. Seager, S., 319–346
- Dauphas, N., & Chaussidon, M. 2011, *Annual Review of Earth and Planetary Sciences*, 39, 351
- Davis, D. R., & Ryan, E. V. 1990, *Icarus*, 83, 156
- Dermott, S. F., Grogan, K., Holmes, E., & Kortenkamp, S. 1999, in *NATO ASIC Proc. 523: Formation and Evolution of Solids in Space*, ed. J. M. Greenberg & A. Li, 565–+
- Dermott, S. F., Jayaraman, S., Xu, Y. L., Gustafson, B. Å. S., & Liou, J. C. 1994, *Nature*, 369, 719
- di Folco, E., et al. 2007, *A&A*, 475, 243
- Dickens, R. J., Kraft, R. P., & Krzeminski, W. 1968, *AJ*, 73, 6
- Dobbie, P. D., et al. 2006, *MNRAS*, 369, 383

- Dohnanyi, J. S. 1969, *J. Geophys. Res.*, 74, 2531
- Dominik, C., & Decin, G. 2003, *ApJ*, 598, 626
- Draine, B. T., & Lee, H. M. 1984, *ApJ*, 285, 89
- Dullemond, C. P., & Dominik, C. 2005, *A&A*, 434, 971
- Durda, D. D., & Dermott, S. F. 1997, *Icarus*, 130, 140
- Eiroa, C., et al. 2010, *A&A*, 518, L131+
- Engelbracht, C. W., et al. 2007, *PASP*, 119, 994
- France, K., McCandliss, S. R., & Lupu, R. E. 2007, *ApJ*, 655, 920
- Franciosini, E., Randich, S., & Pallavicini, R. 2003, *A&A*, 405, 551
- Fuchs, B., Breitschwerdt, D., de Avillez, M. A., Dettbarn, C., & Flynn, C. 2006, *MNRAS*, 373, 993
- Fujiwara, A., Kamimoto, G., & Tsukamoto, A. 1977, *Icarus*, 31, 277
- Fukugita, M., Ichikawa, T., Gunn, J. E., Doi, M., Shimasaku, K., & Schneider, D. P. 1996, *AJ*, 111, 1748
- Gáspár, A., Rieke, G. H., Psaltis, D., Özel, F., & Cooney, A. 2011, *ApJ*
- Gáspár, A., Rieke, G. H., Su, K. Y. L., Balog, Z., Trilling, D., Muzzerole, J., Apai, D., & Kelly, B. C. 2009, *ApJ*, 697, 1578
- Gáspár, A., Su, K. Y. L., Rieke, G. H., Balog, Z., Kamp, I., Martínez-Galarza, J. R., & Stapelfeldt, K. 2008, *ApJ*, 672, 974
- Gatewood, G., & de Jonge, J. K. 1994, *ApJ*, 428, 166

- Gault, D. E., & Wedekind, J. A. 1969, *J. Geophys. Res.*, 74, 6780
- Gautier, III, T. N., Rebull, L. M., Stapelfeldt, K. R., & Mainzer, A. 2008, *ApJ*, 683, 813
- Gautier, III, T. N., et al. 2007, *ApJ*, 667, 527
- Gillett, F. C. 1986, in *Astrophysics and Space Science Library*, Vol. 124, *Light on Dark Matter*, ed. F. P. Israel, 61–69
- Girardi, L., Grebel, E. K., Odenkirchen, M., & Chiosi, C. 2004, *A&A*, 422, 205
- Golimowski, D. A., et al. 2011, *AJ*, 142, 30
- Gomes, R., Levison, H. F., Tsiganis, K., & Morbidelli, A. 2005, *Nature*, 435, 466
- González-García, B. M., Zapatero Osorio, M. R., Béjar, V. J. S., Bihain, G., Barrado Y Navascués, D., Caballero, J. A., & Morales-Calderón, M. 2006, *A&A*, 460, 799
- Gordon, K. D., et al. 2005, *PASP*, 117, 503
- . 2007, *PASP*, 119, 1019
- Gorlova, N., Balog, Z., Rieke, G. H., Muzerolle, J., Su, K. Y. L., Ivanov, V. D., & Young, E. T. 2007, *ApJ*, 670, 516
- Gorlova, N., Rieke, G. H., Muzerolle, J., Stauffer, J. R., Siegler, N., Young, E. T., & Stansberry, J. H. 2006, *ApJ*, 649, 1028
- Gorlova, N., et al. 2004, *ApJS*, 154, 448
- Gorti, U., & Hollenbach, D. 2009, *ApJ*, 690, 1539
- Gray, R. O. 1988, *AJ*, 95, 220

- Gray, R. O., Corbally, C. J., Garrison, R. F., McFadden, M. T., Bubar, E. J., McGahee, C. E., O'Donoghue, A. A., & Knox, E. R. 2006, *AJ*, 132, 161
- Greaves, J. S., & Wyatt, M. C. 2003, *MNRAS*, 345, 1212
- Greaves, J. S., et al. 2005, *ApJL*, 619, L187
- Greenberg, R., Hartmann, W. K., Chapman, C. R., & Wacker, J. F. 1978, *Icarus*, 35, 1
- Grogan, K., Dermott, S. F., & Durda, D. D. 2001, *Icarus*, 152, 251
- Grun, E., Zook, H. A., Fechtig, H., & Giese, R. H. 1985, *Icarus*, 62, 244
- Habing, H. J., et al. 2001, *A&A*, 365, 545
- Haisch, Jr., K. E., Lada, E. A., & Lada, C. J. 2001, *ApJL*, 553, L153
- Halbwachs, J. L., Mayor, M., Udry, S., & Arenou, F. 2003, *A&A*, 397, 159
- Hambly, N. C., Steele, I. A., Hawkins, M. R. S., & Jameson, R. F. 1995, *A&AS*, 109, 29
- Hanbury Brown, R., Davis, J., & Allen, L. R. 1974, *MNRAS*, 167, 121
- Hartmann, L., Calvet, N., Gullbring, E., & D'Alessio, P. 1998, *ApJ*, 495, 385
- Hartmann, W. K., Ryder, G., Dones, L., & Grinspoon, D. 2000, *The Time-Dependent Intense Bombardment of the Primordial Earth/Moon System*, ed. Canup, R. M., Richter, K., & et al., 493–512
- Harwit, M. 1963, *J. Geophys. Res.*, 68, 2171
- Hauck, B. 1981, *A&A*, 99, 207

- Hellyer, B. 1970, *MNRAS*, 148, 383
- Heney, L. G., & Greenstein, J. L. 1938, *ApJ*, 88, 580
- Herbstmeier, U., & Wennmacher, A. 1998, in *Lecture Notes in Physics*, Berlin Springer Verlag, Vol. 506, IAU Colloq. 166: The Local Bubble and Beyond, ed. D. Breitschwerdt, M. J. Freyberg, & J. Truemper, 117–120
- Hernández, J., Briceño, C., Calvet, N., Hartmann, L., Muzerolle, J., & Quintero, A. 2006, *ApJ*, 652, 472
- Hillenbrand, L. A., et al. 2008, *ApJ*, 677, 630
- Holland, W. S., et al. 1998, *Nature*, 392, 788
- . 2003, *ApJ*, 582, 1141
- Hollenbach, D., Johnstone, D., Lizano, S., & Shu, F. 1994, *ApJ*, 428, 654
- Holsapple, K., Giblin, I., Housen, K., Nakamura, A., & Ryan, E. 2002, *Asteroids III*, 443
- Holweger, H., Hempel, M., & Kamp, I. 1999, *A&A*, 350, 603
- Horch, E., Franz, O. G., & Ninkov, Z. 2000, *AJ*, 120, 2638
- Jeffries, R. D., Thurston, M. R., & Hambly, N. C. 2001, *A&A*, 375, 863
- Jenkins, E. B. 2002, *ApJ*, 580, 938
- Jester, S., et al. 2005, *AJ*, 130, 873
- Johansen, A., Klahr, H., & Henning, T. 2006, *ApJ*, 636, 1121
- Johnson, H. L. 1952, *ApJ*, 116, 640

- Jones, B. F., & Cudworth, K. 1983, *AJ*, 88, 215
- Jones, B. F., & Stauffer, J. R. 1991, *AJ*, 102, 1080
- Jordi, K., Grebel, E. K., & Ammon, K. 2006, *A&A*, 460, 339
- Jutzi, M., Michel, P., Benz, W., & Richardson, D. C. 2010, *Icarus*, 207, 54
- Kalas, P., Graham, J. R., Beckwith, S. V. W., Jewitt, D. C., & Lloyd, J. P. 2002, *ApJ*, 567, 999
- Kalas, P., et al. 2008, *Science*, 322, 1345
- Kamp, I., & Paunzen, E. 2002, *MNRAS*, 335, L45
- Kellerer, A., Petr-Gotzens, M. G., Kervella, P., & Coudé du Foresto, V. 2007, *A&A*, 469, 633
- Kenyon, S. J., & Bromley, B. C. 2004, *AJ*, 127, 513
- Kim, J. S., et al. 2005, *ApJ*, 632, 659
- King, J. R., Villarreal, A. R., Soderblom, D. R., Gulliver, A. F., & Adelman, S. J. 2003, *AJ*, 125, 1980
- Klein Wassink, W. J. 1927, *Publications of the Kapteyn Astronomical Laboratory Groningen*, 41, 1
- Kobayashi, H., & Tanaka, H. 2010, *Icarus*, 206, 735
- Koschny, D., & Grün, E. 2001a, *Icarus*, 154, 391
- . 2001b, *Icarus*, 154, 402
- Kraus, A. L., & Hillenbrand, L. A. 2007, *AJ*, 134, 2340

- Kresak, L. 1976, *Bulletin of the Astronomical Institutes of Czechoslovakia*, 27, 35
- Krist, J. E., et al. 2010, *AJ*, 140, 1051
- Krivov, A. V., Löhne, T., & Sremčević, M. 2006, *A&A*, 455, 509
- Krivov, A. V., Mann, I., & Krivova, N. A. 2000, *A&A*, 362, 1127
- Krivov, A. V., Müller, S., Löhne, T., & Mutschke, H. 2008, *ApJ*, 687, 608
- Krivov, A. V., Sremčević, M., & Spahn, F. 2005, *Icarus*, 174, 105
- Kuchner, M. J., & Stark, C. C. 2010, *AJ*, 140, 1007
- Lagrange, A.-M., et al. 2010, *Science*, 329, 57
- Lallement, R. 1998, in *Lecture Notes in Physics*, Berlin Springer Verlag, Vol. 506, IAU Colloq. 166: The Local Bubble and Beyond, ed. D. Breitschwerdt, M. J. Freyberg, & J. Truemper, 19–28
- Lallement, R., Ferlet, R., Lagrange, A. M., Lemoine, M., & Vidal-Madjar, A. 1995, *A&A*, 304, 461
- Laor, A., & Draine, B. T. 1993, *ApJ*, 402, 441
- Lebreton, Y., Fernandes, J., & Lejeune, T. 2001, *A&A*, 374, 540
- Leinhardt, Z. M., & Stewart, S. T. 2011, *ArXiv e-prints*
- Leliwa-Kopystyński, J., Burchell, M. J., & Włodarczyk, I. 2009, *Meteoritics and Planetary Science*, 44, 1929
- Liseau, R., Brandeker, A., Fridlund, M., Olofsson, G., Takeuchi, T., & Artymowicz, P. 2003, *A&A*, 402, 183

- Lissauer, J. J., & Griffith, C. A. 1989, *ApJ*, 340, 468
- Lissauer, J. J., & Stewart, G. R. 1993, in *Protostars and Planets III*, ed. E. H. Levy & J. I. Lunine, 1061–1088
- Liu, M. C., Matthews, B. C., Williams, J. P., & Kalas, P. G. 2004, *ApJ*, 608, 526
- Löhne, T., Krivov, A. V., & Rodmann, J. 2008, *ApJ*, 673, 1123
- Loktin, A. V. 2000, *Astronomy Letters*, 26, 657
- Love, S. G., & Brownlee, D. E. 1993, *Science*, 262, 550
- Lutz, T. E., & Kelker, D. H. 1973, *PASP*, 85, 573
- Lutz, T. E., & Lutz, J. H. 1977, *AJ*, 82, 431
- Lyo, A.-R., Lawson, W. A., Feigelson, E. D., & Crause, L. A. 2004, *MNRAS*, 347, 246
- Mamajek, E. E., Lawson, W. A., & Feigelson, E. D. 1999, *ApJL*, 516, L77
- Mamajek, E. E., Meyer, M. R., Hinz, P. M., Hoffmann, W. F., Cohen, M., & Hora, J. L. 2004, *ApJ*, 612, 496
- Mamajek, E. E., Meyer, M. R., & Liebert, J. 2002, *AJ*, 124, 1670
- Mannings, V., & Barlow, M. J. 1998, *ApJ*, 497, 330
- Marois, C., Macintosh, B., Barman, T., Zuckerman, B., Song, I., Patience, J., Lafrenière, D., & Doyon, R. 2008, *Science*, 322, 1348
- Marsh, K. A., Velusamy, T., Dowell, C. D., Grogan, K., & Beichman, C. A. 2005, *ApJL*, 620, L47

- Marshall, J. P., et al. 2011, *A&A*, 529, A117+
- Martín, E. L., Dahm, S., & Pavlenko, Y. 2001, in *Astronomical Society of the Pacific Conference Series*, Vol. 245, *Astrophysical Ages and Times Scales*, ed. T. von Hippel, C. Simpson, & N. Manset, 349–+
- Martínez-Galarza, J. R., Kamp, I., Su, K. Y. L., Gáspár, A., Rieke, G., & Mamajek, E. E. 2009, *ApJ*, 694, 165
- Mason, B. D., Hartkopf, W. I., McAlister, H. A., & Sowell, J. R. 1993, *AJ*, 106, 637
- Mathis, J. S., Rimpl, W., & Nordsieck, K. H. 1977, *ApJ*, 217, 425
- Matsui, T., Waza, T., & Kani, K. 1984, *J. Geophys. Res.*, 89, 700
- Matsuyama, I., Johnstone, D., & Hollenbach, D. 2009, *ApJ*, 700, 10
- Matthews, B. C., et al. 2010, *A&A*, 518, L135+
- Mayor, M., & Queloz, D. 1995, *Nature*, 378, 355
- Mendoza, E. E. 1967, *Boletín de los Observatorios Tonantzintla y Tacubaya*, 4, 149
- Mermilliod, J.-C., Duquennoy, A., & Mayor, M. 1994, *A&A*, 283, 515
- Mermilliod, J.-C., & Mayor, M. 1999, *A&A*, 352, 479
- Mermilliod, J.-C., Weis, E. W., Duquennoy, A., & Mayor, M. 1990, *A&A*, 235, 114
- Meyer, D. M., Lauroesch, J. T., Heiles, C., Peek, J. E. G., & Engelhorn, K. 2006, *ApJL*, 650, L67
- Meyer, M. R., et al. 2004, *ApJS*, 154, 422
- . 2008, *ApJL*, 673, L181

- Meynet, G., Mermilliod, J.-C., & Maeder, A. 1993, *A&AS*, 98, 477
- Moór, A., Ábrahám, P., Derekas, A., Kiss, C., Kiss, L. L., Apai, D., Grady, C., & Henning, T. 2006, *ApJ*, 644, 525
- Morales, F. Y., Rieke, G. H., Werner, M. W., Bryden, G., Stapelfeldt, K. R., & Su, K. Y. L. 2011, *ApJL*, 730, L29
- Morbidelli, A., Petit, J.-M., Gladman, B., & Chambers, J. 2001, *Meteoritics and Planetary Science*, 36, 371
- Müller, S., Löhne, T., & Krivov, A. V. 2010, *ApJ*, 708, 1728
- Najita, J., & Williams, J. P. 2005, *ApJ*, 635, 625
- Nilsson, R., et al. 2010, *A&A*, 518, A40+
- Nissen, P. E. 1988, *A&A*, 199, 146
- Noriega-Crespo, A., van Buren, D., & Dgani, R. 1997, *AJ*, 113, 780
- O'Brien, D. P., & Greenberg, R. 2005, *Icarus*, 178, 179
- Odenkirchen, M., Soubiran, C., & Colin, J. 1998, *New Ast.*, 3, 583
- Oja, T. 1985, *A&AS*, 61, 331
- Ortega, V. G., de la Reza, R., Jilinski, E., & Bazzanella, B. 2002, *ApJL*, 575, L75
- Otero, S. A., Fieseler, P. D., & Lloyd, C. 2000, *Information Bulletin on Variable Stars*, 4999, 1
- Pace, G., & Pasquini, L. 2004, *A&A*, 426, 1021
- Palla, F., & Stahler, S. W. 1993, *ApJ*, 418, 414

- Paparo, M., & Kollath, Z. 1990, in *Astronomical Society of the Pacific Conference Series*, Vol. 11, *Confrontation Between Stellar Pulsation and Evolution*, ed. C. Cacciari & G. Clementini, 336–339
- Papovich, C., et al. 2004, *ApJS*, 154, 70
- Patience, J., et al. 2011, *A&A*, 531, L17+
- Paunzen, E., Kamp, I., Weiss, W. W., & Wieseemeyer, H. 2003, *A&A*, 404, 579
- Perryman, M. A. C. 2000, *Reports on Progress in Physics*, 63, 1209
- Perryman, M. A. C., et al. 1998, *A&A*, 331, 81
- Peterson, D. M., et al. 2006, *Nature*, 440, 896
- Preibisch, T., Brown, A. G. A., Bridges, T., Guenther, E., & Zinnecker, H. 2002, *AJ*, 124, 404
- Randich, S., & Schmitt, J. H. M. M. 1995, *A&A*, 298, 115
- Raymond, S. N., et al. 2011, *A&A*, 530, A62
- Rebull, L. M., et al. 2007, *ApJS*, 171, 447
- . 2008, *ApJ*, 681, 1484
- Rieke, G. H., et al. 2004, *ApJS*, 154, 25
- . 2005, *ApJ*, 620, 1010
- . 2008, *AJ*, 135, 2245
- Roccatagliata, V., Henning, T., Wolf, S., Rodmann, J., Corder, S., Carpenter, J. M., Meyer, M. R., & Dowell, D. 2009, *A&A*, 497, 409

- Shu, F. H., Adams, F. C., & Lizano, S. 1987, *ARA&A*, 25, 23
- Sibthorpe, B., et al. 2010, *A&A*, 518, L130+
- Siegler, N., Muzerolle, J., Young, E. T., Rieke, G. H., Mamajek, E. E., Trilling, D. E., Gorlova, N., & Su, K. Y. L. 2007, *ApJ*, 654, 580
- Silverstone, M. D., et al. 2006, *ApJ*, 639, 1138
- Smith, B. A., & Terrile, R. J. 1984, *Science*, 226, 1421
- Smith, R., & Wyatt, M. C. 2010, *A&A*, 515, A95+
- Smoluchowski, M. V. 1916, *Zeitschrift fur Physik*, 17, 557
- Soderblom, D. R., & Mayor, M. 1993, *AJ*, 105, 226
- Song, I., Caillault, J.-P., Barrado y Navascués, D., & Stauffer, J. R. 2001, *ApJ*, 546, 352
- Spangler, C., Sargent, A. I., Silverstone, M. D., Becklin, E. E., & Zuckerman, B. 2001, *ApJ*, 555, 932
- Stapelfeldt, K. R., et al. 2004, *ApJS*, 154, 458
- Stauffer, J. 1982, *PASP*, 94, 678
- Stauffer, J. R., Hartmann, L. W., Prosser, C. F., Randich, S., Balachandran, S., Patten, B. M., Simon, T., & Giampapa, M. 1997, *ApJ*, 479, 776
- Stauffer, J. R., Schultz, G., & Kirkpatrick, J. D. 1998, *ApJL*, 499, L199+
- Stauffer, J. R., et al. 2005, *AJ*, 130, 1834
- Stewart, S. T., & Leinhardt, Z. M. 2009, *ApJL*, 691, L133

- Strom, R. G., Malhotra, R., Ito, T., Yoshida, F., & Kring, D. A. 2005, *Science*, 309, 1847
- Strubbe, L. E., & Chiang, E. I. 2006, *ApJ*, 648, 652
- Su, K. Y. L., Rieke, G. H., Stapelfeldt, K. R., Smith, P. S., Bryden, G., Chen, C. H., & Trilling, D. E. 2008, *ApJL*, 679, L125
- Su, K. Y. L., et al. 2005, *ApJ*, 628, 487
- . 2006, *ApJ*, 653, 675
- Taff, L. G. 1985, *Celestial mechanics: A computational guide for the practitioner*, ed. Taff, L. G.
- Takagi, Y., Mizutani, H., & Kawakami, S.-I. 1984, *Icarus*, 59, 462
- Talbot, Jr., R. J., & Newman, M. J. 1977, *ApJS*, 34, 295
- Tango, W. J., Davis, J., Thompson, R. J., & Hanbury, R. 1979, *Proceedings of the Astronomical Society of Australia*, 3, 323
- Taylor, B. J. 2006, *AJ*, 132, 2453
- Tera, F., Papanastassiou, D. A., & Wasserburg, G. J. 1973, in *Lunar and Planetary Institute Science Conference Abstracts*, Vol. 4, Lunar and Planetary Institute Science Conference Abstracts, 723--+
- Tera, F., Papanastassiou, D. A., & Wasserburg, G. J. 1974, *Earth and Planetary Science Letters*, 22, 1
- Thébault, P., & Augereau, J.-C. 2007, *A&A*, 472, 169
- Thébault, P., Augereau, J. C., & Beust, H. 2003, *A&A*, 408, 775

- Thébault, P., & Wu, Y. 2008, *A&A*, 481, 713
- Thommes, E. W., Bryden, G., Wu, Y., & Rasio, F. A. 2008, *ApJ*, 675, 1538
- Trail, D., Mojzsis, S. J., & Harrison, T. M. 2007, *Geochim. Cosmochim. Acta*, 71, 4044
- Trilling, D. E., et al. 2008, *ApJ*, 674, 1086
- Tsvetkov, T. G. 1993, *Ap&SS*, 203, 247
- Turcotte, S., & Charbonneau, P. 1993, *ApJ*, 413, 376
- Ueta, T., et al. 2006, *ApJL*, 648, L39
- Upgren, A. R., Weis, E. W., & Deluca, E. E. 1979, *AJ*, 84, 1586
- Vandenberg, D. A., & Bridges, T. J. 1984, *ApJ*, 278, 679
- Vandenbussche, B., et al. 2010, *A&A*, 518, L133+
- Venn, K. A., & Lambert, D. L. 1990, *ApJ*, 363, 234
- Wang, J. J., Chen, L., Zhao, J. H., & Jiang, P. F. 1995, *A&AS*, 113, 419
- Weinberger, A. J., Becklin, E. E., & Zuckerman, B. 2003, *ApJL*, 584, L33
- Weis, E. W. 1981, *PASP*, 93, 437
- Wennmacher, A., Lilienthal, D., & Herbstmeier, U. 1992, *A&A*, 261, L9
- Whitmire, D. P., Matese, J. J., & Whitman, P. G. 1992, *ApJ*, 388, 190
- Williams, J. P., & Andrews, S. M. 2006, *ApJ*, 653, 1480
- Williams, J. P., & Cieza, L. A. 2011, *ARA&A*, 49, 67

- Wolszczan, A., & Frail, D. A. 1992, *Nature*, 355, 145
- Woolf, N., & Angel, J. R. 1998, *ARA&A*, 36, 507
- Wyatt, M. C. 2008, *ARA&A*, 46, 339
- Wyatt, M. C., Clarke, C. J., & Booth, M. 2011, *Celestial Mechanics and Dynamical Astronomy*, 39
- Wyatt, M. C., & Dent, W. R. F. 2002, *MNRAS*, 334, 589
- Wyatt, M. C., Greaves, J. S., Dent, W. R. F., & Coulson, I. M. 2005, *ApJ*, 620, 492
- Wyatt, M. C., Smith, R., Su, K. Y. L., Rieke, G. H., Greaves, J. S., Beichman, C. A., & Bryden, G. 2007, *ApJ*, 663, 365
- Young, E. T., et al. 2004, *ApJS*, 154, 428
- Zhao, C., & Newberg, H. J. 2006, *ArXiv Astrophysics e-prints*
- Zuckerman, B., & Becklin, E. E. 1993, *ApJ*, 414, 793